HEINRICH HEINE
UNIVERSITÄT DÜSSELDORF

Fluorescence Spectroscopy and Imaging of polymer bound fluorophores and immobilised bio-molecules

Inaugural-Dissertation

zur Erlangung des Doktorgrades
der Mathematisch-Naturwissenschaftlichen Fakultät
der Heinrich-Heine-Universität Düsseldorf

vorgelegt von

Stefan Marawske
aus Hilden

Düsseldorf, November 2011

aus dem Institut für Physikalische Chemie und Elektrochemie II

der Heinrich-Heine Universität Düsseldorf

Gedruckt mit der Genehmigung der
Mathematisch-Naturwissenschaftlichen Fakultät der
Heinrich-Heine-Universität Düsseldorf

Referent: Prof. Dr. Claus A.M. Seidel
Koreferent: Prof. Dr. Peter Gilch

Tag der mündlichen Prüfung:
20.12.2011

Summary

The possible applications of fluorophores as optical sensors for local mechanical forces were explored. To that end a custom tailored chromophore (OPV5) consisting of an aromatic backbone strained by sterically demanding alkyloxy side-chains have been used. A flexible PVC matrix served to align the fluorophores by stretching. Transfer of mechanical strain from the matrix induced a geometrical change in the chromophore. Consistent with the results of semiempirical calculations on the same system, this caused a decrease in the fluorescence life-time by 2.5% (25 ps) and an increase of the emission energy by 0.2% which corresponds to a blue-shift of 1.2 nm at tensile stresses of 12 N/mm^2. The study proves the feasibility of fluo-rescence-based local force probes for polymers under tension. Necessary improvements can be achieved by developing more sensitive fluorophores and possibly by increasing the effi-ciency of force transmission from the matrix to the probe, i.e. by using modified end-groups to attach additional polymer chains as handles. Improved optical sensors of this type should in principle be able to monitor local mechanical stress in transparent samples down to the single molecule level, which can be used for reliability studies of the materials and also harbour promising further applications in polymer nano science and technology.

The high resolution imaging method iPAINT presented in this thesis successfully applied the general PAINT approach to intercalating dyes with immobilised λ-DNA molecules. It was qualitatively shown that the affinity of the intercalators to the target molecules can be influ-enced by the presence of mono- and divalent metal ions in the buffer. Very high average local-isation precision (<LP>~10-15 nm) of the analysed hits with sufficient label densities on the target molecules is achieved to yield the desired total resolution. It was also pointed out that increased label densities can even be used by further modifications of the fit algorithm.

First single molecule FRET experiments of immobilised Holliday-Junction molecules were performed. The analysis of the corresponding traces yielded relaxation rates of $\lambda=7\ s^{-1}$ which are in good accordance to already published results with the present concentrations of divalent metal ions.

Zusammenfassung

Die Anwendungsmöglichkeiten von Fluorophoren als optische Sensoren für lokale mechanische Kräfte sind untersucht worden. Dazu wurde ein eigens für diese Anwendung entwickelter Chromophor (OPV5) verwendet, der aus einem aromatischen Rückgrat und räumlich ausgedehnten Alkyloxy-Seitenketten besteht. Eine flexible PVC-Matrix wurde für die Ausrichtung der Fluorophore durch Streckung benutzt. Der Transfer von mechanischem Zug der Matrix induzierte eine geometrische Änderung im Chromophor. Im Einklang mit den Resultaten semiempirischer Berechnungen des gleichen Systems wurden eine Abnahme der Fluoreszenzlebensdauer um 2.5% (25 ps) und eine Zunahme der Emissionenergie von 0.2%, die einer Blauverschiebung von 1.2 nm entspricht, bei einer Zugbelastung von 12 N/mm^2 bestimmt. Die Untersuchungen beweisen die Realisierbarkeit von fluoreszenzbasierten lokalen Kraftsensoren zur Charakterisierung von Polymeren unter Zugspannung. Weitere nötige Verbesserungen könnten durch die Entwicklung empfindlicherer Fluorophore und durch eine Steigerung der Kraftübertragung von der Matrix auf die Probe erreicht werden. Verbesserte optische Sensoren dieser Art sind im Prinzip in der Lage lokale mechanische Kräfte in transparenten Proben auf einzelmolekularer Ebene zu untersuchen.

Die in dieser Arbeit vorgestellte hochauflösende Abbildungsmethode basierend auf dem allgemeinen PAINT Ansatz ist erfolgreich auf ein System von interkalierenden Farbstoffen und immobilisierten DNA Molekülen angewendet worden. Qualitativ wurde gezeigt, dass die Farbstoffaffinität zum Zielmolekül durch die Zugabe von mono- und bivalenten Metall Ionen beeinflusst werden kann. Sehr hohe Lokalisationsgenauigkeiten (10-15 nm) der untersuchten Treffereignisse konnten dabei mit ausreichend hohen Trefferdichten am Zielmolekül erreicht werden die für die gewünschte Gesamtauflösung benötigt werden. Es wurde auch hervorgehoben, dass noch höhere Trefferdichten durch weitere Modifikationen des verwendeten Verfahrens erzielt werden können.

Erste Einzelmolekül-FRET-Experimente an immobilisierten Holliday-Junction Molekülen sind durchgeführt worden. Die Auswertung der entsprechenden Fluoreszenzspuren ergab Relaxationsraten um $\lambda=7\ s^{-1}$, die im Einklang mit bereits veröffentlichten Ergebnissen unter Berücksichtigung der vorliegenden Konzentrationen von bivalenten Metall Ionen sind.

Table of Contents

Table of Figures

1 Introduction

The phenomenon of ”fluorescence” was already observed thousands of years ago. Even longer is the human mankind eager to investigate and understand the basic building blocks of life. But only from the 19th and 20th century on scientific findings lead to deeper insight in the understanding of fluorescence. The scientists David Brewster (1833), John Herschel (1845), Edmond Becquerel (1842) and George Gabriel Stokes (1852) investigated the emission of light from various fluorescent materials. The first fluorescent compounds were synthesised by William H. Perkin (mauve, 1856) and Adolph von Baeyer (fluorescein, 1871). In the beginning of the 20th century E. Nichols and E. Merrit were the first who measured an excitation spectrum of a dye. In the year 1919 Stern and Volmer described the quenching of fluorescence. S.J. Vavilov (1924) was the first who determined the fluorescence yield and one year later F. Perrin formulated his theory on fluorescence polarisation. In the year 1935 A. Jablonski developed his famous diagram and in 1948 T. Föster described the theory of dipole dipole interactions (Barbieri 2010).

All of these important works (and many more) lead to the fact that fluorescence techniques play a major role in the investigation of chemical and biological samples in modern science. The possibility of investigations on a single molecule level even allowed a deeper understanding of the dynamics and interactions of biomolecules.
An important prerequisite to detect fluorescence is the presence of a suitable fluorescent probe. These fluorophores are in many cases covalently attached to various kinds of samples. In this way molecular dynamics or interactions are investigated by analysing the fluorescence information of the attached fluorophores in great detail.

In the past years an increasing number of commercially available fluorophores have been developed but there is still a great request in new fluorophores with further improved fluorescence properties for special applications. Especially the combination of force and fluorescence experiments to investigate materials such as synthetic polymers has to be mentioned. Since many decades synthetics play a steadily increasing economical role. A lot of these materials are exposed to statical and dynamical forces. Detailed knowledge about these forces is the key for further improvement of any material. The fundamental target of this work is to study relations between the force impact on the molecular framework of a custom-tailored fluorophore and the manipulation of fluorescence properties of competing primary processes after electronic excitation. As a model system thin foils of highly diluted fluorophores and special polymers have been produced. The effects of applied mechanical

load on conformational changes of the fluorophores have been analysed in the framework of Multi-parameter Fluorescence Detection (MFD) on the basis of single photon counting.

A short introduction to fluorescence which is necessary to understand the analysis of this work is given in chapter 2. The home-made confocal setup (Kühnemuth and Seidel 2001) described in section 3.2 was used for the investigation of the changes in the fluorescent properties of a custom tailored fluorophore which is embedded in a polymer matrix upon stretching due to an applied external force. The custom tailored fluorophore and the experimental methods and results of this analysis are described in chapter 4. The manuscript of the corresponding publication and the supporting information to that work are found in chapter 7.

Optical microscopy is also often used to image biological samples in order to monitor structural changes or binding kinetics of interaction partners. The spatial resolution of classical far-field microscopy is limited due to the diffraction of light. As a result, the smallest structures of a sample that can be resolved are in the range of 200-300 nm in lateral dimension and 0.5-1 μm in axial dimension. In the last decade various fluorescence techniques have been developed to overcome this limit of diffraction.

The techniques can be classified into two different strategies. The first strategy which is known as RESOLFT (REversible Saturable OpticaL Fluorescence Transition) modifies the excitation conditions with sub-diffraction properties. The methods of Ground State Depletion, Stimulated Emission Depletion (Hell and Wichmann 1994) and Saturated Structured Illumination Microscopy (Keller, Schmidt et al. 2008) have been developed.

Another approach improves the resolution by precise localisation of a single fluorescent emitter. In general, a 2d-Gaussian model function is fitted to the photon distribution of a fluorophore. Within each of the diffraction limited spots only one fluorescent emitter is allowed for the time of observation. The trick is to separate signals from fluorophores in close vicinity in time. Especially the STORM approach (STochastical Optical Reconstruction Microscopy) has become the method most widely applied (Heilemann, van de Linde et al. 2008; van de Linde, Sauer et al. 2008). Here, photoswitchable fluorophores are linked to an immobilised target molecule with the help of a switching buffer. A different approach called PAINT (Points Accumulation for Imaging in Nanoscale Topography) makes use of the repetitive binding and unbinding of a fluorophore on a target molecule. Upon binding, the fluorescence quantum yield is increased by a multiple. This approach was up to now only applied on a system where the fluorophore Nile-Red was repetitively bound to lipid vesicles immobilised on a glass surface (Sharonov and Hochstrasser 2006). In this work, the high resolution imaging concept of PAINT is also successfully extended to a system of intercalating dyes which

repetitively bind to immobilised λ-DNA molecules. Here, the intercalating dye Thiazole Orange (TO) was used to image immobilised λ-DNA molecules by continuously binding and unbinding with high localisation precision (10-15 nm) and with a sufficient number of labels on the target molecules which is necessary to gain a high total resolution of a computed image.

With the help of the Total Internal Reflection Fluorescence (TIRF) setup (Axelrod, Burghardt et al. 1984) which is described in section 3.3 the measurements of the high resolution imaging concept based on the PAINT approach have been performed The theory of high resolution microscopy is described in section 2.1.4. The concept, samples, experimental methods and results of the developed high resolution imaging approach called iPAINT (intercalative Points Accumulation for Imaging in Nanoscale Topography) are described in chapter 5.

Since many years Förster Resonance Energy Transfer (FRET) measurements of molecules in solution have been performed in the group of Prof. Seidel (Widengren, Schweinberger et al. 2001; Kalinin, Felekyan et al. 2007; Sindbert, Kalinin et al. 2011). Here, the observation time of a single molecule that freely diffuses in solution is limited to the dwell time within the confocal detection volume (~ms). In this work first single molecule FRET experiments in the group of Prof. Seidel were performed to investigate immobilised biomolecules with observation times of ~30 s. Here, double labelled Holliday Junction molecules which have been studied in previous FRET experiments in solution (Valeri 2009) served as biomolecules that were immobilised and analysed.

A further modification of the TIRF setup which is described in section 3.3.2 was necessary to investigate the energy transfer of excited donor molecules to acceptor molecules in close vicinity of double labelled biomolecules which were immobilised on a surface. The theory of the Förster Resonance Energy Transfer (FRET) is described in section 2.1.3. The concept and results of the single molecule FRET measurements of immobilised biomolecules are described in chapter 6.

2 Theory

2.1 Fluorescence

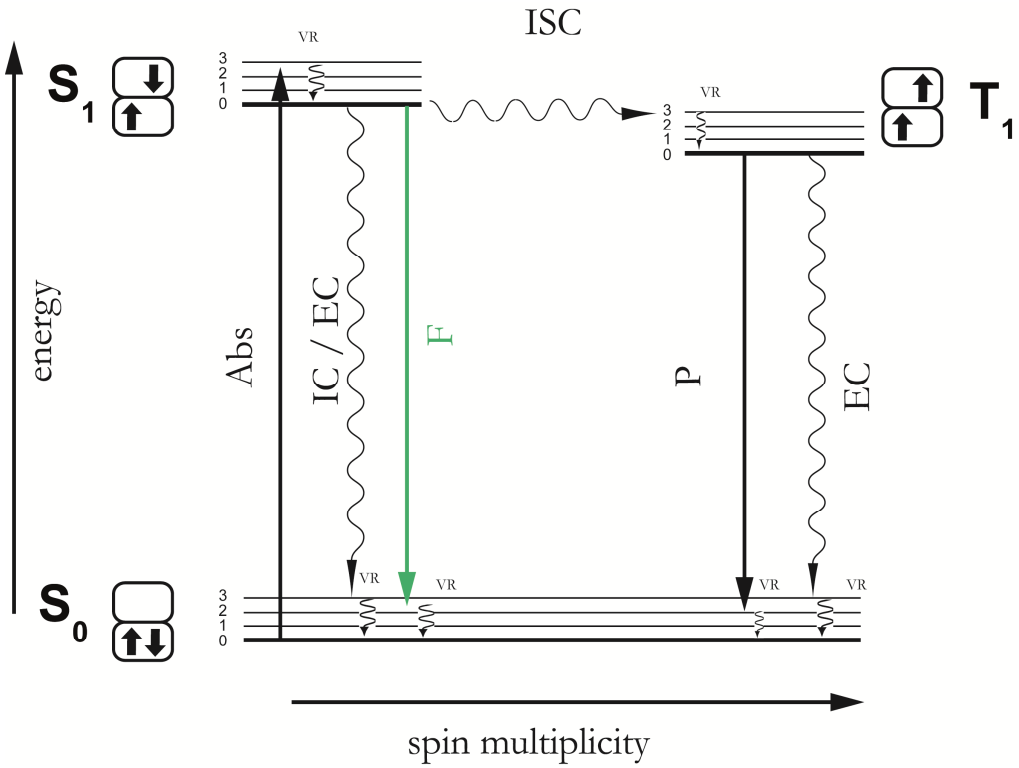

Figure 1 Jablonski Diagram

Scheme of the electronic states and the corresponding vibrational substates of a fluorophore. Excitations into higher electronic states are not shown. **S_0**: singlet ground state, **S_1**: first excited singlet state, **T_1**: first excited triplet state. Possible transitions between the states are also shown. **Abs**: absorption of radiation and transition into a higher electronic singlet state (any vibrational substate), **F** (fluorescence): radiative transition from S_1 to S_0, **IC** (internal conversion): radiationless transition between two state with the same spin multiplicity, **ISC** (intersystem crossing): isoenergetic radiationless transition between two states having different spin multiplicity, **EC** (external conversion): A radiationless transition which leads to the depopulation of an excited state due to collisions and quenching with other molecules or by energy transfer to the solvent or other unexcited molecules, **P** (phosphorescence): radiative transition between T_1 and S_0, **VR**: vibrational relaxation to the lowest vibrational state of the corresponding electronic state. The arrows indicate the spin multiplicity.

When any kind of specimens absorb electromagnetic radiation and subsequently re-emit light, the process is described as photoluminescence. The wavelength domain in which the specimen absorbs and emits the light is determined by the energy levels of its electronic states.

The electronic states and the transitions between the states can be described by a Jablonski diagram (according to the physicist Aleksander Jablonski) which is shown in Figure 1. The states are ordered

vertically with respect to energy (electronic states (thick lines) and vibrational substates (thin lines)) and horizontally with respect to spin multiplicity (arrows in boxes). A detailed discussion about all possible transition pathways is described in many textbooks (Turro 1991; Lakowicz 2006).

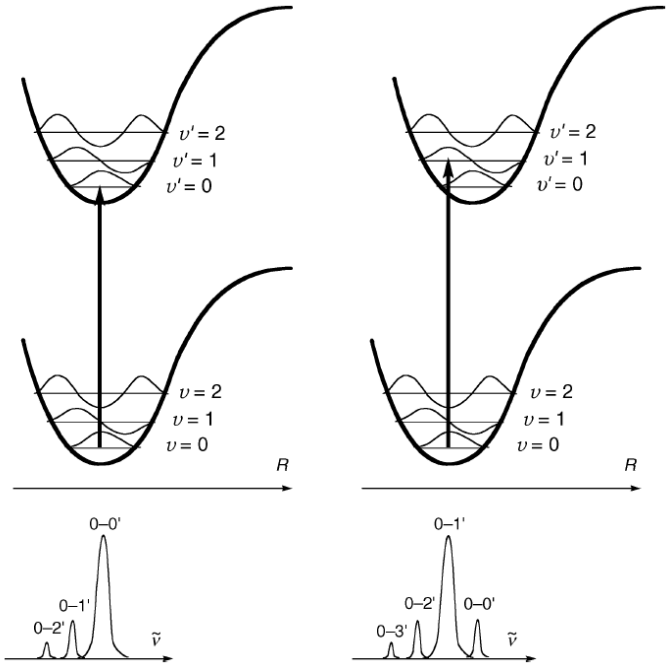

Figure 2 Franck-Condon principle

The intensity of a vibronic transition is proportional to the square of the Franck-Condon integrals between the vibrational wavefunctions of the two states which are involved in the transition. The band shape of an electronic transition is dependant on the displacement of the excited electronic state relative to the ground state. This is shown in the upper diagrams. The lower diagrams show the vibrational structure of the absorption bands. The illustration was taken from (Klàn and Wirz 2009).

After absorption of a photon with suitable energy, an electron is promoted from the ground state S_0 to a state of higher energy, an excited state. As the mass of an electron is much smaller than the mass of the nuclei ($m_e/m_p \sim 1836$), an electronic transition happens takes places on a very fast time scale so that any displacement of the nucleus can be neglected. In a classical view the nuclei start to oscillate around their original equilibrium coordinates (Atkins and de Paula 2001). All electronic transitions are vertical and the probability to populate a vibrational level of the excited state is highest where the vibrational wave functions of the ground state and that of the excited state show the most significant overlap. This phenomenon is well-known as the Franck-Condon principle (Condon 1926; Franck and Dymond 1926), which is illustrated in Figure 2. The Franck–Condon principle is applied equally to absorption and to fluorescence which is explained later in this section. After absorption ($\sim 10^{-15}$s), the molecule relaxes (vibrational relaxation, VR, $\sim 10^{-12}$s) to the lowest vibrational state of the first excited state (typical lifetime of $\sim 10^{-8}$s), which is known as Kasha's rule (Kasha

1950), from which the electron for example can return into the ground state via the emission of a photon.

From the quantum-mechanical perturbation theory following "Fermi's golden rule" one can derive the transition probabilities from one state to another calculating the corresponding transition matrix elements. A resulting selection rule tells us that only those electronic transitions are "allowed" (non-zero transition matrix element) where the spin multiplicity of the electrons (e.g. singlet-singlet transition: $M= 2S+1 =1$ ($\Delta S=0$)) is conserved. States with anti-parallel electron spin correlation are called singlet states. The electronic ground state is called S_0 and all other singlet states are called S_1, S_2, S_3 … ordered in ascending order with respect to their energy levels. Molecules are typically excited into their singlet states. Usually the excitation energy is chosen to excite a molecule into its S_1 state from which the electron returns into any vibrational state of the ground state S_0 under the emission of a photon. This process is called fluorescence (green arrow in Figure 1).

Electronic transitions from singlet states into states with electron spin multiplicity M=3 (triplet states T_1, T_2, T_3…) are called "forbidden" which means that the transition between these states are very unlikely but not impossible.

In addition to fluorescence, there are competing processes which also lead to the depopulation of the excited states. If a radiationless transition from the excited state S_1 to a highly excited vibrational state of the ground state S_0 occurs (in general a radiationless transition between two electronic states of the same multiplicity), the process is called "internal conversion" (IC). A radiationless transition which leads to the depopulation of an excited state due to collisions with other molecules or by energy transfer to the solvent or other unexcited molecules is called "external conversion" (EC). A "forbidden" transition between singlet state S_1 and triplet state T_1, which can nevertheless occur due to spin-orbit coupling, is called "inter system crossing" (ISC). Furthermore, the triplet state T_1 is depopulated either by "external conversion" as explained or by the emission of a photon. The lifetime of the triplet state T_1 is around 10^{-6}s (up to s) and the photon emission from that state is called phosphorescence.

The kinetics of these processes is described by their corresponding rate constant (k_i).

The fluorescence emission spectrum of typical fluorescent molecules shows a red-shift in wavelength in comparison to its absorption spectrum. The reasons for this effect is on the one hand the very fast relaxation to the vibrational ground level of the excited state (loss of energy) from which the emission of a fluorescence photon occurs (Franck-Condon principle, Kasha's rule) and on the other hand the relaxation of nearby solvent molecules which leads to a decrease of the excited state energy level. This effect was first observed by Sir George Gabriel Stokes in 1852 (Stokes 1852) and is known as the Stoke-Shift. A direct consequence of Kasha's rule is also that the fluorescence emission spectrum is generally independent on the excitation wavelength.

2.1.1 Fluorescence Lifetime and Quantum Yield

Two of the most important parameters of fluorescent molecules are the fluorescence lifetime (τ) and the fluorescence quantum yield (Φ_F). The fluorescence quantum yield is generally defined as the ratio between the number of adsorbed photons and the number of emitted photons by fluorescence:

$$\Phi_F = \frac{\#\text{fluorescence photons}}{\#\text{adsorbed photons}} \leq 1 \qquad \text{Equation 1}$$

If we only consider depopulation transitions of the first excited state S_1 that are mentioned in section 2.1, the fluorescence quantum yield can be defined by the corresponding rate constants of these processes,

$$\Phi_F = \frac{k_F}{k_F + k_{IC} + k_{ISC}} \qquad \text{Equation 2}$$

k_i are the corresponding rate constants of the involved depopulations processes as already discussed. The time-dependant behaviour of fluorescence emission from a sample of excited molecules is governed by the involved depopulation processes of the first excited state S_1. If we blank at first the nonradiative processes and only consider fluorescence, the time rate of change for the number of excited molecules is:

$$\frac{dS_1}{dt} = -k_F \cdot S_1 \qquad \text{Equation 3}$$

The integration of this differential equation leads to

$$F(t) = F(0) \cdot \exp(-k_F \cdot t) \qquad \text{Equation 4}$$

where F(0) is the fluorescence emission at t=0 which is proportional to the number of excited molecules. The time at which the fluorescence signal has dropped to 1/e of its initial value is called the natural lifetime or the radiative lifetime $\tau_0 = 1/k_F$.

Usually, the nonradiative processes cannot be neglected so that a more realistic view on the time dependant behaviour leads to

$$F(t) = F(0) \cdot \exp\left(-t/\tau\right)$$ Equation 5

with $\tau=1/(k_F+k_{ISC}+k_{IC})$ which is the observed lifetime also called fluorescence lifetime. The fluorescence lifetime τ is therefore generally smaller (maximum equal) than the natural lifetime τ_{rad}.

For any kind of fluorescence analysis it is important to know the lifetime of a fluorophore's excited state.

A detailed description of the natural fluorescence rate k_F and therefore the related radiative lifetime τ_{rad} was derived by Strickler & Berg (Strickler and Berg 1962) from the interaction of photon absorption and fluorescence emission which is valid for a wide range of organic molecules

$$k_F = 2.88 \cdot 10^{-9} \cdot \left\langle \tilde{\nu}_F^{-3} \right\rangle_{av}^{-1} \cdot n^2 \cdot \int \varepsilon(\tilde{\nu})\ d\ \ln(\tilde{\nu}), \text{ with}$$

$$\left\langle \tilde{\nu}_F^{-3} \right\rangle_{av}^{-1} = \int \frac{F(\tilde{\nu})\ d\nu}{\tilde{\nu}^{-3}\ F(\tilde{\nu})\ d\nu}$$ Equation 6

where $\tilde{\nu}$ is the wave number, n the index of refraction of the solvent, ε the molar absorption coefficient and $F(\upsilon)$ describes the spectral distribution of the emission in photons per wavelength interval. Especially the influence of changes in the refractive index on the fluorescence lifetime τ is further discussed in section 4.3.

A mono-exponential decay, as mentioned above, is only valid for an ensemble of identical molecules in identical states in the same environment.

A mixture of different molecules or different states of the same molecule which may occur e.g. due to interactions with the solvent lead to a much more complex temporal behaviour that can be described by a multi-exponential decay model:

$$F(t) = \sum_i A_i(0) \cdot \exp\left(\frac{t}{\tau_i}\right)$$ Equation 7

where A_i are the absolute amplitudes of the corresponding lifetime components. From this one can obtain the species fractions which are defined by $x_i=A_i/\Sigma A_i$.

2.1.2 Fluorescence Anisotropy

Electromagnetic waves with a defined direction with respect to the wave vector are considered to be polarised. The polarisation of light emitted by any fluorescent probe can be attributed to various properties of a molecule such as its conformation, orientation, size etc. as well as its direct environment (e.g. viscosity) in which it is located. In experiments to measure the fluorescence polarisation or the anisotropy, monochromatic and linearly polarised light (along z-axis) is irradiated on the sample. The emitted light is measured in both the parallel and perpendicular planes relative to the excitation polarisation. The fluorescence polarisation and the fluorescence anisotropy are both derived from the measured parallel and perpendicular intensities. The values are mathematically related and easily interconvertible. While anisotropy and polarisation share the same content of information, anisotropy values are from a mathematically point of view easier to handle. The fluorescence anisotropy r is in general defined as follows:

$$r = \frac{F_{\text{II}} - F_{\perp}}{F_{\text{II}} + 2 \cdot F_{\perp}} = \frac{F_{\text{II}} - F_{\perp}}{F_{\text{tot}}} \qquad \text{Equation 8}$$

The parameters $F_{\parallel}$ and $F_{\perp}$ are the parallel and perpendicular polarisation components with respect to excitation polarisation.

In order to absorb polarised light, the transition dipole moments of the fluorophores do not need to be orientated exactly parallel to the incoming light's polarisation. The probability of polarised light to be absorbed by a randomly oriented ensemble of fluorophores is proportional to $\cos^2(\theta)$.

The angle θ is the angle being present between the dipole and the z-axis at the time of absorption, see Figure 3.

The probability of being excited is the same for all molecules with the same angle θ and shows rotational symmetry with respect to the z-axis. This fact leads to a selected population of excited fluorophores which are partially oriented along the z-axis when irradiated with polarised light. This phenomenon is called "photoselection" which means that only those molecules which are oriented properly absorb light, get excited, and subsequently begin to fluoresce.

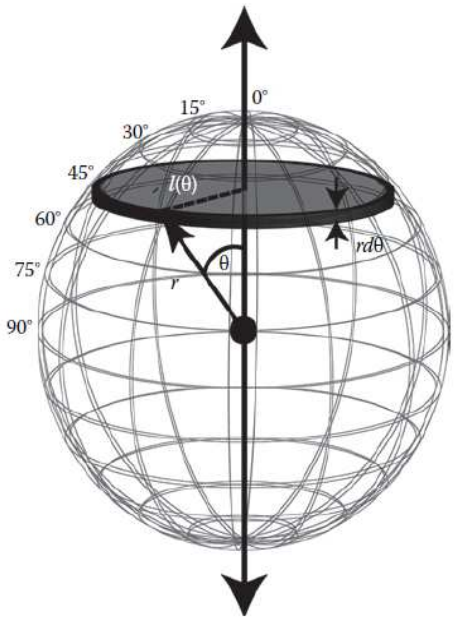

Figure 3 Random dipole orientation distributions

The electric field orientation of a linearly polarised light source is represented by a double arrow and the absorption dipole moment of a fluorophore is indicated by a single arrow with an angle θ between these two vectors. All fluorophores with the same angle θ will be excited with the same probability. Here, the population of all fluorophore orientations is represented by the collection of all circles of latitude. The illustration was taken from (Vogel, Thaler et al. 2009)

Taking the parallel and perpendicular components dependant on the angle θ into account which are $F_{\parallel}=\cos^2(\theta)$ and $F_{\perp}=0.5\cdot\sin^2(\theta)$, the averaging of all orientations of an ensemble of randomly oriented fluorophores lead to:

$$r=\frac{3\cdot\left\langle\cos^2(\theta)\right\rangle-1}{2},\quad \left\langle\cos^2(\theta)\right\rangle=\frac{\int_0^{2\pi}\cos^2(\theta)f(\theta)d(\theta)}{\int_0^{2\pi}f(\theta)\mathrm{d}(\theta)}=\frac{3}{5}\quad\uparrow\uparrow \qquad \text{Equation 9}$$

Here, the anisotropy depends on the average value of $<\cos^2(\theta)>$. The maximum value of the fluorescence anisotropy is 0.4 which corresponds to a collinear orientation (↑↑) of the absorption and emission dipole in the absence of any depolarisation process.

In a more realistic view, the observed anisotropy is not only influenced by the effect of photoselection as just explained but also depends on the relative orientation between the absorption and emission dipoles of an ensemble of molecules.

In case of an isotropic ensemble in solution all dipole moment orientations of absorption and emission occur with equal probability resulting in an averaged orientation at the time of excitation. The angle between absorption and emission dipole moment (orientation of the transition dipole moment) is defined as the angle β.

If the orientation of the transition dipole moment does not change for the excited state, the fundamental anisotropy r_0 can be defined as follows:

$$r_0 = \frac{2}{5} \cdot \frac{3 \cdot \cos^2(\beta) - 1}{2} \qquad \text{Equation 10}$$

The data range of the angle β is $0 \leq \beta \leq \pi/4$. Thus, it follows the data range of the fundamental anisotropy $-0.2 \leq r_0 \leq 0.4$. The fundamental anisotropy is an intrinsic property of the fluorophore being investigated. This property can only be observed if all other depolarisation effects such as e.g. rotational diffusion are absent or suppressed. Therefore, measurements of the fundamental anisotropy are often performed in viscous medium such as glycerol.

At this point it is also important to point out that the minimum and maximum values just given are only true for a randomly oriented ensemble of molecules. From the general definition of the fluorescence anisotropy given in Equation 8 it is clear that the maximum value for the anisotropy is equal to 1 for a selection of molecules with collinear orientation with respect to excitation and defined angle $\beta=0$ between absorption and emission dipoles.

The previous argumentation assumes no degeneracy of the energy levels.

Further aspects of anisotropy will not be discussed in this thesis. A detailed description about anisotropy can be found in literature (Kusba and Lakowicz 1999; Lakowicz 2006).

2.1.3 Förster Resonance Energy Transfer (FRET)

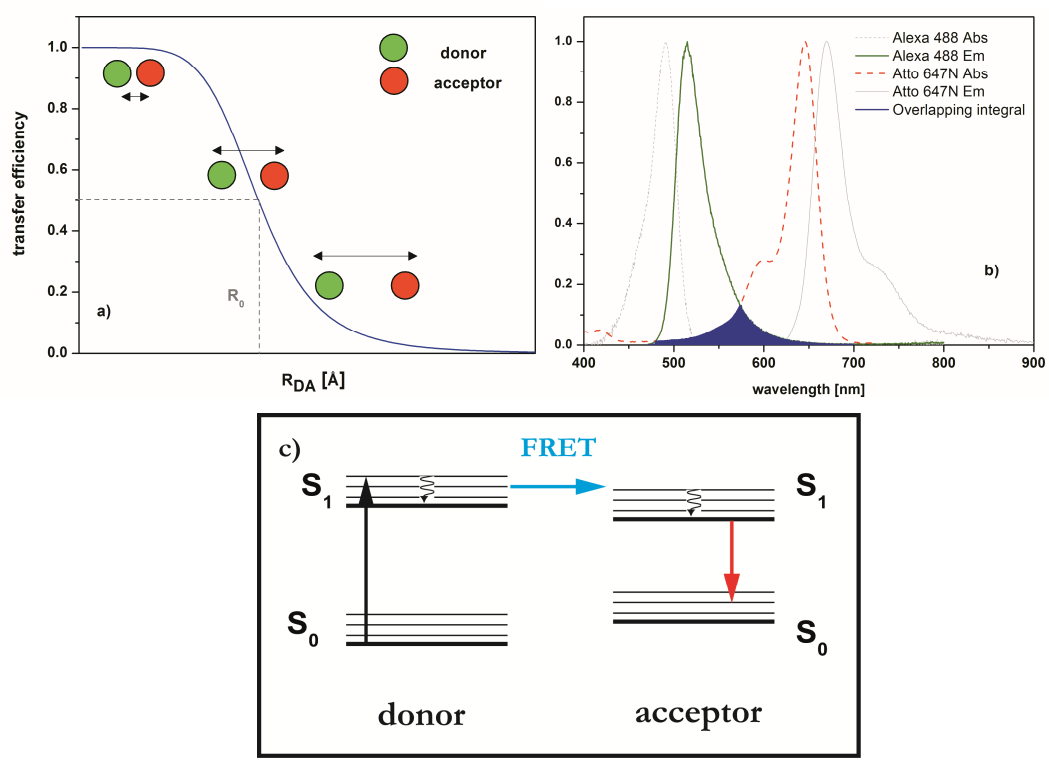

Figure 4 Förster Resonance Energy Transfer

a) the Förster Resonance Energy Transfer efficiency is strongly dependant on the distance between the two fluorophores. b) a spectral overlap (blue) between the emission spectrum of the donor (green) and the absorption spectrum of the acceptor (red) is also required (centre graph). c) if the orientation of the dipole moments of donor and acceptor (not shown) match, the energy absorbed by the donor is transferred to the acceptor which further on can emit a fluorescence photon in order to return to its electronic ground state.

The Förster Resonance Energy Transfer (FRET) is a radiationless energy transfer mechanism where the energy of a donor molecule is transferred to an acceptor molecule by dipole-dipole interactions (Förster 1948). A characteristic of this transfer is the conservation of electron spin configuration. That is why this transfer mechanism is typically considered as a singlet-singlet-transfer. Several conditions have to be fulfilled simultaneously to let this energy transfer happen. At first, the acceptor has to be in very close vicinity to the donor. Secondly, the emission spectrum of the donor and the absorption spectrum of the acceptor have to show a certain overlap. Thirdly, the orientations of the dipole moments of donor and acceptor have to match to some extend. The dependency of these orientations can be described by the orientation factor κ^2 (see also Equation 12).

The FRET transfer efficiency (E_T) and therefore the quantum yield of the energy transfer is defined in accordance to the fluorescence quantum yield

$$E = \frac{k_{FRET}}{k_F + k_{FRET} + \sum_i k_i}$$ Equation 11

where k_{FRET} is the rate constant of the energy transfer, k_F the fluorescence rate constant and k_i the rate constants of any other depopulation processes being involved.

The rate constant of the energy transfer k_{FRET} is dependant on the orientation factor κ^2, the fluorescence quantum (Φ_{FD}) of the donor without an acceptor being present, the refractive index n of the solvent, the fluorescence lifetime ($\tau_{D(0)}$) of the donor without an acceptor, the distance between donor and acceptor (R_{DA}) and the overlapping integral ($J(\lambda)$) of donor emission and acceptor absorption as shown in Equation 12.

$$k_{FRET} = 8.79 \cdot 10^{23} \cdot \frac{\kappa^2 \Phi_{FD} J(\lambda)}{n^4 \tau_{D(0)} R_{DA}^6} s^{-1}$$ Equation 12

Giving this, the energy transfer efficiency can also be expressed by the distance of the donor and the acceptor molecules:

$$E = \frac{1}{1 + \left(\frac{R_{DA}}{R_0} \right)^6}$$ Equation 13

Here, R_0 is the distance (also known as the Förster radius) at which the energy transfer efficiency is equal to 0.5. A detailed description of the Förster Resonant Energy Transfer can be found in literature (Clegg 1992). First single molecule experiments on FRET were performed in 1996 (Ha, Enderle et al. 1996). As the energy transfer efficiency is strongly dependant on the distance of the two molecules, FRET has also become a molecular ruler for in particular many dynamical biological systems (Stryer 1978; Schuler, Lipman et al. 2002; Schuler and Eaton 2008).

In order to reveal the actual transfer efficiencies or the actual distances between donor and acceptor, a number of correction parameters have to be introduced (e.g. dipole orientations, background, quantum yields or spectral cross-talk). The FRET efficiency can be calculated from fluorescence lifetimes or from fluorescence intensities which are both accessible in FRET solution experiments.

In case of a single molecule experiment where a double labelled probe is immobilised on a surface, an apparent energy transfer efficiency E_{app} which is also called proximity factor (PF) is introduced which is defined in Equation 14.

$$E_{\text{app}} = \text{PF} = \frac{F_A}{F_A + F_D} \qquad \text{Equation 14}$$

The fluorescence intensities F_A and F_D are the background corrected acceptor and donor intensities. The apparent FRET efficiency reflects just an approximation of actual donor acceptor distance because of the uncertainties in the orientation factor κ^2 and further correction parameters mentioned above as the labelled molecule is bound to a surface. A corrected FRET efficiency E_T can further on be calculated

$$E = \left(1 + \gamma \frac{F_A}{F_D}\right)^{-1} \frac{F_A}{F_A + F_D}, \quad \gamma = \frac{\Delta F_A}{\Delta F_D} \qquad \text{Equation 15}$$

where ΔF_A and ΔF_D are the differences for the corresponding intensities to change in donor intensity and upon acceptor bleaching respectively (Roy, Hohng et al. 2008).

Further optimisation strategies to reveal the actual FRET efficiencies can be found in literature (McCann, Choi et al. 2010).

2.1.4 Superresolution Microscopy

In the last years many different techniques have been developed to further increase the resolution in fluorescence microscopy. In order to understand these improvements, a short overview will be given in order to describe the physical limitations for the enhancement of resolution and to point out the benefits of these techniques.

The Italian physicist and mathematician Francesco Maria Grimaldi was one of the first who analysed the propagation of light at an aperture which could not be explained by geometrical optics and coined the word diffraction. The explanation for this phenomenon was given by Thomas Young in 1802. In his famous double slit experiment he demonstrated the wavelike properties of light that have been proposed by Christiaan Huygens and rejected by other physicists such as Sir Isaac Newton for more than a century.

Diffraction or interference occurs when waves with fixed temporal and spatial phase shift (coherence), which is true for laser light, hit a barrier (aperture) and overlay at a certain point behind that

aperture due to the superposition principle. Hereby, the size of the aperture has to be smaller than the wavelength of the incident waves. At each point within the aperture, spherical waves are generated that interfere with each other due to the Huygens principle.

In general there are two different kinds of diffraction. In the case of incident and diffracted plane waves the phenomenon is called Fraunhofer diffraction which describes the far-field approximation of diffraction. If the curvature of the incident and diffracted waves cannot be neglected due to close vicinity of the origin and the observation point to the aperture, the Fresnel diffraction describes the near-field character.

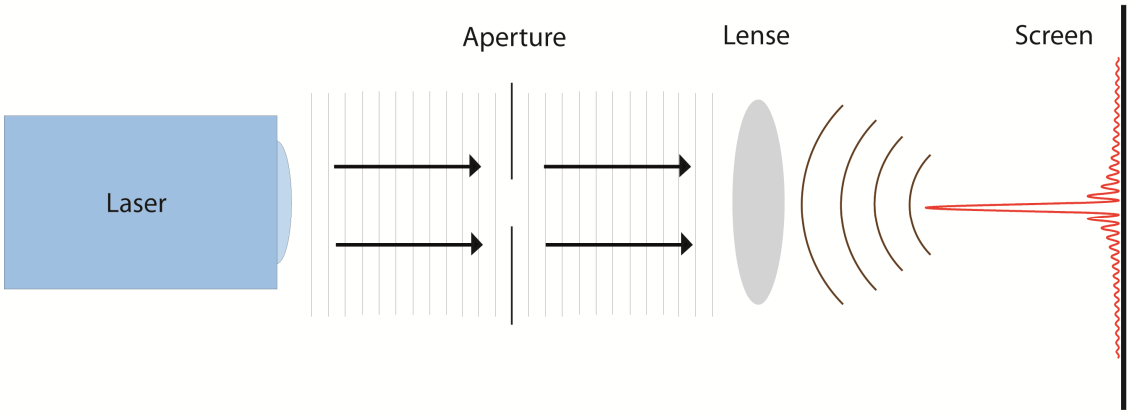

Figure 5 Optical arrangement scheme for diffraction in a microscope

Coherent laser light hits an aperture and overlays on a screen (focused by a lense) behind that aperture due to the superposition principle (red: diffraction pattern). If the light source and the screen are far away from the aperture the curvature of the incident and diffracted waves can be neglected and approximated as planar waves (light grey lines). The far field approximation of diffraction is described by the Fraunhofer diffraction.

If $a^2/\lambda L < 1$, where a describes the area of the aperture, L the distance between observation point and aperture and λ the wavelength, the Fraunhofer diffraction theory can be applied to describe the diffractive conditions for a microscope which is shown in Figure 5.

A mathematical description in case of Fraunhofer diffraction based on a boundary value problem was given by Gustav Kirchhoff assuming scalar waves. This is justified for many problems in optics:

$$\Psi(u,v) = C\iint f(x,y)e^{-i(ux+vy)}dxdy \qquad \text{Equation 16}$$

where f(x,y) reflects the geometry of the aperture and (u,v) the coordinates of a point in the diffraction pattern. In case of a microscope a circular aperture is present so that a change to polar coordinates is necessary (see Equation 17).

$$x = \rho \cdot \cos(\varphi) \qquad y = \rho \cdot \sin(\varphi)$$
$$u = \xi \cdot \cos(\vartheta) \qquad v = \xi \cdot \sin(\vartheta)$$

Equation 17

The polar coordinates (x,y) describe a point inside the aperture and polar coordinates (u,v) a point in the diffraction pattern. If r is the radius of the aperture the integral can be written as:

$$\Psi(\xi,\vartheta) = C\int_0^r \int_0^{2\pi} e^{-i\rho\xi\cos(\vartheta-\varphi)}\,\rho d\rho d\vartheta$$

Equation 18

This integral can be solved with the help of the Bessel function of the first kind of order one. The fact that the observed intensity is the square of the wave function results in:

$$I(P) = \left|\Psi(\xi,\vartheta)\right|^2 = I_0\left|\frac{2J_1(\xi r)}{r\xi}\right|^2$$

Equation 19

The solution for the diffraction pattern is independent on the angle ϑ. The 3d diffraction pattern and the radial dependency of the intensity are shown in Figure 6.

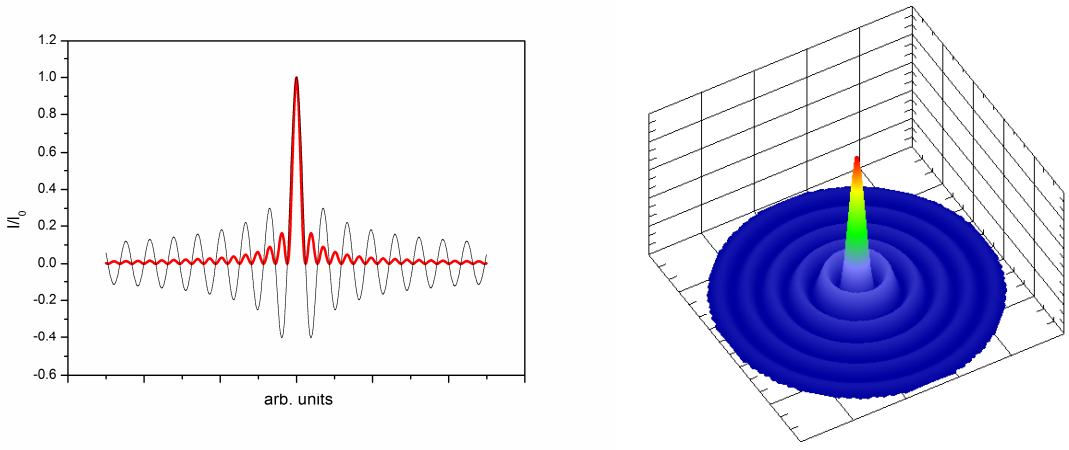

Figure 6 Diffraction pattern at a circular aperture

The radial dependency (arbitrary units) of the wave function (black) and the of the intensity (red) is shown on the left hand side. On the right hand side a 3d illustration of the wave function is given.

The function $y=2J_1(x)/x$ (black curve) is 1 at x=0 and is decreasing at first with increasing x and later oscillating around Zero with further decreasing amplitude. The minima of this function dependant on the radial distance r can be found at:

$$\sin(\vartheta) \approx 1.22\lambda/2r, 2.23\lambda/2r, \ldots\ldots \qquad \text{Equation 20}$$

The intensity distribution within the first minima is also called the "airy disc" which holds around 85% of the total intensity information. A complete mathematical description on diffraction can be found in literature (Born and Wolf 1980).

From this it follows the definition for the resolution of an optical system which is known as the Rayleigh criterion.

Two spots of light can still be "resolved" if the distance of the two main maxima is not smaller than the distance of the main maxima to the first minima of one of the diffraction patterns, see also Figure 7.

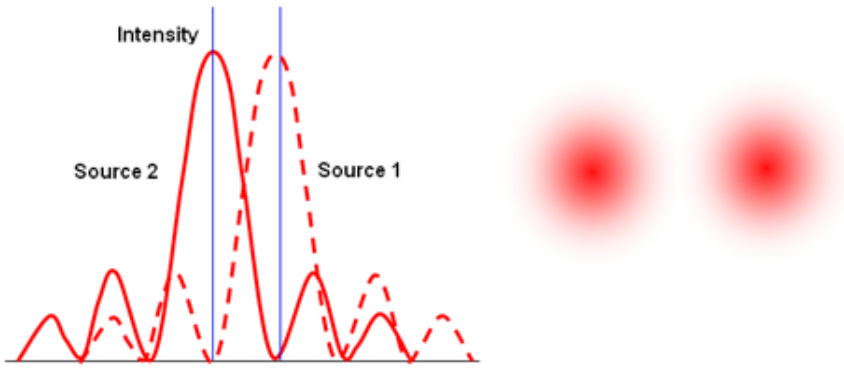

Figure 7 Rayleigh criterion

Two spots of light can still be "resolved" if the distance of the two main maxima is not smaller than the distance of the main maxima to the first minima of one of the diffraction patterns. The illustration was taken from (TAP 2011).

The resolution in case of a microscope was described by Ernst Karl Abbe,

$$d = \frac{1.22\lambda}{2 \cdot NA} \qquad \text{Equation 21}$$

where NA=n sin(ϑ) is called the numerical aperture which described the opening angle of an objective, n the refractive index and d is the minimum distance of any 2 spots that can be resolved.

But even with modern objectives with very high numerical aperture (e.g. Olympus APON 60XOTIRF, NA=1.49) the best resolution that is achieved is, as a rule of thumb, half of the wavelength of the incident light. The lowest available wavelength for modern lasers with necessary performance is 400 nm for observations in the visible spectral range so that the minimum size of an object still to be resolved in lateral direction is about 150 nm. In the last decade a couple of techniques in fluorescence microscopy have been developed to break this diffraction limit. In general, these techniques can be roughly divided into two different approaches.

At first, the strategy to modify the excitation conditions with sub-diffraction properties is classified as RESOLFT (REversible Saturable OpticaL Flurorescence Transitions) method. A fluorophore can selectively been switched between a bright and a dark state by irradiation with light of a specific wavelength.

The dark state is either a long-lived state such as the triplet state (GSD, Ground State Depletion) or the electronic ground state (STED, STimulated Emission Depletion). In addition to a standard excitation laser a second laser with a doughnut-shaped profile at high intensities (Zero intensity in the center) is used to deplete the region around the excitation area. As the size of the overlay pattern is not limited by diffraction, a super-resolution image can be obtained by sequential scanning of the sample. The STED technique was first described in 1994 (Hell and Wichmann 1994) and successfully applied on organic fluorophores (Kasper, Harke et al. 2010), on biological samples such as proteins (Kittel, Wichmann et al. 2006; Sieber, Willig et al. 2006) or vesicles in living cells (Westphal, Rizzoli et al. 2008).

Another technique that makes use of the RESOLFT principle is Saturated Structured Illumination Microscopy (SSIM). Here, a line-shape modulated excitation pattern with alternating intensity maxima and minima is generated. In addition, the excitation leads to signal saturation creating dark lines adjacent to lines with high fluorescence signal. A stepwise rotation while scanning the sample and post-procession of the recorded "negative" images lead to a 3d reconstruction as shown in case of a long-term embryonic development observation of a Zebrafish (Keller, Schmidt et al. 2008; Keller, Schmidt et al. 2010).

The optical resolution for all of these techniques is determined by the actual size of the point spread function. A nice overview and further details of these techniques just described can be found in literature (Huang, Bates et al. 2009; Schermelleh, Heintzmann et al. 2010).

Secondly, the resolution can dramatically be improved by precise localisation of a single fluorescent emitter's position. A mandatory prerequisite is to generate measurements conditions that guarantee only a single emitter within a diffraction limited spot at the same time. One trick is to separate the fluorescence signals of two fluorophores that are close together in time.

Fitting an appropriate model function to the diffraction limited intensity distribution of such a single isolated fluorophore, a synthetic superresolution image can be created by superimposing all individual localisations within a series of images. A well suitable model for the intensity distribution would be an airy-distribution, but as this model is rather complicated and time consuming, it was shown that under typical conditions of single molecule detection a 2d-gaussian distribution is well justified (Cheezum, Walker et al. 2001). In case of a fixed dipole orientation of a fluorophore one has to keep in mind that the point spread function is in general asymmetric so that a symmetric 2d-gaussian model function will not achieve the theoretical localisation accuracy (Enderlein, Toprak et al. 2006; Stallinga and Rieger 2010).

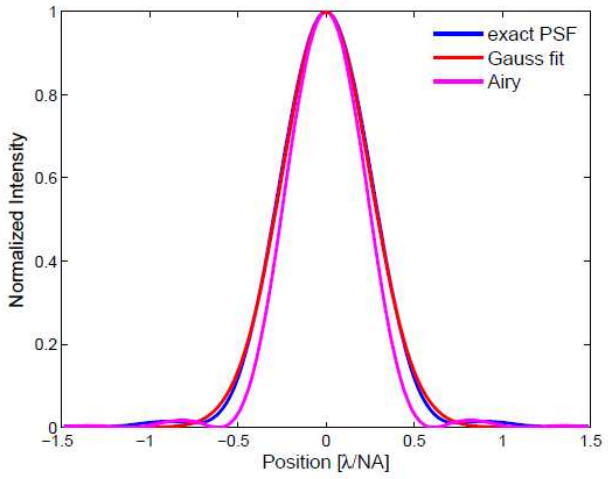

Figure 8 2d-gaussian distribution approximation

Dipole orientation averaged point spread function. This diagram was taken from (Stallinga and Rieger 2010)

A mathematical description of the 2d-gaussian model function is given in Equation 22:

$$f(x,y) = A \cdot \exp\left[-\frac{(x-x_0)^2}{2\sigma_x^{\,2}} - \frac{(y-y_0)^2}{2\sigma_y^{\,2}} \right] + B \qquad \text{Equation 22}$$

Here, A is the amplitude of the Gaussian distribution, x_0 and y_0 the centre positions, σ_x and σ_y the measures of the width of the distribution and B the background contribution. The most important feature is that even if the observable size of an object is limited by diffraction, the centre of an object can be determined with very high precision for a certain number of photons (Bobroff 1986). Later on, a full mathematical description has been derived (Thompson, Larson et al. 2002) giving an overall error estimation of the localisation precision LP:

$$LP = \sqrt{\frac{\sigma^2}{N_F} + \frac{a^2/12}{N_F} + \frac{8\pi \cdot \sigma^4 \cdot N_B}{a^2 \cdot N_F^2}} \qquad \text{Equation 23}$$

with σ being the standard deviation of the model function, a the effective pixel size, N_B the number of background photons and N_F the number of primary fluorescence photons. The localisation precision of the centroid position is mainly dependant on the overall fluorescence intensity of the emitter if the background noise is comparatively low. The higher the number of photons emerged by fluorescence, the smaller the uncertainty in localisation precision.

Throughout the years a variety of techniques were established, all make use of the just explained improved localisation, the difference is more or less the way how the measurement conditions are chosen that justify the just mentioned treatment of the data. These techniques are embraced by the term localisation microscopy.

The FIONA technique (Fluorescence Imaging with One Nanometer Accuracy) makes use of stabilising the fluorescence signal by an oxygen-scavenging system that lead to a localisation precision of around 1nm (Kural, Balci et al. 2005; Yildiz and Selvin 2005). Here I have to mention that this work mixed the definition of background and background noise which is not in accordance to the original mathematical description (Thompson, Larson et al. 2002). The denoted ratio of 10000 fluorescence photons over 1 background photon within an integration time of 1 s used in their calculations seems also quite questionable to me.

The STORM approach (STochastic Optical Reconstruction Microscopy) uses photoswitchable fluorophores attached to biomolecules that can be cycled between a dark and a bright state for hundreds of seconds if a second dye is in close vicinity. A red laser excites the Cyanine5 (Cy5) dye and further switches the dye to its dark state whereas a secondary green laser returns it back to the fluorescent state in an alternating manner (Rust, Bates et al. 2006). The recovery rate is strongly dependant on the close proximity of the secondary dye Cyanine3 (Cy3). The STORM approach was further evolved to dSTORM (direct STORM) where only one fluorophore is needed. Here, a long-lived dark state is created by the usage of a switching buffer in combination with high excitation power of the red laser. This technique was also successfully applied to cells (Heilemann, van de Linde et al. 2008; van de Linde, Sauer et al. 2008).
Another publication which uses an approach very similar to dSTORM showed high resolution imaging of DNA molecules with intercalating dyes. The dimeric cyanine dye TOTO-1 with very high

affinity for DNA shows almost no fluorescence quantum yield if freely diffusing in solution but a strong increase when intercalating into DNA. A single green laser at high excitation power and a switching buffer very similar to that used for dSTORM let the dyes blink to be distinguishable in time. With this technique a resolution of around 40 nm is achieved (Flors, Ravarani et al. 2009). A further sophisticated work on a similar system has reported a resolution of around 14 nm (Schoen, Ries et al. 2011). The PALM approach (photoactivated localization microscopy) isolates single molecules by photoactivation and subsequent photobleaching of photoactivatable fluorescent protein for many cycles where a localisation precision of 10nm was achieved (Betzig, Patterson et al. 2006). A similar system that was developed in parallel is published as FPALM (fluorescence photoactivation localization microscopy) yielding a full wifth at half-maximum of around 80nm (Hess, Girirajan et al. 2006).

A final example for localisation microscopy is the PAINT approach (points accumulation for imaging in nanoscale topography). Here, the separation of fluorophores is achieved by consecutive binding and unbinding of a non-fluorescent dye Nile-Red if in solution with dramatically increased fluorescence quantum yield when bound to lipid vesicles attached to a glass surface. A resolution down to 25nm was achieved (Sharonov and Hochstrasser 2006). A further advanced application of the PAINT approach takes advantage of immobilised DNA origami which is called DNA-PAINT. Here, a fluorescent labelled DNA imager strand shows transient binding to an immobilised DNA docking strand. Upon hybridisation high fluorescence signal is detected. The increased resolution is of the order of 30nm (Jungmann, Steinhauer et al. 2010).

For all of the localisation strategies mentioned above it is possible to tune the overall localisation precision by selecting a threshold so that only molecules that can be localised within a tolerated accuracy will be kept for further analysis (ZEISS 2011). In order to expose details of the observed sample in the framework of a supperresolution approach the localisation precision alone is not sufficient enough. In addition, the overall image resolution is also dependant on the labelling densities on the sample to be resolved. In consequence of the Nyquist-Shannon sampling theorem, the average distance between neighbouring localisations and therefore the labelling density on the sample has to yield at least two localisations per resolution unit.

$$R_{Nyq} = \frac{2}{(\text{label density})^{1/d}} \qquad \text{Equation 24}$$

In accordance to this, a Nyquist resolution R_{Nyq} can be defined as follows (see Equation 24) with d referring to the dimension of the investigated field. If the labelling density is not high enough the tiny details of a probe will be undersampled and cannot be resolved (Jones, Shim et al. 2011).

From the localisation precision and the Nyquist resolution a total resolution R_{tot} can be calculated which is given in Equation 25.

$$R_{tot} = \sqrt{LP^2 + R_{Nyq}^2} \qquad \text{Equation 25}$$

3 Experimental Section

The fluorescence excitation and emission spectra presented in this thesis have been measured with conventional spectrometers which are either a Fluoromax or a Fluorolog-3 both from Jobin Yvon Horiba. The absorption spectra were measured with a Cary-300 Bio from Varian.

3.1 List of Chemicals

Name	CAS#	Supplier
3-(Glycidoxypropyl)dimethylethoxysilane (Epoxysilane)	68123-26-2	ABCR
4-(Phenylazo) benzoic acid (Azo)	1562-93-2	Aldrich
6-Hydroxy-2,5,7,8-tetramethylchroman-2-carbonacid (Trolox)	53188-07-6	Aldrich
Bis(tributylzinn)oxide (BBTO)	56-35-9	Acros Organics
Catalase	9001-05-2	Sigma
Chloroform	67-66-3	Acros Organics
D-(+)-Glucose	50-99-7	Sigma
Dichloromethane		VWR
Diethylether		VWR
Diethyliminodiacetat (DEIDA)	6290-05-7	Acros Organics
Dimethylaminopyridine (DMAP)	1122-58-3	Acros Organics
Dimethylsulfoxid (DMSO)	67-68-5	Acros Organics
Disuccinimidylcarbonate (DSC)	74124-79-1	Acros Organics
Epoxy-PEG-COOH		Iris Biotech
Ethanolamine hydrochloride	2002-24-6	Sigma
Glucose Oxidase	9001-37-0	Sigma
HCL (37%)		VWR
Hexamoll	166412-78-8	BASF
MeO-PEG-NHS		Iris Biotech
Methanole	67-56-1	VWR
N,N Dimethylformamide (DMF)	68-12-2	Aldrich
Neutravidin		Invitrogen
NHS-PEG-Biotin		Iris Biotech
Oligo(paraphenylenevinylene) (OPV5)		AK Prof. Ritter
Polyvinylchloride (PVC)	9002-86-2	Aldrich
Rhodamine 110		Radiant Dyes
Rhodamine 123	62669-70-9	Sigma
Tetrahydrofuran (THF)	109-99-9	Prolabo
Thiazole Orange (TO)	107091-89-4	Fluka
Triethylamine		Fluka
Tris(hydroxymethyl)aminomethane	77-86-1	Sigma-Aldrich

3.2 Confocal Fluorescence Spectroscopy

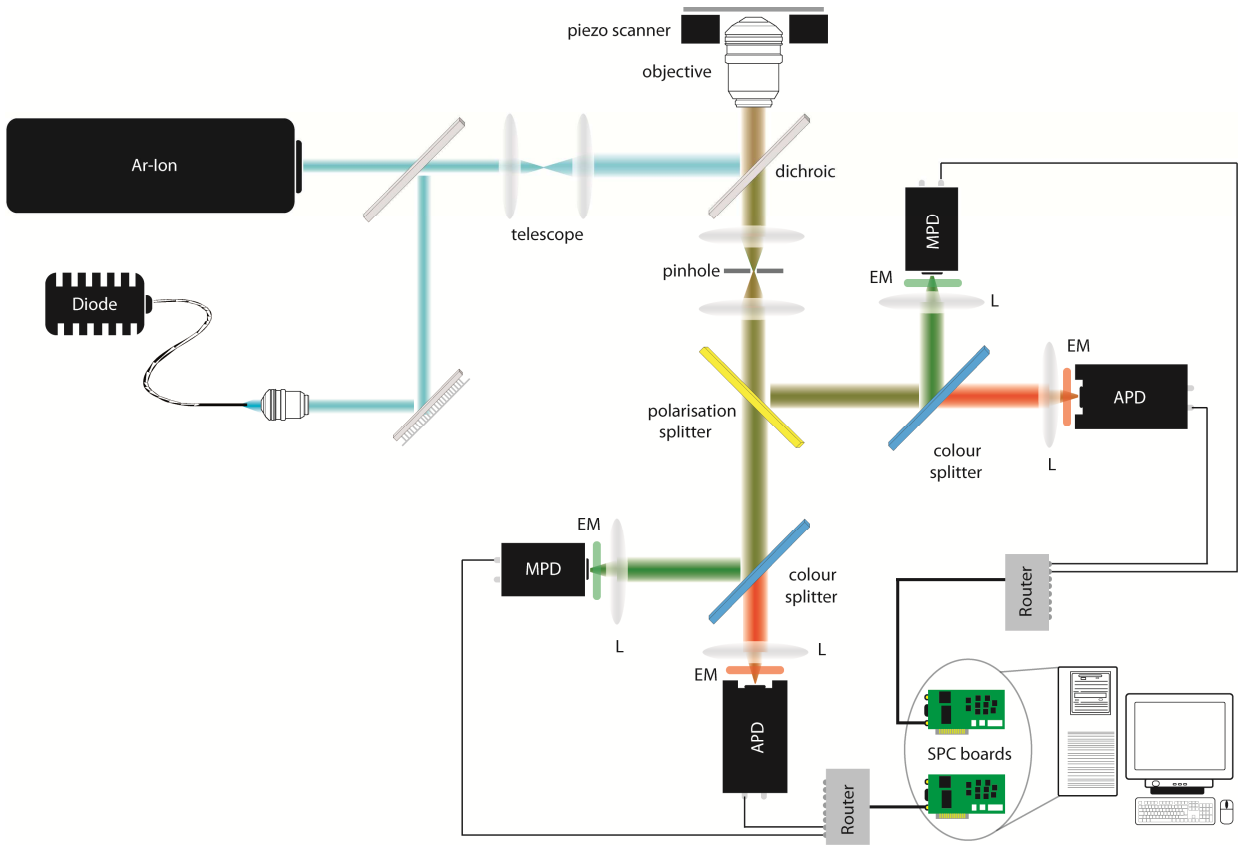

Figure 9 Confocal Setup Scheme

The light source that illuminates the sample is either a linearly polarized, active-mode-locked argon-ion-laser (e.g. 476nm, 73MHz, 150ps) or a blue (468nm) diode laser operating at various repetition rates. The beam size of the lasers is modified with the help of a telescope. The laser light is reflected by a dichroic mirror onto the sample. The fluorescence light emitted by the sample passes the dichroic and enters the inverted fluorescence microscope. The fluorescence light passes a pinhole (50µm) and is at first separated in parallel and perpendicular polarisation components relative to the laser light polarisation (polarisation splitter). These two components are further on separated into different spectral domains (green, red) by colour splitters. Each of the split fluorescence components passes a corresponding emission filter (EM) and is focused on single photon sensitive avalanche photo diodes (MPD/APD). The signals of the green and red components of the same polarisation component are connected to the same router and finally recorded by independent single photon counting (SPC) pc-boards. A 3D-piezo scanner is mounted on top of the inverted microscope that allows for sample scanning with high precision and stability.

The confocal setup which is presented in this thesis is a modified home-made version of the setup that has already been described in literature (Kühnemuth and Seidel 2001). A scheme of this confocal setup is shown in Figure 9. Coherent and linearly polarised and monochromatic light from lasers (light amplification after stimulated emission of radiation) which is either a pulsed Ar-ion laser (Sa-

bre Innova, Coherent) or a pulsed diode laser (Picoquant) operated at a wavelength of 476 nm or 467 nm respectively is used as the source of excitation. A telescope consisting of two quartz lenses with different focal lengths can be used to in- or decrease the diameter of the laser beam which leads two a variation in size of the excitation volume. For the lasers used in our experiments, the lateral profile of the beam is considered to be a Gaussian profile. In order to lead the laser beam to the microscope (IX71, Olympus), a number of mirrors with very high reflectivity are used (~99%).

The laser beam enters the inverted, epi-fluorescence microscope and passes through a dichroic filter that reflects the laser light upwards which is hereupon focussed on the sample by an objective with high numerical aperture (PlanApo 60x\1.2, Olympus). The fluorescence light that emerges from the sample after laser excitation is collected by the same objective. This light is transmitted by the fluorescence excitation filter and leaves the microscope through the left side-port. Thereafter, the fluorescence light passes the confocal pinhole which further decreases the observation volume in lateral direction.

As the excitation laser light is linear polarised, the fluorescence light is split into the parallel and the perpendicular polarisation components relative to the polarisation of the laser light using a polarising beam splitter. The two different polarisation components are further separated into different spectral domains. In our experiment we use BS 560 (AHF Analysetechnik) colour splitters to separate the fluorescence light into "green" and "red" spectral domains. The individual spectral domains of the fluorescence light passes emission filters (EM) which match the emission spectra of the dyes used in the experiment (green: HQ 520/66, red: HQ 580/130, AHF Analysetechnik) and are finally focused by lenses (L) on the detector elements of single photon sensitive detectors which are either Micro-Photon-Devices PDM 50CT (MPD) or Perkin-Elmer SPCM-AQR-14 (APD). Both kinds of detectors base on photon avalanche diodes, the abbreviations are used for a clear discrimination.

The TTL signals of the APDs (Perkin-Elmer 2011) and the NIM signals of timing output of the MPDs (Micro-Photon-Devices 2011) which yield a much better time resolution than the TTL outputs are connected to two independent single photon counting pc-boards SPC-150 fabricated by Becker & Hickl via two TTL routers HRT-82 from the same company. The NIM signals are transformed into TTL signals by home-build converters which provide very stable TTL output signals. The setup is designed in a way that all signals that come from detectors which collect perpendicular polarisation components are connected to module #1 whereas all detectors that collect parallel polarisation components are connected to module #2. In this way it is possible to correlate photons of different detectors much shorter than the dead time of the instruments (Felekyan, Kuhnemuth et al. 2005).

To every incoming photon a couple of parameters are recorded by the two SPC-boards such as detection channel, macro-time and time of arrival after the excitation laser pulse. In this way it is later on possible to analyse a various number of fluorescence parameters such as anisotropy, fluo-

rescence lifetime or correlation times on a single photon level which can be grouped into single fluorescence bursts.

In addition, a 3D-piezo scanner (P-527, PI) is mounted on top of the inverted microscope that allows for sample scanning with high precision and stability.

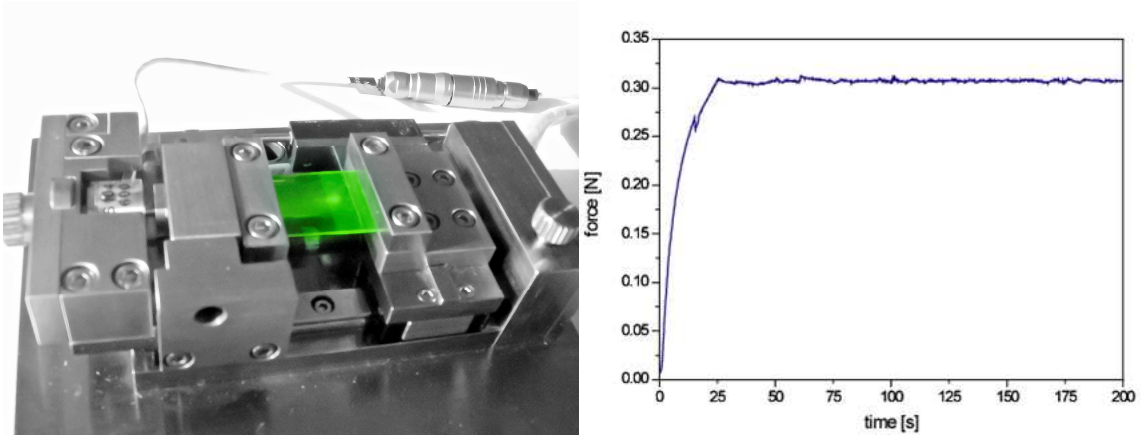

Figure 10 Tensile Stage MTEST 200

An image of the tensile stage is shown on the left hand side. A thin PVC foil (green) is clamped to a pair of jaws and kept centred in the field of view upon stretching. The colour of the foil is intensified to show where it is mounted. The right graph illustrates the precise control of the force the foil is exposed to over a longer period of time.

The combined force and fluorescence measurements which will be described in section 4 required a further modification of the setup. A tensile stage (MTEST 200, Deben) can be mounted upside down on top of the microscope.

The tensile stage, which is shown on the left hand side in Figure 10, is equipped with loadcells in the range of 2 N to 200N. The sample is clamped to a pair of jaws and kept centred in the field of view upon stretching. This device has linear scales for accurate elongation control and optical encoders for precise speed control. It can be operated either in constant load or constant force mode. The accurate force control over a longer period of time is shown on the right hand side in Figure 10. The overall range of travel is 10 mm.

3.3 Total Internal Reflection Fluorescence Microscopy (TIRF)

3.3.1 TIRF setup

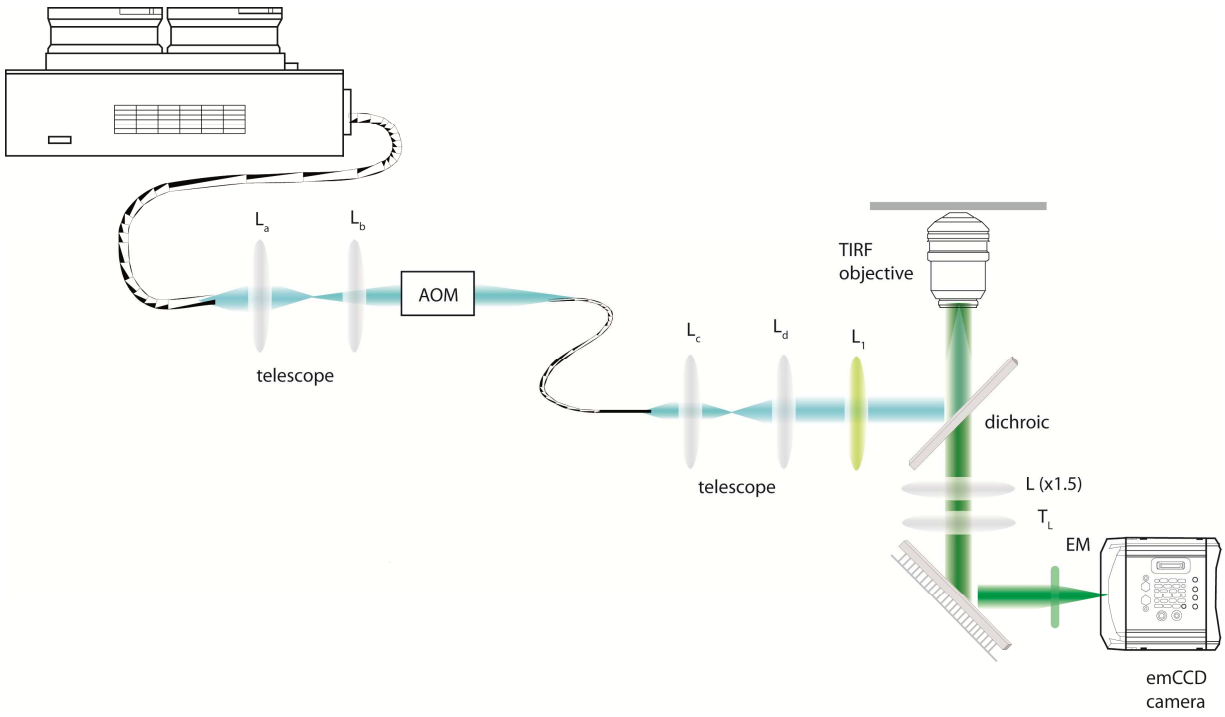

Figure 11 Total Internal Reflection Setup

The light source used to illuminate the sample is a fibre-coupled tunable Ar-ion laser. The beam size of the lasers is modified with the help of a telescope to be coupled to an acousto optical modulator (AOM) that produces an optical grating at which the laser beam is diffracted. The 1st order diffraction maximum is coupled to a second fibre. A second telescope allows for further modification of the beam size of the laser. The lens L_1 focuses the laser light on the back aperture of the TIRF objective which is hereby reflected by a dichroic mirror onto the sample. The fluorescence light emitted by the sample passes the dichroic and is focused on an electron multiplying charge coupled device (emCCD camera).

Conventional fluorescence techniques such as widefield or confocal microscopy which are extensively applied in science are based on a relatively broad illumination profile. Especially widefield fluorescence microscopy suffers from a poor resolution along the optical axis making it difficult to resolve details of a florescent probe that are overlayed by out of focus background fluorescence.
In case of confocal microscopy the resolution along the optical axis (~0.5-0.7µm) is higher in comparison to standard widefield microscopy (Schermelleh, Heintzmann et al. 2010) but as the sample has to be scanned by the laser beam it is not possible to detect fluorescence from a larger area of a sample at the same time. In particular fluorescence experiments of immobilised single molecules (e.g. time trace measurements such as bleaching) become very tedious as one has to observe the

individual molecules one after another although modern laser scanning systems can scan the sample at very high speed.

In contrast, total internal reflection fluorescence microscopy (TIRFM) makes use of an incoming evanescent wave that restricts the illumination along the optical axis close to a glass-/ aqueous medium interface. The differences of the two refractive indices define the relationship between the angles of incidents and refraction of a passing beam of light which is described by Snell's Law. At a critical angle of an interface from higher to lower refractive index the beam is totally reflected leaving just a very small electromagnetic field that penetrates the medium with lower refractive index.

The evanescent electric field intensity I(z) follows an exponential decay with increasing distance z away from the interface

$$I(z) = I_0 \cdot e^{-z/d}, \quad d = \frac{\lambda_0}{4\pi} \cdot \left[n_1^2 \cdot \sin^2(\theta) - n_2^2\right]^{-1/2} \qquad \text{Equation 26}$$

where n_1 and n_2 are the refractive indices of the glass and the aqueous media ($n_1 > n_2$) and λ_0 is the wavelength of the light in vacuum. For typical TIRF conditions the initial intensity is below 50% at 100 nm and has almost vanished at 1 μm away from the interface. Thus, the TIR microscopy is well suited to investigate immobilised fluorescent molecules which are located in close vicinity on top of a previously discussed interface with very high contrast at good signal to noise ratio.

This technique was first described and applied on fluorescent samples in the early 1980's (Axelrod, Burghardt et al. 1984) and has become a very powerful tool in modern fluorescence microscopy.

The total internal reflection fluorescence experiments presented in this thesis were performed on a home-build setup. A scheme of our setup is shown in Figure 11.

The light source is a fibre-coupled tunable Ar-ion laser (543-AP-A02, Melles Griot). The size of the laser beam is reduced by a first telescope (f_a=100 mm, f_b=12.5 mm) to be coupled in an acousto optical modulator (AOM-80, APE). Inside the AOM ultrasonic waves are induced in a crystal resulting in an optical grating at which the laser beam is diffracted. The 1st order diffraction maximum is coupled to a second fibre. In this way the AOM allows for handy manipulation of the laser intensity and works also as a very fast shutter that can also be triggered by external signals. Leaving the 2nd fibre, the size of the collimated laser beam is increased again to maximise the field of view by a second telescope (f_c=40 mm, f_d=200 mm). A prerequisite for objective-based TIRF measurements is the fact that coherent light has to be focussed on the periphery of an objective's back aperture to further satisfy the conditions for total reflection. The lens L_1 (f_1=200 mm) fulfils the focussing on the back aperture of the objective in use. A dichroic filter which is located inside a fluorescence microscope (IX70, Olympus) reflects the laser light to enter the objective and furthermore transmits

the collected fluorescence. This dichroic filter is a very crucial part of the whole setup. The region of illumination is very restricted due to the evanescent excitation conditions. Any irregularities in thickness of the dichroic influence the quality of the illumination spot dramatically. Therefore, a 2mm thick dichroic (zt 491 RDCXT, AHF Analysetechnik) with very high flatness is used (Blom 2010). The total internal reflection conditions are finally created by the usage of special TIRF objectives (PlanApo 60x\1.45 or Apo N 60x\1.49, Olympus) with very high numerical apertures.

The necessary translation of the laser beam is hereby realised by a tilt of the closest mirror to the microscope. The fluorescence light from the sample is collected by the same objective, transmitted through the dichroic filter, passes a bandpass filter EM (HQ 535/50, AHF Analysetechnik) and is finally focussed on an ultra-sensitive (quantum efficiency > 90%) and back-illuminated electron multiplying charge-coupled device (emCCD, DV887 ECS-BV, Andor). An additional magnification lens (x1.5) can be inserted in the detection pathway to increase the overall magnification and therefore reduce the effective pixel size of the system. The first alignment of the setup followed a step-by-step instruction that has been published online (Microscopy-Resource-Center 2011).

The information which is directly available from the emCCD camera is the number of multiplied electron counts because the function of the CCD camera is based on the photoelectric effect. The sensitivity and gain factors of the CCD camera have to been known to later on calculate the number of primary photons which caused the electron cascade. I will distinguish between the number of fluorescence CF and background counts CB and the number of primary fluorescence NF and background photons NB. The photon numbers will be used in the calculation of the localisation precision which is given in Equation 23. Further details will be given in section 5.2.1.

3.3.2 Optosplit modification

The single molecule FRET measurements of immobilised biomolecules (see section 6) have also been performed on the TIRF setup described in section 3.3.1. Here, the green signals of donor molecules and the red signals of acceptor molecules have been detected simultaneously. This was realised by a further modification of the detection pathway as illustrated in Figure 12. A commercially available image splitter (Optosplit, Cairn) was installed between the microscope and the CCD camera. Here, a colour splitter separates the overlaying fluorescence signals of donor and acceptor. The red component of the fluorescence signal is transmitted and the green component is reflected. The two spectral components further pass bandpass filters (green: HQ 535/50, red: HQ 680/60, AHF Analysentechnik) and are later on focussed on the CCD camera. As a result, the image is divided into two separate, spatially equivalent components that can be displayed side by side on a single CCD. A crucial part of the system is to focus the two different components of the fluorescence signal equally good on the camera chip. Tiny irregularities in thickness of the dichroic filter or even a

small curvature of the filter lead to different focal planes for the two detection channels. A special colour splitter (HC BS 580 Imaging, AHF Analysentechnik) especially recommended for imaging applications was used. Nevertheless, the different focus conditions for the two detection channels were still not good enough to perform single molecule experiments with necessary quality. Therefore, an additional anti reflex coated correction lens (f=1333 mm, Cairn) was inserted in the red detection channel. The position of this correction was carefully aligned to minimise the differences in the focus conditions of the two channels.

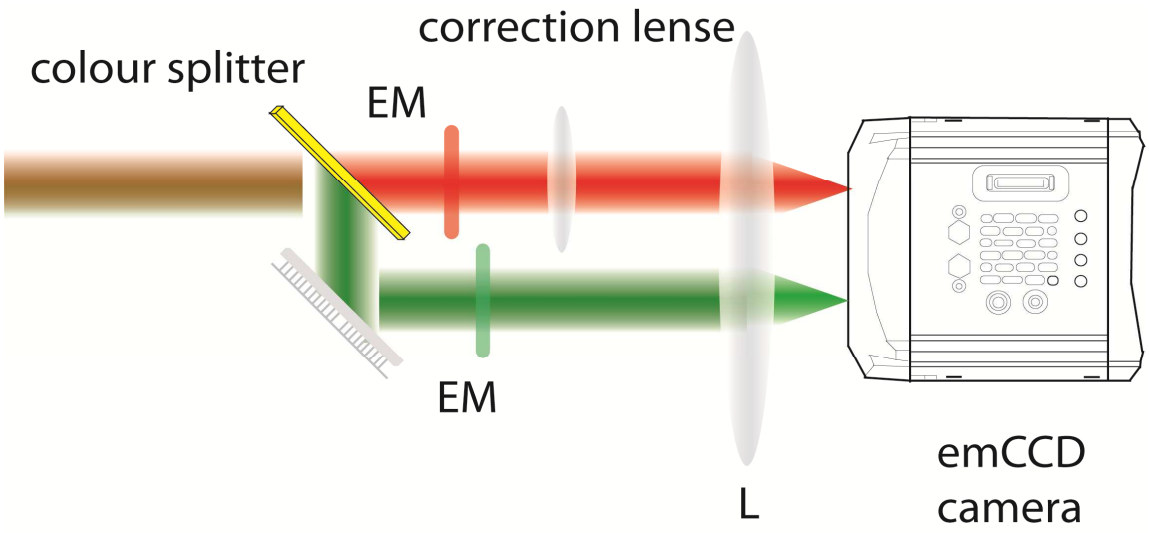

Figure 12 Optosplit modification of TIRF Setup

The general setup is shown in Figure 11. The single molecule FRET experiments of immobilised biomolecules require a modification of the detection pathway. The fluorescence light is separated by a colour splitter into a green and red spectral image. These two fluorescence components pass corresponding emission filters (EM) and are focused side by side with the help of a lens (L) on the chip of a charge coupled device (CCD camera).

4 Fluorophores as optical sensors for local forces

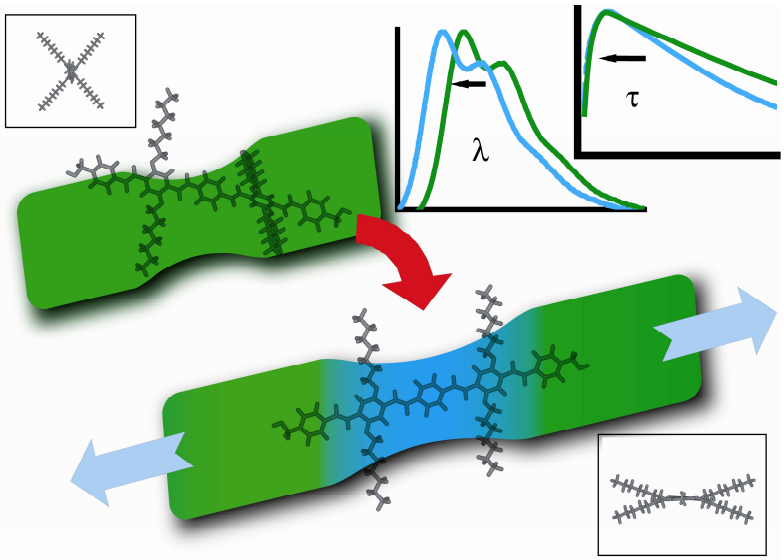

Figure 13 Fluorophores as optical sensors for local forces

A fluorophore (OPV5) is embedded into a PVC matrix (green). Upon stretching the PVC foil, the fluorescence lifetime and the fluorescence spectrum of the fluorophore change due to manipulation of the conjugation system.

4.1 Motivation

The stability and reliability of any industrially fabricated product depends on the quality of the chosen materials and the way of treatment in the process of production. Nowadays, a huge number of products with a broad variety of applications are made of plastics. These synthetic polymers are exposed to numerous external influences such as strong temperature differences, chemical compounds and also mechanical impacts such as drag or shear forces. These external effects lead to fatigue of the materials which the full functionality and finally cause fracture, deformation or cracking. Especially in industrial mass fabrication a complete failure of any compartment can in worst case result in dramatic consequences with in the end huge expenses to restore or repair the production cycle. Thus, the constant control of the material quality and further improvements of a material's lifetime are of major importance. Especially a permanent control of the mechanical forces acting on a component is sometimes hard to realise without disturbing the continuous process of production. Especially synthetic materials are well suited to implement additional substances already in the stage of production due to their wide compatibility with any kind of additives. Our idea was to implement custom-tailored fluorophores which change their fluorescence properties upon exposition of forces

on the carrier material. Fluorescence techniques have become powerful and reliable tools to investigate and analyse chemical or biological samples with outstanding temporal and spatial resolution. With all the benefits of applied fluorescence techniques that will be discussed in this thesis we have developed a reliable and non-destructive method to measure local forces. Further advancements can lead to useful applications in sense of quality inspection. The method also shows potential even to map local forces on a single molecule level. At the time of this work, various approaches have been followed to change fluorescence properties of fluorophores by direct manipulation of e.g. the molecular framework. These approaches will be discussed in the manuscript of our publication in section 7.1. To our knowledge at this time, no sufficiently characterised fluorescent probe has been described so far. The basic principle of our method is as follows. A custom-tailored fluorophore which is described in section 4.2.2 is embedded within a polymer matrix. Details on this matrix are described in section 4.2.1. Laser light of suitable wavelength is irradiated on the sample. Finally we have investigated force induced changes of the fluorescent properties of a fluorophore as we stretch the polymer matrix. A sketch of the basic principal of our experiments is shown in Figure 14.

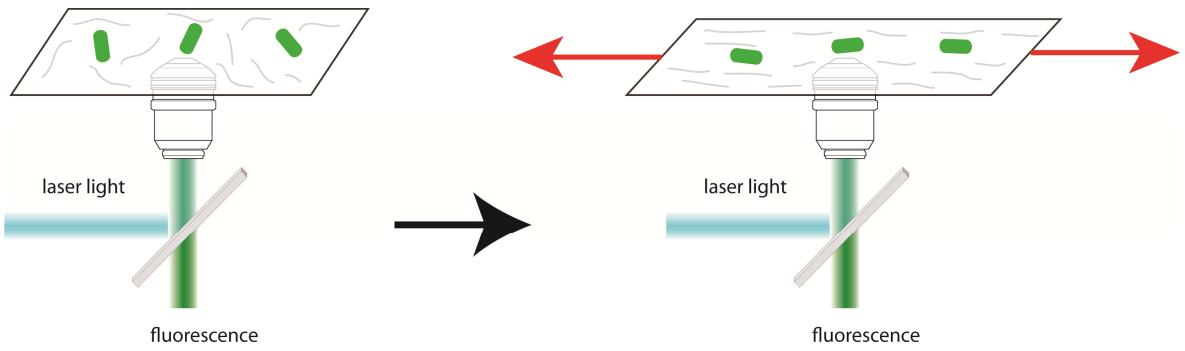

Figure 14 Basic principal to measure force induced changes of fluorescence properties

Fluorophores (green spots) are embedded into a polymer matrix (black rectangle). Laser light is irradiated on the sample and the fluorescence parameters are measured with and without an external force exposed on the matrix and the fluorophores.

4.2 Samples

4.2.1 Polyvinylchloride (PVC) foils

Polyvinylchloride is one of the most produced plastics worldwide. It is a highly versatile polymer which is compatible with a huge variety of additives. Especially the softness and the flexibility can be easily influenced by the addition of plasticisers. The extraordinary properties of PVC such as light weight, high strength and long-term stability are recommended in many industrial applications. PVC

is widely used in the production of clothings, serves as an insulator on electric wires and is one of the most commonly used materials in gas transportation, water service lines such as irrigations and sanitary sewer pipes. Because of this and due to its suitable optical characteristics, PVC was found to be best carrier material for our force mapping experiments based on fluorescence techniques.

The PVC polymer (0.3 g, Aldrich, CAS# 9002-86-2, Mn: 47000) was dissolved in THF (5 mL, Prolabo, CAS# 109-99-9, AnalaR NORMAPUR) together with hexamoll® (0.045 g, BASF Ludwigshafen, CAS# 166412-78-8), a plasticiser which is necessary to make the foil flexible enough to be stretched. This solution was then cleaned with activated charcoal which was afterwards removed by centrifugation. To the polymer solution (5 ml) OPV5 (21.5 ng, 21.4 pmol, the concentration is far below excimer formation) was added and filled into a petri dish. THF was evaporated at room temperature until the foil gained its solid state. Finally the foil was dried for 5 hours under highvacuum conditions, yielding substrates with a glass-temperature of 46 °C. The resulting foil showed a thickness of around 50 μm.

4.2.2 Oligo(paraphenylenevinylene) (OPV5)

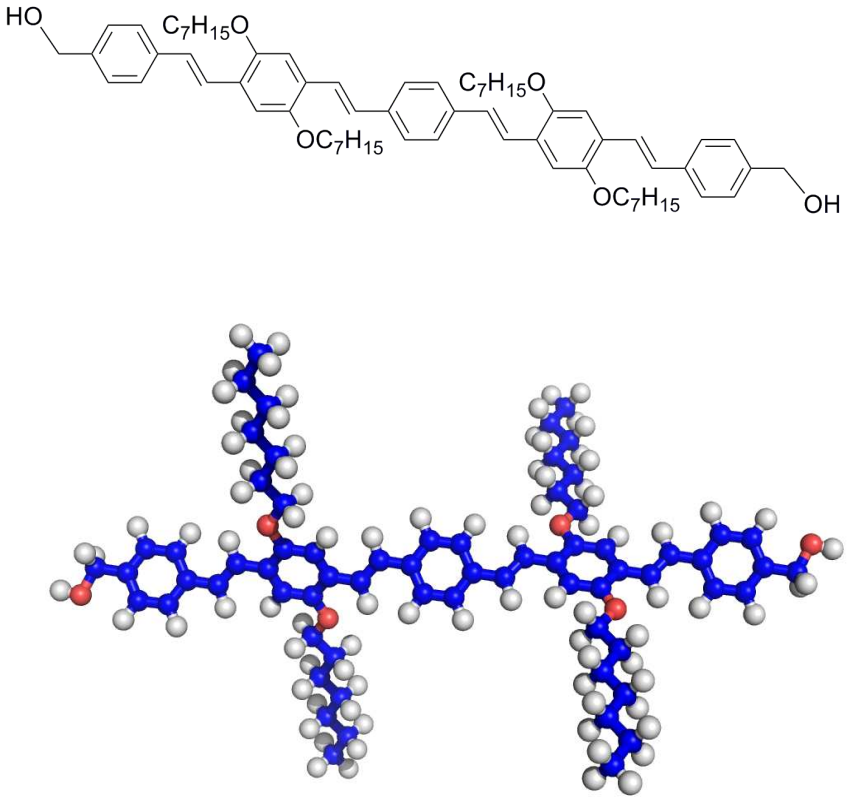

Figure 15 Oligo(paraphenylenevinylene) (OPV5)

The fluorophore oligo(paraphenylenevinylene) 5 (OPV5) has been especially developed for this project. The synthesis, characterisation and clean-up procedures have been carried out in the group of Prof. Dr. H. Ritter at the "Lehrstuhl für Präparative Polymerchemie" by Daniel Schmitz. The structure of the fluorophore, which is shown in Figure 15, consists of 5 benzene rings which are connected by alkenes forming a widely extended conjugated π-system. This molecular backbone is twisted by attaching sterically demanding side-groups to the second and fourth benzene ring which disturb the conjugation of the system. An external force applied on the whole molecule is supposed to affect the fluorescence properties due to a change in sterical tensions. The fluorescence absorption and emission spectra are shown in Figure 16.

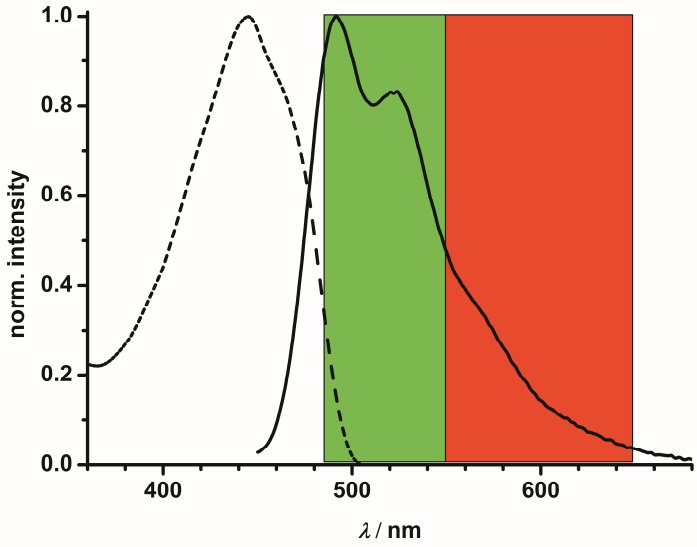

Figure 16 OPV5 spectra in PVC

Absorption spectrum (dashed line) and fluorescence spectrum (solid line) of OPV5 in PVC. The green box indicates the spectral detection domain for our green detection channel and the red box of our red detection channel respectively.

Further details of the synthesis and characterisation of OPV5 can be found in the supporting information in section 7.1.1 and in the dissertation of Daniel Schmitz (Schmitz 2009).

	λ_{abs} [nm] [a]	λ_{max} [nm] [b]	τ_1 [ns] [c]	τ_2 [ns] [c]	τ_{av} [ns] [d]	Φ_F [e]	r_o
THF	**432.1**	**485.2**	**0.83 (0.77)**	**0.52 (0.23)**	**0.78**	**0.53**	**0.398**
PVC	**444.6**	**491.6**	**0.97 (0.97)**	[f]	**1.03**	**0.81**	

Table 1 Fluorescence properties of OPV5

[a] Absorption maximum. [b] Fluorescence maximum. [c] Fluorescence lifetime components, τ_i (amplitudes, x_i). [d] Fluorescence weighted average lifetime τ_{av} [e] Fluorescence quantum yields, measured in THF and extrapolated by correcting for refractive index in case of PVC (for details refer to the supporting information of the publication in section 7.1.1). [f] Typically a minor component of ~2.2 ns was observed, probably due to background fluorescence of the polymer matrix or distorted OPVs. Lifetimes in PVC were determined from p-polarized fluorescence in the green spectral window to maximize signal-to-noise ratio.

4.2.3 Rhodamine 123 (Rh123)

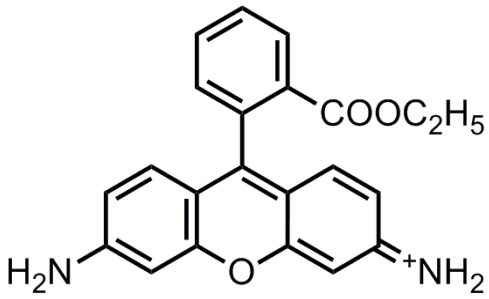

Figure 17 Rhodamine 123 (Rh123)

The commercially available fluorophore Rhodamine 123 (Rh123, Radiant Dyes) with similar absorption and emission spectra (see Equation 19) served as a reference dye for the negative control measurements. From the geometrical structure, which is illustrated in Figure 17, much smaller force related changes of its fluorescence properties are expected. Because of its rather spherical shape, no main axis to which the transition dipole moment is oriented can be directly addressed by an external force like in the case of OPV5. Therefore, reorientation effects measured by fluorescence anisotropy are also expected to be small.

4.3 Experimental Methods

4.3.1 Data Acquisition

Before each experiment the alignment of the setup is checked in order to guarantee optimum and stable detection efficiency.

Therefore, typically a reference dye (Rhodamine 110) at single molecule concentration and well known diffusion coefficient is used to perform fluorescence correlation spectroscopy (FCS) which is not discussed in detail in this thesis. This technique is able to determine the number of molecules in the confocal detection volume at very low concentrations (fl) and can measure the diffusion time of the molecules and determine the shape of the detection volume using a 3D Gaussian assumption.

The shape of the volume (ratio between axial and lateral extension), the diffusion time of the reference dye in the volume and the calculated count rate per molecule are the main quality parameters for the alignment of the setup.

The setup that was used to perform these measurements has already been described in section 3.2. The SPC-150 boards were controlled by Becker & Hickl's software SPC (Version 8.8) whereas the tensile stage MTEST 200 was operated by the software Microtest (Version 4.10) provided by Deben.

At first we tried to collect a full pulling experiment within one fluorescence data stream but it turned out that it was very laborious to extract the different force levels from that stream and to assure equal conditions throughout the whole experiment. Therefore, we decided to acquire the fluorescence information related to a certain force level stepwise. As the tensile stage allows for precise control of the force applied to the sample, we increased the load in steps of 0.5 N, see Figure 18. At each of these force levels three independent measurements were performed to sense inconsistencies in the acquired data. For each of the measurements a xy-scan using the piezo-scanner P-527 fabricated by PI with a scan size of 98x98 μm^2 was realised that lasted for around 60s. This scan was chosen to minimise photo-bleaching effects and also be more independent on local heterogeneities within the foil.

The fixed period of the scan also guaranteed comparable conditions for all force levels and a more or less constant number of photons which emerged from fluorescence events except the change in fluorescence due to the reorientation of the fluorophore as being discussed in section 4.3.3.

4.3.2 Data Analysis

4.3.2.1 Force data

The software which controls the tensile stage allows for definition of a certain force the whole foil is exposed to. This is realised by increasing the distance of two clamps between which the PVC foil is clamped. A typical pulling experiment is shown in Figure 18. The applied force is increased in steps of 0.5 N (red curve). In order to maintain the force levels, the stage has to move continuously due to slight relaxation of the PVC foil (blue curve). As the PVC foil gets tighter and thinner the further it is pulled apart, the force information alone is not suitable to compare the real loads at the different force levels. A much better parameter to compare the different force levels is the mean tensile stress, which is actually the force per cross-section of the foil.

At the beginning and at the end of each experiment the width (with a calliper) and the thickness of the foil (by performing a xz-scan) was determined. The initial area A_{start} and final area A_{end} of the foil were calculated by multiplying the two corresponding parameters.

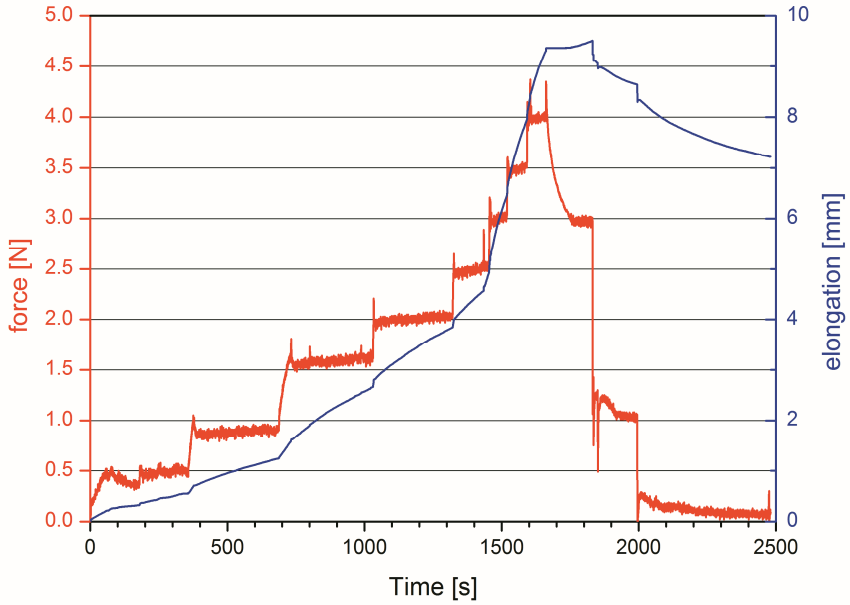

Figure 18 Elongation and externally applied force versus time

The general procedure of the combined force and fluorescence measurements is shown. The external force is increased in steps of 0.5 N. (red). At each force level three independent fluorescence measurements have been performed. As the foil is flexible, the tensile stage has to increase the distance of between the two jaws the foil is clamped to keep the force level or to further increase the force (blue). After the tensile stage reached the maximum range of travel the foil relaxes and the force decreases.

It is not possible to measure especially the width of the foil during the measurement due to the fact that the tensile stage has to be removed from the setup as it is mounted upside down on top the microscope. Therefore, the corresponding area of the foil for each measurement was calculated using the following equation:

$$A(t) = A_{start} - \left[\left(A_{start} - A_{end} \right) \cdot \frac{\Delta L(t)}{\Delta L_{end}} \right] \qquad \text{Equation 27}$$

The elongation of the foil is recorded by the Microtest software from which one can extract the elongation of the corresponding measurement L(t) and the final elongation L_{end} of the foil as the stage reaches its range of travel which is around 10mm.

4.3.2.2 Fluorescence data

At first, the two individual data streams from the two SPC-150 boards are combined to one using the Merge-SPC software provided by Becker & Hickl. This step has to be done manually for each individual measurement.

In order to analyse the fluorescence lifetime of the molecules we have to build up the decay curves. From the single photon information the Labview programme "Jordi is my girlfriend" builds up the TAC (time to amplitude converter) histograms. The finite bandwidth of the TAC circuitry leads to a nonlinearity of the TAC characteristics which influences the correct construction of a continuous macroscopic time axis (Felekyan, Kuhnemuth et al. 2005). This is why a TAC linearization procedure is also included at this stage. As the time of each fluorescence photon relative to the exciting laser pulse is known (TAC time or micro time), the decay curves are build up by adding up the TAC times of all photons within the time domain of the laser repetition rate, e.g. for the pulsed AR-ion laser at 73.5MHz the repetition time is 13.6 ns. In the beginning, the creation of the TAC histograms had to be done manually for each measurement and for each colour set. The "Jordi" software was modified by me for batch processing in order to automatically create the histograms for a complete experiment.

A Matlab programme was used to perform the final analysis of the fluorescence data. Before the fitting of the data, the TAC histograms have to be converted into a suitable data format for this Matlab programme using "jordi2ibh", which is a tool also written in Matlab. This conversion had to be done for each of the 4 channels individually.

The following fluorescence model function is used to fit the data,

$$F(t) = IRF \otimes [A_1 \cdot \exp(-t/\tau_1) + A_2 \cdot \exp(-t/\tau_2)] + B \qquad \text{Equation 28}$$

where IRF is the instrumental response function, B is the background, $\tau_{1/2}$ are the individual lifetime components and $A_{1/2}$ their corresponding absolute amplitudes. From this one can obtain the species fractions which are defined by $x_i = A_i/(A_1+A_2)$. The background contribution was excluded from the list of free fit parameters and determined by averaging from a region of the TAC histogram where the fluorescence almost completely decayed. This approach was applied to stabilise the fit procedure. The total amplitude is defined as 1 (see also section 2.1.1). The measured signal is always a combination of the "real" signal and the instrumental response to that. Imagine a Dirac δ-function, which is, if considered as a distribution, a Gaussian distribution with infinite small standard deviation and infinite high amplitude, as the maximum limit for a "real" signal representing an excitation laser pulse. What you will measure is a broadened signal peak because the detector cannot react infinitely fast to that signal. The mathematical description of the obtained signal is a convolution of the instrumental response function and the "real" signal.

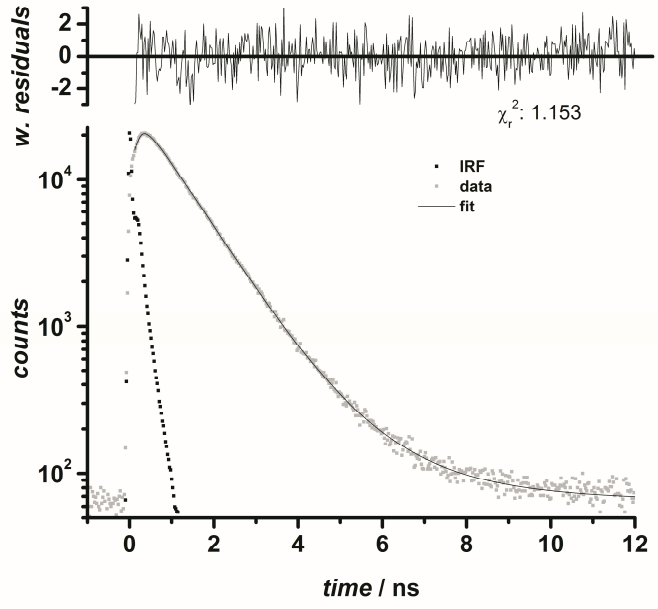

Figure 19 Decay histogram of OPV5 in PVC

In the lower diagram the instrument response function (black dots), the fluorescence decay data (grey dots) and the fit to the data (grey line) is shown. In the upper diagram weighted residuals are displayed.

In practice, the model function is iteratively convoluted with the instrumental response function in the framework of a χ^2-minimisation. The instrument response function is usually recorded from a pure water measurement.

A typical fluorescence decay histogram of the fluorophore OPV5 together with the instrumental response function, the fitted model and the weighted residuals is shown in Figure 19.
In the PVC foil the fluorescence decay shows a single dominant lifetime component (species fraction is 97%) of 0.97 ns. The decay contains also a minor contribution (species fraction is ~3%) of a longer second fluorescence lifetime of 2.2 ns, which may be attributed to background fluorescence of the polymer matrix or distorted OPVs. As the number of photons in our experiment was limited due to photobleaching, the two different lifetime components were difficult to separate.

On the other hand, the fluorescence weighted average lifetime of OPV5 was found to be a stable parameter for further fluorescence lifetime analysis which was calculated using the following equation:

$$\tau_{av} = (x_1 \cdot \tau_1^2 + x_2 \cdot \tau_2^2)/(x_1 \cdot \tau_1 + x_2 \cdot \tau_2) \qquad \text{Equation 29}$$

From the individual fluorescence decay histograms we also calculate the total number of background corrected photons which we call the fluorescence signal. The fluorescence signals of the 2 individual polarisation detection channels in the same spectral domain are used to calculate the "green" fluorescence anisotropy,

$$r = (F_{\parallel} - g \cdot F_{\perp})/(F_{\parallel} + 2 \cdot g \cdot F_{\perp}) \qquad \text{Equation 30}$$

The parameter g is a correction factor that accounts for different detection efficiencies in the two green detection channels. In order to determine this g-factor a Labview programme called "Paris" is used. This programme calculates the g-factor from a decay histogram of the reference dye Rh110 in a micro time domain where all variations due to rotation or scatter can be neglected. As there is an inverse definition of the g-factor in "Paris", we have to take the inversed value of the g-factor in the calculation of the anisotropy.
The fluorescence signals of all 4 channels are in the end used to calculate the ratio between the total fluorescence signal in the green and in the red spectral domain (see Figure 16) using the equation,

$$\frac{F^G}{F^R} = (F_{\parallel}^G + 2 \cdot g^G \cdot F_{\perp}^G)/(F_{\parallel}^R + 2 \cdot g^R \cdot F_{\perp}^R) \qquad \text{Equation 31}$$

where g^G and g^R are the correction factors for the differences in the green and red detection channels respectively.

The next step is to assign a change in the ratio of the fluorescence signal in the green and red detection domains to an actual change in the emission wavelength. Using the emission spectrum of OPV5 in PVC where no force is applied we can calculate the theoretical green to red intensity ratio taking into account the transmission spectra of all filters involved, the corresponding wavelength dependant fluorescence quantum yields of the different detectors and the wavelength dependant collection efficiency of the used objective. The normalised transmittance/intensity of the components just mentioned, is shown in Figure 20. Further on, we estimated how the green to red fluorescence ratio will change if a spectral shift of the OPV5 emission spectrum is expected.

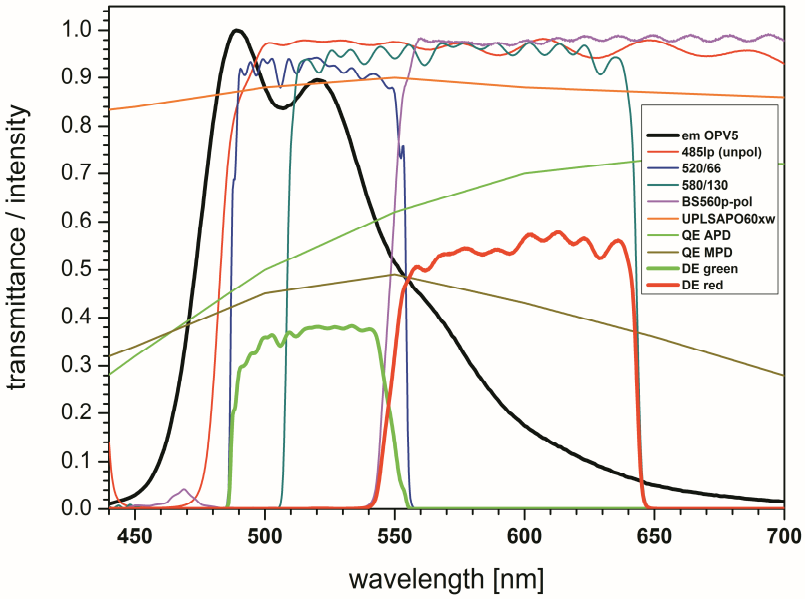

Figure 20

Transmittance / Collection -/ detection efficiencies

The normalised fluorescence spectrum of OPV5 in PVC is shown (black). The transmittances of all filters included in the setup are also shown. Transmittances have been measured from one individual exemplar of the corresponding filter with the help of an absorption spectrometer. The collection efficiency of the objective (UPLSAPO 60x w) and the quantum efficiencies of the two types of detectors (QE APD, QE MPD) were adapted from reference curves provided by the producers and may not be completely identical with the actual efficiencies of the components in use. From all of these transmittances, collection- and quantum efficiencies the overall detection efficiencies (DE) in the green and red detection channels have been calculated (thick lines).

Thus, we artificially blue shifted the actual emission spectrum by integers of nanometres, see Figure 21. We have also checked a combination of blue and red shift which yielded very similar results. For simplicity, only the blue shifted analysis is presented.
We assume that the changes in the overall shape of the emission spectra are of minor importance.

The absolute shift of the spectra will be indicated by the peak position of the corresponding spectrum P_{max}. Next, we calculated the integrated (summed) green and red fluorescence signals of all of these spectra (see Figure 22 and Table 2) in the green and red detection channels as indicated in Figure 20.

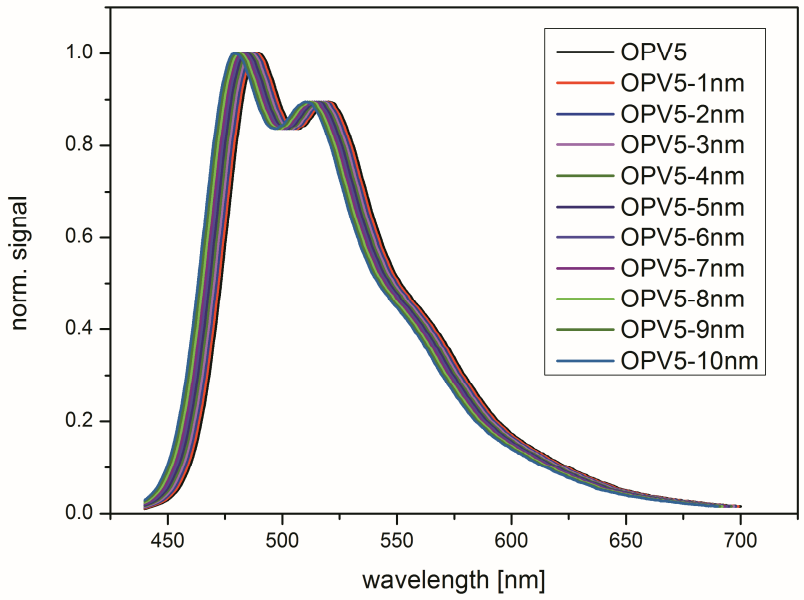

Figure 21 Simulation of blue shifted OPV5 fluorescence spectrum

The fluorescence spectrum of OPV5 in PVC is blue shifted in steps of Δ=1 nm. Changes in the overall shape of the spectra are assumed to be of minor importance.

From these integrated (summed) fluorescence signals the calculated green to red fluorescence ratio $(F^G/F^R)_{calc}$ is derived, see also Table 2. The relative spectral shift in nanometres is then plotted against $(F^G/F^R)_{calc}$. A 2nd order polynomial is used to assign the spectral shift to changes in the calculated green to red fluorescence ratio, see Figure 23.
The in this way calculated green to red fluorescence ratio shows differences to the actual measured green to red fluorescence ratio $(F^G/F^R)_{meas}$ obtained directly from the measured data. The calculated green to red fluorescence ratio has been obtained taking the transmittances of all of involved filters and the quantum efficiencies of the detectors into account.

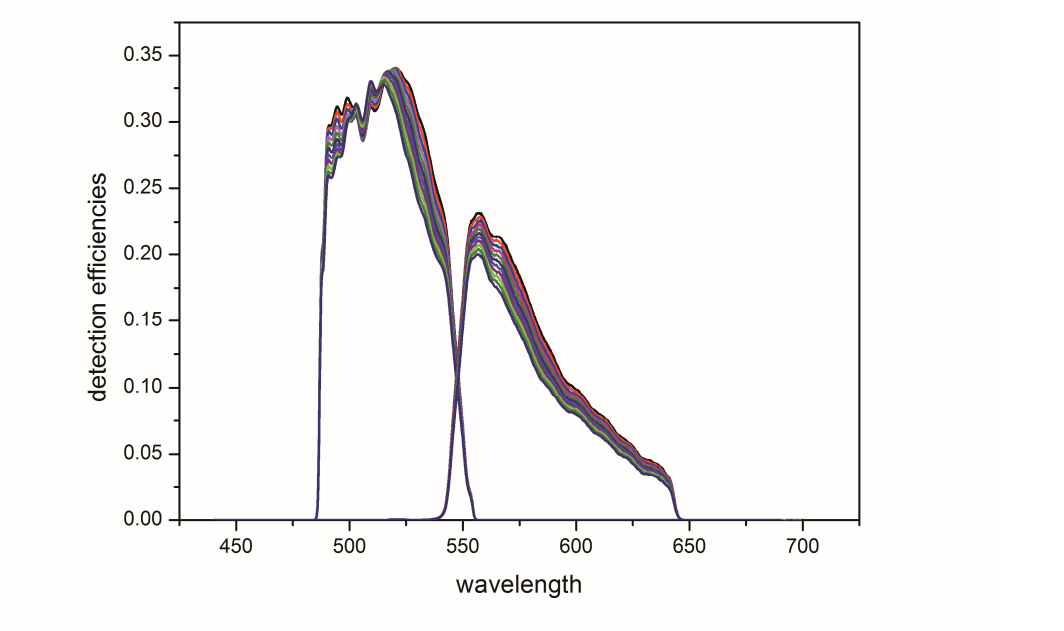

Figure 22 Calculated detection efficiencies for simulated shift of OPV5 spectra

With the calculated detection efficiencies in the green and red detection channels shown in Figure 20 and the stepwise blue shift of the fluorescence spectrum of OPV5 in PVC (see Figure 21) the overall detection efficiencies in the two detection channels are calculated.

The observed differences can be easily explained as these values just describe an averaged or typical spectral dependency. Furthermore, individual differences for the detection efficiencies in the four detection channels of the setup are not considered in the calculation.

Sum(Green)	Sum(Red)	$(F^G/F^R)_{calc}$	Δ[nm]
86.91	51.38	1.6913	0
86.03	50.19	1.7142	-1
85.11	49.02	1.7363	-2
84.16	47.87	1.7579	-3
83.18	46.75	1.7791	-4
82.19	45.66	1.8001	-5
81.19	44.59	1.8209	-6
80.19	43.54	1.8419	-7
79.19	42.50	1.8631	-8
78.19	41.49	1.8846	-9
77.20	40.49	1.9066	-10

Table 2 Calculation of the green to red fluorescence ratios from blue-shifted OPV5 spectra

With the determined overall detection efficiencies in the two spectral domains as shown in Figure 22, the corresponding integrated (summed) fluorescence signals have been calculated. The calculated green to red fluorescence ratio $(F^G/F^R)_{calc}$ is also shown dependant on the shift of the OPV5 fluorescence spectrum.

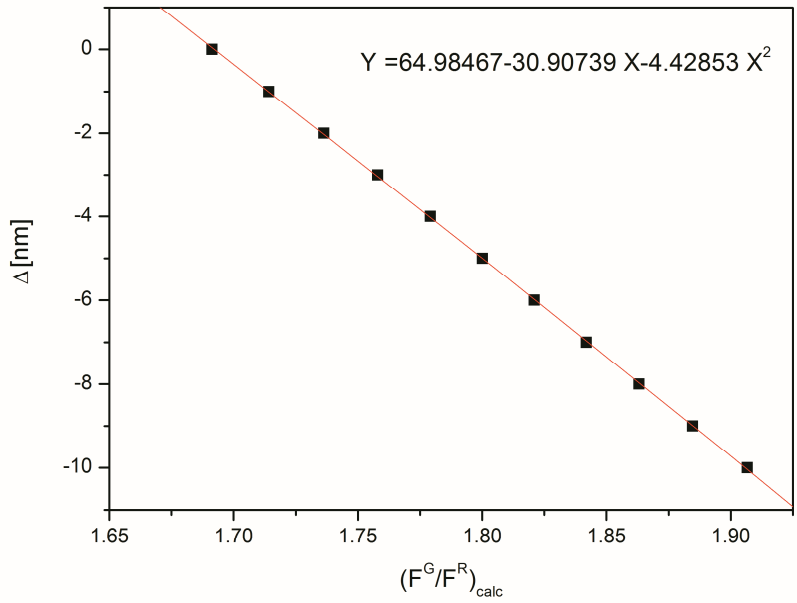

Figure 23 Spectral shift [nm] versus calculated green to red ratio $(F^G/F^R)_{calc}$

A 2nd order polynomial is used to described the relationship between the shift Δ of the OPV5 fluorescence spectrum and the calculated green to red fluorescence ratio $(F^G/F^R)_{calc}$.

In order to correctly assign the measured green to red fluorescence ratios to the calculated ones, we introduce a correction factor as indicated in Equation 32.

This correction factor is derived from the calculated green to red fluorescence ratio of the non-shifted emission spectrum divided by the averaged measured green to red fluorescence ratio from three individual measurements before applying any external force to the foil.

$$\left(\frac{F^G}{F^R}\right)_{corr} = \frac{\left(F^G/F^R\right)_{calc}(\Delta = 0nm)}{\left(F^G/F^R\right)_{meas}(F = 0N)} \qquad \text{Equation 32}$$

All measured green to red fluorescence ratios are finally multiplied by the normalisation factor given in Equation 32 to obtain the experimental green to red fluorescence ratios $(F^G/F^R)_{exp}$ as denoted in Table 3.

The 2nd order polynomial obtained from the simulation of the shifted OPV5 fluorescence spectrum as just explained is finally used to determine the actual shift Δ_{exp} of the fluorescence spectrum of OPV5. This shift is also expressed by the peak position of the corresponding spectrum.

mean tensile stress [N/mm²]	$(F^G/F^R)_{meas}$	$(F^G/F^R)_{exp}$	Δ_{exp} [nm]	P_{max} [nm]
0.00	1.3450	1.6947	-0.11	491.49
0.00	1.3430	1.6922	0.00	491.60
0.00	1.3390	1.6871	0.23	491.83
1.04	1.3340	1.6808	0.52	492.12
1.19	1.3430	1.6922	0.00	491.60
2.25	1.3410	1.6897	0.12	491.72
2.30	1.3440	1.6934	-0.06	491.54
2.36	1.3410	1.6897	0.12	491.72
4.11	1.3490	1.6997	-0.34	491.26
4.19	1.3570	1.7098	-0.81	490.79
4.29	1.3590	1.7123	-0.92	490.68
5.31	1.3460	1.6960	-0.17	491.43
5.40	1.3520	1.7035	-0.52	491.08
6.74	1.3510	1.7023	-0.46	491.14
6.86	1.3560	1.7086	-0.75	490.85
8.29	1.3550	1.7073	-0.69	490.91
8.41	1.3610	1.7149	-1.04	490.56
8.51	1.3570	1.7098	-0.81	490.79
9.87	1.3580	1.7111	-0.87	490.73
10.00	1.3540	1.7060	-0.63	490.97
10.12	1.3550	1.7073	-0.69	490.91
11.72	1.3610	1.7149	-1.04	490.56
11.76	1.3580	1.7111	-0.87	490.73

Table 3 Data of a combined force and fluorescence experiment

The stepwise procedure of force increase in our experiment is shown in Figure 18. From these force values the mean tensile stress is calculated as explained in section 4.3.2.1. The measured green to red fluorescence ratio $(F^G/F^R)_{meas}$ is also shown. A correction parameter $(F^G/F^R)_{corr}$ which is given in Equation 32 is introduced to account for differences between measured and calculated green to red fluorescence ratios which were not considered in the calculation. In this way we obtain the experimental green to red fluorescence ratio $(F^G/F^R)_{exp}$. With the help of the 2nd order polynomial which is shown in Figure 23 the actual shift Δ_{exp} of the OPV5 fluorescence spectrum is calculated. This shift is also expressed by the peak position of the corresponding spectrum.

4.3.3 Results

Three major optical effects can be observed simultaneously. At first, the fluorescence anisotropy increases Figure 25, which indicates a reorientation of the fluorophores within the matrix. In the force experiment the polarization of the exciting laser light and the pulling direction were chosen to be parallel to maximise excitation probability.

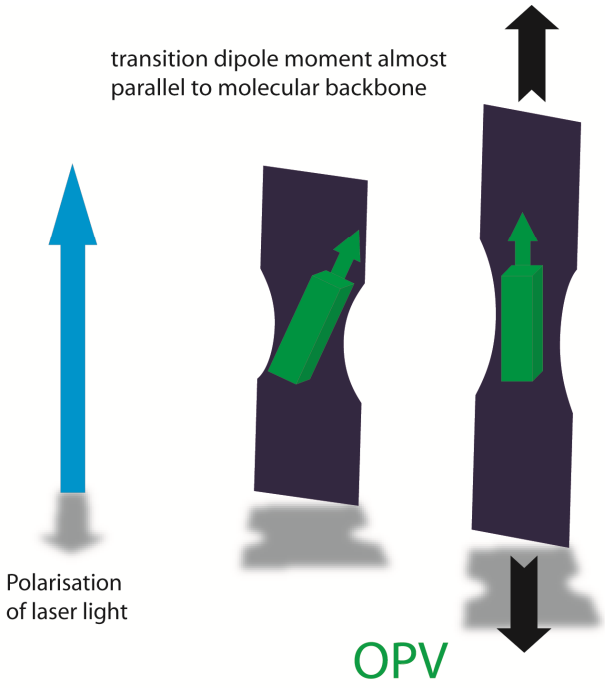

Figure 24 Geometrical measurement conditions for pulling experiments

The polarisation of the excitation light is indicated by the blue arrow. The dark tailed shape indicates the PVC foil. The black arrows show the direction of the pull which is parallel to the polarisation of the incident light. The transition dipole moment of OPV5 (green arrow) is almost parallel to its molecular backbone (green box). The further the pull the more OPV5 molecules are oriented parallel to the polarisation of the laser light.

As the transition dipole moments of OPVs are oriented almost parallel to their molecular backbones (Spano 2002) the increase in fluorescence intensity as well as in anisotropy while the foil is stretched shows that the fluorophores change the orientation of their long axis towards the direction of tension. This fluorescence increase and the nearly irreversibility of this effect prove that the molecular rotation of OPV5 in PVC is almost negligible, making it an ideal marker to probe local orientations of suitable polymer matrices. Figure 25 illustrates the strict correlation between the elongation of the foil (blue) and the change of the fluorescence anisotropy (black) dependant on the mean tensile stress. The black arrows to the right indicate the stretching part of the experiment, the black arrows to the left the relaxation part of the experiment.

If we compare the change in anisotropy between OPV5 (green) and the control dye Rh123 (black) as shown in Figure 26 it is clearly visible that the anisotropy very sensitively reflects the reorientation of OPV5 whereas in case of Rh123 just the expected small change is observed.

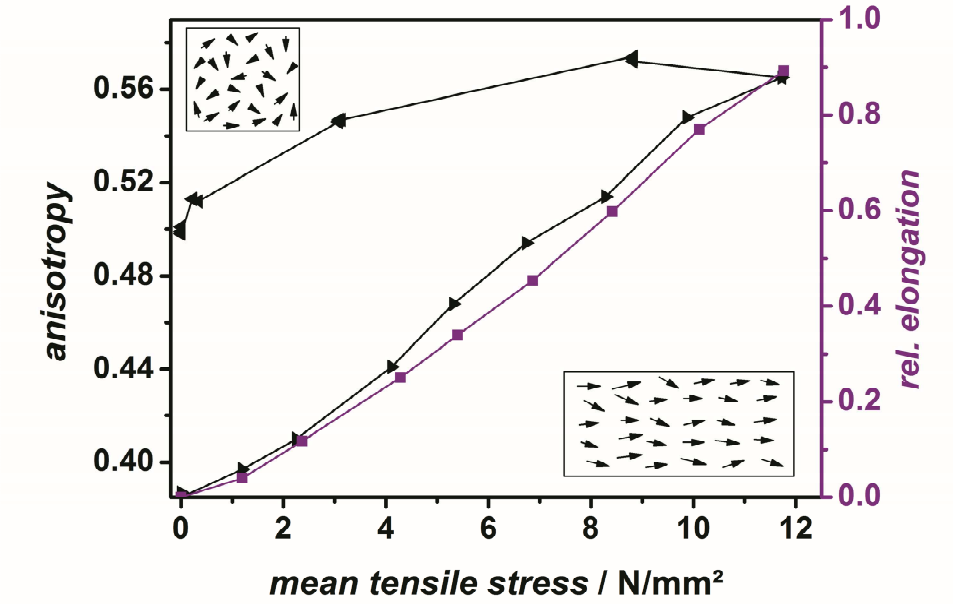

Figure 25 Fluorescence anisotropy and relative elongation versus mean tensile stress

Relative elongation of the PVC foil (black triangles) and the fluorescence anisotropy of OPV5 (blue squares) versus mean tensile stress. The orientation of the triangles indicates the phase of pulling (right) and the phase of relaxation (left).

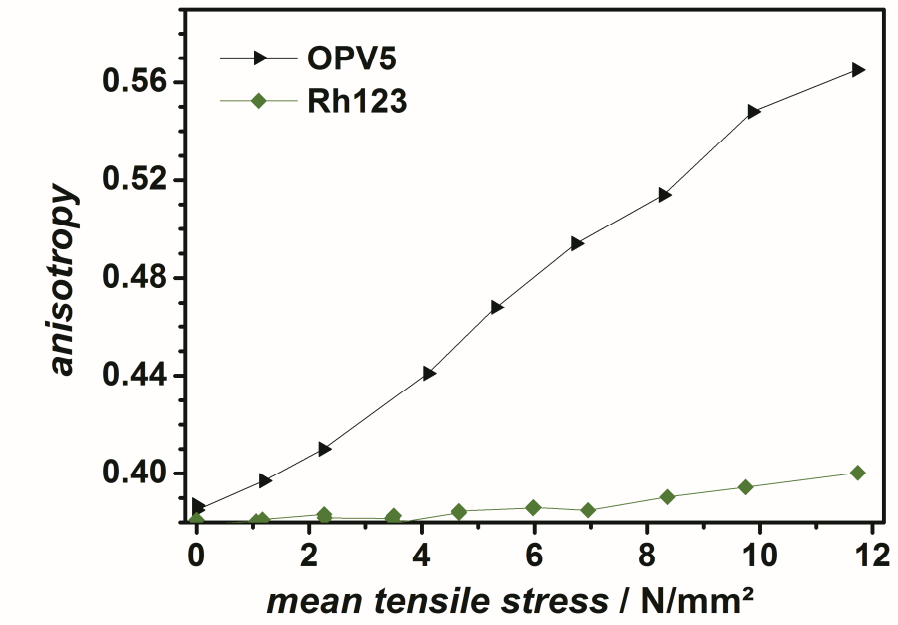

Figure 26 Comparison of the fluorescence anisotropy of OPV5 and Rh123 versus mean tensile stress

With increasing tensile stress the OPV5 fluorophore (black triangles) shows a distinct reorientation whereas in case of Rh123 (green squares) the effect is remarkably smaller.

For the analysis of the fluorescence lifetime in our combined force and fluorescence experiments we exclusively used data recorded by an ultra-fast single-photon sensitive detector Micro-Photon-Device (MPD), with an instrument response function of ~30ps FWHM. The results of a detailed analysis of the fluorescence decay time of OPV5 as a function of the mean tensile stress is displayed in Figure 27. With increasing stress the fluorescence lifetime is decreasing by $\Delta\tau = 25 \pm 2.5$ ps at the highest applicable stress of 12 N/mm^2. The given values are obtained from linear regression.

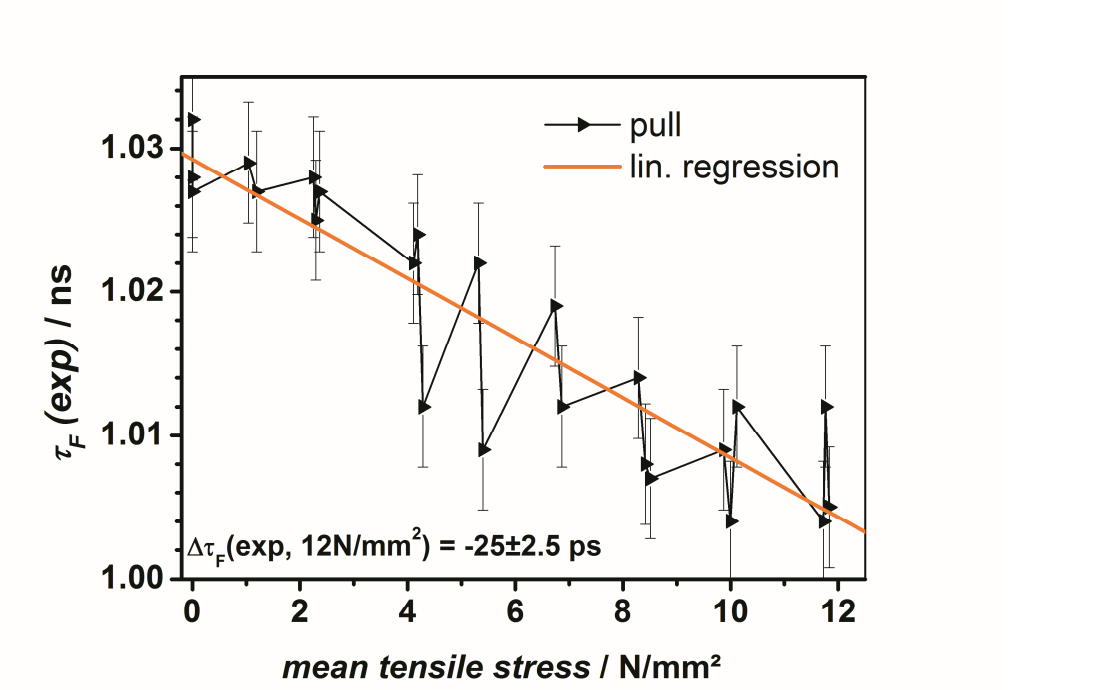

Figure 27 Fluorescence lifetime of OPV5 versus mean tensile stress

A typical fluorescence lifetime measurement (black triangles) of the pulling phases (right triangles). The linear regression analysis (orange) yielded a maximum change of the fluorescence of 25 ps. The error-bars represent the shot-noise limited uncertainty of the lifetime fits of about 4 ps.

In addition to the combined force and fluorescence experiments, theoretical calculations on the OPV5 have been performed. In view of its size, the OPV5 chromophore was described by semiempirical methods. The theoretical study involved the selection of the most suitable semiempirical model, computation of ground-state potential curves for elongation of the chromophore, reoptimisation of the resulting geometries in the first excited singlet state using multi-reference configuration interaction and calculation of spectral properties at this level. The calculations have been performed in the group of Prof. Dr. W. Thiel at the "Max-Planck-Institut für Kohlenforschung" by Dr. A. Koslowksi and You Lu.

These theoretical calculations basically determined the force which is necessary to increase the distance between the outermost carbons of a single OPV5 (see also Figure 15). This distance of each

step was fixed during subsequent partial geometry optimisation to finally determine the force dependant fluorescence lifetime and emission energy values.

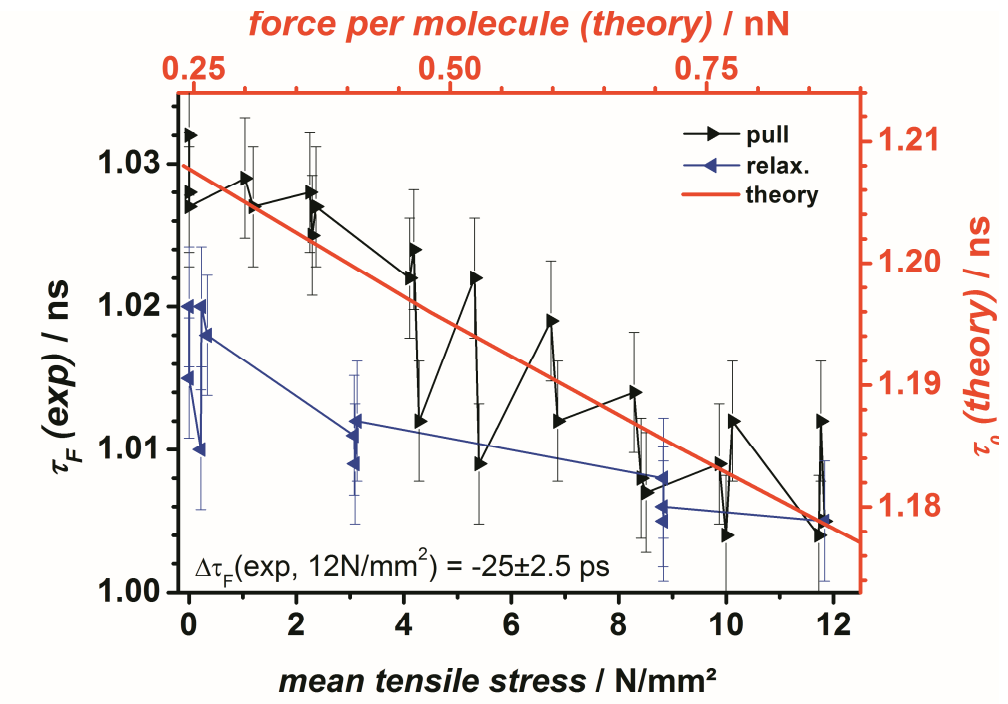

Figure 28 Fluorescence lifetime of OPV5 versus mean tensile stress with theoretical data

Comparison between a typical fluorescence lifetime measurement (black axes) and theory (AM1/MRCI, red): The PVC foil was stretched (black) and subsequently relaxed (blue).The error-bars represent the shot-noise limited uncertainty of the lifetime fits of about 4 ps. Both ordinates are scaled to equal relative range of lifetimes.

Changes of the emission energy can be easily related to a spectral shift. Further details of these theoretical calculations can be found in section 7.1.1. Figure 28 shows the relation between measured and calculated fluorescence lifetimes. The black curve again shows the first part of the experiment (pulling) while the blue curve describes the second step (relaxation). The subsequent relaxation of the fluorescence lifetime as the external force is no longer applied to the foil indicates that the observed changes in the fluorescence lifetime are related to the force and not only on reorientation alone. The axis for the theoretical calculated fluorescence lifetimes τ_0 (red ordinate) was scaled such that its relative change corresponds to the relative change of the measured fluorescence lifetimes τ_F (black ordinate). In a second step, we scaled the abscissa for the theoretical calculated force values such as this line (red) fitted to the linear regression. In this way we can attribute the theoretically calculated force per molecule to the mean tensile stress the foil is exposed to which is the best suitable parameter accessible from experiment.

In addition to the fluorescence anisotropy and lifetime analysis, spectral changes have also been measured and theoretically calculated. Figure 29 shows the dependency of the experimental green to fluorescence ratio on the mean tensile stress.

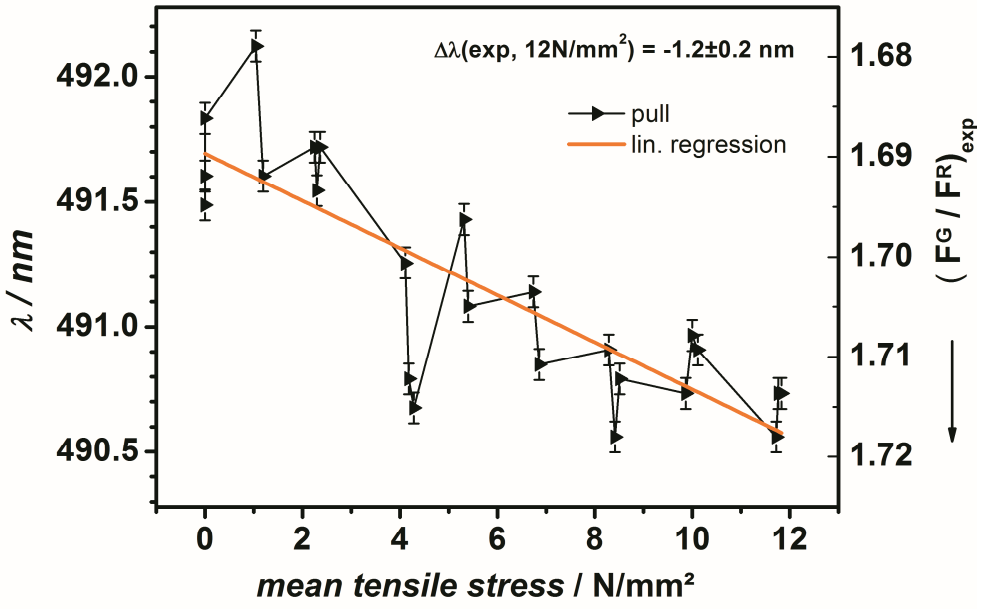

Figure 29 Spectral shift of OPV5 versus mean tensile stress

Spectral shift (black) of OPV5 indicated by the experimental green to red fluorescence ratio and the position of the peak of the spectrum. A linear regression analysis (orange) yielded a maximum spectral shift of $\Delta\lambda$=-1.2 nm upon stretching.

Furthermore, the graph in Figure 29 also indicates the relation between the experimental green to red fluorescence ratio (right ordinate) and the resulting spectral shifts (left ordinate) as explained in detail in section 4.3.2.2. A linear regression yielded a maximum spectral change of $\Delta\lambda$ = -1.2 ± 0.2 nm at the highest mean tensile stress of around 12 N/mm^2.

In accordance to the fluorescence lifetime analysis we also assigned the measured spectral changes to the theoretically calculated ones as shown in Figure 30. Again, the black curve shows the first part of the experiment (pulling) while the blue curve describes the second step (relaxation) indicating that the observed effect is related to the external force. The axis of the theoretically calculated spectral shifts (red ordinate) is also scaled to show the same relative spectral changes as in case of the measured spectral shifts (black ordinate). The linear regression was also used as a reference.

The probabilities of radiative transitions (e.g. the radiative decay rate) can be very different dependant on the optical characteristics of the surrounding medium. Hereby, a crucial parameter is the index of refraction of this medium.

These impacts are due to variations of the electric fields which act on the molecular dipole moments, if one takes the interactions between a molecule and its environment into account. As the PVC which represents the surrounding medium of our fluorophores is stretched in our experiments, we likely induce changes of the optical characteristics of the foil.

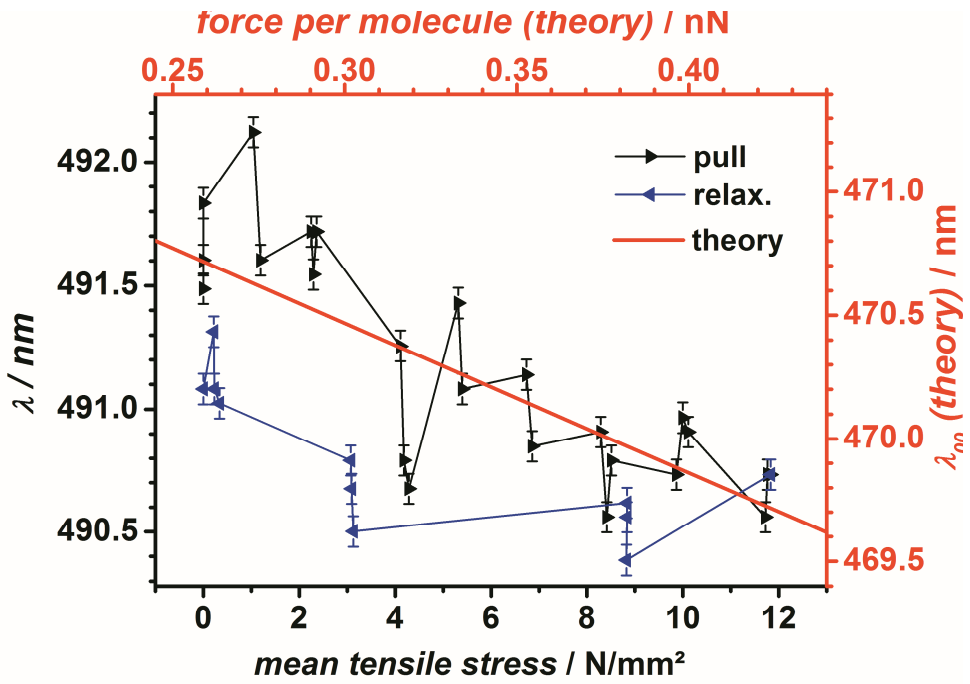

Figure 30 Spectral shift of OPV5 versus mean tensile stress in comparison to theoretical calculations

The PVC foil was stretched (black triangles) and subsequently relaxed (blue triangles). Also shown is the calculated (AM1/MRCI, red) spectral shift as function of the force applied on a single molecule. Both ordinates are scaled to equal relative spectral range. The error-bars represent shot-noise. The real error is larger probably due to chromatic aberrations caused by mismatch of refractive index of PVC foil (n=1.53) and objective design (corrected for n=1.33). The aberrations depend strongly on the focus position inside the foil and change upon stretching.

The observed changes in the fluorescence lifetime and emission wavelength upon stretching are relatively small. Therefore, we estimated the maximum effect from changes in the refractive index on the observed changes of the fluorescence parameters. In this way we can separate the observed changes of the fluorescence parameters due to matrix effects from those which arise from changes in the conjugation of the fluorophore OPV5. As we were not able to measure the index of refraction of our thin PVC foils directly, we relied on previously obtained results, which correspond to measurement conditions similar to our experiments.

At first, we estimated changes of the PVC density $\Delta\rho \approx 0.001$ g/cm^3 at 100% extension obtained from literature (Jabarin 1991). Changes of the density can be related to changes of the index of refraction with the help of the Lorentz-Lorenz equation given in Equation 33

$$n = \sqrt{\frac{M_w + 2\rho RD}{M_w - \rho RD}}; \qquad RD = \frac{M_w}{\rho}\frac{\left(n^2 - 1\right)}{\left(n^2 + 2\right)}$$ Equation 33

The parameter M_W is the molecular weight and RD is the molar refraction of the polymer.

From the changes of the PVC density upon stretching the foil, we find a maximum change of the refractive index $\Delta n \approx 4.6\ 10^{-4}$. In addition to changes in the index of refraction due to density changes, the effect of birefringence has to be considered. Birefringent media split incoming light in two polarised components with perpendicular orientation to each other as a result of different index of refraction dependant on the polarisation and direction of propagation of the incoming light.

The influence of birefringence upon stretching is estimated to be $\Delta n \approx 3.1\ 10^{-3}$ as reported for similar samples (Rider and Hargreaves 1970; Jabarin 1991).

The overall changes of the fluorescence lifetime dependant on the index of refraction were calculated by a modified and further advanced Strickler-Berg approach (see also section 2.1.1) which is explained in detail in literature (Toptygin 2003). This approach considers basically two cavity models of interest how a fluorophore is enclosed in its surrounding medium.

In the case of a fluorescent molecule in solution (or in a solid medium), the solvent is expelled from the volume occupied by the fluorescent molecule. As a result, a cavity is created, in which the fluorescent molecule is located. An empty spherical cavity model (ESC) and an empty ellipsoidal cavity model (EEC) are proposed dependant on the assumed shape of the cavity. The dependencies of the radiative lifetimes τ_r on the index of refraction are given in Equation 34 in case of the empty spherical cavity model and in Equation 35 in case of the empty ellipsoidal cavity model respectively.

$$\Delta\tau_0 = \tau_{0,1}\left(\left(\frac{n_1}{n_2}\right)^5\left(\frac{2n_2^2 + 1}{2n_1^2 + 1}\right)^2 - 1\right)$$ Equation 34

$$\Delta\tau_0 = \tau_{0,1}\left(\frac{n_1}{n_2} - 1\right)$$ Equation 35

The calculated results of the estimated influences of refractive index and birefringence on the fluorescence lifetime are shown in Table 4. The difference between fluorescence lifetime and radiative lifetime is explained in section 2.1.1 and section 7.1.1.

The values presented in Table 4 shall be considered as an upper limit for the influence of the surrounding medium on the observed fluorescence lifetime in which the fluorophore resides.

The maximum influence is on the fluorescence lifetime is $\Delta\tau_F$ ~-2.87 ps in case of an empty spherical cavity model if the effect of birefringence is considered. Here, we have to point out that an empty ellipsoidal cavity model is to be favoured due to the geometrical structure of the fluorophore OPV5 as shown in Figure 15.

OPV5	Δn	$\Delta\tau_F$(ESC) [ps]	$\Delta\tau_F$(EEC) [ps]	$\Delta\lambda$ [nm]
refractive index	$4.6\text{x}10^{-4}$	-0.42 (0.04%)	-0.25 (0.02%)	0.022
birefringence	$3.1\text{x}10^{-3}$	-2.87 (0.28%)	-1.69 (0.16%)	0.146
experiment		-25 ± 2.5		-1.2 ± 0.2

Table 4 Refractive index and birefringence effects on the fluorescence properties of OPV5

Influence of the matrix due to refractive index changes on the fluorescence properties of OPV5. Effects on the fluorescence lifetime assumed by an empty spherical cavity model (ESC) and an empty ellipsoidal cavity model (EEC). Effects on solvatochromic shifts of the emission spectra by applying Onsager theory.

If we compare this value with the average value for changes of the fluorescence lifetime obtain from a series of independent experiment it is clear that the observed effect cannot be explained by refractive index changes alone.

The corresponding results of analogous calculations for the fluorophore Rh123 are given in Table 5. In case of Rh123, the empty spherical model is to be favoured due to its geometrical structure (see also Figure 17). The comparison of the relative lifetime changes for OPV5 (green) and Rh123 (black) together with an interpolated curve representing the maximum matrix effects (dashed orange) is shown in Figure 31.

Rh123	Δn	$\Delta\tau_r$(ESC) [ps]	$\Delta\tau_F$(ESC) [ps]	$\Delta\lambda$ [nm]
refractive index	4.6×10^{-4}	-1.59 (0.05%)	-1.47 (0.05%)	0.063
birefringence	3.1×10^{-3}	-10.71 (0.33%)	-9.92 (0.32%)	0.42
experiment		6 ± 10		0.4 ± 0.2

Table 5 Refractive index and birefringence effects on the fluorescence properties of Rh123

Influence of the matrix due to refractive index changes on the fluorescence properties of Rh123. Effects on the fluorescence lifetime assumed by an empty spherical cavity model (ESC) and an empty ellipsoidal cavity model (EEC). Effects on solvatochromic shifts of the emission spectra by applying Onsager theory.

The negative control experiments performed with the reference dye Rh123 showed relative changes of the fluorescence lifetime which are of the order of the induced changes by the matrix alone. Whereas the relative change of the fluorescence lifetime in case of OPV5 shows a clear dependence on the mean tensile stress with a maximum effect of $\Delta\tau_F$~2.5 % at the highest applied mean tensile stress of around 12 N/mm^2.

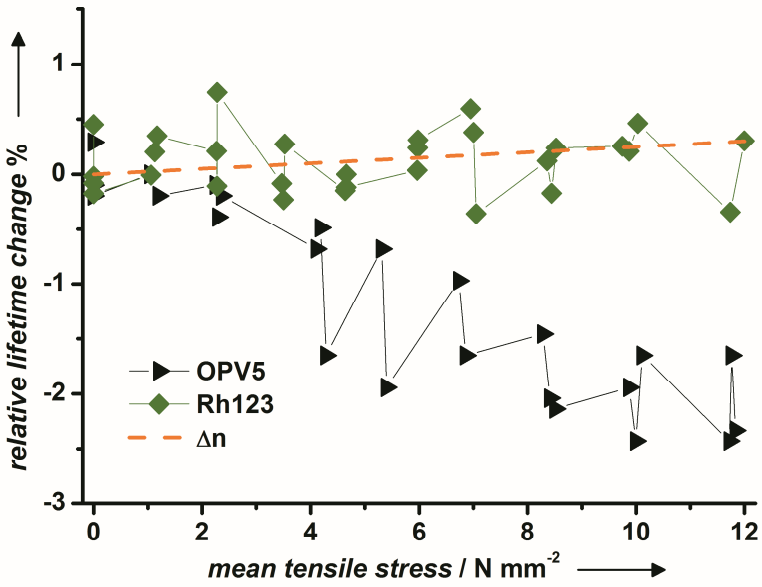

Figure 31 Relative lifetime change in % of OPV5 and Rh123 versus mean tensile stress

Comparison of the relative fluorescence lifetime change between OPV5 (black) and Rh123 (green). Upon stress the fluorescence lifetime of the OPV5 fluorophore decreases up to 2.5% at a maximum tensile stress of around 12 N/mm² whereas Rh123 only shows a slight increase close to the noise level which is consistent with expected changes due to refractive index changes of the matrix (Δn, dashed orange).

The analysis of the refractive index effects of the PVC foil on the fluorescence properties of the fluorophores also included another aspect which is known as the solvatochromic effect or solvatochromic shift. This effect is related to a strict dependence of absorption and emission spectra of a fluorophore on the polarity of the surrounding medium. Since the polarities of the ground and the 1st excited state of a fluorophore are different, variations in the polarity of the PVC matrix will change the stability of the ground and 1st excited states. This will finally lead to changes in the energy gap between these two electronic states. A detailed mathematical analysis on the solvatochromic effect has been derived by Onsager (Onsager 1936) and was later on further modified (Mataga, Kaifu et al. 1955; Mataga, Kaifu et al. 1956). A simplified relation between the emission frequency and the refractive index is given in Equation 36.

$$\nu = \nu_0 + const \cdot \left(\frac{n^2 - 1}{2n^2 + 1} \right) \qquad \text{Equation 36}$$

The parameter ν_0 describes the energy gap between the vibronical ground states of the ground state and the 1st excited state. Given this, we calculated the PVC matrix effects on the emission wavelength upon stretching the foil. In case of OPV5, the calculated results of the spectral shift $\Delta\lambda$ are shown in Table 4. The corresponding results of the reference dye Rh123 are given in Table 5.

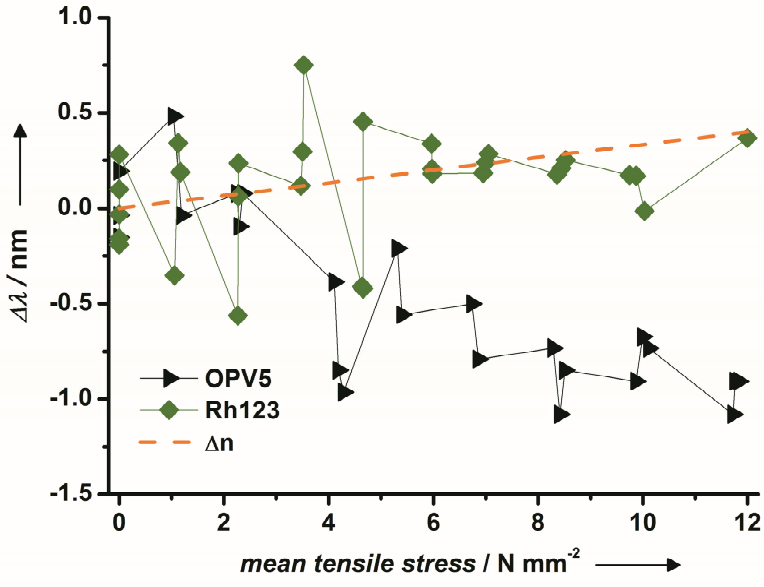

Figure 32 Relative spectral change in % of OPV5 and Rh123 versus mean tensile stress

Comparison of the relative spectral shift of OPV5 (black) and Rh123 (green). At the maximum tensile stress of around 12 N/mm² the spectrum of OPV5 features a blue-shift of 1.2 nm whereas the spectrum of Rh123 reveals a small red-shift consistent with estimations of the influence of the matrix alone due to refractive index changes (dashed orange).

The maximum estimated change of the emission wavelength for the reference fluorophore Rh123 is $\Delta\lambda$~0.42 nm, which is in accordance to the average spectral shift obtained from a series of independent measurements. In case of OPV5 we estimated a maximum shift of the emission wavelength due to matrix effects of $\Delta\lambda$~0.146 nm. In contrast, the observed average spectral shift obtained from different independent experiments is $\Delta\lambda$~-1.2 nm. This is another important proof that the observed changes are really due to the force impact on the molecular framework of the custom-tailored fluorophore OPV5. Further details of the overall analysis including experimental results and theoretical calculations can be found in the manuscript of the publication in section 7.1 and in the corresponding supporting information in section 7.1.1. The exact values used for the estimation of the maximum matrix effects on the fluorescence properties of OPV5 and Rh123 are also described in the supporting information in 7.1.1.

In summary, we have explored possible applications of fluorophores as optical sensors for local mechanical forces. To that end a custom tailored chromophore consisting of an aromatic backbone strained by sterically demanding alkyloxy side-chains has been synthesized. A flexible PVC matrix served to align the fluorophores by stretching. Transfer of mechanical strain from the matrix induced a geometrical change in the chromophore. Consistent with the results of semiempirical calculations on the same system, this caused a decrease in the fluorescence lifetime by 2.5% (25 ps) and an increase of the emission energy by 0.2% which corresponds to a blue-shift of 1.2 nm at tensile stresses of 12 N/mm^2. From a different point of view the force of 0.2-0.55 nN acting on a single molecule can be interpreted as an equivalent energy difference of 0.15 – 0.8 kcal mol^{-1} (refer to the supporting information, Table 8).

Our study proves the feasibility of fluorescence-based local force probes for polymers under tension. Necessary improvements can be achieved by developing more sensitive fluorophores and possibly by increasing the efficiency of force transmission from the matrix to the probe, i.e. by using modified end-groups to attach additional polymer chains as handles. Improved optical sensors of this type should in principle be able to monitor local mechanical stress in transparent samples down to the single molecule level, which can be used for reliability studies of the materials and also harbour promising further applications in polymer and nano science and technology.

5 Superresolution – iPAINT with DNA

Many insights into biological processes have been obtained by direct visualisation of interactions between various kinds of biological samples and their binding partners. In the beginning, the investigations focused on interactions on a cellular level, but detailed understanding of the processes required a closer look at the biological building blocks such as DNA molecules or proteins. Different microscopy applications have been developed throughout the years, whereas fluorescence microscopy has become one of the most established techniques because of its superior temporal resolution and the possibility of directed and specific labelling of the biomolecules. In contrast to other imaging techniques such e.g. electron microscopy, fluorescence microscopy suffers from rather poor spatial resolution due to the diffraction limit of light. As a rule of thumb, only structures in the lateral direction can be directly observed with a minimum size of half the observation wavelength. Regarding excitation wavelength of modern lasers that can be used to excite fluorophores with optimised fluorescence properties such as high fluorescence quantum etc., structures smaller than ~200 nm are not directly accessible. As many of the biological building blocks are of much smaller size, further advanced strategies had to be developed to improve the optical resolution. A basic introduction to diffraction and the different strategies to overcome the limitations due to diffraction has already been given in section 2.1.4.

Here, we concentrate on the enhancements of the concept of points accumulation for imaging in nanoscale topography (PAINT). As already explained this high resolution microscopy concept is based on a continuous binding and unbinding of a fluorescent probe to an immobilised target molecule. Up to now, this concept was only successfully applied to immobilised vesicles and transient binding to an immobilised DNA docking strand upon hybridisation.

The concept of high resolution imaging of immobilised DNA molecules with intercalating dyes has already been realised in the framework of a dSTORM concept (see also section 2.1.4). Here, blinking of covalently linked intercalating dimers with very high affinity to DNA is induced to establish the necessary one emitter per diffraction limited spot conditions to apply the strategy of improved localisation precision by fitting a suitable model to the photon distribution of each dye. This work has also proofed to have very slow dynamical exchange of the intercalating dyes on the DNA molecules on timescales of minutes (Schoen, Ries et al. 2011).

In this work, the successful application of high resolution imaging on a system of immobilised λ-DNA molecules with intercalating monomers based on the PAINT approach will be shown. This method is called intercalative Points Accumulation for Imaging in Nanoscale Topography (iPAINT). Hereby, the affinity of intercalating monomers is influenced by the addition of mono- and divalent metal ions to achieve a fast exchange of these intercalators. The fast dynamical exchange of our sys-

tem allows for fast change of the surrounding media which is important to investigate biological processes which can quickly react on environmental changes. Our approach also minimises the overall measurement time of the experiments due to the fast exchange of intercalating dyes in combination with an increased number of bright fluorescence events due to the addition of dark-state quenchers. In this way we are able to achieve high resolution images with improved localisation precisions of around 10 nm with adequate label density which is also required to resolve structures of lowest size due to the sampling theorem of Nyquist.

The measurements for our high resolution concept have been performed on a TIRF setup which is described in section 3.3.1. In order to analyse the data and to apply the concept of improved localisation precision, Labview based software called "Analecta" has been developed completely from scratch. The software is also capable of processing the recorded data online. A step by step explanation of the fit algorithm which has been development is explained in detail in section 5.2.1.

A general overview of the high resolution imaging method iPAINT is illustrated in Figure 33.

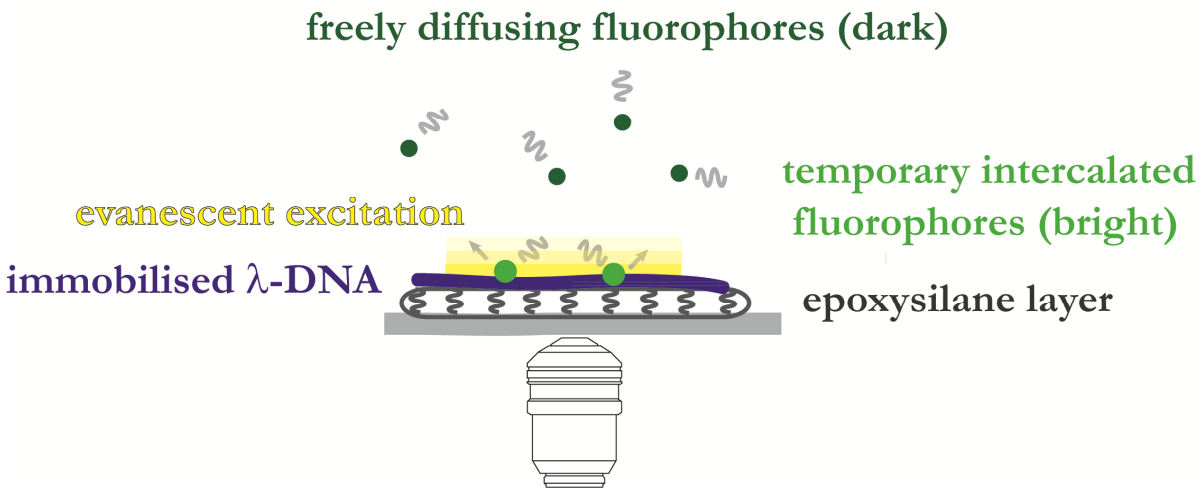

Figure 33 Overview of the high resolution method iPAINT

An epoxysilane layer (dark grey) is deposited on a previously cleaned coverglass. A target molecule (λ-DNA, blue) is strongly connected to the epoxysilane surface which leads to an immobilisation of DNA. In a droplet on top of the whole surface an intercalative dye molecules freely diffuse (dark green) in the buffer solution and are dark due to very low fluorescence quantum yield. Upon intercalation within the basepairs of the λ-DNA the intercalators emit fluorescence (bright green) due to strong increase of the fluorescence quantum yield. The measurement conditions are chosen to have low affinity of the intercalator to the λ-DNA so that the whole DNA molecule is continuously targeted by new intercalating fluorophores. In addition, evanescent excitation conditions (yellow) assure fluorescence excitation only in close vicinity to the surface.

5.1 Samples

5.1.1 λ-DNA

Commercially available λ-DNA (CAS#: 7732-18-5, #base pairs ~48502, Fermentas) served as an example of immobilised biomolecules to be visualised by the interaction with an intercalating dye.

5.1.2 Thiazole Orange (TO)

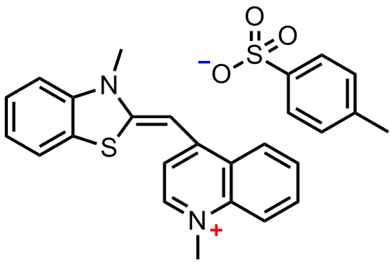

Figure 34 Chemical structure of the intercalating dye Thiazole Orange (TO)

The unsymmetrical cyanine dye Thiazole Orange (TO, CAS#: 107091-89-4, Fluka) was used as the fluorescence probe to visualise immobilised λ-DNA molecules by means of high resolution micros copy. The chemical structure of TO with the corresponding counter ion is shown in Figure 34.

The fluorescence quantum of free TO in solution is Φ_F(free)=0.0002 and dramatically increases when TO interacts with e.g. double-stranded DNA molecules such as calf-thymus DNA Φ_F(ctDNA)=0.11 (Nygren, Svanvik et al. 1998). Unsymmetrical cyanine dyes can interact with poly-nucleotides via groove binding and intercalation. In case of TO it was shown that the main interaction motif is monomeric intercalation with a stoichiometrical characteristic of one dye per base pairs when bound to double stranded DNA (Nygren, Svanvik et al. 1998; Armitage 2005).

As already explained, our high resolution microscopy concept is based on the PAINT principle, where a continuous binding and unbinding of a fluorescent probe to an immobilised target molecule is required. The knowledge to influence the interaction and therefore the affinity of intercalating dyes to DNA molecules by changing the concentrations of mono- and divalent metal ions (Lepecq and Paoletti 1967; Petty, Bordelon et al. 2000) is essential to realise our high resolution concept. The higher the concentration is the lower the affinity. The concentration of TO in case of the high resolution single molecule experiments is 1 nM.

5.1.3 Buffer conditions

The standard buffer which will be called magic buffer used for the high resolution imaging method iPAINT consists of 20 mM Tris (pH 7.5), 20 mM NaCl and 200 mM $MgCl_2$. Any changes in the buffer conditions will be denoted. In addition, the radical quencher Trolox which is a vitamin E derivative widely used in high resolution microscopy and the triplet quencher 4-(Phenylazo)benzoic acid (Azo) (Pfiffi 2010) are also used to further stabilise the fluorescence signal of the intercalating dye. The chemical structures of Trolox and Azo are shown in Figure 35. The concentration of the quenchers were in each case 300 μM (Dörr 2011).

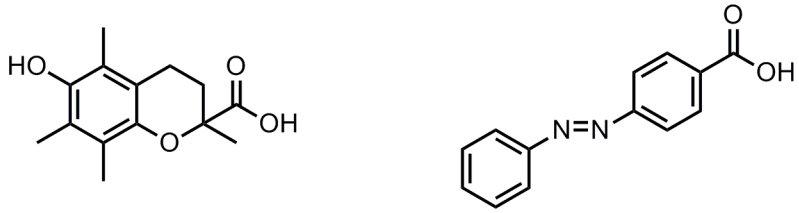

Trolox 4-(Phenylazo)benzoic acid (Azo)

Figure 35 Chemical structures of Trolox and Azo

5.1.4 Surface and sample preparation

1. Cleaning of coverglasses
   - sonification in 5% Hellmanex for 20min
   - thoroughly washing of coverglasses in ddH_2O
   - sonification in ddH_2O for 20min
   - drying of coverglasses under nitrogen gas

2. Silanisation
   - incubation of coverglasses with 3-(Glycidoxypropyl)dimethylethoxysilane for at least 30 min at 80°C in drying chamber
     (use 50μl per coverglass sandwich in petri dish)
   - thoroughly washing of coverglasses with chloroform
     (4 ml per coverglass)

3. Addition of λ-DNA
   - add 50µl of λ-DNA (1:5 dilution of commercial stock with 20 mM Tris/HCl buffer)
   - incubation for at least 15 min before measurement

4. Addition of Thiazole Orange intercalator
   - add 1 nM of Thiazole Orange in buffer to DNA droplet directly before measurement
     (typical buffer: 20 mM TrisHCl, 20 NaCl, 200mM $MgCl_2$

An overview of the high resolution method iPAINT including surface immobilisation and the general concept is shown in Figure 33.

5.2 Experimental Methods

5.2.1 Analecta – Data Analysis

a) Localisation precision

The high resolution method presented in this thesis is based on the precise localisation of a single emitter's position by fitting a 2d-gaussian model function to the photon distributions (refer to section 2.1.4). In order to handle the data obtained from the CCD camera and to further analyse the data, Labview based software called "Analecta" has been developed. At first, the strategy of the fit procedure will be explained. A flow chart of this procedure is shown in Figure 37.

The measured data is represented by a series of images (512x512 pixels). Before beginning the analysis, a minimum T_{min} and maximum T_{max} threshold (counts) has to be chosen by the user together with an offset parameter which defines a region of interest. The definition of the region of interest around a hit is illustrated in Figure 36. The algorithm loops over all images present in this series. Within each image, the algorithm searches for points of interest (hits) that show count values within the previously defined threshold environment. The number of all in this way identified hits of all images will be called N_{all}. Within each region of interest, the coordinates of the pixel with the highest counts are determined and will be kept as the centres of the regions of interest (hits). In addition, within a region of interest (± the offset parameter), no other point of interest is allowed. The number of hits with no close neighbour for all images will be called N_{nb}. Otherwise this part of the image will be ignored.

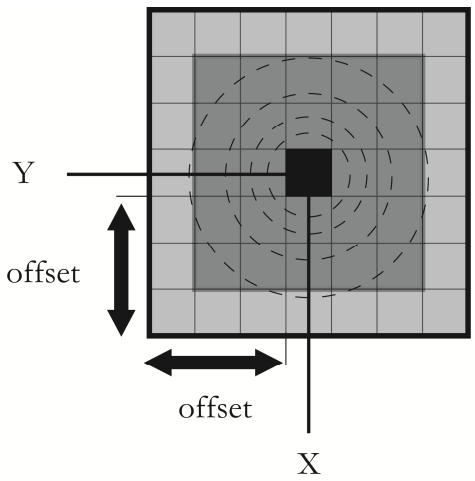

Figure 36 Definition of region of interest around a hit

Example of a region of interest with a size of 7x7 pixels which corresponds to an offset parameter of 3. The black box indicates the pixel with the highest counts (X,Y), the dark grey box the pixels which contain most of the signal and the light grey area the region from which the average background $<C_B>$ is calculated. Dashed circles indicate the photon distribution within a region of interest.

In order to prevent bad memory allocation due to a huge number of hits as a result of bad threshold selection, a maximum number of hits per image can be chosen by the user. If the number of hits N^i_{nb} of an image exceeds this value, the complete image will be skipped and the algorithm continues with the next image. If the number of hits is less than the maximum number of hits per image, the algorithm starts to loop over all hits N^i_{nb} within the i^{th} image. For each hit, the average background $<C_B>$ is calculated from the "outer ring" (light grey region in Figure 36) of the corresponding region of interest (± offset) around each hit. In the beginning, background was a free fit parameter of the 2d-gaussian model function (see also Equation 22 in section 2.1.4). With the rather small number of pixels within a region of interest, the reliability of the fit has not been found sufficient enough (not shown here). Therefore, the background contribution is averaged as just explained in order to reduce the number of free fit parameter. A further reduction would be the realisation of a symmetric fit function. The fact that the point spread function of a fixed emission dipole is in general non-centrosymmetric (Enderlein, Toprak et al. 2006) lead to the understanding of keeping an asymmetric model function with good stability of the fit procedure. In order to get a first estimate of the improved central positions of the photon distribution, the centre of mass coordinates (x,y) for each hit are calculated. The user can choose, if the calculated centres of mass coordinates are already sufficient enough for the purpose of the analysis. If yes, the algorithm continues with the next image. A much higher localisation precision (factor of two) is obtained by fitting a 2d-gaussian model function to the photon distributions as reported from other high resolution experiments (Sharonov and Hochstrasser 2006). For this purpose, initial parameters for the fit to converge have to be given. These initial parameters are the background corrected maximum counts C_{max} of the central pixel of each region of interest for the amplitude A, the (x,y) coordinates determined from the centre of mass calculation as the centre positions x_0 and y_0 and an initial value of σ_{init}=1 [pixel] (which corresponds to 178 nm) for the measures of the widths σ_x and σ_y of the model function. The average background contribution in each region of interest is calculated as already explained and kept constant for each fit individually. In order to assure reliable fit results, further quality criteria have to be fulfilled. At first, the fit has to converge within a given number of iterations (N_i=200). If not, the fit gets a flag and will be ignored. The number of hits after the convergence quality filter of all images will be called N_{conv}. A second quality parameter is the eccentricity of the obtained measures of the widths σ_x and σ_y which is defined in Equation 37.

$$\varepsilon = \left| \frac{\sigma_x - \sigma_y}{\sigma_x + \sigma_y} \right| < 0.3 \qquad \text{Equation 37}$$

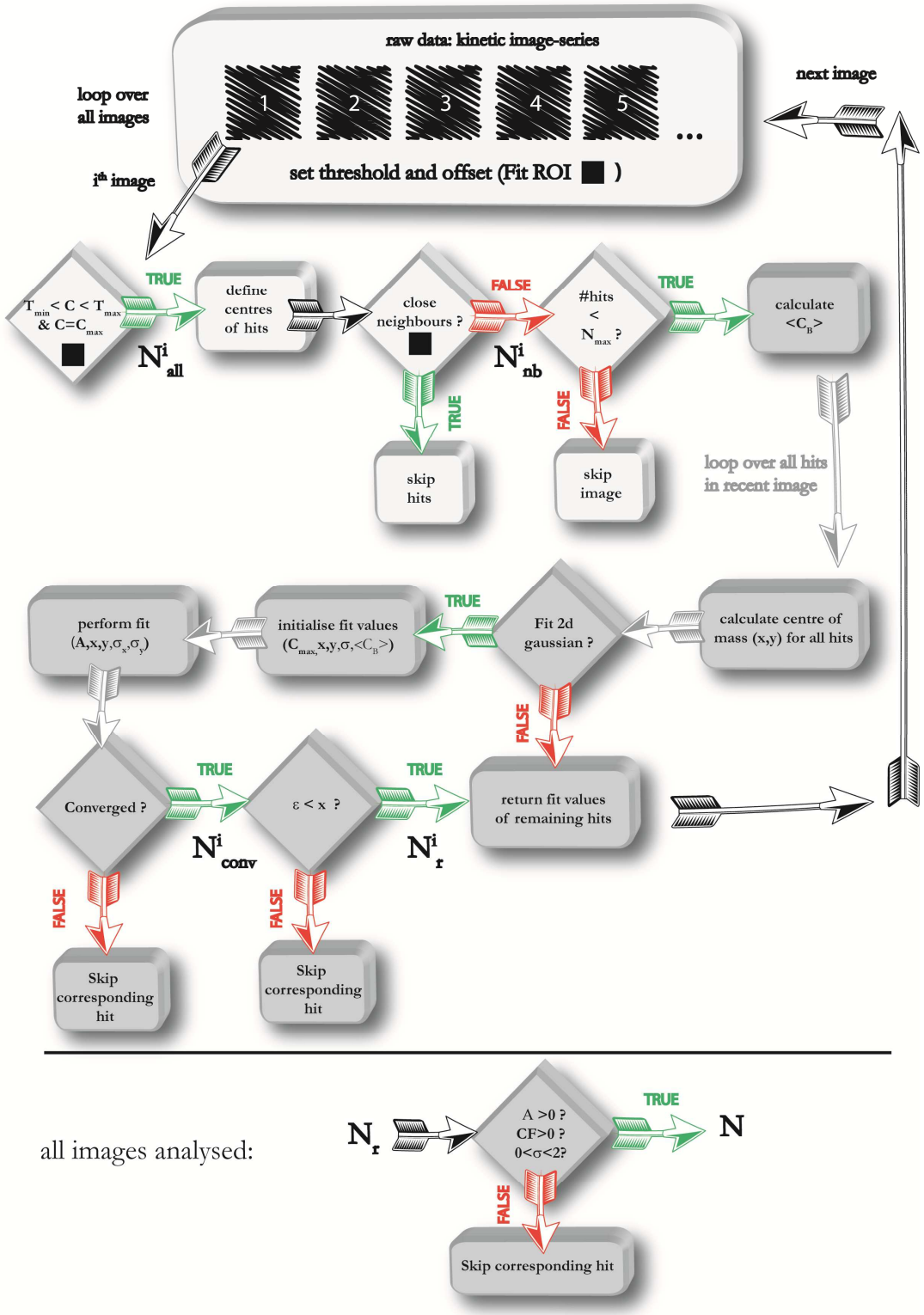

Figure 37 Flow chart of fit the procedure in Analecta

Images of a kinetic series are analysed one after another. All hits (N_{all}) with signals (C) within the defined threshold range are identified and the pixel with the highest counts within the defined size of the region of interest will be set as the centre of the corresponding hit. The previously defined offset determines the size of the region of interest around each hit (see also Figure 36). All identified hits that are within the chosen region of interest of another hit will be skipped leaving a number of hits with no close neighbours N_{nb}.

If the number of hits N_{nb} exceeds a previously defined maximum number of hits the complete image will be ignored. If not, the average background $<C_B>$ for each hit within the define region of interest is calculated (light grey area in Figure 36). In a first step, the centre of mass coordinates of each hits are calculated. If fitting of a 2d-gaussian model is required, the background corrected signal C_{max} of the central pixel, the previously determined centre of mass coordinates and the calculated average background $<C_B>$ will be used as the initial parameters for each fit within the region of interest of the hits. If the fit did not converge within 200 iterations the hit will be ignored leaving a number of hits N_{conv}. A further filter to assure good fit results removes hits that show too high eccentricity leaving a number of remaining hits N_r. The fit results of the remaining hits are kept and the algorithm continues with the next image until the final image of the series is analysed. The grey boxes indicate a loop over hits. Afterwards, a final filter removes few hits with negative amplitude and total number of fluorescence counts C_F. In addition, the measures of the widths σ_x and σ_y are also required to be $0 < \sigma < 2$ [pixels]. The number of hits for all images after this final filter will be called N.

Typically, the eccentricity was required to be less than 0.3 otherwise the corresponding hit is also ignored. The remaining number of hits after the eccentricity quality filter for all images will be called N_r. The values of the remaining hits are saved and the algorithm continues with the next image until the final image of the series is processed. Afterwards, a final filter removes few hits with negative amplitude and total number of fluorescence counts C_F. In addition, the measures of the widths σ_x and σ_y are also required to be $0 < \sigma < 2$ [pixels]. The number of hits for all images after this final filter will be called N.

An overview of the frequency histograms of the average background (grey), the measures of the widths σ_x (green) and σ_y (red) and the total fluorescence signal C_F (orange) of a quantum dots sample of around 4400 hits is shown in Figure 38. With the given effective pixel size of a=178 nm the average measure of the widths $<\sigma>$=0.98 pixel (174 nm) is in accordance to previously reported results with an effective pixel size of a=167 nm and an average measure of the width σ=150 nm (Sharonov and Hochstrasser 2006).

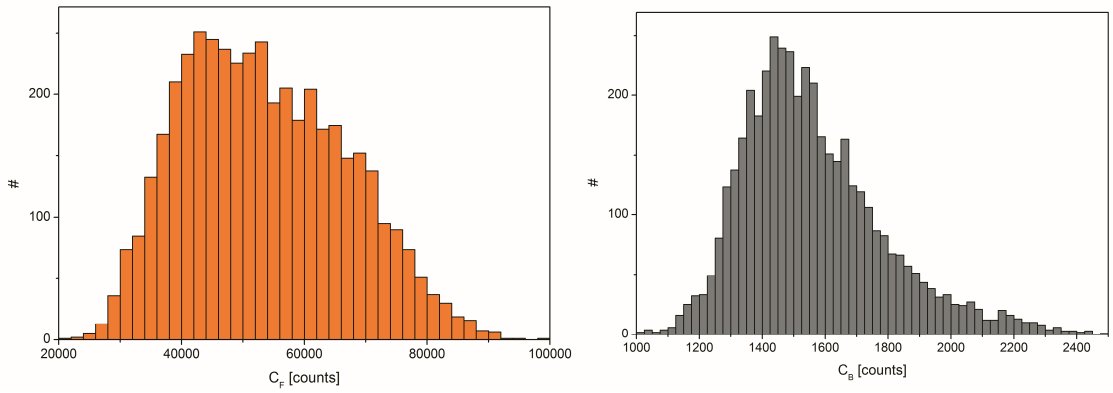

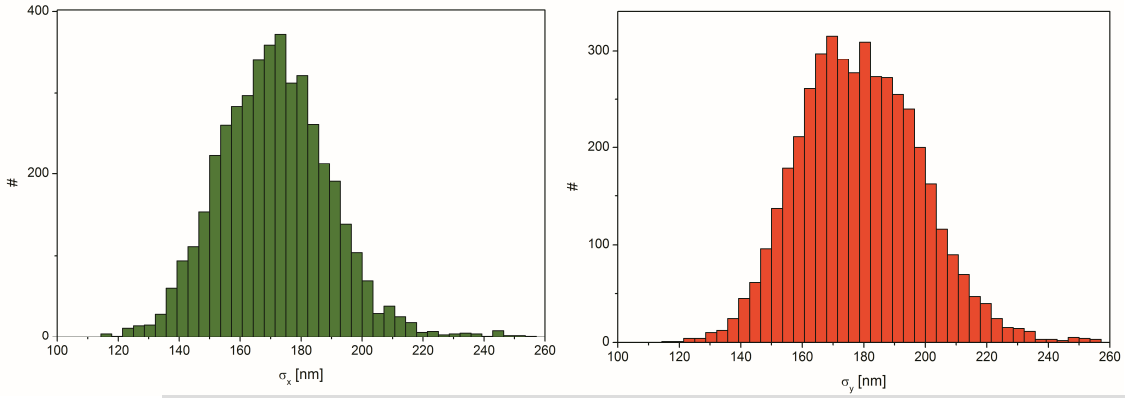

Figure 38 Exemplary 2d Gaussian fit results of a quantum dot sample

The frequency histograms of the fluorescence signal C_F (orange) the background C_B (grey) and the measures of the width σ_x (green) and σ_y (red) of 4400 hits from a quantum dot sample are shown. The quantum dots were added to a clean coverglass surface in deionised water and dried in the open air to be fixed. The excitation power at the objective was 500 µW. The cycle time was 0.1 s recorded in frame transfer mode of the CCD camera. The applied threshold was T_{min}=8000 counts.

These fit values are further used to calculate the corresponding localisation precision of each hit. However, the total signal (orange histogram in Figure 38) obtained from the fit is given in counts recorded by the electron multiplying CCD camera. In order to calculate the localisation precisions, the corresponding numbers of primary fluorescence and background photons have to be known. The number of primary fluorescence photons N_F is calculated with the help of Equation 38.

$$N_F = \frac{C_F \cdot \text{sensitivity(CCD)}}{\text{EM gain}} \cdot \text{quantum efficiency} \qquad \text{Equation 38}$$

The same formula is also used to calculate the number of background photons N_B. Here, the sensitivity of the CCD camera is 12.76 electrons/count in case of a 10 MHz amplifier and a factor of 5.2x for the pre-amplifier, the software EM gain is 3400 which corresponds to an actual gain of 200 and the average quantum efficiency within the spectral detection range is found to be 0.9 from the technical note of the CCD camera. A value of 1 electron per photon is denoted. Further camera parameters can also be found in the technical note of the CCD camera. The frequency histograms of the primary signal photons (orange) and the primary background photons (grey) are shown in Figure 39. The number of primary signal and background photons, the measures of the widths σ_x and σ_y and the effective pixel size of 178 nm is used to calculate the localisation precision of each hit (see Equation 23). The localisation precision frequency histograms in x- (green) and y-direction (red) are shown in the lower graphs of Figure 39.

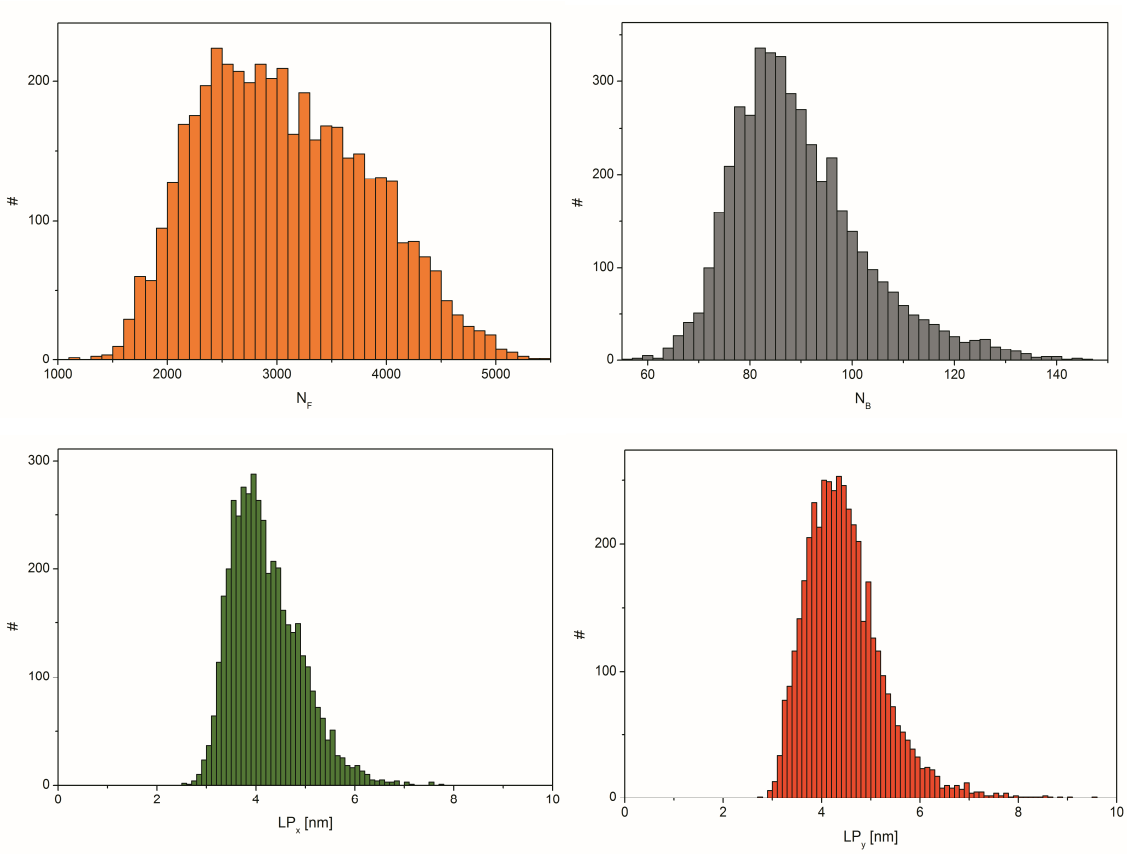

Figure 39 Exemplary localisation precision histograms of a quantum dot sample

The upper left graph (orange) shows the primary fluorescence photons N_F frequency histogram and the upper right graph (grey) the background photons N_B frequency histogram. The values were calculated from the corresponding counts histograms with the help of Equation 38. The lower left graph (green) shows the calculated localisation precision frequency histogram in x-direction and the lower right graph (red) the corresponding frequency histogram in y-direction. The localisation precisions were calculated with the help of Equation 23 and the corresponding measure of widths frequency histograms which are shown in Figure 38. Average localisations given later in this thesis are averaged values obtained from these histograms.

The average localisation precisions as well as the average signal and background photons which will be given later in this thesis are calculated from these frequency histograms.

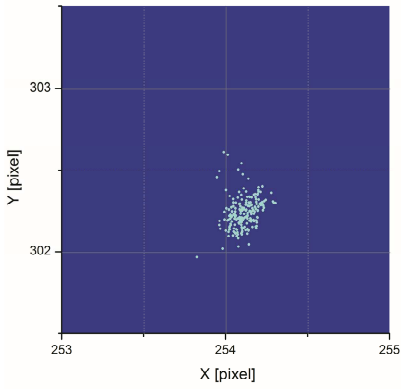

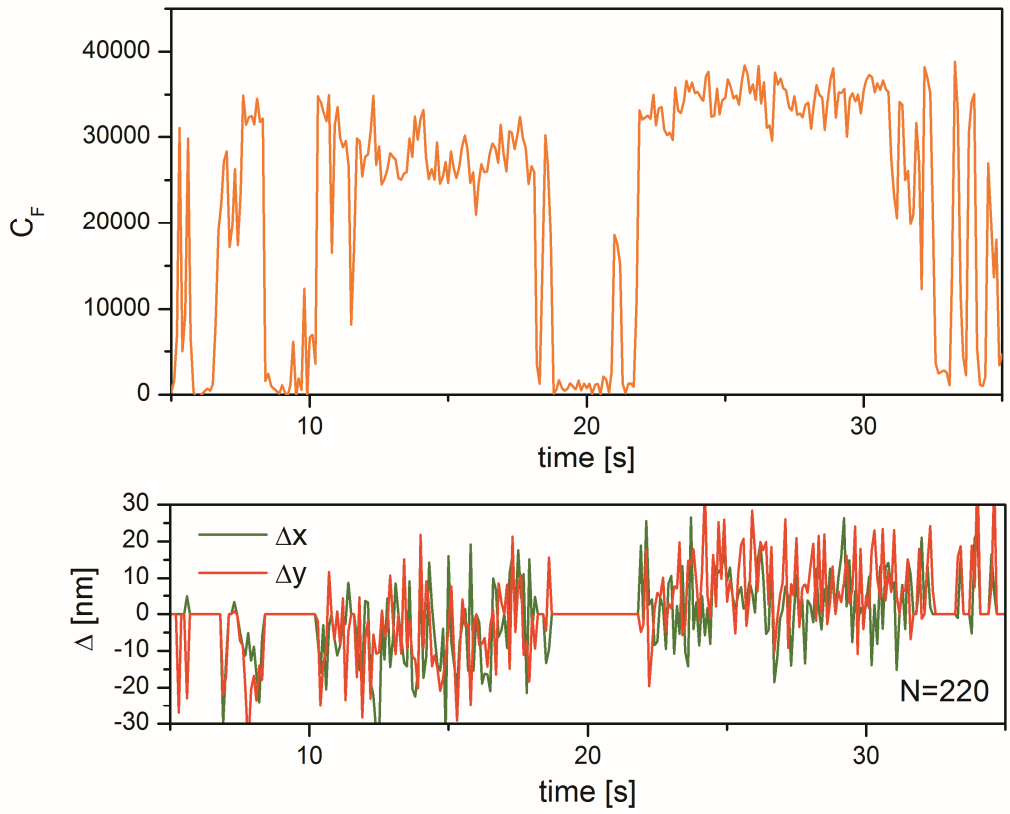

Figure 40 Localisation of a single quantum dot

The upper graph shows the hits that are assigned to a single quantum dot. The middle graph shows the corrected fluorescence time trace (C_F) obtained from a 5x5 pixel area around the centre of the quantum dot which is calculated from the positions of the assigned hits. The lower graph shows the differences of the position of the hits in x- and y-direction relative to the corresponding mean value calculated from all assigned hits whenever the algorithm found a hit to be analysed. Here, 220 hits were assigned to the quantum dot.

The localisation of a single quantum dot from a number of corresponding hits N assigned to the quantum dot is shown in the upper graph of Figure 40. The middle graph of Figure 40 shows the corresponding corrected fluorescence time trace (C_F) obtained from a 5x5 pixel area around the calculated centre of the object from the positions of the assigned hits.

The lower graph of Figure 40 shows the differences Δx and Δy from the hits with respect to the corresponding mean value of the hits assigned to the quantum dot whenever the algorithm found a hit to be analysed. The two graphs of Figure 41 show the corresponding frequency histograms of Δx and Δy. A fit with a Gaussian model function yielded a measure of the width of σ=12.2 nm in x-direction and σ=14.9 nm in y-direction. . The analysis of Δx and Δy is in good agreement if we take into account the actual size of a quantum dot (d~10-20 nm). Each of the assigned hits is localised with an average localisation precision of <LP>~4.5 nm. Therefore, Δx and Δy values larger than the

average localisation precision can be attributed to the size of an object to be investigated or to investigate the presence of an instrumental drift.

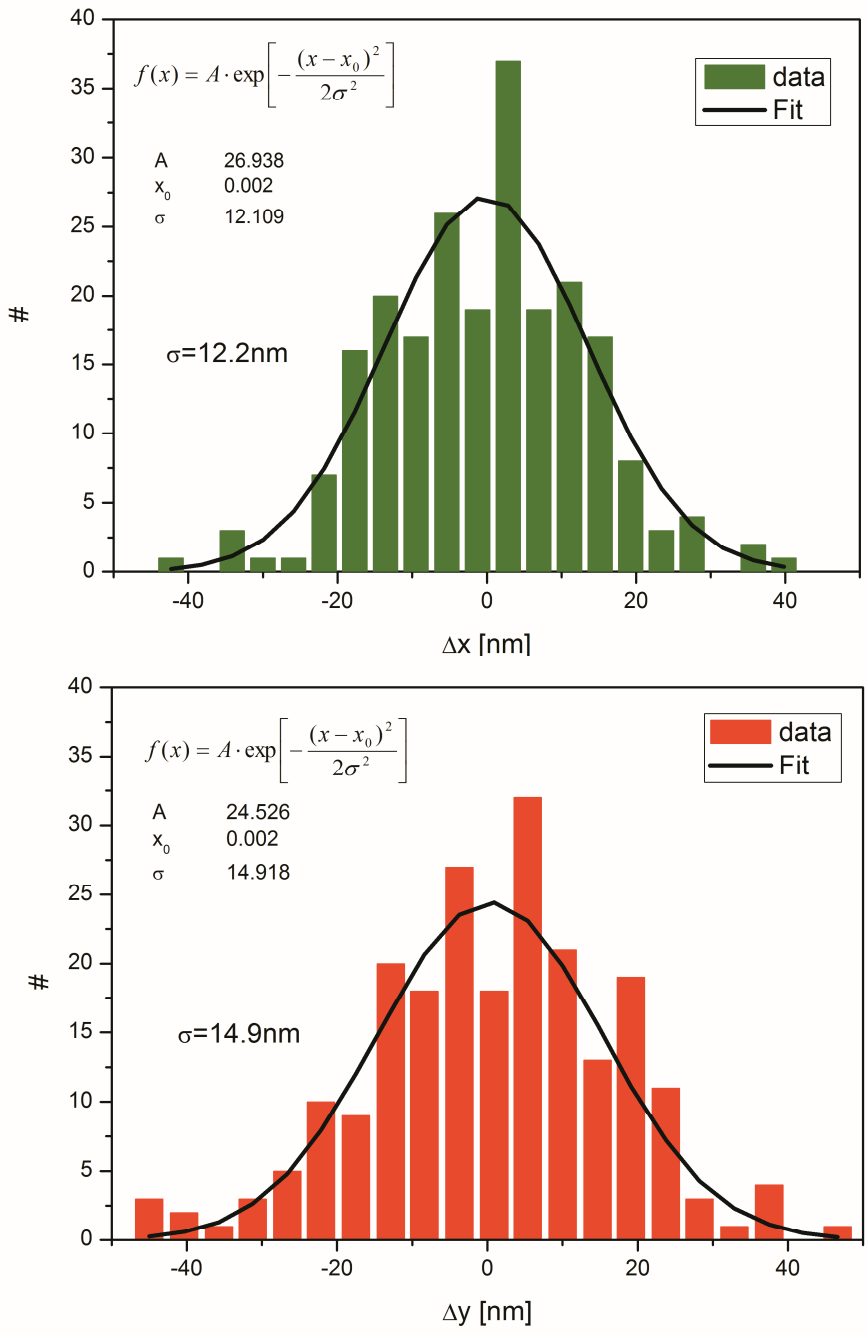

Figure 41 Frequency histograms of Δx and Δy

The frequency histograms of Δx (green) and Δy (red) are shown. The Δ-values show the differences of the localised position of a hit relative to the corresponding mean value of the hits which are assigned to an object. A fit with a Gaussian model function yielded a measure of the width of σ=12.2 nm in x-direction and σ=14.9 nm in y-direction. These results are in good accordance to the size of the investigated quantum dots (d~10-20 nm).

b) Time traces (background and excitation profile correction)

The software is not only able to determine the position of points of interest with high precision, it can also build fluorescence time traces of region of interest. A correction that accounts for background and the underlying excitation profile has been designed.

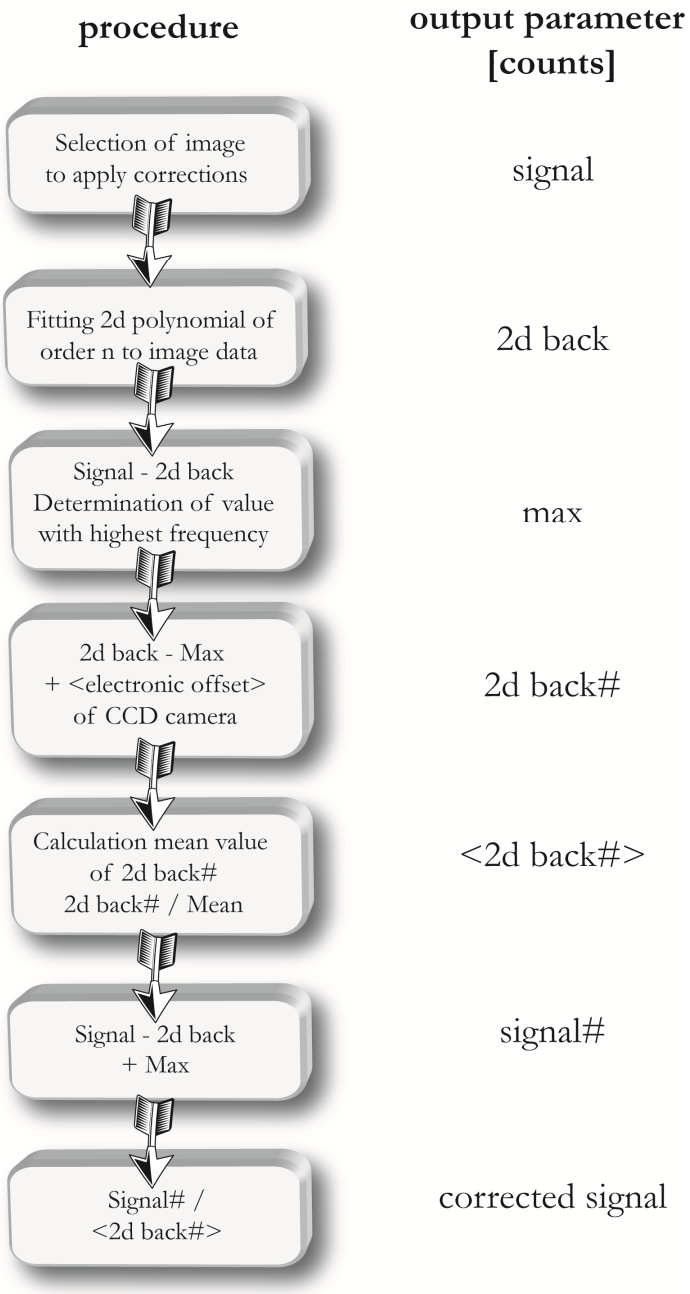

Figure 42 Flow chart of background and excitation profile correction

A flow chart of the combined background and excitation profile correction is shown in Figure 42. At first, an image of the kinetic series is chosen to which a combined background and excitation profile correction is applied. This combined correction is later on applied to all images of the series.

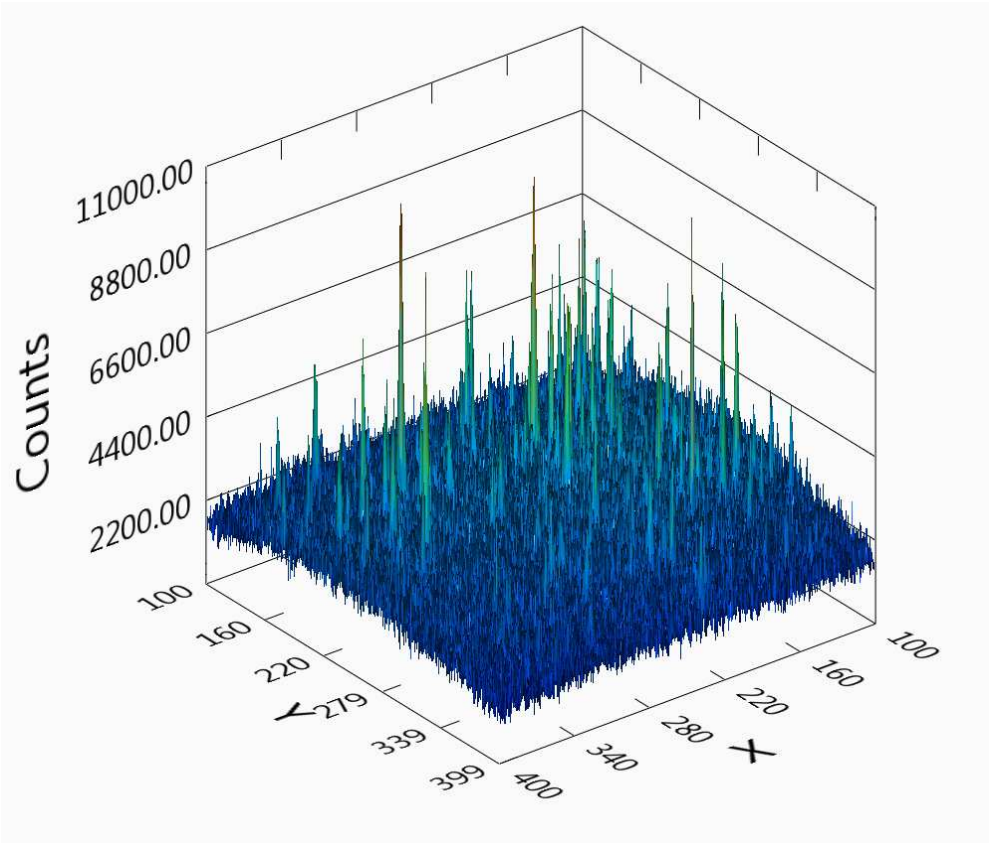

Figure 43 "Raw" Signal C_S of Rh110 molecules

A 3d illustration of an image obtained from a CCD camera is shown.

The 3d illustration of a signal image recorded by a CCD camera is shown in Figure 43. The determination of the background and of the excitation profile is obtained directly from the measurement. With a total number of pixels N_{Pixel}= 512x512 = 562144 the number of pixels which contain mainly fluorescence information in our single molecule experiments is low (see also Figure 43) so that the corrections applied mainly depend on pixels which do not contain significant fluorescence information.

A 2d polynomial of order n (typically order 3 is used) is fitted to the signal information. The result is called 2d back. From the signal the 2d back is subtracted and the intensity with the highest occurrence is determined (max). This maximum value is used to compensate deviations from the 2d polynomial fit so that the average background is distributed around zero. This step is implemented in the procedure to account for the included fluorescence information which may change the overall position of the background plane. From the 2d back array the value with the maximum frequency is

subtracted and the average electronic offset (here 110 counts) is also considered. The result is called 2d back#. The shape of this intermediate background plane is illustrated in Figure 44. From this array the mean value is calculated and the whole array is divided by this mean value which we call <2dback#>. With the help of this array we can correct for differences in the excitation profile. If we subtract the 2d back array from the signal and add the value with the highest frequency as previously calculated we account for background contributions which we call signal#. The combined correction of background and excitation profile is applied by calculating the ratio of signal# over <2d back#>.

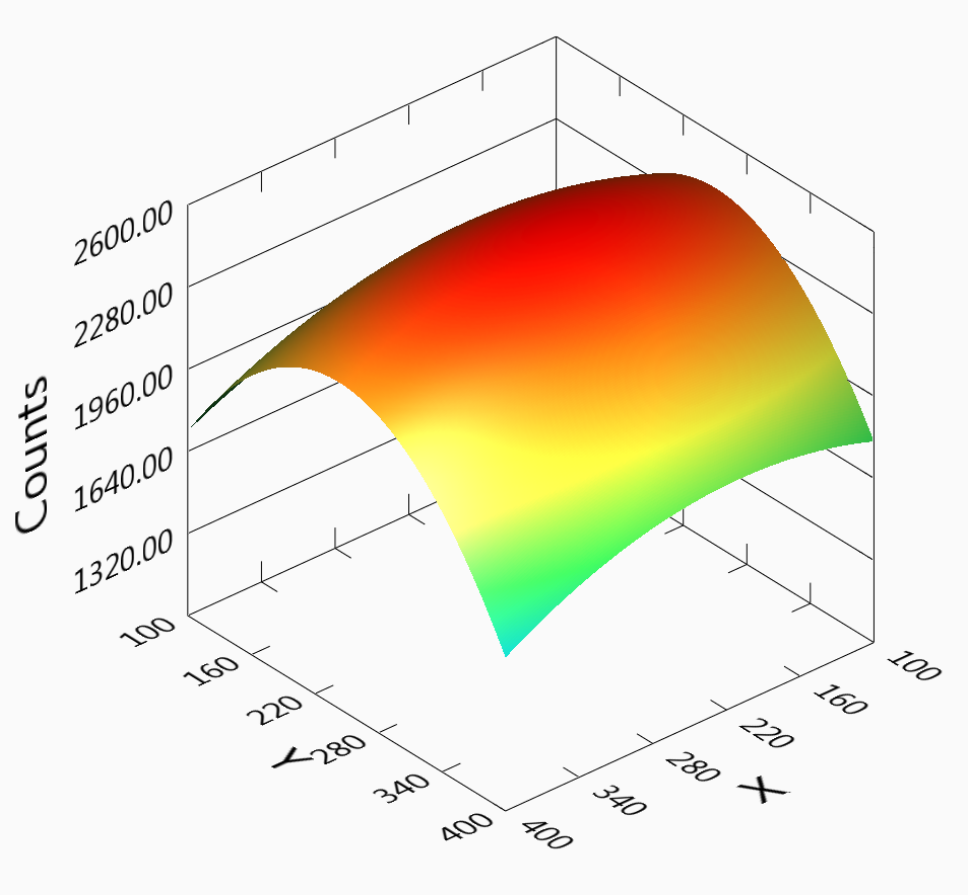

Figure 44 Background plane 2d back#

A 3d illustration of the intermediate background plane 2d back# is shown.

The complete application of the combined correction is shown in Figure 45. The combined background and excitation profile correction can be applied before or after the 2d Gaussian fit procedure. In order to calculate and compare the localisation precisions, the combined correction is not applied for the fit because the actual background is needed in the calculations.

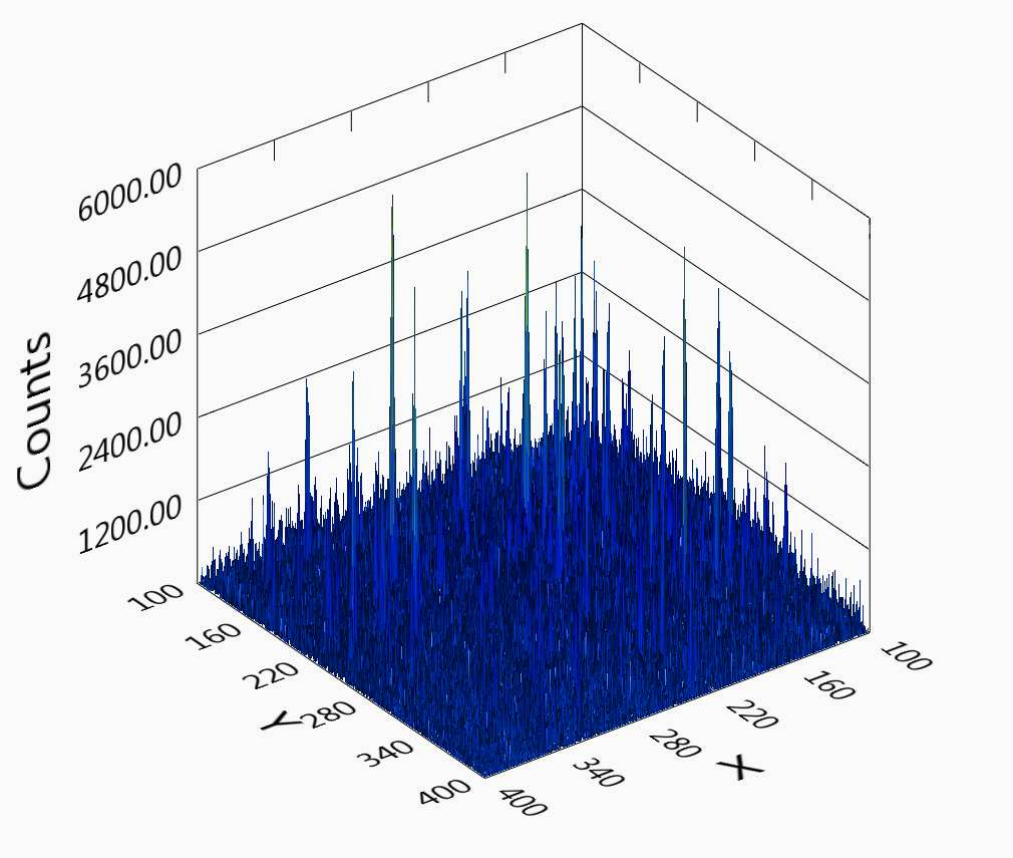

Figure 45 Background and excitation profile corrected signal C_S

A 3d illustration of overall corrected signal is shown.

5.2.2 Results

The interactions between the intercalating dye Thiazole Orange (TO) and different kinds of DNA molecules have been analysed in great detail (Nygren, Svanvik et al. 1998). One of the possible binding modes shows an absorption spectrum similar to that of the free TO monomer. The shape is characterised by a shoulder on the short wavelength side of the maximum of the spectrum. This binding mode was found to be the dominant one for all examined double stranded (ds)-DNA molecules. In order to verify the monomeric binding mode of TO with the double stranded λ-DNA absorption spectra have been measured.

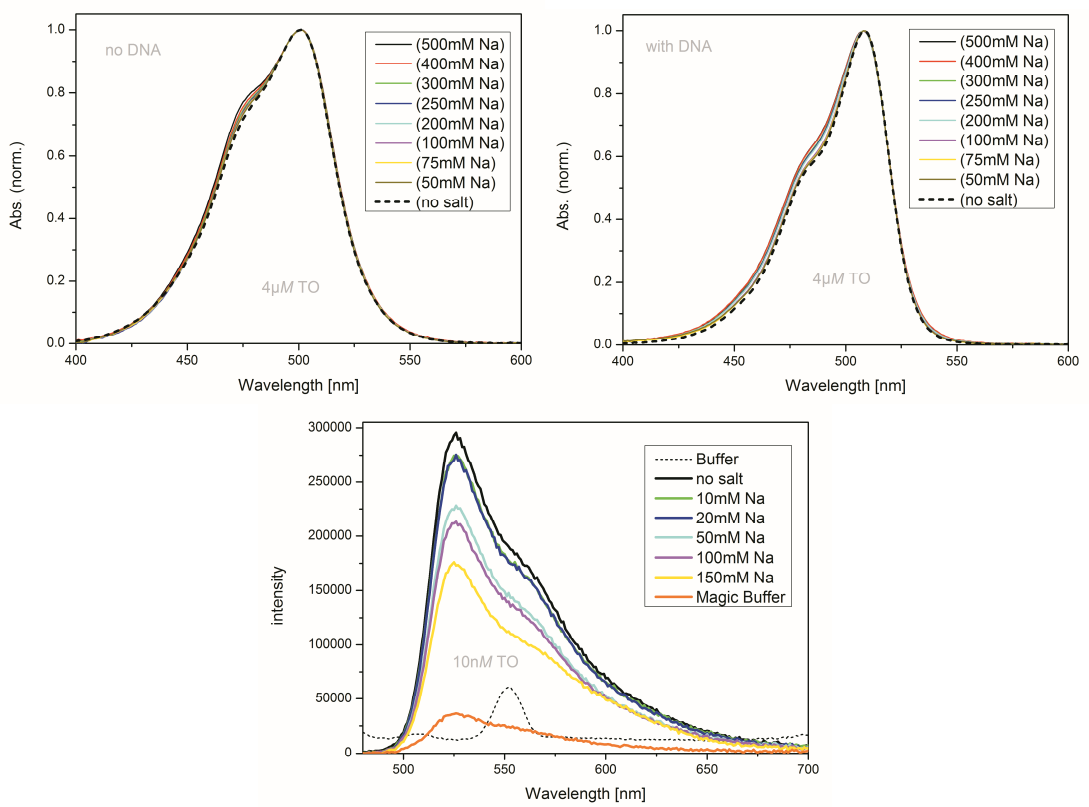

Figure 46 Absorption and emission spectra of TO (NaCl)

The absorption spectra of TO without (upper left graph) and with the presence of DNA (upper right graph) which are dependant on the concentration of NaCl are shown. The dashed black lines represent pure Tris buffer conditions. All other curves represent Tris buffer with the given concentration of NaCl only. In the absence and presence of DNA the fraction of dimeric TO molecules is slightly increased which is indicated by a small increase of the short wavelength side of the maximum of the spectra. The overall shape of the spectra indicates a monomeric binding mode to DNA. In the lower graph the fluorescence emission spectra of TO in presence of DNA which are dependant on the concentration of NaCl are shown. The higher the concentration of NaCl the lower is the intensity. This indicates a weaker affinity of TO to DNA. The orange line represents the corresponding spectrum under magic buffer conditions.

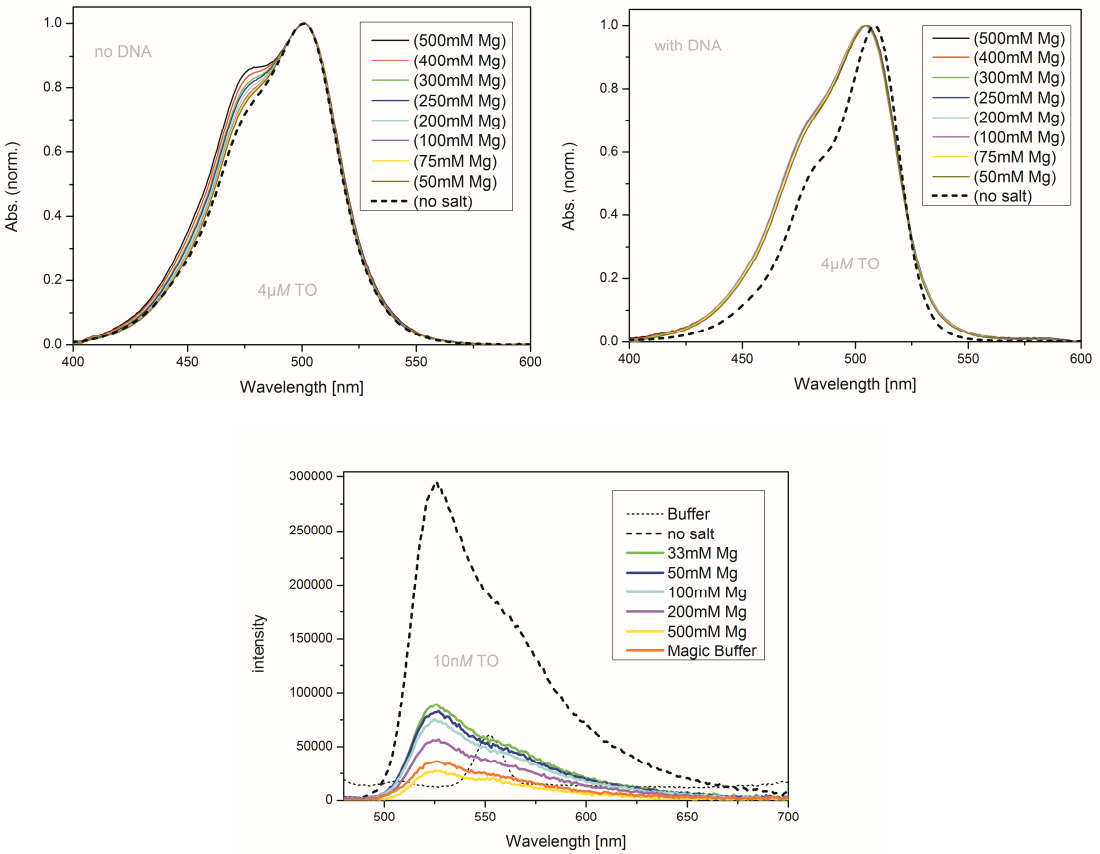

Figure 47 Absorption and emission spectra of TO ($MgCl_2$)

The absorption spectra of TO without (upper left graph) and with the presence of DNA (upper right graph) which are dependant on the concentration of $MgCl_2$ are shown. The dashed black lines represent pure Tris buffer conditions. All other curves represent Tris buffer with the given concentration of $MgCl_2$ only. In the absence of DNA the fraction of dimeric TO molecules is increased which is indicated by an increase of the short wavelength side of the maximum of the spectra. In presence of DNA a broadening of all spectra representing buffer conditions with $MgCl_2$ in comparison to the Tris buffer without metal ions is observed. Still, the overall shape of the spectra indicates a monomeric binding mode to DNA. In the lower graph the fluorescence emission spectra of TO in presence of DNA which are dependant on the concentration of $MgCl_2$ are shown. The higher the concentration of $MgCl_2$ the lower is the intensity. This indicates a much weaker affinity of TO to DNA in comparison to the measurements with NaCl (see Figure 46). The orange line represents the corresponding spectrum under magic buffer conditions.

As already mentioned, the affinity of the intercalating dye to the λ-DNA is influenced by the presence of mono- and divalent metal ions. Therefore, absorption spectra of TO with and without the presence of λ-DNA have been measured which are dependant on the concentrations of mono- (NaCl) (upper graphs in Figure 46) and divalent metal ($MgCl_2$) ions (upper graphs in Figure 47). The absorption spectrum of TO is just slightly dependant on the concentration of monovalent metal ions, the presence of divalent metal ions lead to an increased formation of TO dimers indicated by an increase of the shoulder on the short wavelength side of the peak. Nevertheless, the overall shape

of the spectrum indicates that the TO molecules intercalate into the basepairs of ds-DNA in a monomeric manner. The fluorescence emission spectra of TO in the presence of λ-DNA have also been measured which are dependant on the concentration of mono- and divalent metal ions. These fluorescence emission spectra are shown in the lower graphs of Figure 46 and Figure 47 respectively. The fluorescence signal in the presence of mono- and divalent metal ions is increased with a much stronger impact in case of the divalent metal ions. These differences in the fluorescence intensity indicate changes in the affinity of the intercalative dye to the λ-DNA dependant on the concentration of the metal ions due to more effective electrostatic shielding. From these spectra alone a quantitative analysis of the influence of the metal ions on the affinity is not possible.

In order to further characterise the interaction between the intercalative dye TO and the λ-DNA, bleach and recover experiments have been performed. Here, low excitation power of 100 μW at the objective was used to identify immobilised λ-DNA recording the fluorescence from the intercalating dye. The excitation power was increased (10 mW) for a period of around 20 s to bleach the the already intercalated dyes. The excitation power is reduced again to 100 μW and the recovery of fluorescence signal is recorded. For each measurement the procedure has been followed twice. The fluorescence recovery without any metal ions present in the buffer (Tris, no salt) and of a sample with the presence of mono- and divalent metal ions (MB, concentration as given in 5.1.3) are illustrated in Figure 48.

The graph shows the fluorescence signal of a 20 x 20 pixel area (3.5μm x 3.5μm) normalised to the initial fluorescence signal at t=0 with low excitation power of 100 μW. The blank parts within the curves correspond to the bleaching period at 10 mW. The red curve shows the fast fluorescence recovery under magic buffer (MB) conditions. In both recovery periods the fluorescence quickly reaches the steady state level present before the first step of bleaching. A mono exponential growth model is applied to the data (dots). The results of the fit within the periods of recovery are also shown in Figure 48 (lines). From this analysis a recovery time of t_{rec}=2.5 s is obtained in the presence of mono- and divalent metal ions. In case of pure buffer conditions with no metal ions present the recovery time cannot be determined because of the short recovery intervals. From the data, recovery times > 20 s can be assumed.

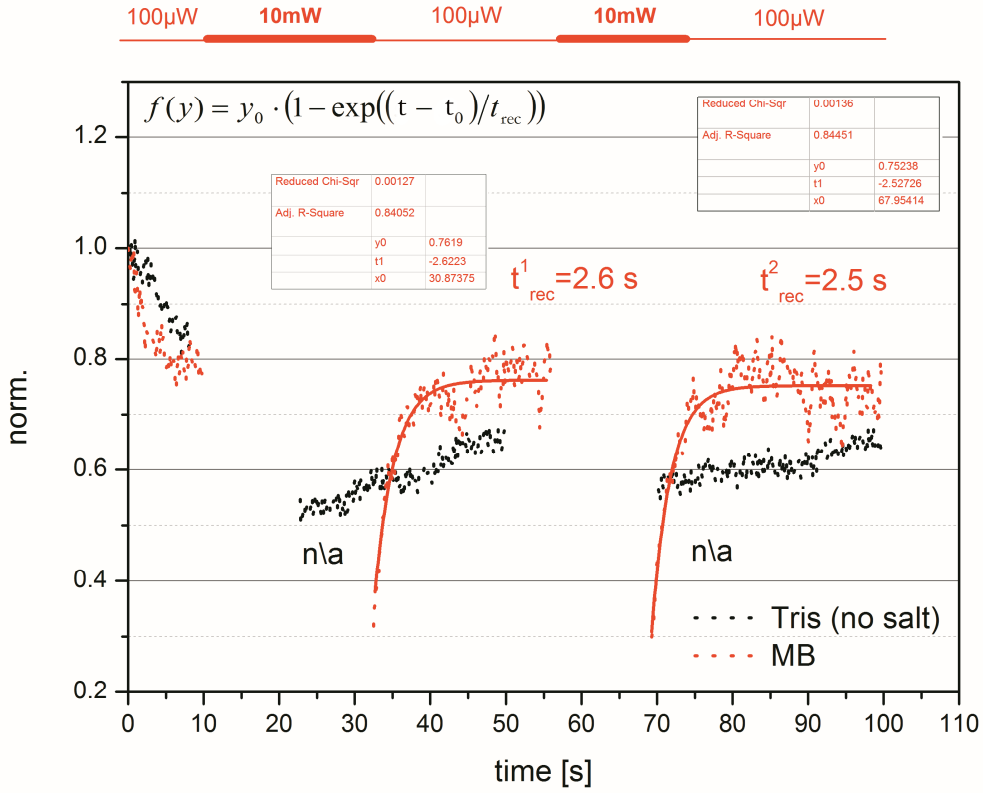

Figure 48 Fluorescence recovery traces after photobleaching

The graph shows the fluorescence recovery of spots (20x20 pixels) where TO intercalated into the basepairs of λ-DNA. The total signal is normalised to the initial intensity. The graph shows the periods of the measurement with a low excitation power of 100µW at the objective. The empty spaces in between are periods of high excitation power 10mW at the objective in order to bleach the fluorescence signals. In the case of magic buffer conditions (red, MB, mono- and divalent metal ions present), the fluorescence returns quickly to the final value before the first bleaching period whereas in case of pure Tris buffer conditions without any salt (black, Tris) the fluorescence recovery is much slower. Fitting an exponential growth model (the formula is given in the upper left corner of the graph) the recovery time in case of MB was found to be ~2.5 s whereas under pure Tris conditions the recovery time is assumed to be longer than 20 s. Fit results were not accessible.

From this analysis it is clear, that the presence of metal ions is required to change the affinity of TO to the λ-DNA to obtain fast repetitive binding and unbinding. In general, the corresponding recovery rate is attributed to the binding rate which is of course also influenced by the unbinding rate of the intercalating dye. Because of the observed fast exchange of the intercalating dyes a further detailed analysis on the unbinding rate was not possible at the time of this work.

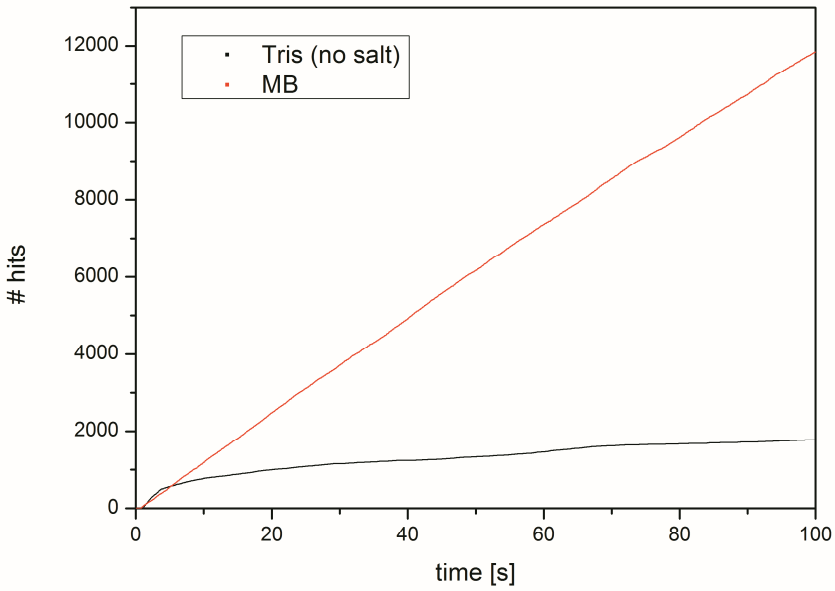

Figure 49 Accumulated number of hits versus time

The graph shows the accumulated number of hits to which the high resolution analysis is applied measured under pure Tris buffer conditions (black) and under magic buffer conditions (red). The same threshold was applied to each of the data set. In case of magic buffer conditions the curve shows a more or less constant number of hits per frame whereas in case of Tris buffer conditions half of the total number of hits is obtained already within the first 15 s. In addition, the presence of metal ions leads to a much higher number of hits (in the present case a factor of 6 x) indicating a much faster exchange of the intercalating dyes.

A further indicator of the fast exchange of the intercalating dyes on the λ-DNA molecules has been found by analysing the accumulated number of hits at image i or time t which have been identified by the algorithm due to the previous selection of a threshold. For all of these hits the high resolution fitting procedure is applied as already explained in section 5.2.1.

The number of accumulated hits identified by the algorithm at time t in pure Tris buffer and under magic buffer conditions is shown in Figure 50. In case of magic buffer conditions a more or less constant number of hits in all images are observed whereas in case of Tris buffer without any metal ions 50% of the total hits are already identified within the first 15 s of the measurement. In addition, the overall number of hits under magic buffer conditions is around a factor of 6x higher in contrast to Tris buffer conditions.

A typical result of the high resolution procedure is shown in Figure 50. On the left hand side an accumulation of 1000 images (100 ms cycle time) corresponding to a measurement time of 100 s is shown. In addition, the computed high resolution localisation image of the same measurement is overlayed (light blue dots).

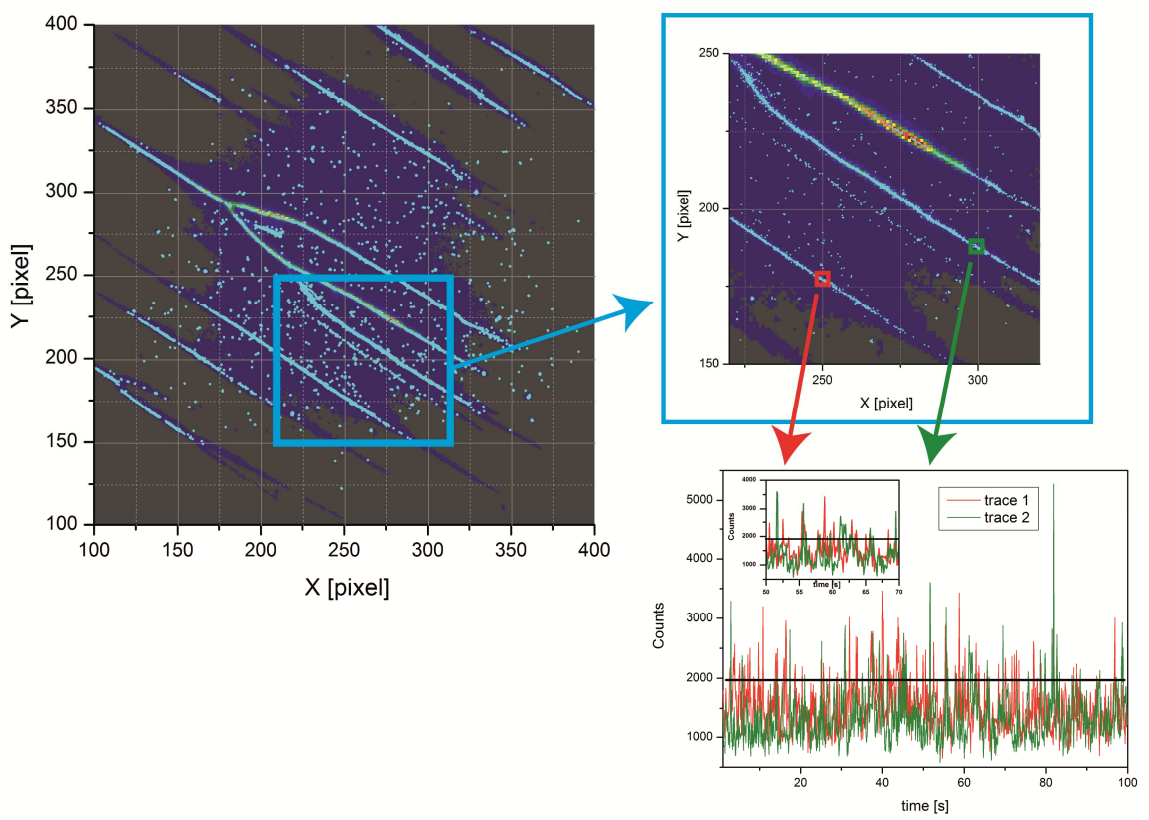

Figure 50 Fluorescence time traces of TO molecules intercalated into λ-DNA

The upper left image (300x300 pixels which corresponds to ~ 50µm x 50µm) shows the accumulation of 1000 images of a kinetic series. In addition, the computed high resolution image is overlayed (light blue dots). The upper right graph shows a zoom of same image. Each of the light blue dots represents a spot which could be identified with an average localisation precision of <LP> ~12.5 nm. In the lower right graph, two exemplary time traces of selected spots of the λ-DNA are shown (red and green squares in the upper right image). The ordinate represents the uncorrected maximum counts within a region of 5x5 pixels (0.9µm x 0.9µm). The inlet shows a zoom of the time traces (20 s). The black line indicates a threshold at which a fluorescence event is selected to be fitted. From the time traces it is visible, that the λ-DNA is continuously targeted by the intercalating dyes (signals above threshold). The excitation power at the objective was 0.5 mW and the measurement time was 100 s.

Each of the light blue spots corresponds to single fluorescent events that are localised with an average localisation precision of <LP> ~ 13.5 nm. The upper right graph shows a zoom of the same image. In the lower right graph the fluorescence time traces of two different spots with a size of 5x5 pixels (0.9µm x 0.9 µm) are shown. Here, the ordinate represents the uncorrected maximum counts within each region to show that these regions where λ-DNA molecules are located are indeed continuously targeted by the intercalating dyes indicated by signals higher than the selected threshold of 2000 counts.

A nice effect of the measurement conditions is shown in Figure 51. If the λ-DNA molecules are added to the modified surface the formation of branched structures is often observed after an incubation time of 1day or even longer.

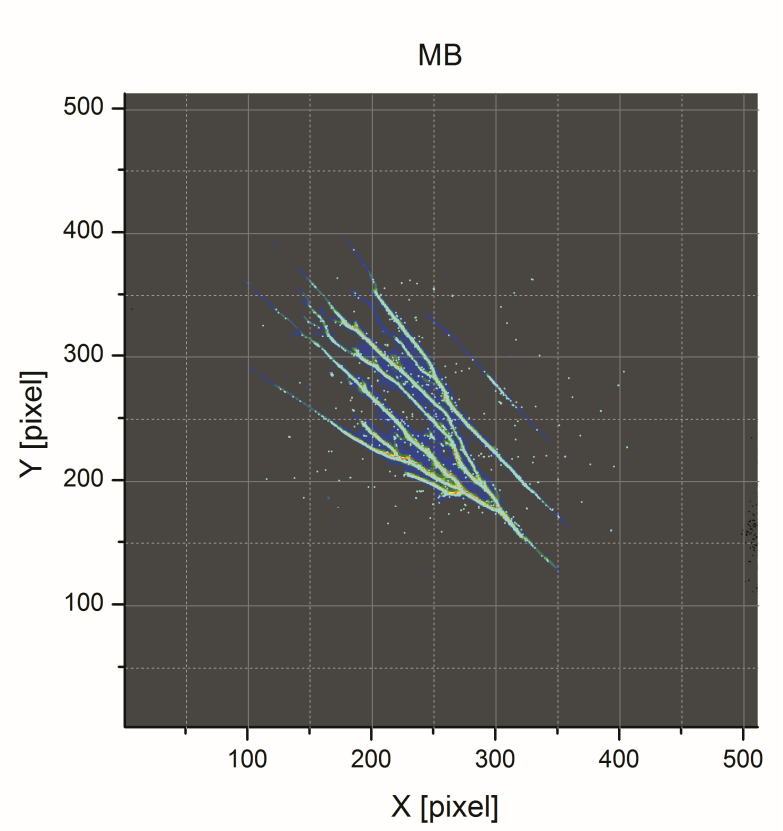

Figure 51 Branched DNA structures after 1 day incubation on the surface

The image (300x300 pixels which corresponds to ~ 50µm x 50µm) shows the accumulation of 1000 images of a kinetic series. In addition, the computed high resolution image is overlayed (light blue dots). If the λ-DNA molecules are added to the surface a formation of branched structures is often observed after an incubation time of 1 day and more (droplet is air dried). The excitation power at the objective was 1 mW and the measurement time was 100 s.

In order to optimise the measurement conditions of the high resolution method, power series have been performed to figure out the appropriate excitation power. The results of such a power series are summarised in Table 6. The power was measured at the objective with the excitation laser light going straight through the objective. The value of the threshold is somehow arbitrary as the number of counts recorded by the CCD camera depends on the individual intensities of signal and background that are not strictly linear with the excitation power. For each excitation the threshold was chosen in a way that a comparable number of hits could be found by the algorithm. For all excitation power measurement the same area of a surface was analysed. In Table 6 the number of hits and the average number of fluorescence (N) and background (b^2) photons which were calculated from

the corresponding frequency histograms (not shown) are given. The number of fluorescence and background photons are the two most significant factors in the calculation of the average localisation precision which is also given.

power [μW]	# hits	photons (N_F)	BG photons (N_B)	<localisation precision> [nm]
110	2540	367	18	15.0
230	3177	467	28	13.6
460	2362	609	33	11.0
680	2674	763	47	11.0
1100	2815	938	83	11.5
2300	2797	1417	219	13.7

Table 6 Power series

The table shows the number of hits, the number of fluorescence (N) and background (b2) photons and the calculated average localisation precision dependant on the excitation power. The thresholds were chosen to obtain comparable numbers of hits. The best average localisation precision was achieved at excitation powers in the range of 500-1000 μW.

The best localisation precision was obtained at excitation powers in the range of 500-1000 μW. With increasing excitation power the average number of fluorescence photons also increases like the average number of background photons. For the highest excitation power used in the power series the background contribution is increased relatively stronger than the number of the fluorescence photons. The increase relative to the lowest excitation power of 100 μW of the number of fluorescence N_F (black) and background photons N_B (red) which is dependant on the excitation power is shown in Figure 52. The increase of the number of fluorescence photons N_F shows a linear dependence on the excitation power which is increased by a factor of ~4x at the highest excitation power of 2300 μW. The number of background photons N_B does not show a linear relation to the excitation power and is increased by a factor of ~12x at the highest excitation power of 2300 μW.

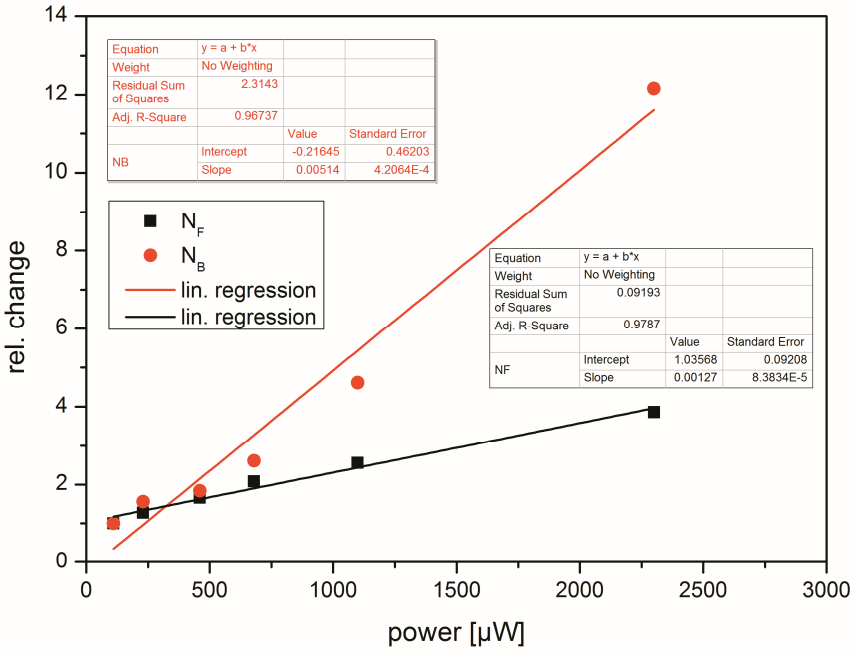

Figure 52 Relative change of N_F and N_B dependant on the excitation power

The increase relative to the lowest excitation power of 100 µW of the number of fluorescence N_F (black) and background photons N_B (red) which is dependant on the excitation power is shown. The increase of the number of fluorescence photons N_F shows a linear dependence on the excitation power which is increased by a factor of ~4x at the highest excitation power of 2300 µW. The number of background photons N_B does not show a linear relation to the excitation power and is increased by a factor of ~12x at the highest excitation power of 2300 µW.

The threshold parameter is a crucial part of the analysis. The higher the selected threshold the higher is the average number of primary fluorescence photons of the analysed hits. As the calculated localisation precision strongly depends on the number of primary fluorescence photons, a higher threshold also results in a better localisation precision on average.

The influence of the threshold on the total number of hits, the average number of fluorescence and background photons and the calculated average localisation precision of one experiment is shown in Table 7. The higher the threshold the higher is the number of fluorescence photons and therefore the average localisation precision. On the other hand, a higher threshold also results in a reduced number of identified hits. At the highest applied threshold of 4000 counts the average localisation precision is around 6 nm but the total number of hits is reduced to 2.3 % in comparison to the total number of hits at the lowest threshold. The relation of the total number of hits and the localisation precision dependant on the threshold is also shown in Figure 53.

threshold [Counts]	# hits N	photons (N_F)	BG photons (N_B)	<localisation precision> [nm]
4000	693	1281	41	6.4
3800	990	1237	40	6.6
3500	1351	1174	40	6.9
3300	1770	1132	40	7.2
3000	2609	1055	40	7.8
2800	3360	1000	39	8.3
2500	4884	904	39	9.1
2200	7259	786	38	10.3
2000	9571	700	37	11.5
1800	12766	615	36	12.6
1600	17018	523	34	14.1
1400	30176	422	32	16.3

Table 7 Influence of the threshold on the number of hits and the localisation precision

The table shows the influence of the chosen threshold on the number of hits N, the number of fluorescence N_F and background N_B photons and the calculated average localisation precision.

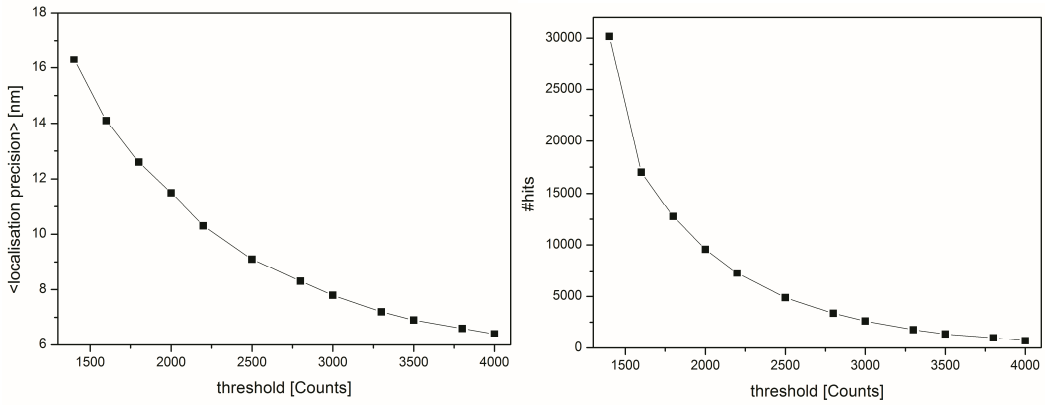

Figure 53 Influence of the threshold on the number of hits and the localisation precision

The left graph shows the average localisation precision calculated from the corresponding frequency histograms as explained in 5.2.1. The higher the selected threshold the better the average localisation precision. In this case a maximum average localisation precision of <LP> ~6 nm is achieved. On the right hand side the total number of hits dependent on the selected threshold is shown. With increasing threshold the total number of hits is reduced. At the maximum threshold of 4000 counts almost no hit was found by the algorithm. In order to achieve a good total resolution, a high localisation precision together with a reasonable number of hits is required. The measurement was performed under magic buffer condition including triplet and radical quencher.

The total resolution that can be achieved is a combination of the localisation precision of each spot and the label density on a target molecule which is directly related to the number of hits (refer to section 2.1.4). A good localisation is not sufficient enough to resolve tiny features of a sample if the label density on a target molecule is low and vice versa.

In order to increase either the number of fluorescence photons emerging from an intercalation event and or to increase the number of hits N with a sufficient number of photons to be identified and further analysed by the algorithm, a triplet quencher (Azo) and a radical quencher (Trolox) have been added to the buffer. Further details of these quenchers can be found in section 5.1.3. The concentration of the triplet quencher (Azo) and of the radical quencher (Trolox) was 300 µM each.
In Figure 54 the accumulations of 1000 images overlayed by the computed high resolution image (light blue dots) for one of the three measurements for each buffer condition are displayed. The surfaces were always prepared the same way as describe in section 5.1.4 with the same concentration of λ-DNA molecules. The concentration of TO molecules in the buffer was in all cases 1 nM.

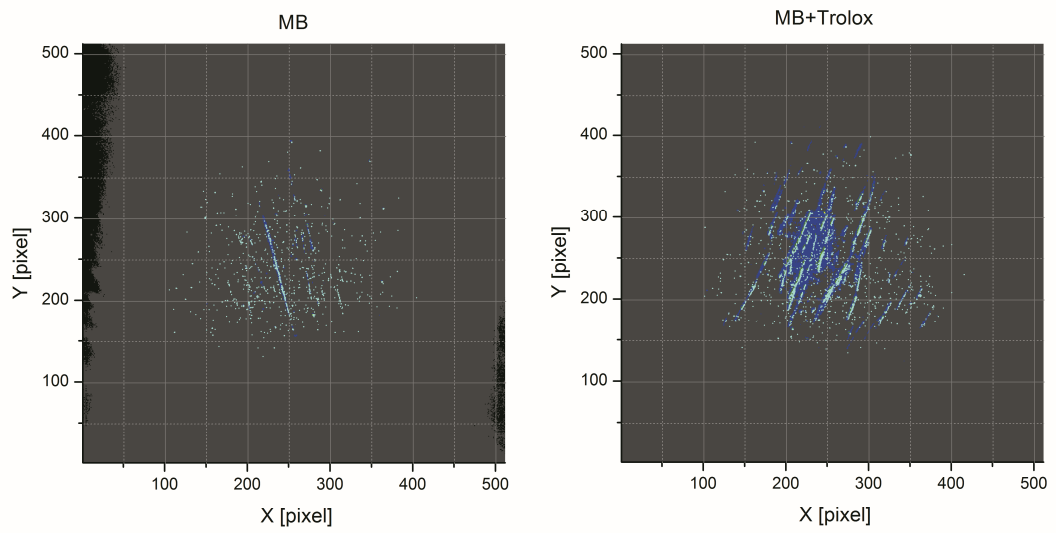

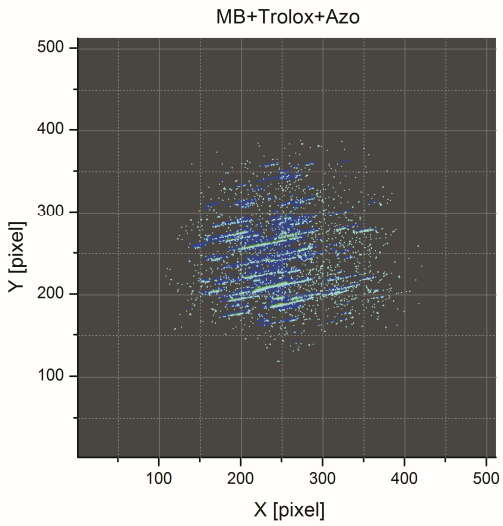

Figure 54 Accumulated images overlayed by computed high resolution images

The accumulations of 1000 images overlayed by the computed high resolution image (light blue dots) for one of the three measurements for each buffer condition are shown (see title of the graphs). The size of each image corresponds to 50 μm x 50 μm. The excitation power at the objective was in all cases 500 μW.

The results of the analysis under magic buffer conditions with the addition of the triplet and radical quenchers are shown in Figure 55. The diagrams show the average number of fluorescence photons N_F (orange), the average number of background photons N_B (grey) and the number of hits N (blue) which past all quality criteria previously mentioned. The same threshold (T_{min}=2000 counts) was applied to the different measurements. The error bars indicate deviations from three different areas of a sample for each of the three different buffer conditions.

The number of fluorescence photons N_F as well as the number of background photons N_B do not show a significant change when either Trolox or a combination of Trolox and Azo is added to the buffer. In contrast, the number of hits N identified by the algorithm is almost twice as high when adding only Trolox in comparison to the standard magic buffer conditions. The combination of Trolox and Azo shows even an increase of more than a factor of 5x in comparison to magic buffer conditions. This means that the localisation of each spot which is mainly dependant on the fluorescence and background photons of each hit is more or less not affected by the presence of triplet and radical quenchers. The number of hits N and therefore the label density of the intercalating fluorophores on the λ-DNA are significantly increased. In the end this also leads to a higher total resolution because a higher number of hits on the target molecule allow for increase of the threshold which in the end leads to an increase of the average localisation precision of the spots with still a sufficient number of labels on the λ-DNA.

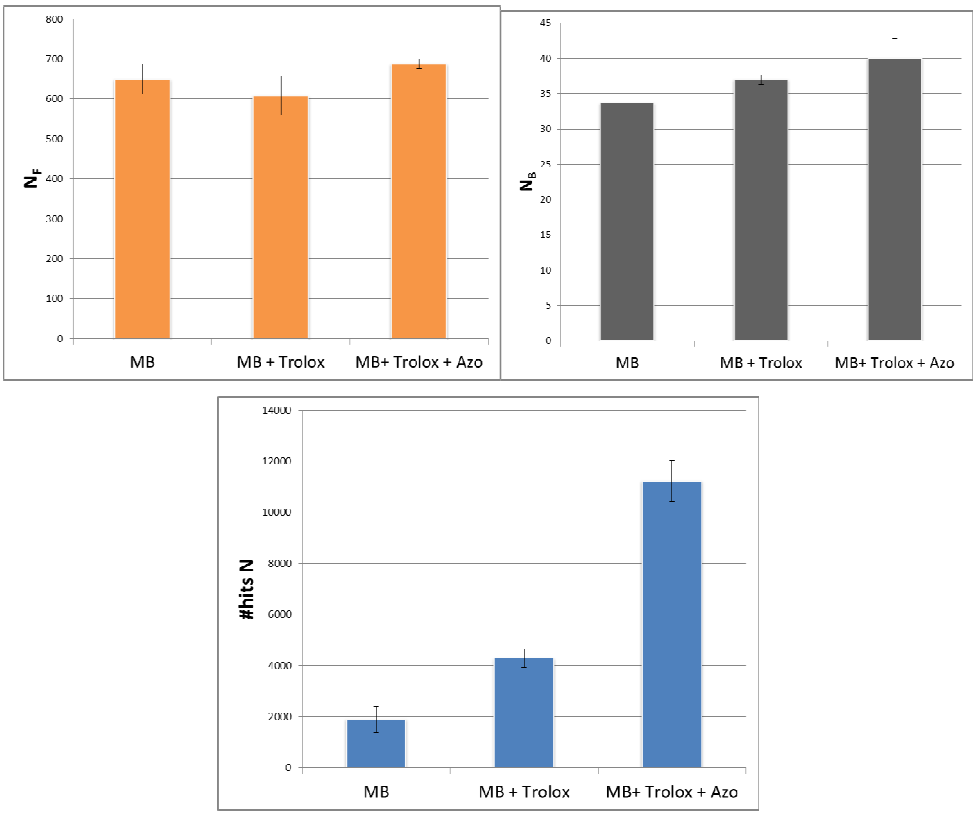

Figure 55 Influence of the radical quencher (Trolox) and the triplet quencher (Azo)

The results of hits detected from the full area from image series of 1000 images (100 s measurement times) which passed all quality criteria are shown. For each buffer combination, three independent measurements have been performed. Values correspond to averaged values obtained from the three measurements each. The upper graph (orange) shows the average number of photons under magic buffer conditions (MB), with the addition of radical quencher Trolox (MB+Trolox) and with a combination of radical quencher Trolox and triplet quencher Azo (MB+Trolox+Azo). The addition of quenchers does not influence the average number of fluorescence photons significantly. The same observation is also true for the average background photons which are shown in the middle graph (grey). The lower graph shows the number of hits N which past all quality criteria previously mentioned. Upon addition of both quenchers, the number of hits is increased by factor of 5x in comparison to magic buffer conditions.

Here I have to mention that the differences of the number of hits N also arise from different number of λ-DNA molecules present in a measurement although the surfaces were always prepared in the same way as mentioned in section 5.1.4 of this chapter. The number of unspecific adsorbance of TO molecules is hereby also included in the number of hits N (see images in Figure 54).

Thus, a further detailed analysis of the label densities of TO molecules on the target λ-DNA molecules will be given later in this section.

	MB		MB+Trolox		MB+Trolox+Azo	
	#	%loss	#	%loss	#	%loss
N_{all}	2355		7596		20178	
N_{nb}	2246	4	6166	18	14689	22
N_{conv}	2199	6	6012	20	14315	24
N_r	1956	16	4559	39	11874	37
N	1898	19	4279	43	11225	41

Table 8 Loss of hit information due to quality filter of the fit procedure

The average values from three independent measurements for each buffer condition of the total number of identified hits N_{all} bright enough to be above the applied threshold, the number of hits N_{nb} without neighbouring hits in close vicinity, the number of hits N_{conv} where the algorithm converged within 200 iterations, the number of remaining hits N_r that passed the eccentricity filter and the number of hits N after final cleanup are shown. The definitions of the different number of hits are also shown in Figure 37. In case of magic buffer conditions the loss of hit information after all quality filters relative to all identified hits is ~20%, in case of the presence of radical quencher Trolox and a combination of radical quencher Trolox and triplet quencher Azo the loss of hit information is even ~40%.

The various stepwise quality filters exclude a certain number of identified hits which are in principle bright enough to contribute to the final number of hits that in the end determine the label density on the target molecules and therefore the total resolution that can be obtained. The investigation of the relative loss of hit information of the analysis presented in Figure 55 is shown in Table 8. The definitions of the various numbers of hits is illustrated in Figure 37 and further explained in the corresponding section. In case of magic buffer conditions the overall loss of hit information after all quality filters is ~20% with the eccentricity filter being the one with the highest number of hits excluded. In the presence of radical quencher Trolox and a combination of radical quencher Trolox and triplet quencher Azo the overall loss of hit information is ~40%. The close neighbour and the eccentricity filter exclude hereby identified hits to almost equal amounts (~20% each). The number of hits excluded by the eccentricity filter can easily be reduced by changing the value at which hits are excluded. The recovery of hits excluded by the neighbourhood filter requires further modification of the fit algorithm. The rather tight settings of this filter were chosen to assure conditions of one fluorescent emitter within a diffraction limited spot so that a 2d-Gaussian approximation is justified. A recent work in the field of high resolution imaging called DAOSTORM has shown that hits in close vicinity can be recovered to increase the label densities with high localisation precision to yield a higher total resolution of an image (Holden, Uphoff et al. 2011).

From the number of hits N the label densities of TO molecules on immobilised l-DNA molecules under different buffer conditions were analysed. This analysis was performed on different measurement to those just presented where more λ-DNA molecules were identified on the surface. The accumulation of 1000 images and the overlayed high resolution image of the analysed measurement under magic buffer conditions is shown in Figure 50. The accumulation of 1000 images and the overlayed high resolution image of the analysed measurement under magic buffer conditions in presence of Trolox and Azo is shown in Figure 51.
Unfortunately, the investigation of the loss of hit information has been performed recently short before the submission of this thesis. It was just discovered that in case of measurement under magic buffer conditions only ~80% of all identified hits (N_{all}=69394) passed all quality filters. The neighbouring filter alone excluded ~70% of all identified hits. In the presence of Trolox and Azo only ~87% of all identified hits (N_{all}=124908) passed all quality filter. Here, the neighbouring filter was also the filter with the highest number of excluded hits (~83%). As just mentioned, the recovery of hits excluded by the neighbouring filter is possible but requires further modifications of the fit algorithm that were not possible to realise before the submission of this thesis.
Because of this, the label densities obtained in the following analysis can be considered as a lower value for the label densities which are obtained by the high resolution iPAINT method.

From synthetic high resolution images a detailed analysis of the label density with and without the presence of triplet and radical quenchers in the buffer has been performed. Spots with higher label density in comparison to parts of an image where only a few hits were identified due to e.g. unspecific adsorption of the fluorophores have been addressed for the analysis. A box with a corresponding size of 500 nm x 100 nm is applied to areas where λ-DNA molecules were identified. The orientation of the length of the box was carefully chosen to be as parallel as possible to the segment of the λ-DNA molecule (centred). In this way two different label densities are defined. On the one hand, the number of hits within this box is normalised to the length of the box which will result in a longitudinal label density ρ_L. On the other hand, the number of hits within the box is projected to the width of the box resulting in a transversal label density ρ_T. The definitions of these two label densities are also illustrated in Figure 56.

With the transversal label density ρ_T line profiles can be visualised. The width of the box is further on separated into small δ-environments (e.g. 10 nm) transversal to the axis of the DNA molecule. The number of hits within each of the δ-environments is plotted versus its position along the width of the box. In this way a total resolution in 1d is indicated to show how good a single DNA molecule is localised or even two DNA molecules in close vicinity can be separated.

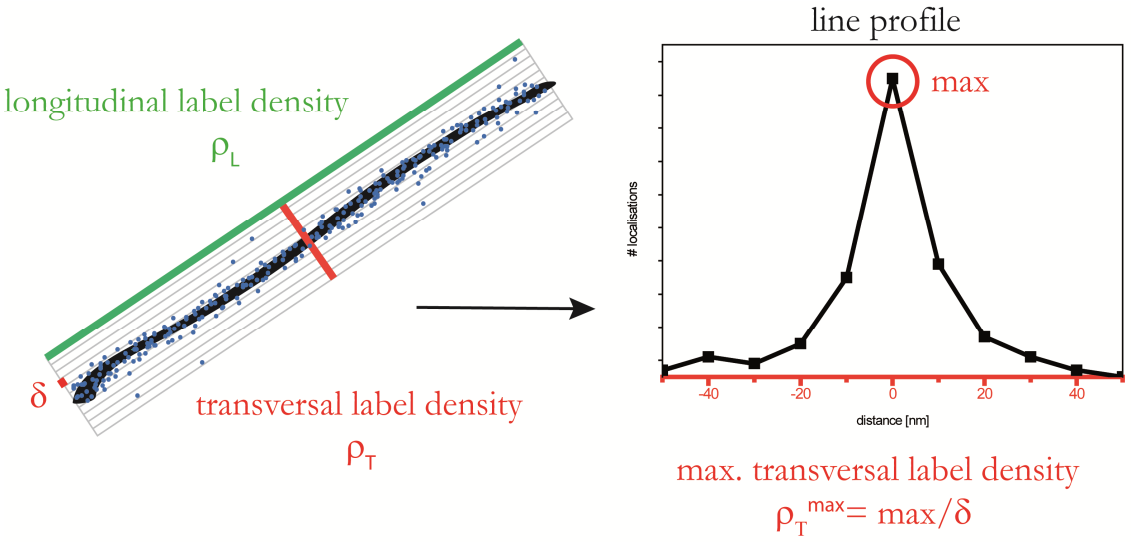

Figure 56

Label densities and line profile

A box is overlayed (centred) on top of an identified target molecule. The length of the box is chosen to be parallel with the molecular axis. All hits on the DNA molecule within this box (blue dots) are used to define a longitudinal label density ρ_L (green line) and a transversal label density ρ_T (red line) with respect to the molecular axis of the DNA molecule. On the right hand side a sketch of a line profile is shown. The line profile is obtained by defining small transversal δ-environments with respect to the molecular DNA axis (red). Within each of the δ-environments around the DNA molecule the number of hits are counted and plotted versus the transversal position. A maximum transversal label density ρ_T^{max} is defined by dividing the maximum number of hits within a δ-environment with the length of one δ-environment.

The transversal label density ρ_T represents an average label density along the width of the box. A maximum transversal label density ρ_T^{max} of a line profile is defined by calculating the ratio between the maximum hit information within a δ-environment over the length of the δ-environment. The definition of the maximum transversal label density ρ_T^{max} is also illustrated in Figure 56. The results of the obtained line profiles will be discussed later in this section. The transversal label density ρ_T strongly depends on the selected length and width of the box whereas the label density ρ_L is more or less independent on the length of the box if the width is not too small and if the DNA is homogeneously targeted by the intercalating fluorophores.

A high resolution approach based on the STORM principle (refer to section 2.1.4) also used a system of immobilised λ-DNA molecules and dimeric intercalating dyes with much stronger DNA affinity in comparison to a monomeric intercalating fluorophores used in our experiments (Schoen, Ries et al. 2011). The results of this STORM approach have been obtained with an excitation power

two orders of magnitude higher in comparison to excitation powers used in our experiments. The measurement time of the STORM experiments was 25 min, most of our measurements were performed in 100 s. At first, our data is analysed in order to compare the longitudinal label densities ρ_L of the two different high resolution approaches along the λ-DNA molecules. It was shown that the total number of hits and therefore the label densities strongly depend on the selection of the threshold that leads to a certain average localisation precision of the hits. Therefore, the analysis of the longitudinal label densities ρ_L was performed for two different average localisation precisions of <LP>~10 nm and <LP>~15 nm under magic buffer conditions (blue) with the radical quencher Trolox (green) and with a combination of radical and triplet quenchers (red). The results of this analysis are shown as Box-whisker plots in Figure 57. The error bars represent the corresponding minima and maxima of the data set. The central line within the coloured boxes represents the median of the data and the lower and upper line of a box the 25th and 75th percentile respectively. The numbers above the boxes indicate the number of spots that have been analysed in either of the different buffer condition cases. It is clearly visible that the addition of the radical quencher Trolox leads to an increased label density along the DNA molecules. The combination of radical and triplet quencher (Trolox+Azo) even yields a slightly higher label density along the DNA molecules on average. This is in accordance to the analysis of the total number of hits of a measurement with all images that has been shown previously in this section. The increase in label density along the DNA molecule upon the addition of radical quencher and a combination of radical and triplet quencher is visible in both cases of different average localisation precision. Of course, the label densities in case of the higher average localisation precision of ~15 nm are higher because of the weaker exclusion criterion of the selected threshold.

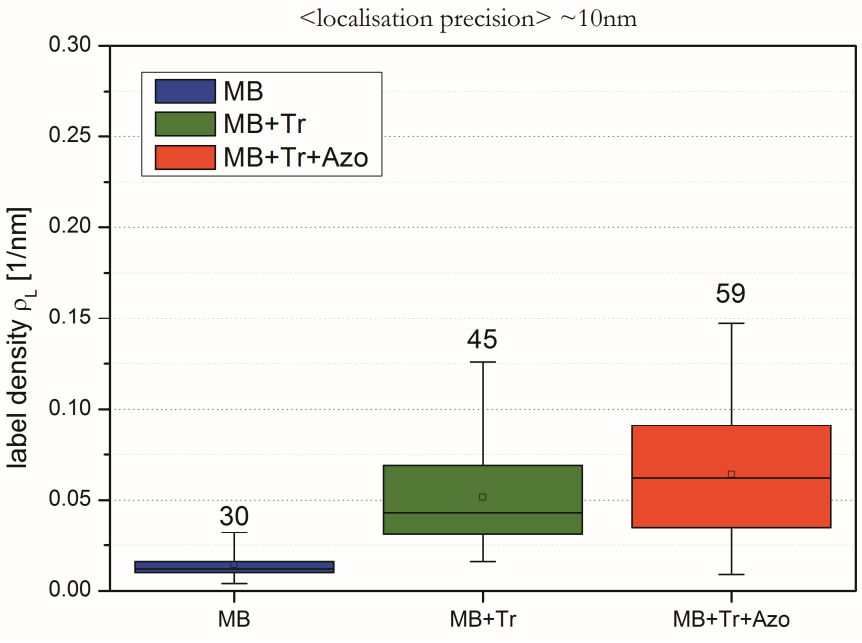

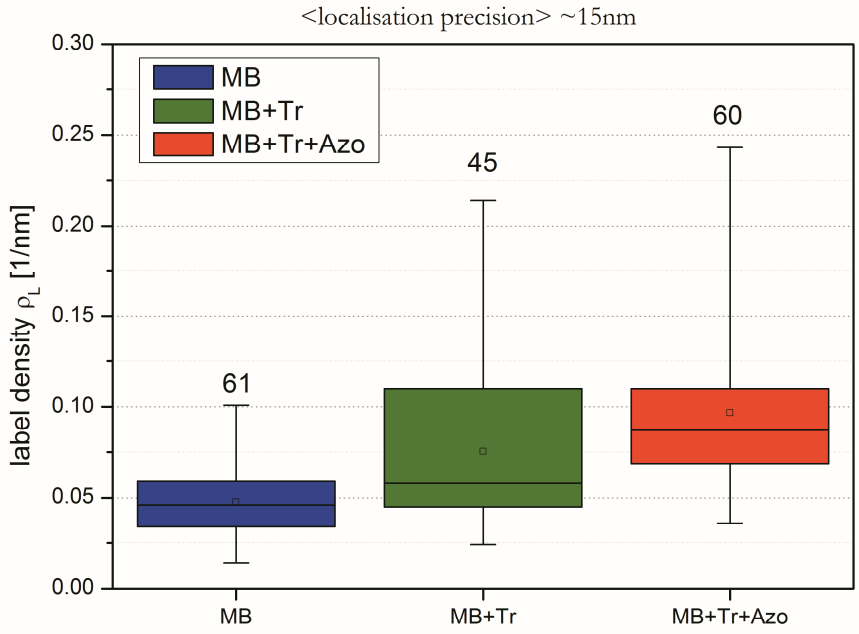

Figure 57 Label density ρ_L under different buffer conditions

The upper Box-whisker plot shows the longitudinal label densities ρ_L in case of magic buffer conditions (MB, blue), with the addition of the radical quencher Trolox (MB+Tr, green) and with the addition of a combination of radical quencher and triplet quencher (MB+Tr+Azo, red) of spots with an average localisation precision of <LP>~10 nm within a measurement time of 100 s. The lower Box-whisker plot shows the corresponding longitudinal label density ρ_L of spots with an average localisation precision of <LP>~15 nm. The excitation power measured at the objective was 500 µW.

In order to compare the longitudinal label densities along the DNA molecules obtained in our experiments with those obtained in the already mentioned similar STORM experiments, we extrapolate our obtained results gathered within a measurement time of 100 s to the measurement time of 25 min of the STORM experiments. At first, a measurement of 5000 images with a corresponding measurement time of 8.3 min serves as a reference to define the extrapolation. The total number of hits (black) at time t of such a measurement is shown in Figure 58. A linear regression (red) which describes the relation between the number of hits and the corresponding time yielded a constant number of hits of around 20 hits/frame. A further analysis (not shown here) of the longitudinal label densities of spots after 1000 images (100 s) and after 5000 images (8.3 min) yielded an increase of the label density by a factor of 4.6x which accounts for differences in the linear behaviour of the number of hits dependant on the time which can also been seen in Figure 58. Differences from a strict linear correlation may arise from a short bleaching period at the very beginning of the measurement until a steady state of exchange is reached (see also Figure 48) and also from a focal drift which is manually corrected (~every 1000 images). A further factor of 3x is required to extrapolate

the longest measurement time of 8.3 min in our experiments to the measurement time of the STORM experiments. This yields an overall factor of 13.9x to extrapolate our results to that of the high resolution STORM results.

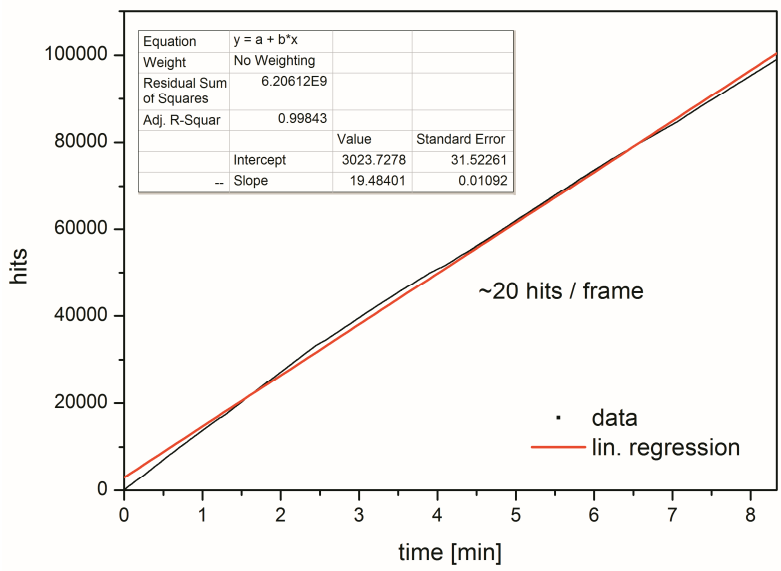

Figure 58 Linear extrapolation

The graph shows the accumulated number of hits at time t (black) for a long-time measurement of 8.3 min. The linear regression analysis indicates a more or less constant number of hits per frame throughout the complete experiment. The measurement was performed under magic buffer condition in presence of radical and triplet quenchers. Differences from a strict linear correlation may arise from a short bleaching period at the very beginning of the measurement until a steady state of exchange is reached (see also Figure 48) and also from a focal drift which is manually corrected (~every 1000 images).

The extrapolated label densities ρ_L along the DNA molecules of our analysis are also shown in the upper Box-whisker plots in Figure 59. In addition, the label densities of the STORM experiments are also shown in the lower Box-whisker plot in Figure 59.

A comparison of the longitudinal label densities ρ_L shows that the best label densities that are achieved in both high resolution methods under certain buffer conditions are on average of the same order of around 0.6/nm. In case of magic buffer conditions with the addition of triplet and radical quencher (upper plot, red) with an average localisation precision of <LP>~10 nm the average label density is slightly higher in comparison to the ROXS buffer conditions of the STORM method (lower plot). If we compare the maximum label densities that have been determined we find our maximum label densities a factor of 2x higher in comparison to the highest label densities of the STORM method.

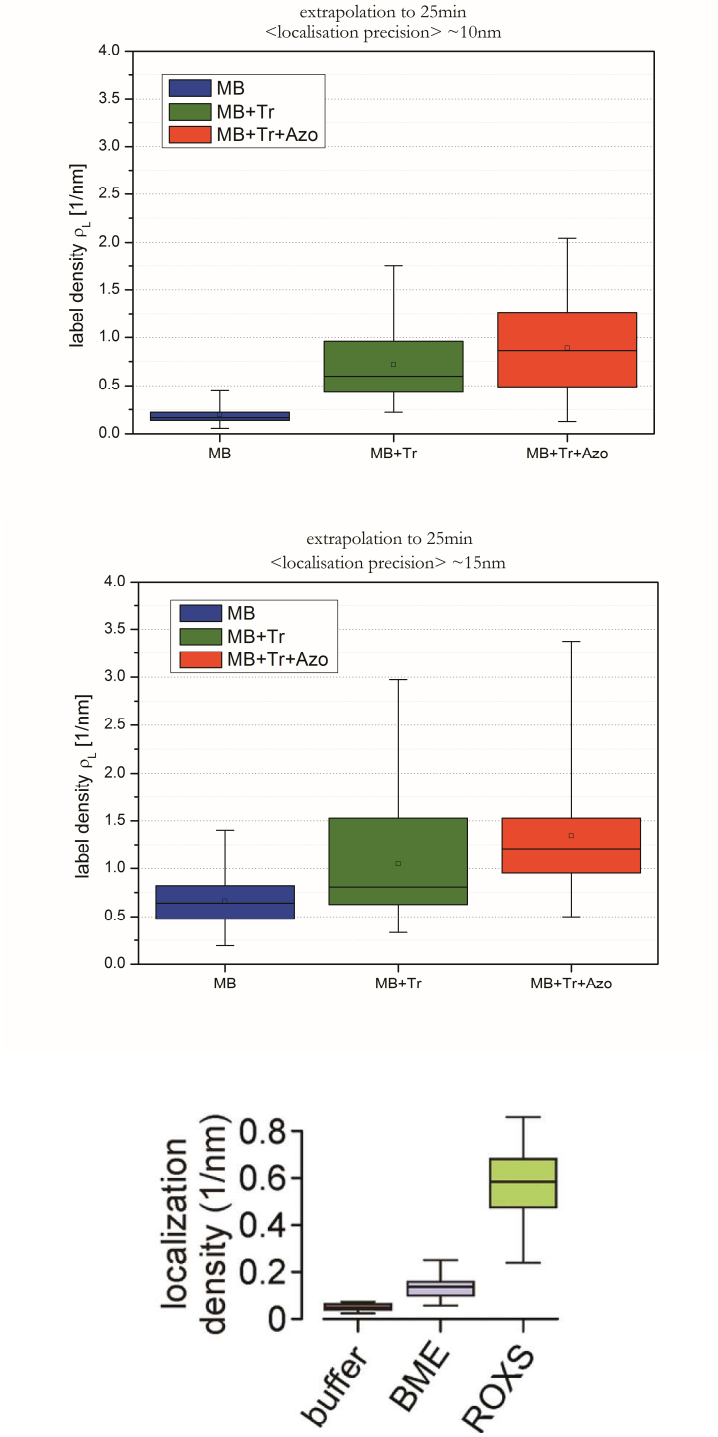

Figure 59

Comparison of the label densities ρ_L between iPAINT and STORM

The upper Box-whisker plot shows the obtained label densities ρ_L in case of magic buffer conditions (MB, blue), with the addition of the radical quencher Trolox (MB+Tr, green) and with the addition of a combination of radical quencher and triplet quencher (MB+Tr+Azo, red) of spots with an average localisation precision of <LP>~10 nm. The middle Box-whisker plot shows the corresponding label density ρ_L of spots with an average localisation precision <LP>~15 nm. The excitation power measured at the objective was 500 µW. The lower Box-whisker plot shows the label densities ρ_L of the STORM experiments (Schoen, Ries et al. 2011).

If we compare the label densities obtained in our experiment with a slightly higher average localisation precision of <LP>~15 nm with the results of the STORM method, the average label density in case of magic buffer conditions in presence of triplet and radical quenchers (middle plot, red) is a factor of 2x higher and the determined maximum label density even a factor of 4x.

The comparison of the label densities shows that the high resolution iPAINT method yields label densities that are not only comparable to the STORM results but also exceed the maximum label densities obtained in the STORM experiments by a factor of 4x with comparable average localisation precisions.

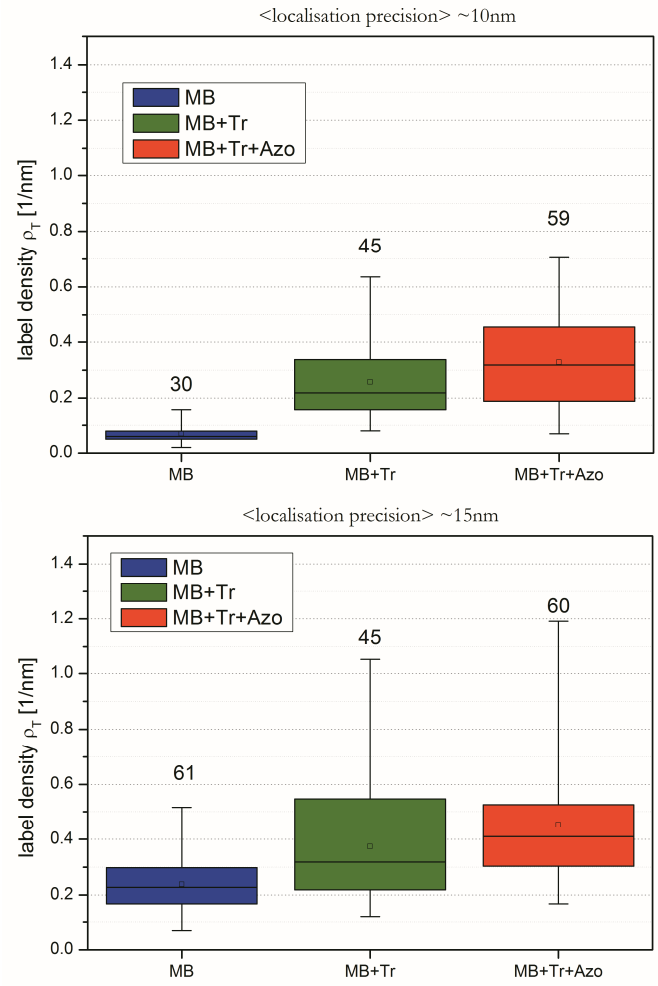

Figure 60 Comparison of the label densities ρ_T under different buffer conditions

The upper Box-whisker plot shows the label densities ρ_T in case of magic buffer conditions (MB, blue), with the addition of the radical quencher Trolox (MB+Tr, green) and with the addition of a combination of radical quencher and triplet quencher (MB+Tr+Azo, red) of spots with an average localisation precision of <LP>~10 nm within a measurement time of 100 s. The lower Box-whisker plot shows the corresponding label density ρ_T of spots with an average localisation precision of <LP>~15 nm. The excitation power measured at the objective was 500 µW.

In order to show the total (1d) resolution of a DNA molecule and to separate two DNA molecules which are in close vicinity to each other, the label density ρ_T perpendicular to the defined molecular axis is the crucial parameter. The label density ρ_T is further on used to create line profiles perpendicular to the DNA molecules as previously described in this section. The results of the average label densities ρ_T along a line of 100 nm transversal to the DNA molecules (red line in Figure 56) for the two different average localisation precisions and under different buffer conditions are also shown as Box-whisker plots in Figure 60. The colour code is the same as in Figure 57.

A comparison to the STORM method is not possible as the results of the label densities ρ_T are not given in detail in the corresponding publication (Schoen, Ries et al. 2011).

In case of magic buffer conditions in presence of triplet and radical quenchers (blue) the obtained average label density ρ_T is already ~0.35/nm within the measurement time of 100 s in case of an average localisation precision of <LP> ~10 nm (upper plot). In case of a worse average localisation precision of <LP>~15 nm the average label density is even above 0.4/nm (lower plot).

The total resolution that is achieved depends on the localisation precision and on the Nyquist resolution R_{Nyq} which depends on the label density (refers to Equation 25 in section 2.1.4). Here, only the 1d case is considered. The dependence of the Nyquist resolution R_{Nyq} on the label density is shown in Figure 61.

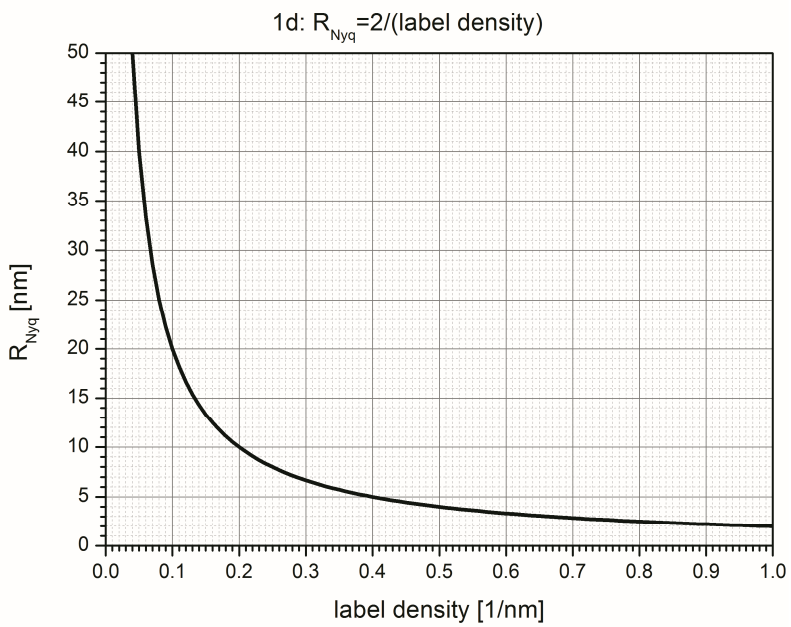

Figure 61 Nyquist resolution R_{Nyq} dependency on the 1d label density

This graph shows that a label density of 0.2/nm is required to achieve a Nyquist resolution of R_{Nyq}=10 nm. At label densities of around 0.4/nm which corresponds to the label densities ρ_T obtained in our experiments. The corresponding Nyquist resolution is R_{Nyq}=5 nm. After a measurement time of 100 s the label density ρ_T is already good enough so that the total resolution in our experiments mainly depends on the localisation precision of the spots. If we extrapolate the obtained label densities ρ_T to a measurement time of 25 min (see Figure 62) it is obvious that the label densities ρ_T perpendicular to the molecular axis of the DNA molecules are not the limiting factor in our experiments to perform the line profile analysis.

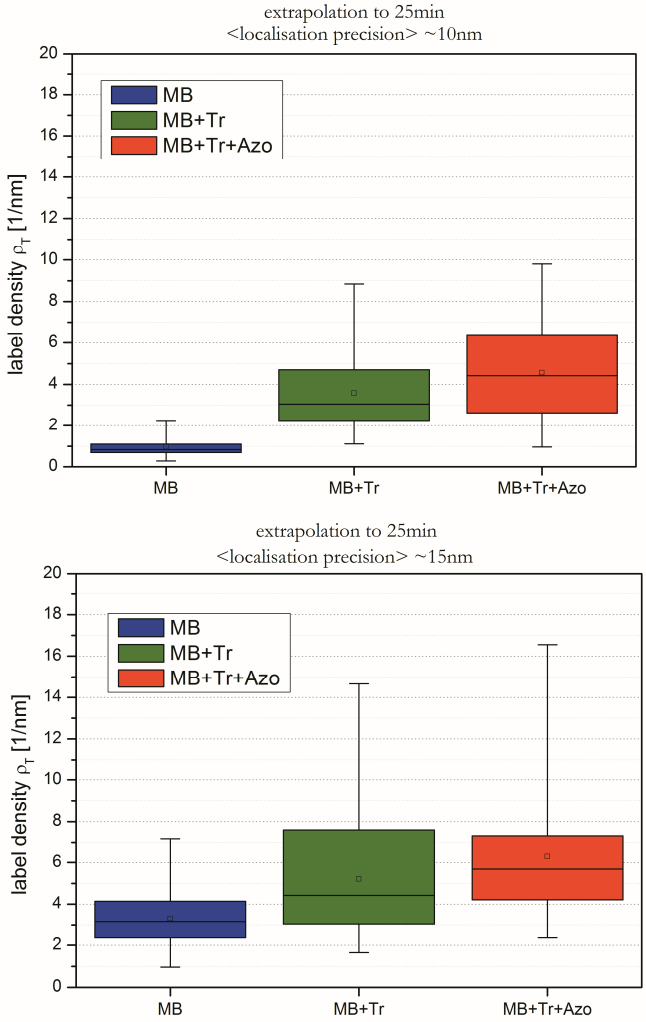

Figure 62 Label density ρ_T extrapolation to 25min

The upper Box-whisker plot shows the extrapolated label densities ρ_T in case of magic buffer conditions (MB, blue), with the addition of the radical quencher Trolox (MB+Tr, green) and with the addition of a combination of radical quencher and triplet quencher (MB+Tr+Azo, red) of spots with an average localisation precision of <LP>~10 nm. The lower Box-whisker plot shows the corresponding label density ρ_T of spots with an average localisation precision of <LP>~15 nm. The excitation power measured at the objective was 500 µW.

As already mentioned, the average transversal label densities ρ_T are the average values along a line of 100 nm transversal to the molecular DNA axis. These values also vary with the length of the defined box. Therefore, the maximum transversal label densities ρ_T^{max} achieved from line profile analysis has also been calculated. The definition of the maximum label density ρ_T^{max} is also shown in Figure 56. The results of the maximum transversal label density ρ_T^{max} analysis shown Figure 63 are in accordance to the previously presented results of the label densities. The results of this analysis also highlight the fact that the necessary label density to achieve a high Nyquist resolution and therefore a high total resolution with sufficient localisation precision is already achieved within a measurement time of 100 s.

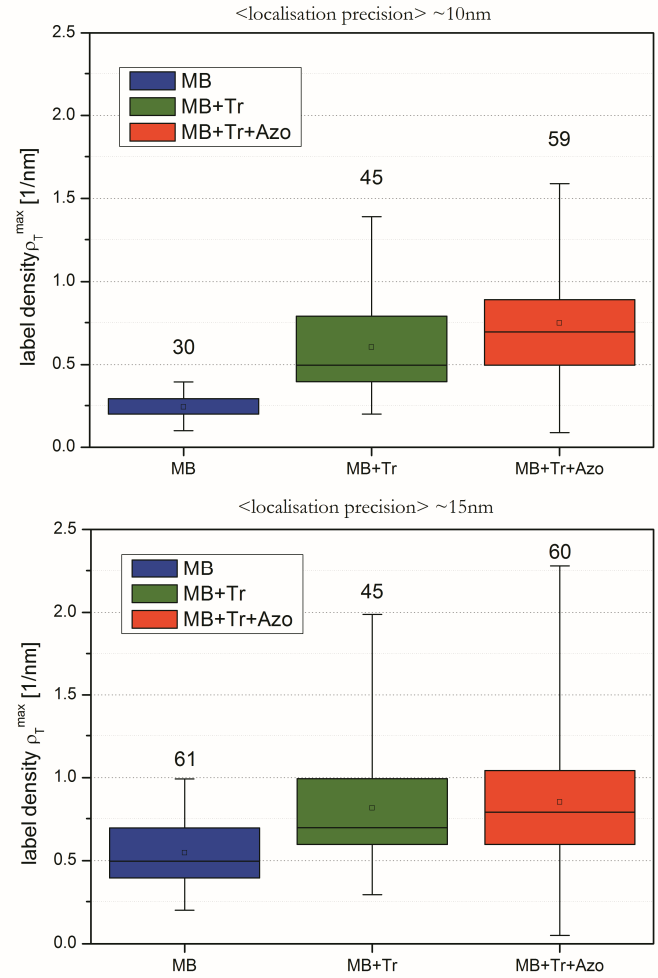

Figure 63 Comparison of the maximum label densities ρ_T^{max} under different buffer conditions

The upper Box-whisker plot shows the maximum label densities ρ_T^{max} in case of magic buffer conditions (MB, blue), with the addition of the radical quencher Trolox (MB+Tr, green) and with the addition of a combination of radical quencher and triplet quencher (MB+Tr+Azo, red) of spots with an average localisation precision of <LP>~10 nm within a measurement time of 100 s. The lower Box-whisker plot shows the corresponding maximum label density ρ_T^{max} of spots with an average localisation precision of <LP> of ~15 nm. The excitation power measured at the objective was 500 µW.

The highest maximum transversal label density of the corresponding STORM experiments is estimated to be ~15/nm (~30 hits within a δ-environment of δ=2 nm) from one of the given line profiles (Schoen, Ries et al. 2011). An extrapolation of the maximum transversal label densities in our experiment (not shown) of the analysed data sets yield an average value which is comparable to that of the STORM experiments. The maximum transversal label density of our analysis is even a factor of 2x higher in comparison to the STORM results.

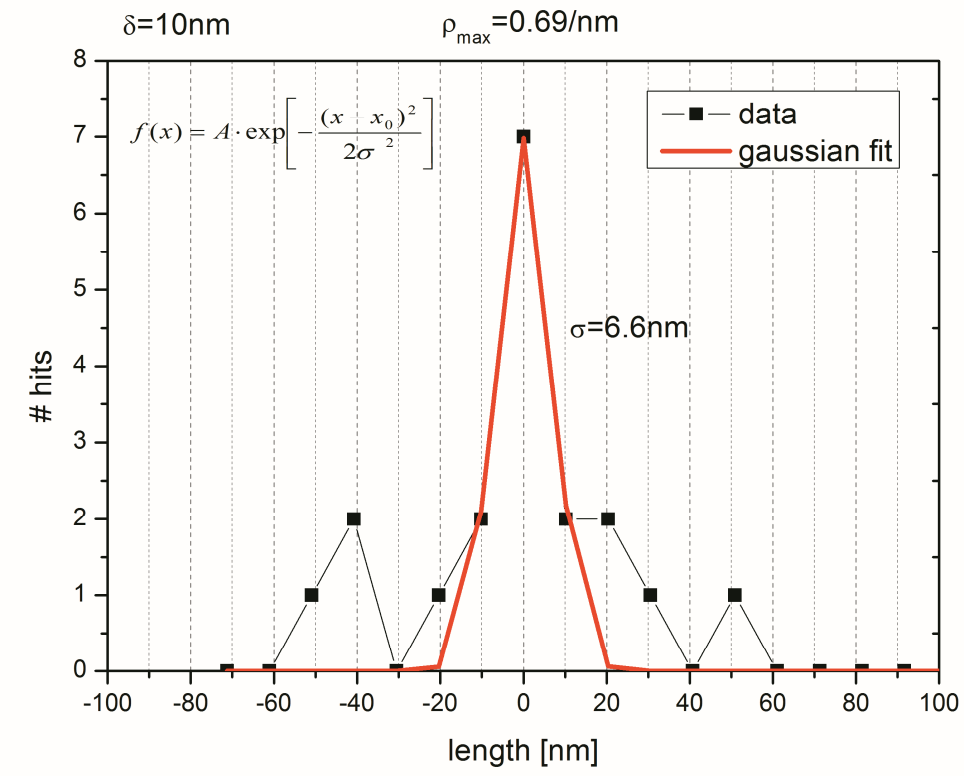

Figure 64 Line profile of a single λ-DNA molecule

The line profile has been obtained from the transversal label densities ρ_T along a line of 100 nm in segments of δ=10 nm perpendicular to the axis of a DNA molecule. The average localisation precision of the hits is <LP>=~10 nm. The maximum label density is ρ_T^{max}=0.69/nm. A Gaussian model function has been fitted to the data with all parameters free in the fitting procedure. The measure of the width of the model function is σ=6.6 nm.

Two examples of the line profile analysis are shown in Figure 64 and in Figure 65. Both line profile have been obtained from the label densities ρ_T along a line of 100 nm in segments of δ=10 nm transversal to the axis of the DNA molecules. The average localisation precision of the hits is <LP>=~10 nm. The maximum label density is in both cases ρ_T^{max}=0.69/nm. Figure 64 shows the line profile of a single λ-DNA molecule. This data was fitted with a single Gaussian model function

with all parameters free in the fit procedure. The measure of the width of the model function is σ=6.6 nm.

Figure 65 shows the line profile of two λ-DNA molecules in close vicinity to each other. A double Gaussian model function is fitted to the data. Again, all parameters of the model function are free in the fitting procedure. The measures of the widths of the model function were found to be σ_1=8.8 nm and σ_2=9.9 nm respectively. The distance between the peaks of the two Gaussian is x=44.5 nm.

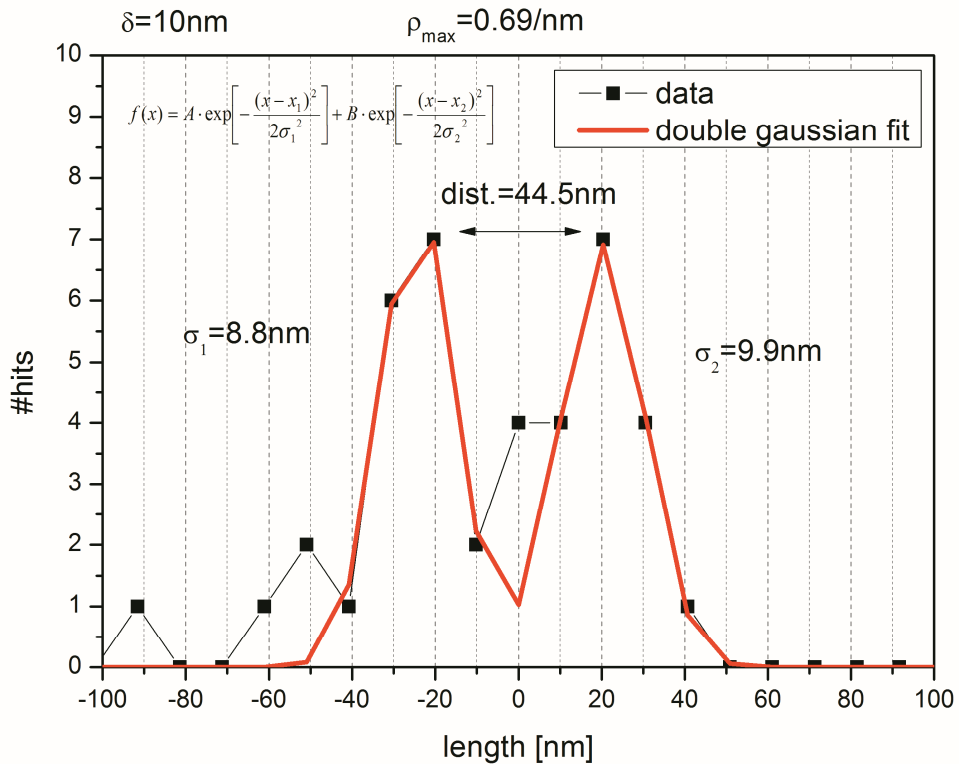

Figure 65 Line profile of two λ-DNA molecules in close vicinity to each other

The line profile has been obtained from the transversal label densities ρ_T along a line of 100 nm in segments of δ=10 nm perpendicular to the axis of the DNA molecules. The average localisation precision of the hits is <LP>=~10 nm. The maximum label density is ρ_T^{max}=0.69/nm. A double Gaussian model function has been fitted to the data with all parameters free in the fitting procedure. The measures of the widths of the model function were found to be σ_1=8.8 nm and σ_2=9.9 nm respectively. The distance between the peaks of the two Gaussian is x=44.5 nm.

5.2.3 Outlook

The high resolution imaging method iPAINT presented in this thesis successfully applied the general PAINT approach to intercalating dyes with immobilised λ-DNA molecules. It was qualitatively shown that the affinity of the intercalators to the target molecules can be influenced by the presence of mono- and divalent metal ions in the buffer. A very high average localisation precision (<LP>~10-15 nm) of the analysed hits with sufficient label densities on the target molecules is achieved. It was also shown that especially the applied neighbourhood filter to exclude hits in close vicinity reduces the number of all hits identified by the algorithm to 20%. Recent work (Holden, Uphoff et al. 2011) has shown that especially these hits can be recovered by further modification of the fit algorithm. This will lead to much higher label densities than those presented in this thesis. This will in the end also lead to a higher localisation precision of the hits due to an increased selection of bright hits so that the total resolution of an image is even further increased.

First home-made simulations (not shown) have proofed the possibility of identifying a protein complex with a size of ~15 nm that binds to a specific sequence of plasmid DNA by the iPAINT approach. Hereby, the complex will be identified by the absence of identified intercalators in the region where the complex covers the basepairs of the plasmid DNA. The simulations have shown that longitudinal label densities of ρ_L~60/nm are sufficient enough to visualise the "shadow" in the computed high resolution image. A recovery of the lost hits as just mentioned shall yield the estimated label densities within a reasonable measurement time. Nevertheless, the factor of instrumental drift has to be considered in case of long-term measurement. Therefore, a special component for the microscope to stabilise a focus drift (z-direction) is now available and a drift correction in x- and y-direction is still necessary to perform those measurements.

A further improve of the iPAINT method would be another intercalating dye with similar affinity to DNA in comparison to TO, but with a much higher fluorescence quantum yield upon intercalation (TO: Φ_F=0.1). This would yield an increased number of primary fluorescence photons that are necessary to obtain even higher localisation precisions.

6 smFRET Imaging

Single molecules methods have become a very popular and widespread tool to investigate the complex activities of individual biomolecules. Especially analysis techniques for single molecule FRET experiments have been evolved tremendously due to its powerful and unique possibilities to investigate a molecule's function, structure and dynamics without the averaging of many molecules in standard ensemble experiments.

Single molecule FRET experiments in solution which were supervised by the group leader Prof. Dr. C.A.M. Seidel of the molecular physical chemical department at the Heinrich-Heine-University in Düsseldorf have already a long tradition (Kühnemuth and Seidel 2001; Widengren, Schweinberger et al. 2001; Diez, Zimmermann et al. 2004; Eggeling, Widengren et al. 2006; Kalinin, Felekyan et al. 2007; Wozniak, Schroder et al. 2008; Gansen, Valeri et al. 2009; Kalinin, Valeri et al. 2010; Sisamakis, Valeri et al. 2010; Sindbert, Kalinin et al. 2011). Here, double labelled molecules diffuse freely in solution at very low concentrations to ensure single molecule events when travelling through the confocal detection volume. The analysis of the photon bursts of each single molecule event resolves sub-milliseconds variations of the signals as the photon data is collected at very high speed and can later on be divided into time bins of microseconds to milliseconds. The great disadvantage of this method is the fact that long-time observations of molecular dynamics are impossible as the typical dwell time of the molecules within the confocal detection volume due to diffusion is of the order of milliseconds.

Therefore, additional strategies have to be introduced to immobilise individual molecules to be observed for seconds up to minutes. The immobilisation of single molecules such as DNA or proteins has been established successfully in the past. Especially for experiments to combine the benefits of fluorescence spectroscopy and atomic force microscopy (AFM) the immobilisation protocols have been developed and established.

First FRET experiments of immobilised double labelled biomolecules have been started but the quality and quantity of these experiments was rather poor. Here, a diffraction limited confocal laser spot was first scanning the surface in a stepwise manner using a piezo scanner to identify the positions of the molecules. After completion of the scan the beam had to be moved to a molecule of interest of which further on the fluorescence signals were recorded. This procedure had to be repeated many time in order to achieve a significant number of single molecule traces with adequate statistics. Such measurements were very time consuming and cumbersome.

Hence, this work aimed on the establishment of an experimental setup which allows for long time observations of immobilised biomolecules based on a FRET framework. A home built total internal

reflection fluorescence (TIRF) setup has been developed which allows for simultaneous observation of many immobilised molecules due to the lateral widefield excitation conditions and the field of view of the CCD camera in use. The disadvantage of this approach is the lower time resolution of the system in comparison to the confocal system previously described as the fastest cycle time of the CCD camera is about 10-30ms. Custom tailored software to identify the individual molecules and to build up the corresponding time traces for further analysis has been developed. In order to extract the actual energy transfer efficiencies a lot of parameters have to be known to apply the right corrections to the recoded data as mentioned in section 2.1.3.

As the immobilised biomolecule can interact with the local environment of the surface it is connected to its mobility and therefore its biological function may be influenced or even hindered. The side of interaction with a binding partner could be sterically blocked, so great care has to be taken for the immobilisation protocol not to hinder the interaction that wants to be observed. Also the fluorophores which are directly attached to the biomolecules can interact with the surface in close vicinity. These interactions can lead to strong changes in the fluorescence properties of the fluorophores which in the end distort the calculation of the actual FRET efficiencies. In solution FRET experiments, the fluorescence properties such as fluorescence quantum yield of fluorescence lifetime can be measured rather easily even under ensemble conditions. In case of the described surface immobilised FRET measurements, the application for all correction factors was not possible. One problem is the determination of the detection efficiency for the acceptor signal. It was suggested to determine the acceptor signal detection efficiency from direct acceptor bleaching experiments. At current times, a suitable laser for direct acceptor excitation was not available and the TIRF setup was not capable for the usage of two different laser beams simultaneously. Therefore, only the "apparent" FRET efficiencies which are also sometimes called "proximity factor" are calculated as described in section 2.1.3.

6.1 Samples

6.1.1 Donor-Acceptor fluorophores

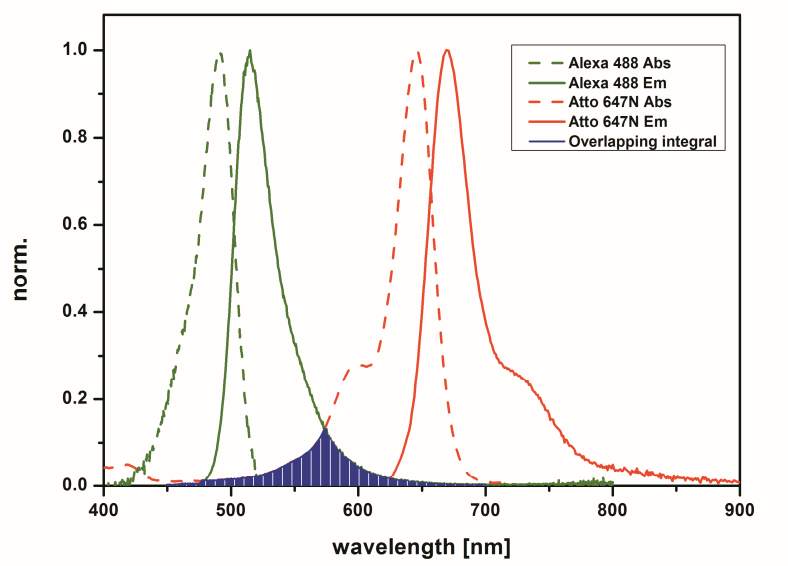

Figure 66 Adsorption and emission spectra of Alexa 488 and Atto647N

The absorption (dashed lines) and emission spectra (solid lines) of Alexa 488(green) and Atto647N (red) are displayed. The highlighted area (royal) indicates the overlapping integral between donor emission and acceptor absorption of the FRET pair

In order to perform single molecule FRET experiments, the donor and acceptor fluorophores have to fulfil several conditions as explained in section 2.1.3. A commonly used FRET pair is Alexa 488 as the donor fluorophore and Atto647N as the acceptor fluorophore. The absorption and emission spectra of these fluorophores are shown in Figure 66. The necessary overlapping integral for the energy transfer is also highlighted (royal sparsed area). The Förster Radius of this FRET pair Alexa488/Atto647N is R_0=49 Å which is suitable to detect conformer transitions in case of the Holliday junction, see also 6.1.2.

	λ_{abs} [nm]	λ_{em} [nm]	Φ_F	τ [ns]	ext.coeff [$cm^{-1}M^{-1}$]
Alexa 488	495 [a]	519 [a]	0.92 [a]	4.1 [c]	73000 [a]
Atto647N	644 [b]	669 [b]	0.65 [b]	3.5 [b]	150000 [b]

Table 9 Fluorescence properties of Alexa 488 and Atto 647N

The table shows the absorption maximum λ_{abs}, the fluorescence emission maximum λ_{em}, the fluorescence quantum yield Φ_F, the fluorescence lifetime τ and the extinction coefficient of the fluorophores. The fluorescence parameters were obtained from a) (Invitrogen 2011), b) (Atto-Tec 2011), c) (ISS 2011).

6.1.2 Holliday-Junction (Biotin-tag)

Homologous recombination plays an important role to protect genomes from strand failures or fractures as well as to keep the genetic diversity going which is the key for successful evolution.
Robin Holliday was the first who described a meanwhile generally accepted model for DNA crossover in 1964. A four-way junction, also called Holliday-junction, intermediates in homologous recombination. It is formed by reciprocal exchange of DNA strands between two almost identical DNA molecules. A general structure of the Holliday-junction is shown in Figure 67.

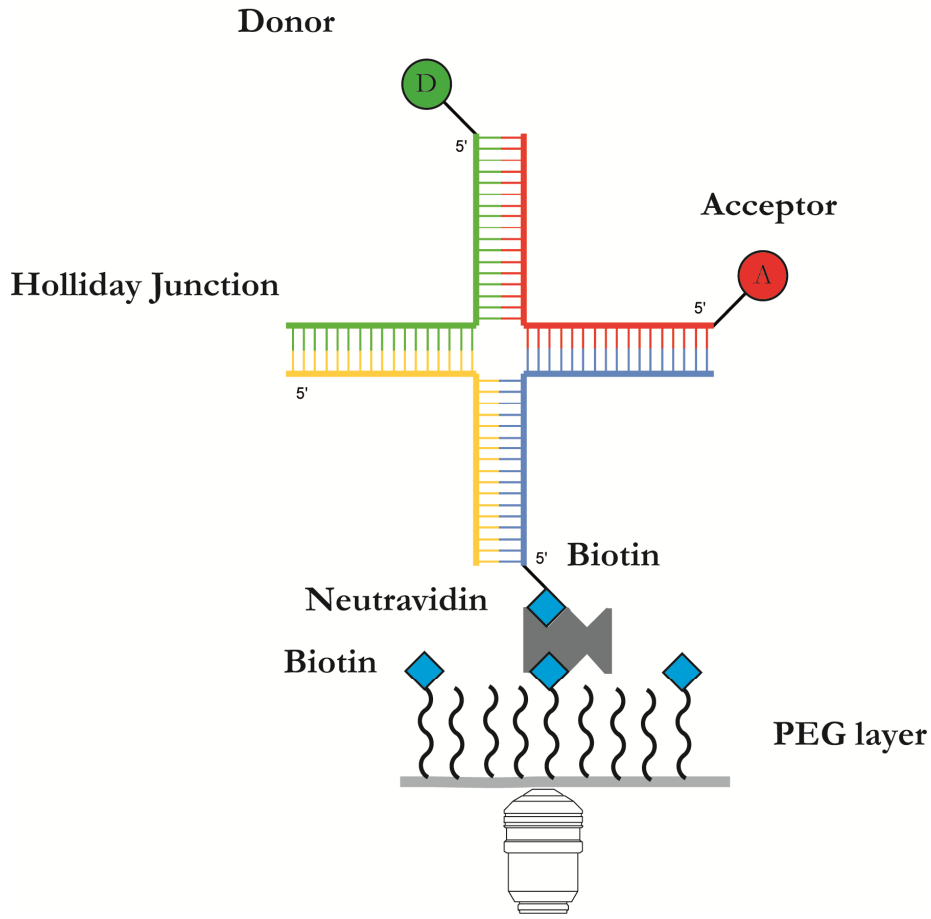

Figure 67 Immobilisation scheme of a Holliday Junction

A coverglass surface is coated with a polyehtylenglycol (PEG)-biotin layer. One of the four arms of the Holliday junction is modified with a biotin tag. The biotin tag of the Holliday junction and the surface biotin are linked by addition of neutravidin. One arm of the Holliday junction is labelled with a donor fluorophore (green circle) and another with an acceptor fluorophore (red circle).

The Holliday junction is not a static structure. The effect of branch migration can be observed by sequential exchange of basepairing so that the Holliday junction effectively migrates along the DNA sequence.

In presence of divalent metal ions such as Mg^{2+} the Holliday-junction overcomes the electrostatic repulsion of the negatively charged phosphates and finally forms folded structures. In general, two different folded conformers dependant on the stacking of the 4 individual arms are possible, see Figure 68. The rate at which the two conformers interconvert is strongly dependant on the concentration of divalent metal ions. The higher the concentration is the lower the rate constant. The Holliday-junction presented in this thesis has been extensively studied (Valeri 2009) on the basis of confocal single molecule FRET experiments in solution.

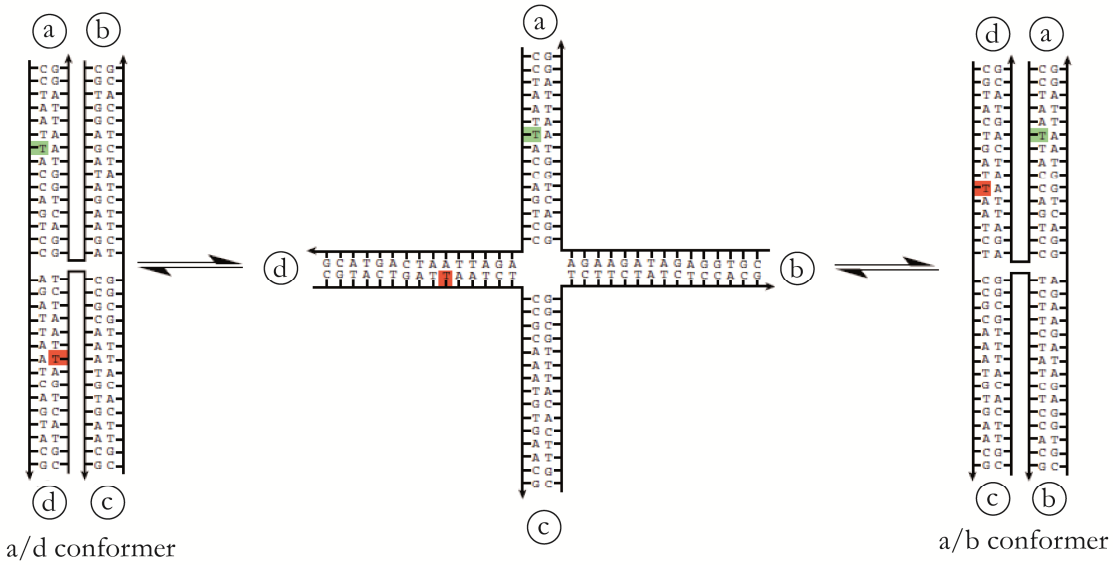

Figure 68 Holliday Junction conformers and labelling positions of fluorophores

The Holliday junction interconvert between the two conformers (a/d) and (a/b) via a short lived intermediate state. The distances $<R_{DA}>_E$ obtained from FRET experiments are in case of the a/b conformer 40 Å and in case of the a/b conformer 50 Å. The illustration was taken from (Valeri 2009).

A slightly modified construct for immobilisation was chosen to serve as a model system to establish and improve the potential of long-term FRET observations of single immobilised molecules. Further advanced Single molecule FRET experiments on similar Holliday junction constructs have already been described even using a three or four colour FRET assay (Lee, Lee et al. 2010; Lee, Lee et al. 2010). The following 4 oligonucleotides (Purimex, Germany) were used to hybridise the final Holliday-junction.

HJ 1N **D2**: 5´-d(CCT AAT **T(Alexa488)** AC CAG TCC AGA TTA ATC AGT ACG)

HJ 2N **A2**: 5´-d(CGT ACT GAT **T(Atto647N)** AA TCT CCG CAA ATG TGA ACG)

HJ_3N_**Bio**: 5´-**Biotin**-d(CGT TCA CAT TTG CGG TCT TCT ATC TCC ACG)

HJ 4N: 5´-d(CGT GGA GAT AGA AGA GGA CTG GTA ATT AGG)

The basepair sequence was also chosen to suppress the effect of branch migration so that the only possible change in conformation is due to interconversion of the two conformers.
In order to investigate conformation changes by single molecule FRET experiments a donor and an acceptor fluorophore were introduced so that the distance differences between these fluorophores for the two conformers are big enough to be resolved in the FRET experiments.

The distances $<R_{DA}>_E$ obtained from FRET experiments are in case of the a/b conformer 40 Å and in case of the a/d conformer 50 Å (Valeri 2009).
In order to specifically immobilise the Holliday-junction to a surface, a Biotin-tag is further integrated in one of the oligonucleotides which is not modified with a fluorescent label.

6.2 Immobilisation of Biotin-tagged biomolecules

The immobilisation of biomolecules to be investigated by single molecule FRET experiments in time domains of seconds up to minutes is of major importance. As soon as these biomolecules are allowed to diffuse, the fluorescence signals of the fluorophores attached to these biomolecules will be lost within a short time period. Therefore, a specific linkage to the surface on which the biomolecules reside is required. A coverglass surface, which is often used in single molecule experiments, is modified to offer specific binding sites dependant on the tag or special molecular endgroups of the biomolecules to be immobilised. The modified surfaces have to satisfy several conditions. At first, the modified surfaces have to be transparent so that the fluorescence is not absorbed by the modification layers of the surface. Secondly, the surfaces have to be clean which means as little autofluorescence as possible. Thirdly, the surface modification must not affect the native function of the biomolecules.
Further useful requirements of the immobilisation procedures are specific and efficient surface linkage, passivation against unspecific adsorption and easy and timesaving handling.
The surface preparation protocols presented in this thesis base on previously applied procedures which have been developed for combined force and fluorescence studies of biomolecules (Janissen 2008). Individual steps of the overall procedures have been further modified and simplified, e.g. the surface activation which is described in step 2 was realised by incubation of the coverglasses in highly concentrated sodium hydrochloride (NaOH) for hours as the plasma cleaner was not available at that time.

The biomolecule which was immobilised by this procedure is the Holliday junction described in section 6.1.2. The final step (4.) introduces Biotin. The addition of neutravidin which can bind up to four different Biotins links the surface Biotin to the Biotin-tag of the biomolecule. The linkage of Biotin-Avidin ($K_d=10^{-15}$ M) is one of the strongest interactions between biomolecules (Sin, Chan et al. 2006).

1. Cleaning of coverglasses
   - sonification in 5% Hellmanex for 20min
   - thoroughly washing of coverglasses in ddH_2O
   - sonification in ddH_2O for 20min
   - drying of coverglasses under nitrogen gas

2. Surface activation
   - activation of coverglass surfaces by plasma cleaner for 10min

3. Amination of the surfaces
   - incubation of coverglasses with 5M ethanolamine hydrochloride in DMSO for at least 12h
   - thoroughly washing of coverglasses in ddH_2O
   - drying of coverglasses under nitrogen gas

4. PEGilation of surfaces
   - incubation of coverglasses with 2mM 5:1 mixture of NHS-PEG-MeO and NHS-PEG-Biotin in chloroform
     triethylamine to unprotect the NHS-group;
     the coverglasses should be sandwiched
   - cleaning of the coverglasses with dichlormethane
   - thoroughly washing of coverglasses in ddH_2O
   - drying of coverglasses under nitrogen gas

5. Introduction of avidin
   - incubation of coverglasses with neutravidin (~20µg/ml) for 10min
   - thoroughly washing of coverglasses in ddH_2O
   - drying of coverglasses under nitrogen gas

6. Addition of biotinilated biomolecules

The reaction scheme for the immobilisation of Biotin-tagged biomolecules is shown in Figure 69. An overview of the immobilisation of a Holliday junction is also illustrated in Figure 67.

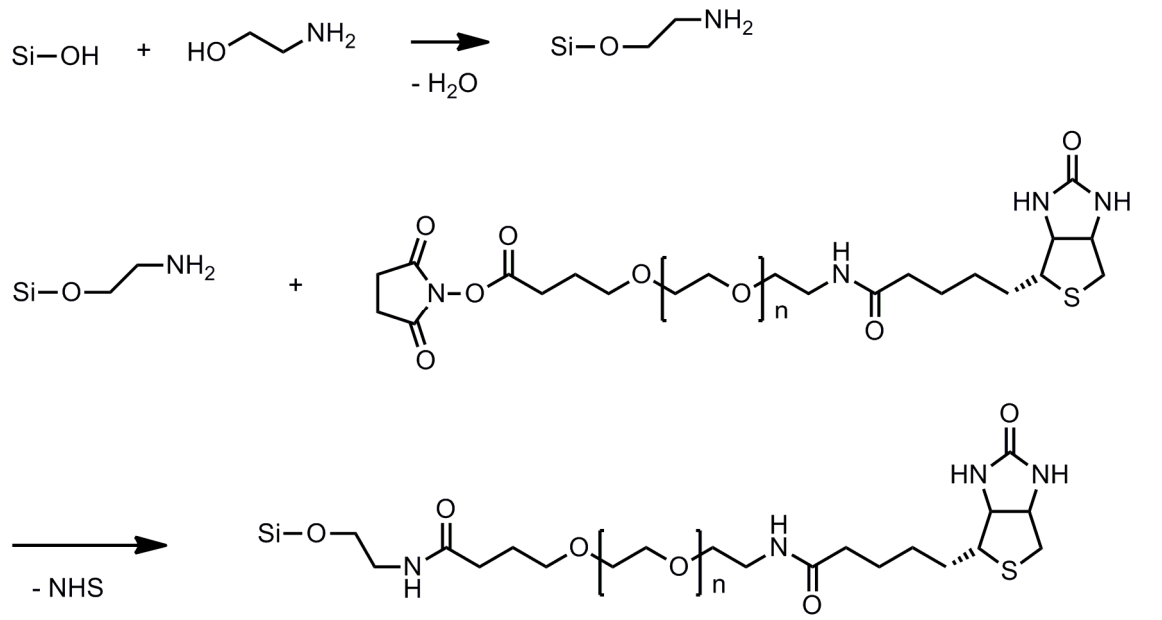

Figure 69 Reaction scheme for surface preparation to immobilise biotinilated biomolecules

The activated hydroxyl group the glass surface reacts with ethanoleamine under the emission of water. In this way amine groups are introduced on the glass surface. In a second step, the chemical compound NHS-PEG-Biotin reacts with the introduced amine groups. The leaving group NHS is removed and PEG-Biotin is attached to the modified glass surface.

6.3 Buffer conditions - Oxygen Scavenging System

The great benefit of single molecule FRET measurements of immobilised samples is the possible long-term observation of an individual biomolecule to which fluorescent labels are attached.

However, the general effect of photobleaching, from which all fluorescence labels have to suffer, limits the overall observation time. Therefore it is essential, to stabilise the fluorescence signals of the fluorophores. In addition, photoinduced blinking, which occurs especially for cyanine dyes, hinders the observation of molecular dynamics as the blinking overlays the signal changes from which the FRET efficiencies due to e.g. conformer transitions are calculated.

On the one hand, molecular oxygen (O_2) is one of the most important factors for photobleaching resulting from a photo-oxidation mechanism. On the other hand, molecular oxygen is also a suitable candidate to quench triplet states. The repetitive population of electronically excited triplet states leads to the effect of blinking of the fluorescence signals. The general strategy to stabilise fluorescence signals is to remove oxygen as much as possible together with the addition of a suitable triplet-state quencher.

An enzymatic oxygen scavenging system has been proposed to remove oxygen from solution (Benesch and Benesch 1953). Enzymatic glucose oxidase transfers glucose, oxygen and water to

gluconic acid and hydrogen peroxide. The bleaching agent hydrogen peroxide reacts with enzymatic catalase to water and elementary oxygen. The concentration and therefore the activity of the enzymatic catalase are chosen to be in access relative to the glucose oxidase so that the highly reactive hydrogen peroxide is directly removed. The reaction scheme of the enzymatic remove of oxygen from solution is shown in Figure 70.

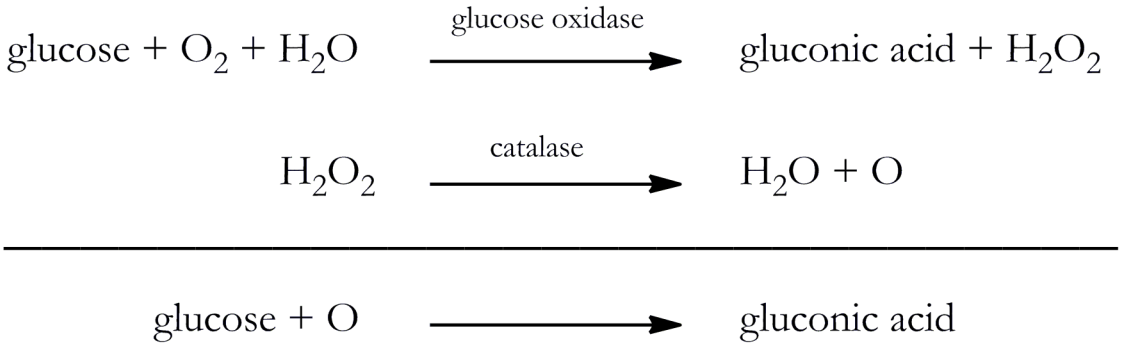

Figure 70 Glucose oxidase and catalase reaction scheme to remove oxygen from solution

A combination of enzymes glucose oxidase and catalase removes oxygen from solution. At first, the oxidase turns glucose, water and oxygen to gluconic acid and hydrogen peroxide. Secondly, the highly reactive hydrogen peroxide is directly removed from solution by the catalase (Benesch and Benesch 1953).

In combination with this oxygen scavenging system, different triplet-state and radical quenchers have been investigated (Rasnik, McKinney et al. 2006; Roy, Hohng et al. 2008). From this work we found Trolox to be a suitable candidate to act as quencher of dark states in our experiments. In case of Trolox, the photostability for various kinds of commonly used fluorescent dyes was at least a factor of two higher in contrast to e.g. β-mercaptoethanole (βME). It also does not cause slow blinking of the fluorescent dye Cyanine 5 (Cy5) which is often used as the acceptor in single molecule FRET experiments.

The standard measurement buffer consists of 50 mM Tris (pH 7.5), 20 mM NaCl and 200 mM $MgCl_2$. In addition, the oxygen scavenging components are 4% glucose, 2 mM Trolox, 200 U glucose oxidase and 2000 U catalase (Richert 2011).

6.4 Experimental Methods

6.4.1 Analecta – Data Analysis

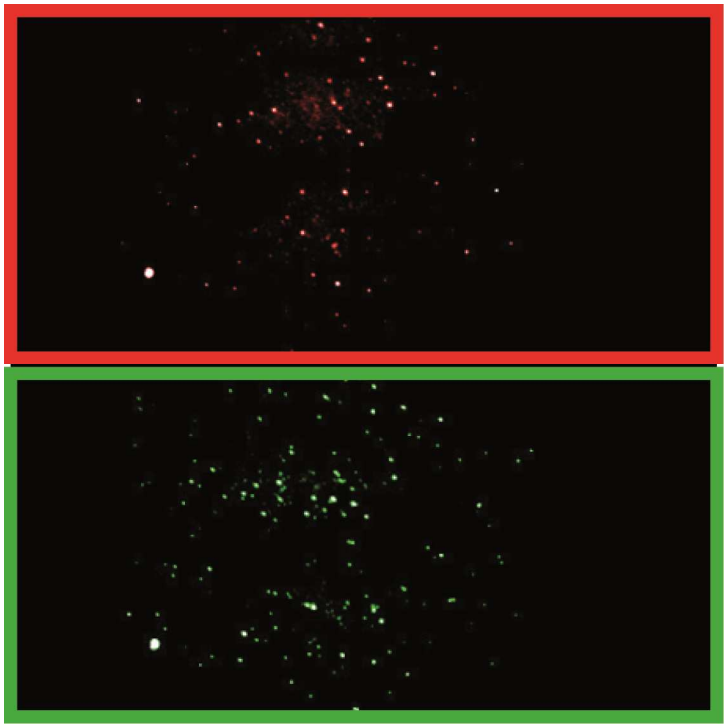

Figure 71 FRET imaging

The accumulation of 1000 images recorded with an emCCD is shown. The upper part (red) shows the red spectral domain (acceptor) and the lower part the green spectral domain (donor) of double labelled and immobilised Holiday Junction molecules upon donor excitation with a wavelength of 488 nm. The colour scales have been modified individually to visualise the presence of donor and acceptor signals.

The single molecule FRET measurements of immobilised biomolecules were performed on the setup as described in section 3.3. The analysis of the data was carried out with home-built Labview software called Analecta. The development of this software is part of the work presented in this thesis. An accumulation of 1000 images from a kinetic series is illustrated in Figure 71. The upper part (red) shows the red spectral domain of the acceptor signals and the lower part (green) the green spectral domain of the donor signals of double labelled Holliday Junctions (see also section 6.1.2). In order to analyse the FRET data, the green- and red sub-images have to be overlayed on top of each other to ensure that the fluorescence signals of the immobilised molecules match in space. The Optosplit is equipped with various screws that allow for shifts of the two sub-images to be aligned on the camera chip. As it is pretty difficult to align the images relative to each other on a pixel level, the final alignment is done by the software. Only parallel shifts along the x- and y-axis are corrected, a rotational correction is not applied as the mathematical implementation of this correction is rather

complicated and for our purpose not needed as we are up to now not interested in a very precise localisation of the spots.

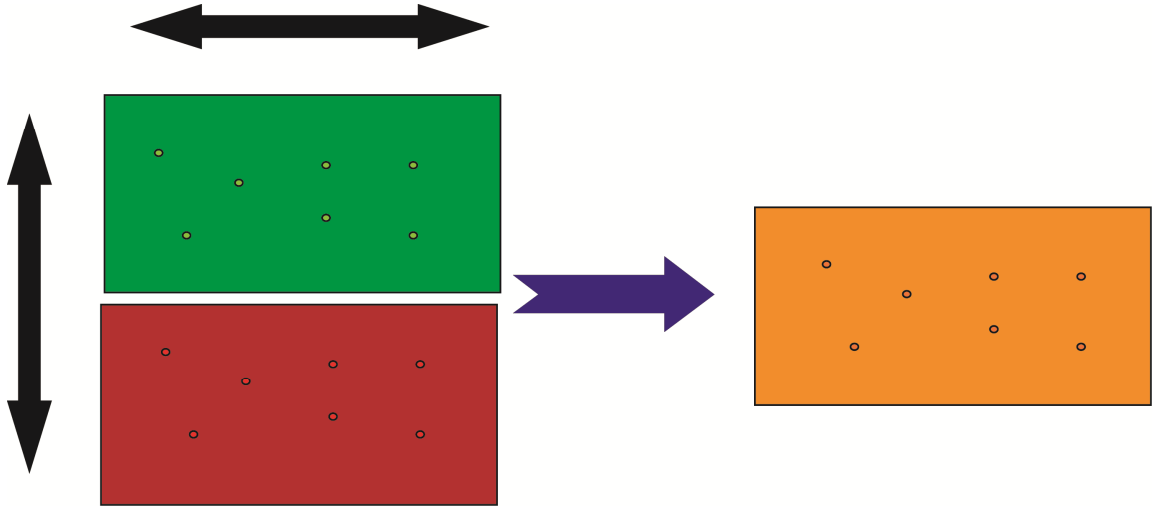

Figure 72 Alignment of green and red detection subimages

The green and red subimages are overlayed on top of each other by horizontal and vertical translation so that the fluorescence events (small dots) of donor and acceptor of the same biomolecule match in space.

A coverglass surface is roughened by a scraper with a diamond tip. Different strategies have been tested in order to have bright objects in the green and red detection channel for alignment. Even the usage of multicolour fluorescent beads was used, but as these beads only fluoresce in a certain spectral domain when excited with a laser of corresponding wavelength, the laser in use was not suitable for a proper application of the beads as they were not bright enough in the red detection channel. The scraper approach was found to be an easy and fast method for the alignment procedure. An image of the scratched surface is loaded and the final shifts are applied to exactly align the two subimages on top of each other. These shifts will be kept constant during the analysis of the fluorescence images. A flow chart of the strategy to obtain single molecule FRET traces of immobilised molecules is shown in Figure 73. After loading the images of the sample, the user can choose an overall image from which a background correction will be applied. Typically, a late image is recommended to be chosen as a lot of the fluorescence signals have been disappeared due to e.g. bleaching so that the majority of the recorded information is the remnant of the actual background. As the background conditions can be different in the two spectral domains, the background correction is applied for each spectral detection channel individually. In a next step, the points of interest have to be located. On the one hand the user can choose a certain number of spots individually by positioning two cursors defining the region of interest. On the other hand it is also possible to define points of interest automatically. As we are heading for FRET imaging, only spots on the surface are of in-

terest where a red signal can be identified as the acceptor is not excited directly but only due to an energy transfer from the excited donor molecule. Therefore, a certain number of red sub-images selectable by the user are accumulated and therefore overlayed on top of each other. This is done in order to identify as many FRET active spots as possible. The same background procedure which is also applied to determine the representative backgrounds of the single sub-images is applied on the accumulated red sub-image data and finally subtracted from the original data. The correction is again designed in a way to correct for a constant offset as well as to correct for the differences in the excitation profile (refer to section 5.2.1). In this way a common threshold together with a given size for the region of interest for the whole accumulated image can be applied to identify the points of interest automatically by using a simple centre of mass determination that can be also easily extended to a much more precise localisation of the spots by 2d Gaussian fitting of the photon distribution if necessary. If two spots will be identified within the region of interest both will not be considered as they are too close too each other to be clearly separated. The coordinates of all identified spots will be saved for further analysis. Next, the user can define the size of the regions of interest from which the overall fluorescence signals are calculated. Typically, a spot size of 5x5 pixels corresponding to an actual size of around 0.9 μm x 0.9 μm was chosen. Finally, each image of the series is loaded, separated into the two sub-images, background corrected and the overall fluorescence signal within each region of interest of all points of interest are calculated. In this way, fluorescence time traces for each point of interest is generated and can be displayed one after another by the user.

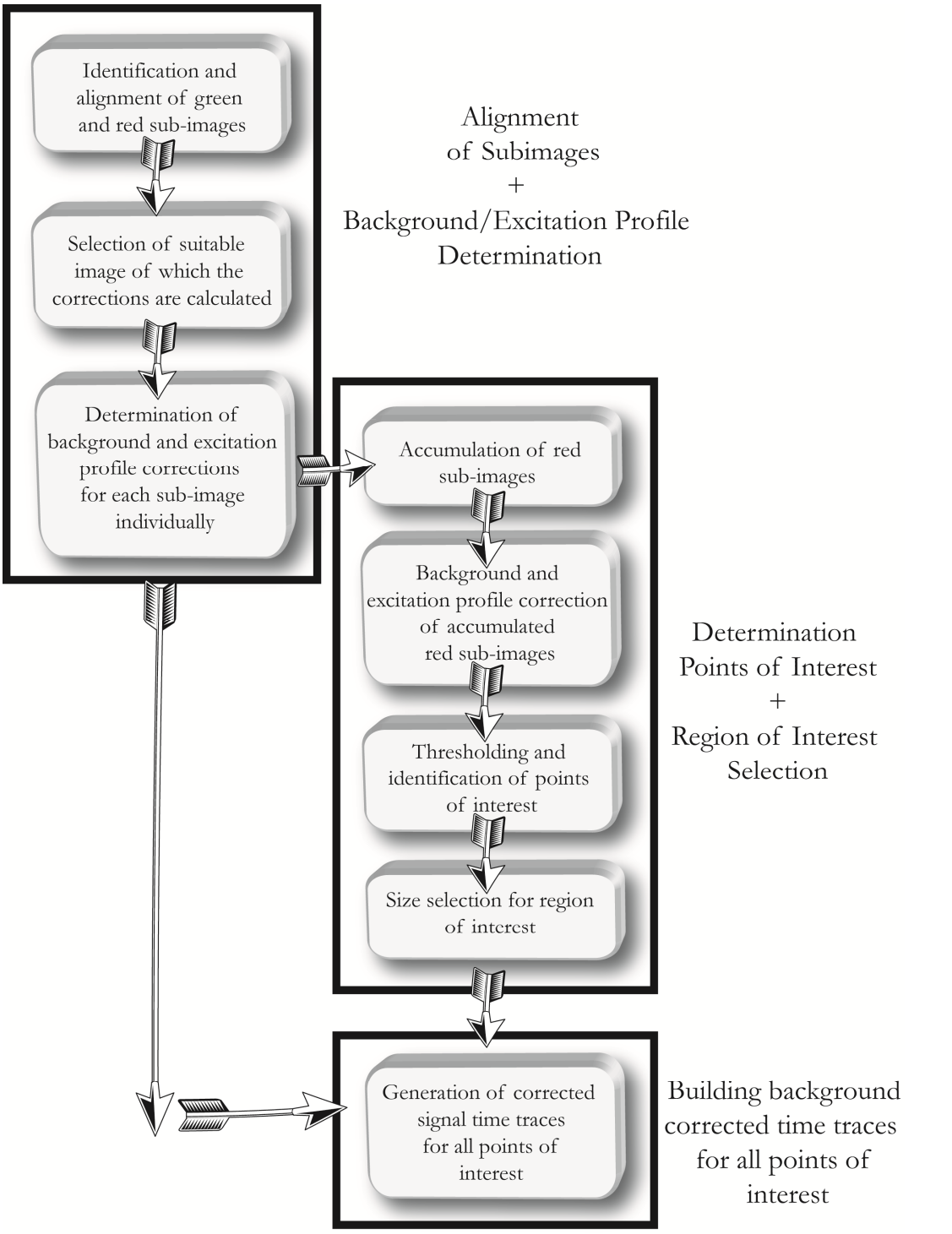

Figure 73 Flow chart for FRET traces

6.4.2 Results

Fluorescence time traces of immobilised biomolecules have been obtained by the data analysis procedure as described in section 6.4.1. In order to smoothen the noise which is present in the data, a moving average with a window size of m=±1 was applied on the individual time traces.
First attempts in order to obtain these single molecule time traces have been tried without the addition of the enzymatic oxygen scavenging system in combination with the radical quencher Trolox (OCT), see also section 6.3. A typical time trace of the normalised green and red fluorescence signals in absence of these additives is shown in Figure 74.

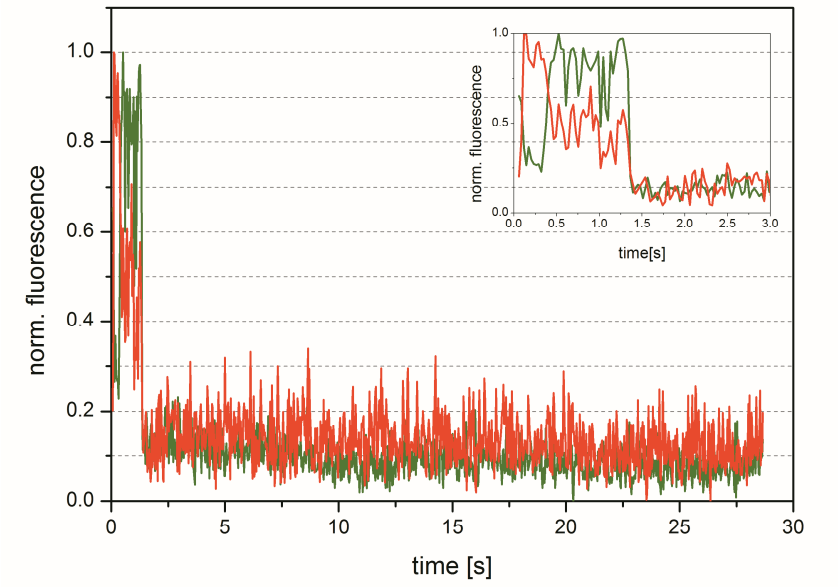

Figure 74 Single molecule FRET trace of an immobilised Holliday junction, no OCT

The graph shows a typical normalised green and red fluorescence time trace without the addition of the enzymatic oxygen scavenging system and Trolox. The small inlet shows a zoom of the first 3 s of the measurement. A short alternating transition of the green and red fluorescence signals can be observed. Both fluorophores are bleached within the first 1.5 s of the measurement.

Here, a short alternating transition from high to low red signal and vice versa is visible, indicating an energy transfer from the donor to the acceptor molecule. Nevertheless, the donor is bleached within the first 1.5 s of the experiments. Without the addition of the fluorescence stabilisers, no alternating green to red fluorescence transitions which lasted longer than ~5 s could be observed. The limited observation time is mainly due to the bleaching of the donor fluorophore. As soon as it is bleached, there is also no energy transfer to the acceptor molecule and the acceptor signal vanishes as well. In

some cases (not shown) the acceptor signal is even bleached before the donor signal which is also bleached later on after a few seconds at most.

One of the main reasons to perform single molecule FRET measurements on immobilised biomolecules is the long-term observation capability of this method. Therefore, the stabilisation of the fluorescent labels attached to these molecules is essential to succeed.

A selected single molecule FRET trace of an immobilised Holliday junction with the stabilisation mixture just described is shown in the upper graph of Figure 75. In order to visualise the alternating changes of the green and red fluorescence signals, these signals are normalised to their corresponding maxima. Here, a continuous alternating change of the donor (green) and acceptor (red) fluorescence signals is observable over the complete measurement time of around 30 s. The lower graph of Figure 75 shows the corresponding proximity factor (PF) calculated with the help of Equation 14 which is introduced in section 2.1.3.

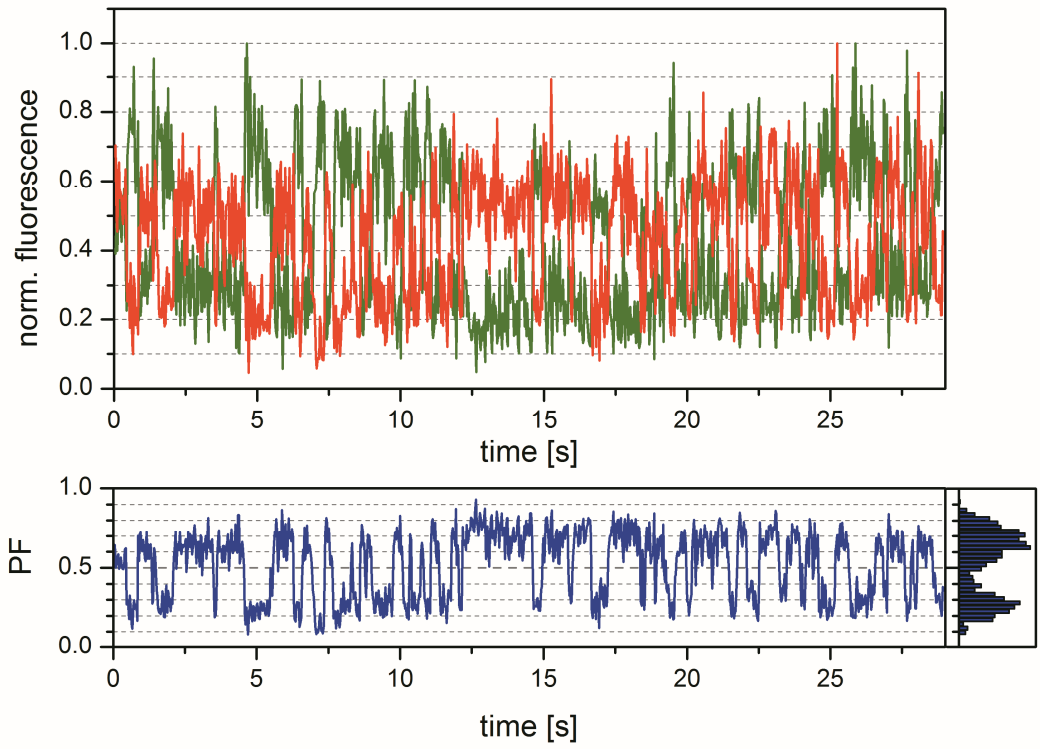

Figure 75 Single molecule FRET trace of an immobilised Holliday junction with OCT

In the upper graph, the normalised donor (green) and acceptor (red) fluorescence time traces are shown indicated by the corresponding colour. A moving average procedure was applied to the data. In the lower left graph, the calculated proximity factor PF (blue) versus time is shown. The acquisition cycle time was 29 ms. In the lower right graph, the frequency histogram of the proximity factor is displayed. This frequency histogram will be further on used to define the FRET levels (see also upper graph in Figure 77). Two different FRET levels which correspond to the two conformers of the Holliday junction are visible. The measurements were performed in standard buffer conditions in presence of OCT. The excitation power at the objective was 5 mW.

On the right hand side of this graph, the corresponding frequency histogram of the proximity factors is displayed. Here, two proximity level populations which correspond to the two different conformers of the Holliday junction (refer to section 6.1.2) are clearly distinguishable.

Very important information that can be extracted from such FRET traces is the dwell time of the geometrical states in which the biomolecule resides. From this, the biological function of a molecule can be analysed as this in many cases depends on the actual state and conformation.

At first we assume a simplified model of the Holliday junction as the open state (see also Figure 68) is even hard to detect in single molecule FRET experiments in solution with much higher temporal resolution. A reaction scheme for the transition between the two conformers with corresponding rate constants is shown in Equation 39.

$$a/d \underset{k_{21}}{\overset{k_{12}}{\Leftrightarrow}} a/b \qquad \text{Equation 39}$$

A useful tool to determine rate constants is the fluorescence correlation spectroscopy (FCS) analysis. This method is not discussed in detail in this thesis. In short words, the method is capable to detect small underlying changes due to e.g. state transitions, rotational correlation or diffusion from noisy signals. A cross-correlation function from the two individual donor and acceptor signals given in Figure 75 was calculated (black dots) which is shown in Figure 76.

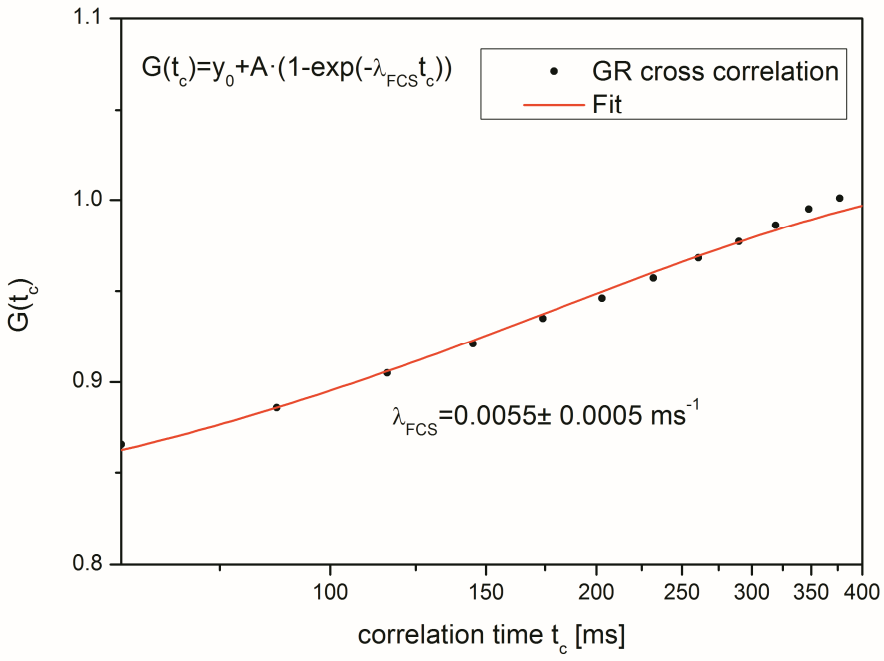

Figure 76 Cross Correlation of donor and acceptor signal

The graph shows the green (donor) to red (acceptor) cross correlation of the time dependant signals of the traces which are shown in Figure 75. A model function which typically is used to describe antibunching is fitted to the data yielding a reaction rate constant of λ=0.0055±0.0005/ms.

The anti correlative nature of the analysed signals is indicated by a rise of the correlation function. A simple exponential model function which is often used to describe the anti bunching term in fluorescence analysis was fitted to the data. The model function and the fit (red line) are also shown in Figure 76. From the cross correlation alone, the individual rate constants cannot be extracted. The parameter λ only reflects the reaction rate constant which is related to the individual rate constants by $\lambda=k_{12}+k_{21}$.

Further level detection strategies to determine the dwell times of the individual states and therefore the rate constants have been developed (Uphoff, Gryte et al. 2011). This method is based on a statistical Markov model where a state is not directly visible (hidden) but the output which is dependant on a state is visible (Hidden Markov Model, HMM). Here, we use a simple approach to obtain the dwell times directly from the data without the use of a rather complicated statistical model. The dwell times of the different occupied proximity levels and so the kinetics of such an immobilised biomolecule was extracted directly from the fluorescence time traces based on a level detection approach of the proximity factor trajectory with was calculated from the alternating donor and acceptor fluorescence signals.

In a first step, the proximity factor histogram is used to define a certain number of proximity level states. In case of the Holliday junction, a simplified two state model is assumed based on the two different conformers of the system. The centre and the width of the levels were defined by applying a model consisting of two Gaussian distributions to the data which is shown in the left graph of Figure 77. In a next step, an algorithm assigns the proximity level of each image to the previously defined levels whenever the proximity level is within at least a 2σ environment around the corresponding centre of a level. The assignment of the measured data to the defined proximity factor levels is illustrated in the right graph of Figure 77.

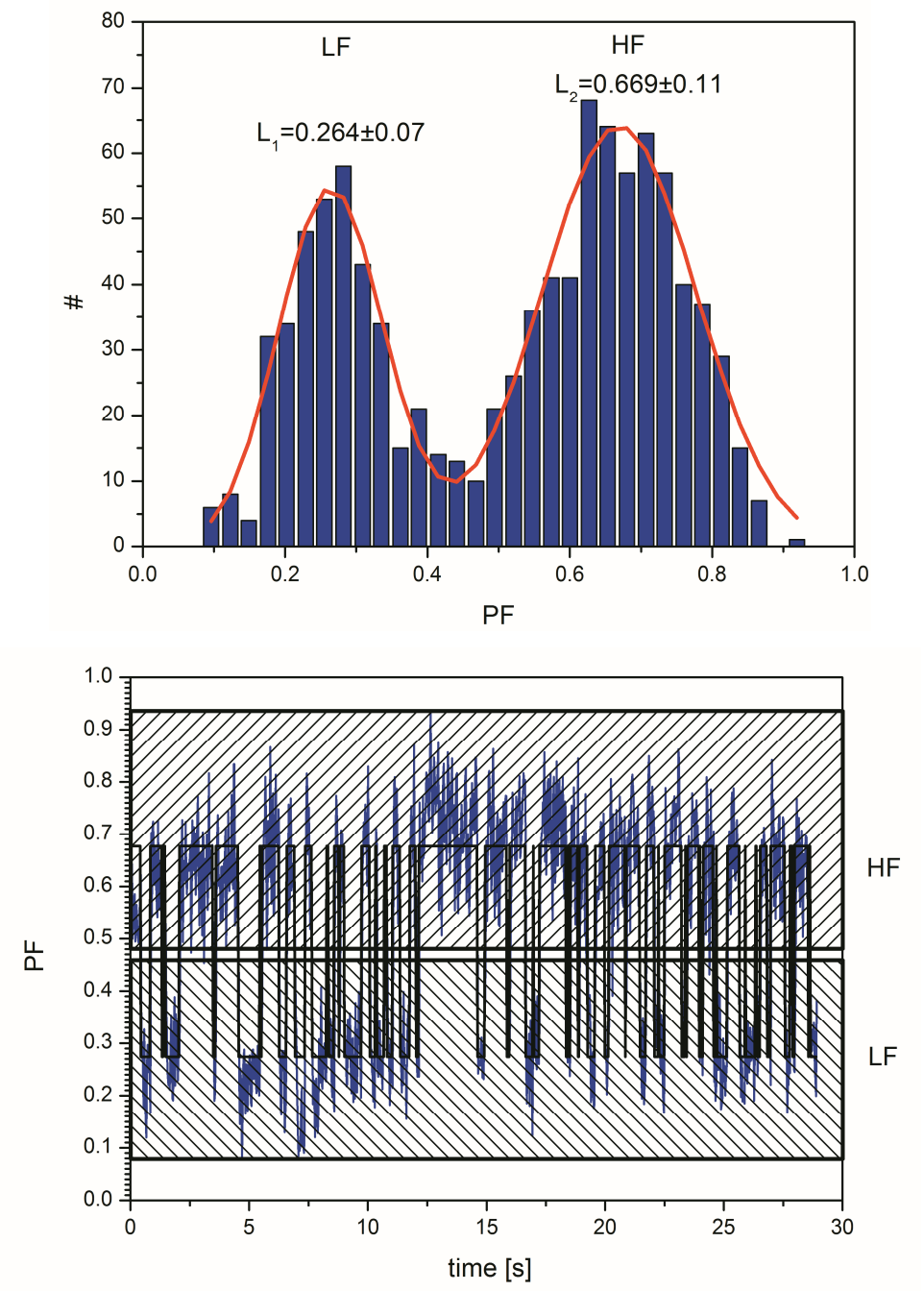

Figure 77

Determination of proximity factor levels

From the frequency histogram of the calculated proximity factors (upper graph) which is also shown in Figure 75, a model of two Gaussians has been fitted to the data. The mean and σ values are also given for the two levels. From the centre and the width of the two Gaussians, two proximity levels have been defined. The first level L_1 is assigned to a low FRET state (LF) and the second defined level L_2 is assigned to a high FRET state (HF). Further on, the algorithm attributes the proximity factors calculated for each image (blue) to these defined levels (black curve indicates the assignment to the FRET states) which is shown in the lower graph. A corresponding environment (min. 2σ) is requested to be assigned to any of the FRET states.

As the proximity levels are assigned to the data, it is easy to determine how long the system rested in the levels as soon as the levels were occupied. The dwell time histograms of the two defined proximity factor levels are shown in the left and right graph of Figure 78 respectively.

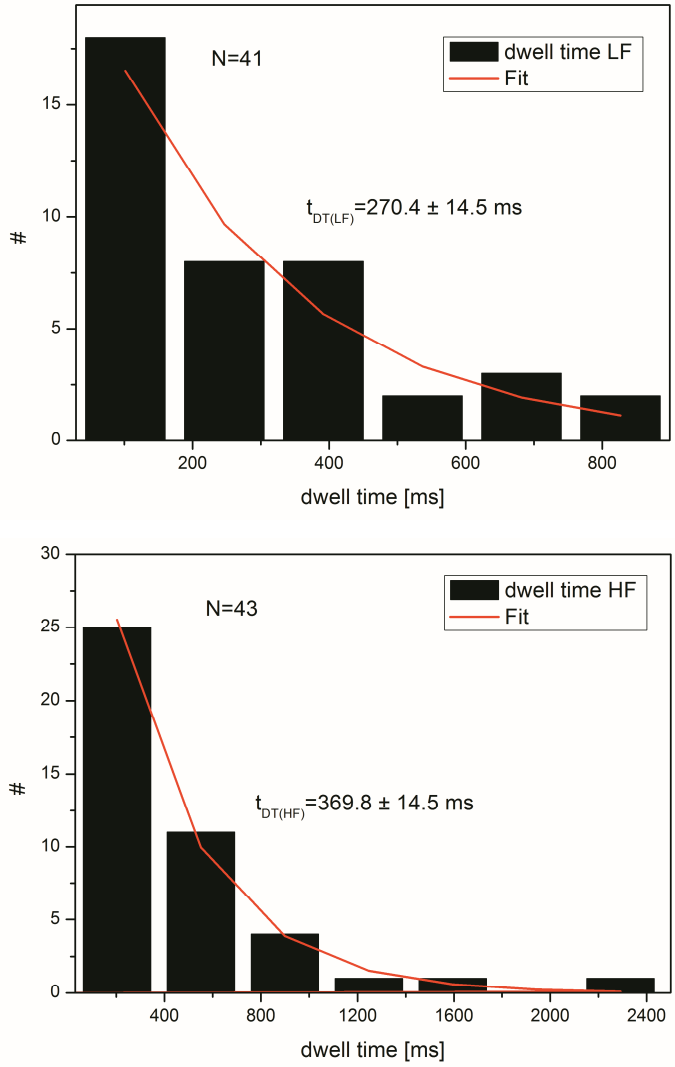

Figure 78 Dwell time histograms for a single Holliday Junction

In the upper graph, the dwell time histogram of the low FRET state LF is illustrated. From a total number of 41 occurrences the lifetime of this state is $t_{DT(LF)}$ = 270.4 ± 14.5 ms obtained by fitting a mono exponential decay model to the data. In the lower graph, the dwell time histogram of the high FRET state HF is shown. A total number of 43 occurrences yielded a lifetime $t_{DT(HF)}$ = 369.8 ± 14.5 ms of the high FRET level.

The lifetime of the low FRET state (LF) was t_{DT1}=270.4 ± 14.5 ms and the lifetime of the high FRET state (HF) t_{DT2}=369.8 ± 14.5 ms obtained from fitting a mono exponential decay model to the dwell time histograms. The corresponding transition rate constants are k_{12}= 3.70 ± 0.20 s^{-1} and k_{21}=2.71 ± 0.11 s^{-1}.

If we now compare the relaxation rate calculated from the dwell time approach, which is λ_{DT}=6.41 ± 0.23 s^{-1}, with the relaxation rate obtained from FCS analysis which is λ_{FCS}=5.50±0.48 s^{-1}, the values obtained by the two different analysis procedures are in good accordance within the statistical limitations of the measurement and analysis methods (see also Equation 40).

$$\lambda_{FCS} \approx \lambda_{DT} = k_{12} + k_{21} = \frac{t_{DT(LF)} + t_{DT(HF)}}{t_{DT(LF)} \cdot t_{DT(HF)}} \qquad \text{Equation 40}$$

In the same way the dwell times of in total 24 different Holliday Junction traces have been analysed all together. The results of this analysis are shown in Figure 79. The relaxation rate calculated from these traces is λ_{DT}=7.16 ± 0.26 s^{-1}.

The relaxation rate obtained from our experiments can be related to relaxation rates found in sccFCS (Species cross correlation Fluorescence Correlation Spectroscopy) of FRET experiments in solution, see left graph in Figure 80. These results have also been found in good accordance to results obtained from PDA (Photon Distribution Analysis) and simulated data (Valeri, Felekyan et al. 2011). In case of the solution measurements a further advanced model with additional intermediate Mg-binding states of the two conformers has been developed which yields two different relaxation times. In case of surface measurements of immobilised Holliday Junction molecules the fast relaxation time is difficult to access due to limitations of the applied methods. The relaxation rate obtained in this thesis, which is shown as a red dot in the right graph of Figure 80, is in good accordance with these simulations and previously published results of surface experiments (McKinney, Declais et al. 2003; Joo, McKinney et al. 2004).

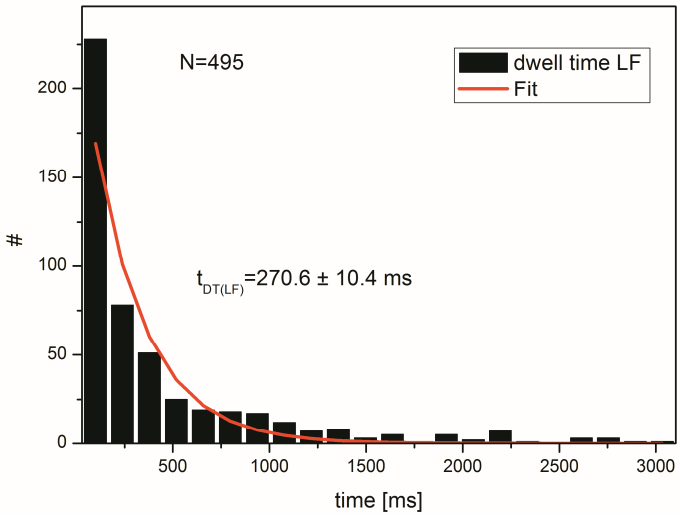

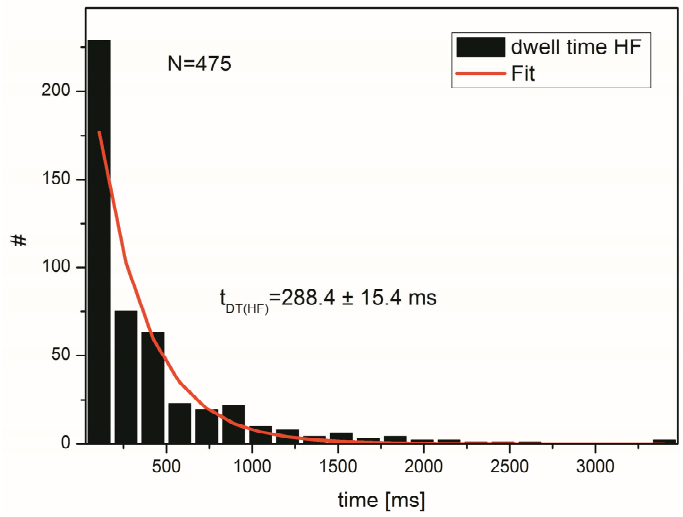

Figure 79 Dwell time histograms for 24 Holliday Junction traces

In the upper graph, the dwell time histogram of the low FRET state LF is illustrated. From a total number of 495 occurrences the lifetime of this state is $t_{DT(LF)}$ = 270.6 ± 10.4 ms obtained by fitting a mono exponential decay model to the data. In the lower graph, the dwell time histogram of the high FRET state HF is shown. A total number of 475 occurrences yielded a lifetime $t_{DT(HF)}$ = 288.4 ± 15.4 ms of the high FRET level.

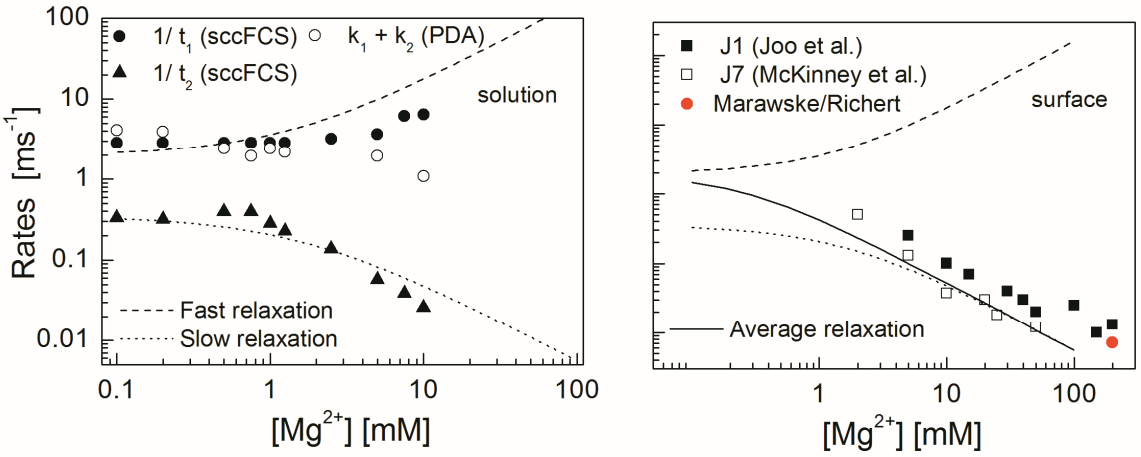

Figure 80 Comparison of reaction rates obtained from different techniques

In the left graph the relaxation rates found in sccFCS are given (Valeri, Felekyan et al. 2011). The fast relaxation ($1/t_1$) and the slow relaxation ($1/t_2$) are represented as filled circles and triangles respectively. The fast relaxation is here compared with the PDA results (open circles). The dashed and dotted lines show the expected Mg-dependence of the fast and slow relaxation respectively (simulated data). In the right graph a comparison of published data of surface measurements with simulations is shown. The black line represents the average between the fast and slow relaxation. The relaxation rate obtained in this analysis at 200 mM $MgCl_2$ is added to the graph (red dot) which fits to the simulated average relaxation.

7 Manuscripts

7.1 Fluorophores as optical sensors for local forces (published)

Chemphyschem. 2009 Aug 24;10(12):2041-8.

Fluorophores as optical sensors for local forces.

Marawske S, Dörr D, Schmitz D, Koslowski A, Lu Y, Ritter H, Thiel W, Seidel CA, Kühnemuth R.

Lehrstuhl für Molekulare Physikalische Chemie, Heinrich-Heine-Universität, Universitätsstr. 1, 40225 Düsseldorf, Germany.

The main aim of this study is to investigate correlations between the impact of an external mechanical force on the molecular framework of fluorophores and the resultant changes in their fluorescence properties. Taking into account previous theoretical studies, we designed a suitable custom-tailored oligoparaphenylenevinylene derivative (OPV5) with a twisted molecular backbone. Thin foils made of PVC doped with 100 nM OPV were prepared. By applying uniaxial force, the foils were stretched and three major optical effects were observed simultaneously. First, the fluorescence anisotropy increased, which indicates a reorientation of the fluorophores within the matrix. Second, the fluorescence lifetime decreased by approximately 2.5% (25 ps). Finally, we observed an increase in the emission energy of about 0.2% (corresponding to a blue-shift of 1.2 nm). In addition, analogous measurements with Rhodamine 123 as an inert reference dye showed only minor effects, which can be attributed to matrix effects due to refractive index changes. To relate the observed spectroscopic changes to the underlying changes in molecular properties, quantum-chemical calculations were also performed. Semiempirical methods had to be used because of the size of the OPV5 chromophore. Two conformers of OPV5 (C(2) and C(i) symmetry) were considered and both gave very similar results. Both the observed blue-shift of fluorescence and the reduced lifetime of OPV5 under tensile stress are consistent with the results of the semiempirical calculations. Our study proves the feasibility of fluorescence-based local force probes for polymers under tension. Improved optical sensors of this type should in principle be able to monitor local mechanical stress in transparent samples down to the single-molecule level, which harbors promising applications in polymer science and nanotechnology.

ARTICLES

Optical force sensor: To explore the use of fluorophores as optical sensors for local mechanical forces a custom-tailored chromophore was synthesized and aligned in a flexible PVC matrix by stretching. Applying tensile stress caused a decrease in the fluorescence lifetime by 2.5% and a blue-shift of the fluorescence spectrum of 1.2 nm, consistent with the predictions from semiempirical calculations.

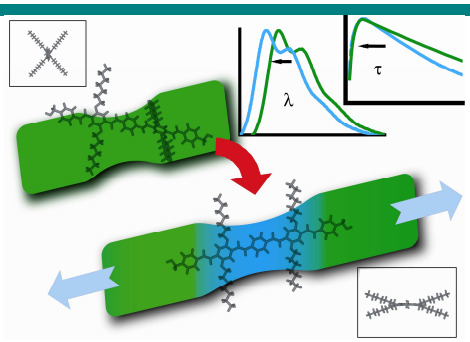

Stefan Marawske, Denis Dörr, Daniel Schmitz, Axel Koslowski, You Lu, Helmut Ritter, Walter Thiel*, Claus A.M. Seidel*, Ralf Kühnemuth**

Fluorophores as optical sensors for local forces

ARTICLES

Fluorophores as optical sensors for local forces

Stefan Marawske, Denis Dörr, Daniel Schmitz, Axel Koslowski, You Lu, Helmut Ritter*, Walter Thiel*, Claus A.M. Seidel*, Ralf Kühnemuth*

The main aim of this study is to investigate correlations between the impact of an external mechanical force on the molecular framework of fluorophores and the resultant changes of their fluorescence properties. Taking into account previous theoretical studies we designed a suitable custom-tailored oligoparaphenylenevinylene (OPV) derivative with a twisted molecular backbone. Thin foils made of PVC doped with 100 nM OPV have been prepared. By applying uniaxial force the foils were stretched. Three major optical effects were observed simultaneously. First, the fluorescence anisotropy increased, which indicates a reorientation of the fluorophores within the matrix. Second, the fluorescence lifetime decreased by approximately 2.5 % (25 ps). Finally we observed an increase of the emission energy of about 0.2% (corresponding to a blue-shift of 1.2 nm). In addition, analogous measurements with Rhodamine 123 as an inert reference dye showed only minor effects which can be attributed to matrix effects due to refractive index changes. To relate the observed spectroscopic changes to the underlying changes in molecular properties, quantum-chemical calculations were also performed. Semiempirical methods had to be used because of the size of the OPV5 chromophore. Two conformers of OPV5 (C_2 and C_i symmetry) were considered which both gave very similar results. Both the observed blue-shift of fluorescence and the reduced lifetime of OPV5 under tensile stress are consistent with the results of the semiempirical calculations. Our study proves the feasibility of fluorescence-based local force probes for polymers under tension. Improved optical sensors of this type should in principle be able to monitor local mechanical stress in transparent samples down to the single molecule level, which harbors promising applications in polymer and nano science and technology.

1. Introduction

Synthetic polymers are increasingly used in mechanically demanding applications. These products show residual stresses which can lead to deformation, fracture or even complete breakage of the material if exposed to e.g. strong variations of temperature or effective mechanical forces. Therefore, a detailed understanding of these residual stresses is essential for quality assessment and further development and improvement of polymers. To test the material properties local probing can be achieved by doping with fluorophores that are sensitive to the environment and forces. Several studies are already available that describe optical properties of low-molecular fluorophores physically mixed with polymeric matrices. Observed effects like spectral shifts have been related to mechanical manipulation in case of simple distance sensors based on force-induced excimer formation and dissociation(Löwe and Weder 2002) or charge-transfer probes(Hofstraat, Veurink et al. 1998). Fluorescence lifetime changes have been proposed to monitor local stress in polymer films(Ikawa, Shiga et al. 2002). Dissolved dyes have been used to probe orientation and alignment of polymer matrices(Springer, Neuert et al. 1983). Specific mechanical manipulation of optically induced cis-trans transitions in polyazobenzenes with DMSO as solvent

[*] D. Dörr,[+] S. Marawske,[+] Dr. R. Kühnemuth, Prof. Dr. C.A.M. Seidel
Lehrstuhl für Molekulare Physikalische Chemie
Heinrich-Heine-Universität
Universitätsstr. 1, D 40225 Düsseldorf
Fax: (+) 49 (0)211 81 12803
E-mail: ralf.kuehnemuth@uni-duesseldorf.de
E-mail: c.seidel@gwdg.de

D. Schmitz, Prof. Dr. H. Ritter
Lehrstuhl für Präparative Polymerchemie
Heinrich-Heine-Universität
Universitätsstr. 1, D 40225 Düsseldorf
Fax: (+) 49 (0)211 81 15840
E-mail: h.ritter@uni-duesseldorf.de

Dr. A. Koslowski, Y. Lu, Prof. Dr. W. Thiel
Max-Planck-Institut für Kohlenforschung
Kaiser-Wilhelm-Platz 1
D 45470 Mülheim an der Ruhr
Fax: (+) 49 (0)208 306 2996
E-mail: thiel@mpi-muelheim.mpg.de

[+] These authors contributed equally to this work.

has been demonstrated on the single molecule level(Hugel, Holland et al. 2002).
According to simulations it is expected that conjugation in distorted or twisted fluorophores, with sterically hindered ground states, can be improved by applying an

external unidirectional force(Röhrig, Troppmann et al. 2003). One class of these fluorophores consists of oligoparaphenylenevinylene derivatives (OPVs)(Tretiak, Saxena et al. 2002; Röhrig, Troppmann et al. 2003). OPVs have been investigated extensively as they are model systems for the corresponding polymers (poly-paraphenylenevinylene, PPV)(Meier, Stalmach et al. 1997), which are of great technological interest for applications in optoelectronic devices like organic light-emitting diodes. Optical properties of PPVs(Vanden Bout, Yip et al. 1997; Schindler, Lupton et al. 2004) and OPVs(Becker, Da Como et al. 2008) are partially governed by the conjugation length of the individual chromophoric unit that is a result of its local chemical environment and deformation. The effect of relative molecular alignment in aggregates and oriented thin films on intermolecular coupling and energy transfer as prominent optical processes in the condensed phases of these chromophores has been studied in detail(Egelhaaf, Gierschner et al. 1996; Gierschner, Ehni et al. 2005). However, in order to avoid fluorophore interactions we reduced the probe concentration to levels approaching the single-molecule regime. Moreover, none of the previous spectroscopic studies could present a complete characterization of the optical properties of a fluorescent probe including lifetime, anisotropy and spectral shifts as a function of the tensile stress in conjunction with a detailed theoretical analysis. The quantitative correlation of these techniques is a prerequisite to understand the underlying fundamental processes and to optimize specialized fluorophores. In this study we designed a custom-tailored endgroup-functionalized OPV as model compound which, based on the available information provided in the earlier reports,(Springer, Neuert et al. 1983; Hofstraat, Veurink et al. 1998; Ikawa, Shiga et al. 2002; Löwe and Weder 2002; Tretiak, Saxena et al. 2002; Röhrig, Troppmann et al. 2003; Becker, Da Como et al. 2008) is expected to show a significant change in the fluorescence properties if an external force is applied.

2. Results and Discussion

2.1 Synthesis

An OPV-type fluorophore **5** (OPV5) with sterically demanding n-heptyloxy side-chains and hydroxyl end-groups was synthesized in a stepwise procedure shown in Scheme 1.

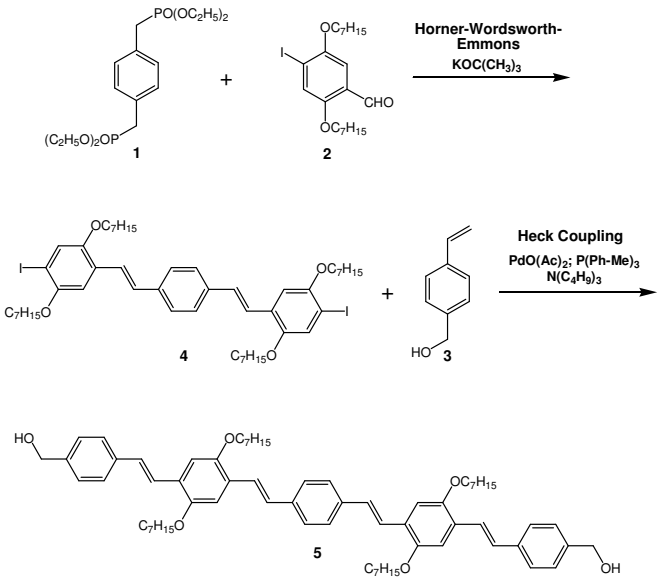

Scheme 1. Synthesis of the 5-ring oligo(paraphenylenevinylene) OPV5 diol

In a first step the double Horner-Wordsworth-Emmons reaction of p-xylylen-bis(diethyl)phosphonate **1** and 4-formyl-1-iodo-2,5-bis(heptyloxy)-benzene **2** gave the styryl-stilbene derivative **4**, which was subsequently reacted with 4-vinylbenzyl alcohol **3** in terms of a Heck reaction to form the wanted OPV5 diol **5**. (Johnstone and Rose 1979; Bao, Chen et al. 1993; Maddux, Li et al. 1997; Egbe, Roll et al. 2002; Bothe and Schmidt-Naake 2003)

2.2 Fluorescence properties of OPV5

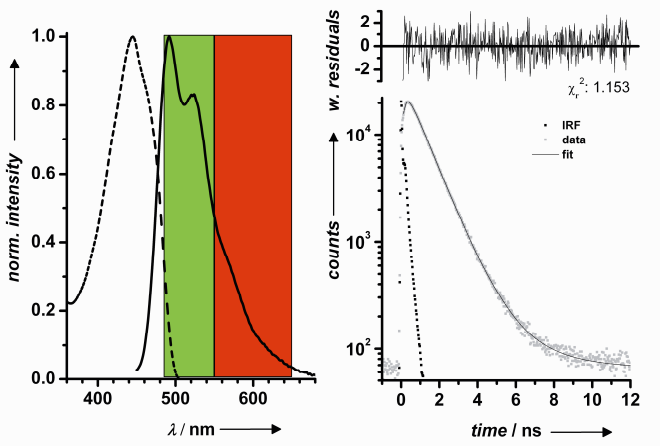

Figure 1. OPV5 in PVC: left: absorption (dashed) and fluorescence (solid) spectra with detection windows for green (478-555 nm) and red (555-645nm); right: decay histogram with double-exponential fit and residuals of OPV5 $F(t) = IRF \otimes [A_1 \cdot \exp(-t/\tau_1) + A_2 \cdot \exp(-t/\tau_2)] + B$; where IRF is the instrumental response function, A_i is the fraction of the particular lifetime component τ_i and B is the background (results listed in Table 1).

The fluorescence properties of OPV5 were investigated by measuring steady state absorption and emission spectra,

anisotropy, fluorescence lifetime, and quantum yield in THF (Table 1). The normalized absorption and fluorescence spectra and a typical result for the fluorescence decay of OPV5 dissolved in PVC are shown in Figure 1. To recover the fluorescence lifetimes from the data by nonlinear regression analysis, the background contribution was determined from the baseline before the laser pulse and a double-exponential decay model was applied, taking into account repetitive excitation.(Fries, Brand et al. 1998) Double and triple exponential decays of OPVs have been described in literature before, the origin of the two longer lifetimes having been assigned to cis-trans isomers. A very fast component of 20-50 ps was related to excited state dynamics of the chromophore(Di Paolo, de Melo et al. 2007). Within the time resolution of our bulk setup we also observe a double exponential fluorescence decay with two significant components in THF (see Table 1).

Table 1. Spectral properties of OPV5 in different environments

OPV in	λ_{Ex}[nm] [a]	λ_F[nm] [b]	τ_1[ns] [c]	τ_2[ns] [c]	τ_{av}[ns] [d]	Φ_F [e]
THF	432	485	0.83 (0.77)	0.52 (0.23)	0.78	0.53
PVC	445	492	0.97 (0.97)	[f]	1.03	0.81

[a] Absorption maximum. [b] Fluorescence maximum. [c] Fluorescence lifetime components, τ_i (amplitudes, A_i). [d] Fluorescence weighted average lifetime $\tau_{av} = (A_1 \cdot \tau_1^2 + A_2 \cdot \tau_2^2)/(A_1 \cdot \tau_1 + A_2 \cdot \tau_2)$. [e] Fluorescence quantum yields, measured in THF and extrapolated by correcting for refractive index in case of PVC (for details see supporting information section 2). [f] Typically a minor component of ~2.2 ns was observed, probably due to background fluorescence of the polymer matrix or distorted OPVs. Lifetimes in PVC were determined from p-polarized fluorescence in the green spectral window to maximize signal-to-noise ratio.

However, in a PVC foil the fluorescence decay shows a single dominant lifetime component (97%) of 0.97 ns. The decay contains also a minor (3-5%) contribution of a longer second fluorescence lifetime of 2.2 ns, which may be attributed to background fluorescence of the polymer matrix or distorted OPVs. Moreover, OPV5 in the foil is brighter than in THF as indicated by an increase of the fluorescence lifetime and quantum yield (Table 1). As the number of photons in our experiment was limited due to photobleaching, the two different lifetime components were difficult to separate. Therefore, the fluorescence weighted average lifetime (Table 1) of OPV5 was found to be a stable parameter for further fluorescence lifetime analysis. Typical spectral properties of OPV5 in different environments are listed in Table 1.

2.3 Quantum-chemical calculations

To relate the observed spectroscopic changes to the underlying changes in the molecular properties, quantum-chemical calculations were performed using semiempirical methods because of the size of the OPV5 chromophore. The theoretical study involved the selection of a suitable semiempirical approach (AM1) through comparison with higher-level results for small model compounds, computation of ground-state potential curves (AM1/SCF) for elongation of the chromophore, reoptimization of the resulting geometries in the first excited singlet state, and calculation of its spectral properties using multireference configuration interaction (AM1/MRCI) methods (for details see supporting information section 3).

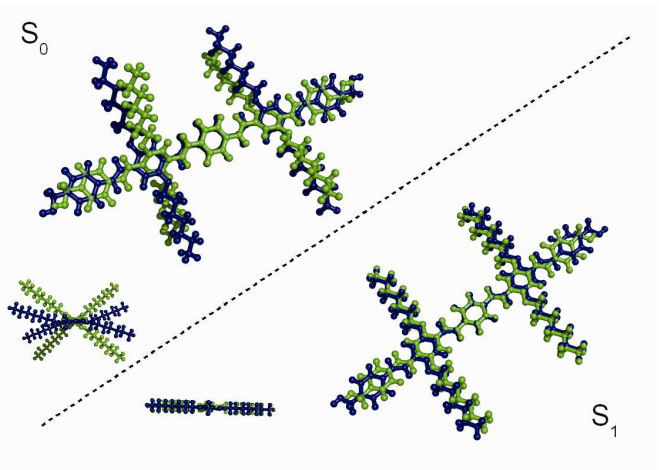

Scheme 2. Simulation of the conformational change in the molecular geometry of OPV5 under C_2 symmetry in the ground state (left) and in the first excited state (right), green: no force applied, blue: 6.9 nN per molecule.

Two conformers of OPV5 (C_2 and C_i symmetry, were considered which both gave very similar results as shown in Figure 2. Scheme 2 shows the C_2 geometries of the ground and the first excited state without (green) and with applied force (blue). The distance of the outermost ring carbon atoms of the chromophore was varied and all other coordinates of the molecule were then allowed to relax. Forces were computed by analytical differentiation of a cubic-spline fit of the computed potential curves. No breakage of any chemical bond was observed even at the highest applied force (6.9 nN). This is consistent with reported rupture forces for C-C single bonds in the range of 2.3 to 13.4 nN(Odell and Keller 1986) taking into account the higher stability of OPV5 due to the partial double bond character of its molecular backbone. In the ground state (Scheme 2, left) an unwinding of the molecular backbone under stress is observed, whereas the first excited singlet state S_1 (Scheme 2, right) remains almost planar throughout. For the range of forces considered (up to 6.9 nN), the AM1/MRCI calculations give a notable increase in the fluorescence energies (wavenumber $\tilde{\nu}$ in cm^{-1}) upon stretching as shown by the black curve in Figure 2, and also an initial increase in the oscillator strengths *f* (for forces up to 4 nN). The resulting fluorescence lifetimes(Klessinger and Michl 1989) $\tau_r = 3/(2f\tilde{\nu}^2)$ as derived from the Einstein coefficients decrease monotonically (up to 16% for the maximum force of 6.9 nN) which is indicated by the green curve in Figure 2. The calculations thus predict a blue-shift of fluorescence and reduced radiative lifetimes upon stretching OPV5 (see also Figure 2) along the conjugated chain.

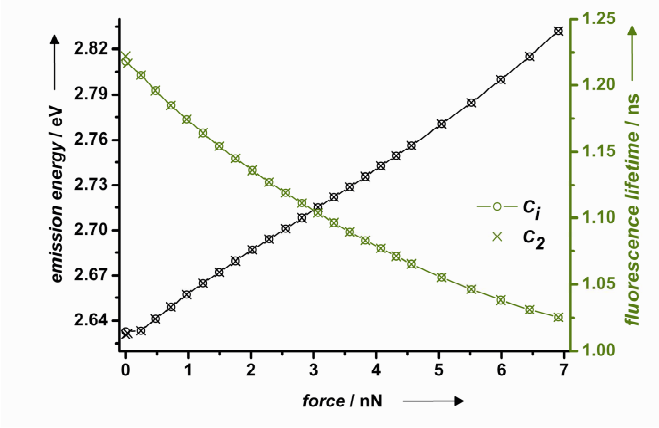

Figure 2. Calculated emission energies (black) and fluorescence lifetimes (green) dependant on the applied force per molecule. Results are shown for two different conformers, one in C_2 symmertry (crosses) and one in C_i symmetry (circles) with nearly identical results super-imposed on top of each other.

2.4 Combined force and fluorescence experiments

In order to investigate the impact of force on the fluorophores, thin foils (~50 µm) made of technical atactic PVC doped with OPV5 (ca. 100 nM) have been prepared. By applying uniaxial force the foil is stretched. As the foil is comparatively thin and the concentration of the dye is low, reabsorption is negligible in our experiments. In order to minimize surface effects great care was taken to keep the laser focus centered in the PVC foil throughout the whole experiment. In this way the observation volume was at least 20 µm away from any surface. At each data point of the fluorescence analysis a xy-scan using a piezo-scanner was performed in order to minimize photobleaching and to be more independent on local heterogeneities of the foil which might occur in the preparation process.

Three major optical effects can be observed simultaneously (Figure 3). First, the fluorescence anisotropy increases (top panel), which indicates a reorientation of the fluorophores within the matrix. Second, the fluorescence lifetime decreases (middle panel) by approximately 2.5% ($\Delta\tau$ = -25±2.5 ps). Finally we observe a blue shift in the emission spectrum by about 1.2 nm (bottom panel), as indicated by an increased background-corrected signal intensity ratio, F_G/F_R, in the green and red spectral detection windows (Figure 1, left). In the next sections we will discuss all three effects in detail. As a negative control measurement we also prepared foils doped with Rhodamine 123 (Rh123) under the same conditions as mentioned. The Rh123 is a rather spherical dye with no pronounced long axis, as in case of OPV5. Moreover Rh123 has a rigid molecular backbone, so that it is expected to be quite insensitive to external forces.

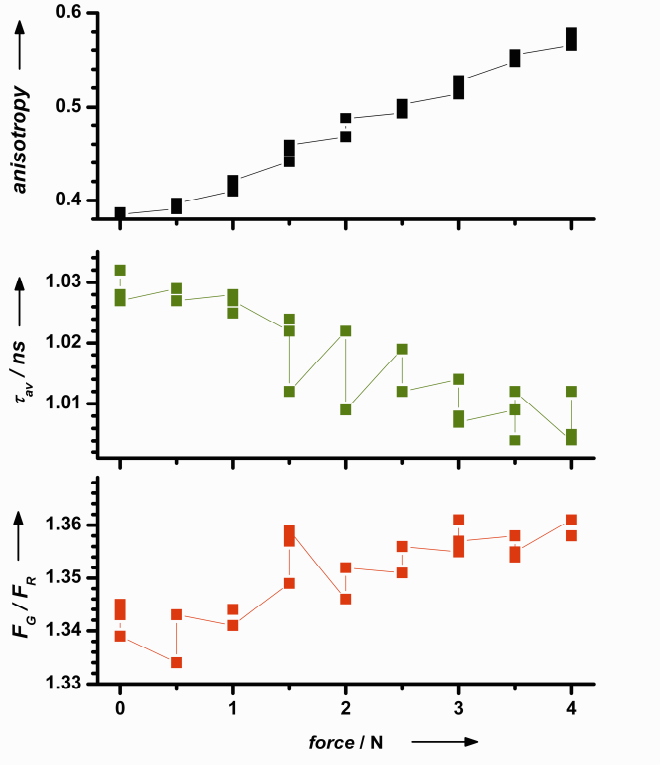

Figure 3. Increasing fluorescence anisotropy (top panel, black), decreasing fluorescence lifetime (middle panel, green) and increasing green to red signal ratio (bottom panel, red) of OPV5 within the PVC foil versus the applied force.

2.4.1 Fluorescence anisotropy

In the force experiment the polarization of the exciting laser light and the pulling direction were chosen to be parallel to maximize excitation probability. As the transition dipole moments of OPVs are oriented almost parallel to their molecular backbones(Spano 2002; Gierschner, Ehni et al. 2005), the increase in fluorescence intensity as well as in anisotropy while the foil is stretched shows that the fluorophores change the orientation of their long axis towards the direction of tension. This fluorescence increase and the irreversibility of this effect prove that the molecular rotation of OPV5 in PVC is negligible, making it an ideal marker to probe local orientations of suitable polymer matrices. This is in accordance with stretch orientation studies of different OPV derivatives dissolved in polyethylene or polystyrene foils.(Damerau and Hennecke 1995) For a quantitative evaluation of the experiments it is necessary to take the individual sample cross-sections S_i (S = thickness x width) of the foil for each point of the measurement into account by calculating the applied mean tensile stresses $F_i/S_i = F_i/[S_S - (S_S-S_E)\cdot(\Delta L_i/(L_E-L_S))]$, F_i being the applied force, S_S and S_E the cross sections at start and end of the experiment and $(\Delta L_i/(L_E-L_S))$ the relative elongation. Figure 4a illustrates the strict correlation between the elongation of the foil (open triangles) and the change of the fluorescence anisotropy (full triangles) dependant on the mean tensile stress. Orientation of the polymer matrix was also confirmed using a polarization microscope. The unstretched unstained foil does not show any preferred direction whereas the stretched foil clearly exhibits birefringence as

expected (not shown)(Rider and Hargreaves 1970). This indicates that the macroscopic pre-alignment of the polymer chains in the unstretched foils is negligible.

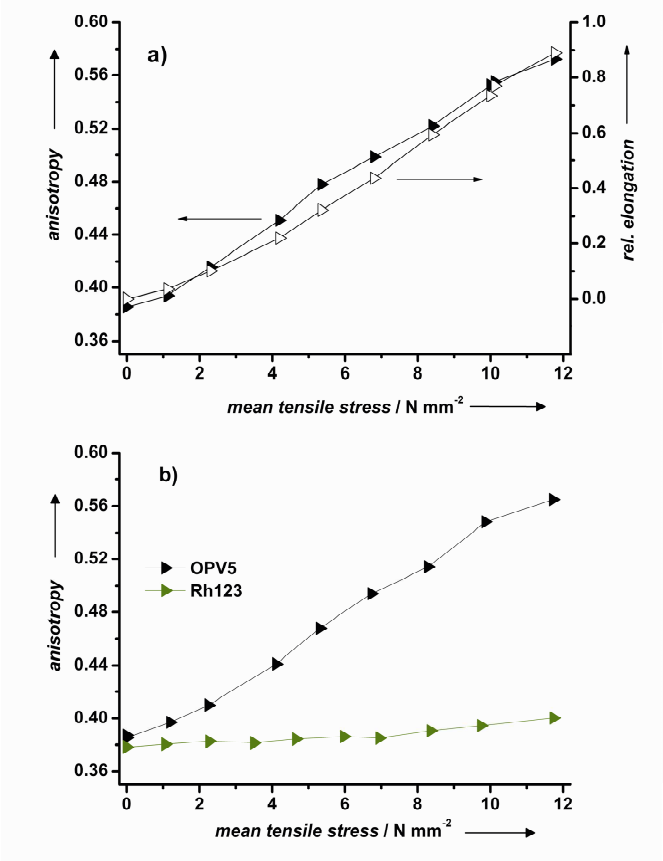

Figure 4a. Relative elongation of the PVC foil (open triangles) and the fluorescence anisotropy of OPV5 (full triangles) versus mean tensile stress. Figure 4b. Comparison of the anisotropy between OPV5 (black) and Rh123 (green). With increasing tensile stress the OPV5 fluorophore shows a distinct reorientation whereas in case of Rh123 the effect is remarkably smaller.

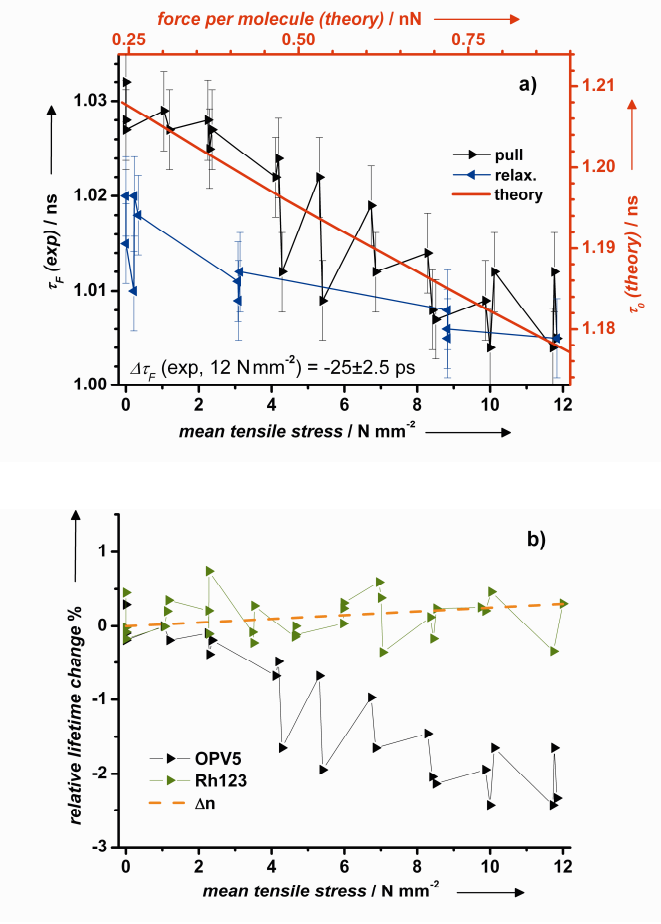

Figure 5a. Comparison between a typical fluorescence lifetime measurement (black axes) and theory (AM1/MRCI, red): The PVC foil was stretched (black) and subsequently relaxed (blue).The error-bars represent the shot-noise limited uncertainty of the lifetime fits of about 4 ps. Both ordinates are scaled to equal relative range of lifetimes. Figure 5b. Comparison of the relative fluorescence lifetime change between OPV5 (black) and Rh123 (green). Upon stress the fluorescence lifetime of the OPV5 fluorophore decreases up to 2.5% at a maximum tensile stress of around 12 N mm^{-2} whereas Rh123 only shows a slight increase close to the noise level which is consistent with expected changes due to refractive index changes of the matrix (Δn, dashed orange).

If we compare the change in anisotropy between OPV5 (black) and the control dye Rh123 (green) as shown in Figure 4b it is clearly visible that the anisotropy very sensitively reflects the reorientation of OPV5 whereas in case of Rh123 just the expected small change is observed.

2.4.2 Fluorescence lifetime

For the analysis of the fluorescence lifetime in our combined force and fluorescence experiments we exclusively used data recorded by an ultra-fast single-photon sensitive detector (Micro- Photon-Device(MPD), IRF ~30 ps, see also experimental section). The results of a detailed analysis of the fluorescence decay time of OPV5 as a function of the mean tensile stress is displayed in Figure 5a. The black curve shows the first part of the experiment (pulling) while the blue curve describes the second step (relaxation). With increasing stress the fluorescence lifetime is decreasing down to $\Delta\tau$ = 25±2.5 ps at the highest applicable stress of 12 N mm^{-2}. The effect is not completely reversible upon relaxation: in the presented experiment the final lifetime at 0 N is lower than the initial value at 0 N by about 10 ps. In a second extension relaxation cycle with the same sample the observed hysteresis was significantly smaller (not shown). We also performed measurements in which the fluorescence lifetime returned to the starting value within the first cycle, indicating slight variations in the local static interactions of fluorophore and matrix for different samples. With different samples we observed

changes of the fluorescence lifetime between 20 and 45 ps

Table 2. Influence of the matrix due to refractive index changes on the fluorescence properties of OPV5 and Rh123. Effects on the fluorescence lifetime assumed by an empty spherical cavity model (ESC) and an empty ellipsoidal cavity model (EEC). Effects on solvatochromic shifts of the emission spectra by applying Onsager theory.

[a,b] change of radiative lifetime [c,d] change of fluorescence lifetime [e] solvatochromic shift.

	Δn	$\Delta\tau_r$ ESC [ps] [a]	$\Delta\tau_r$ EEC [ps] [b]	$\Delta\tau_F$ ESC [ps] [c]	$\Delta\tau_F$ EEC [ps] [d]	$\Delta\lambda$ [e] [nm]
OPV5	**r. index** 4.6×10^{-4}	-0.64 (0.05%)	-0.38 (0.03%)	-0.42 (0.04%)	-0.25 (0.02%)	0.022
	birefr. 3.1×10^{-3}	-4.36 (0.34%)	-2.56 (0.20%)	-2.87 (0.28%)	-1.69 (0.16%)	0.146
	Exp.	-25 ± 2.5 (2.5%)				-1.2 ± 0.2
Rh123	**r. index** 4.6×10^{-4}	-1.59 (0.05%)	n.a.	-1.47 (0.05%)	n.a.	0.063
	birefr. 3.1×10^{-3}	-10.71 (0.33%)	n.a.	-9.92 (0.32%)	n.a.	0.420
	Exp.	6 ± 10 (~0.3%)				0.4 ± 0.2

(average effect is around -26±5 ps for applied tensile stresses of 12 N mm^{-2}). Foils with less plasticizer exhibited a similar, approximately linear dependence of lifetime on the tensile stress only after an offset of up to 10 N mm^{-2} (supporting information section 2.5). An alignment is achieved much faster in soft and flexible samples. This indicates the necessity for at least partial molecular alignment to couple solutes with external forces. Rates of radiative transitions depend on the environment of the chromophore, in particular on the local index of refraction. Two independent effects can cause the refractive index of PVC to change upon stretching (for details see Table 2 and supporting information section 2.3): (1) From reported density changes(Jabarin 1991) the Lorentz-Lorenz equation(Horner 1943) predicts index variations of the order of $\Delta n \approx 4.6\cdot10^{-4}$ for relative elongations of 100%. (2) The observed birefringence due to polymer chain orientation was reported to be around one order of magnitude stronger, ranging up to $\Delta n \approx 3.1\cdot10^{-3}$ (Shindo, Read et al. 1968; Robinson, Bower et al. 1978; Ajji and Renaud 1991; Jabarin 1991; Ozkan, Oskay et al. 1994; Yalcin and Cakmak 2005).

By applying a modified Strickler-Berg approach different cavity models have been developed which should be taken into account to estimate the influence of refractive index changes on the fluorescence lifetime(Toptygin 2003). As the solvent is expelled from the volume occupied by the fluorescent molecule a cavity is created in which the fluorophore is located. In the approximation and depending on the guest molecules shape the empty spherical cavity model (ESC) or the empty ellipsoidal cavity model (EEC) can be used to describe the appropriate boundaries. The OPV5 fluorophore probably is described best by an ellipsoidal model. In case of Rh123 we believe that the empty spherical cavity model more realistically reflects the molecular shape. Corresponding changes of the fluorescence lifetime as estimated using these empty cavity models are expected to be smaller than ca. 3 ps which is a relative change of less than 0.5% (Table 2).(Toptygin 2003)

This is almost an order of magnitude smaller than the lifetime effect we observe. To further characterize the static matrix effect, we also performed measurements with the rigid dye Rh123 dissolved in PVC. We could not observe any significant change in the fluorescence lifetime τ_F. At a fluorescence lifetime of about 3.1 ns we found a change of $\Delta\tau_F = 4\pm8$ ps at 12 N mm^{-2}. Within the statistical errors of around 8 ps the relative change is smaller than 0.3%, which nicely agrees with expected refractive index effects of up to 10 ps (Table 2). In Figure 5b the relative lifetime changes for OPV5 (black) and Rh123 (green) are shown. In case of Rh123 the changes can be attributed to the discussed refractive index changes alone as indicated by the dashed orange curve whereas the fluorescence lifetime of OPV5 shows a clear decrease up to 2.5%, about an order of magnitude larger than by Δn would be predicted (further details can be found in Table 2 and in the supporting information section 2.3). The fluorescence lifetimes from the semiempirical AM1/MRCI calculations are also included in Figure 5a (red part of the graph). They show an almost linear dependence on the applied force, being consistent with the experimental observations. The absolute values of the fluorescence lifetimes differ between theory and experiment, partly because of refractive index effects and nonradiative processes ($\Phi_F < 1$) in the PVC matrix which were not taken into account in the simulations. Moreover, theory directly relates the force exerted on a single molecule to a change in radiative lifetime of S_1 whereas the only experimentally accessible information is the macroscopic mean tensile stress to which the whole foil is exposed. The force per molecule exerted in the foils can be estimated by using the mean molecular cross section of PVC molecules of about 0.3 nm^2. It is around 4 pN per molecule for the maximum force in Figure 6a (see also supporting information section 2.2). This is only a mean value assuming a homogeneous force distribution in the substrate. Forces on individual molecules might locally be higher and can approach the realm where covalent chemical bonds may break (2.3 to 13.4 nN)(Odell and Keller 1986; Grandbois, Beyer et al. 1999). Our measured values as indicated by comparison of theory and experiment are within these limits. Thus elongation induces a change of an apparent local mechanical force of ca. 0.6 nN per molecule (Figure 5a).

2.4.3 Spectral blue-shift of fluorescence

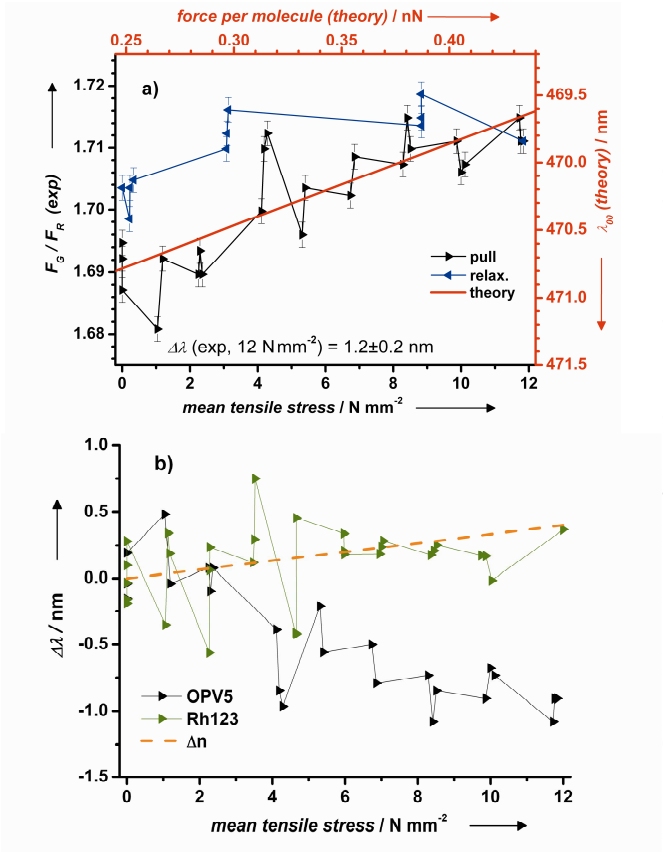

Figure 6a. Green to red fluorescence ratio F_G/F_R from the experiment (black axes) in Figure 5a versus mean tensile stress. The PVC foil was stretched (black) and subsequently relaxed (blue). Also shown is the calculated (AM1/MRCI, red) spectral shift as function of the force applied on a single molecule. Both ordinates are scaled to equal relative spectral range. The error-bars represent shot-noise. The real error is larger probably due to chromatic aberrations caused by mismatch of refractive index of PVC foil (n=1.53) and objective design (corrected for n=1.33). The aberrations depend strongly on the focus position inside the foil and change upon stretching. Figure 6b. Comparison of the relative spectral shift of OPV5 (black) and Rh123 (green). At the maximum tensile stress of around 12 N mm^{-2} the spectrum of OPV5 features a blue-shift of 1.2 nm whereas the spectrum of Rh123 reveals a small red-shift consistent with estimations of the influence of the matrix alone due to refractive index changes (dashed orange).

Simultaneously with the changes in anisotropy and lifetime there is a spectral shift of the fluorescence upon stretching which was detected by monitoring the intensity ratio of the two spectral bands in the emission region ("green" and "red", Figure 1, left). The results of this analysis are shown in Figure 6a. The black curve describes the results of the pulling step, in blue the subsequent relaxation step is shown and in red the results of the theoretical calculations are given. With increasing tensile stress the green to red fluorescence ratio F_G/F_R is increasing, indicating a blue shift of the spectra. Using the spectral shape as determined by steady state measurements of the unstrained foil the observed change in the ratio F_G/F_R for tensile stresses up to 12 N mm^{-2} translates into a blue shift of about 1.2±0.2 nm, as determined by linear regression analysis.

According to the AM1/MRCI calculations, this shift would be consistent with a change of an applied local mechanical force of ca. 0.18 nN per molecule. Using spectral positions given in Table 1 and applying Onsager theory(Onsager 1936) we expect red-shifts in the force experiment due to refractive index changes smaller than $\Delta\lambda \approx 0.15$ nm in case of OPV5. Corresponding reference measurements with Rh123 showed a spectral red-shift of $\Delta\lambda = 0.31\pm0.14$ nm at 12 N mm^{-2}, which is within the expected range for refractive index induced changes of up to 0.4 nm for this dye. In Figure 6b the relative changes of the emission maxima are given for OPV5 (black) and Rh123 (green). A red-shift in case of Rh123 can be assigned to changes due to refractive index as discussed and shown by the dashed orange curve. However, for OPV5 a clear blue-shift of around 1.2 nm is observed (see also Table 2 and the supporting information section 2).

2.5 Overall discussion

The observed force dependences of the lifetime and the measured spectral shift are significantly higher than would be expected from the matrix due to changes in the refractive index, Δn, alone(Rao, Singh et al. 1976; Gierschner, Mack et al. 2002). Taking matrix effects due to changes in Δn into account (see table 2), only a small increase of $\Delta\tau_F$ by up to 12% and a reduction of $\Delta\lambda$ by up to 14% is expected. Thus a net effect of $\Delta\tau_F$ = -22 ps and $\Delta\lambda$ = 1.25 nm can be unambiguously attributed to force. In comparison with theory, these shifts then translate into an apparent mean local force on a single chromophore in a range of ca. 0.2-0.55 nN (see Figure 2). The uncertainty lies within the expected accuracy level of the semi empirical computations.

Due to the visco-elastic properties of the PVC matrix its extension shows only a faint reversibility with the applied force which suggests that the local environment of the fluorophores does not depend on force but on extension. This is corroborated by the orientation of the fluorophores as indicated by anisotropy which is largely dependant on extension of the foil only. However, the observed changes of fluorescence lifetime as well as the spectral shift are mainly reversible with the applied force. Altogether, this indicates only a marginal influence of the matrix on the fluorescence lifetime as well as the emission spectrum of the fluorophore. This clearly proves the concept of a fluorescent probe as a sensor for local forces.

The blue-shift of fluorescence and the reduced lifetime of OPV5 under tensile stress are qualitatively consistent with the results from semiempirical calculations. A more quantitative comparison is not feasible since the force on single OPV5 molecules is not known precisely in the experiment (apparently less than 1 nN). The experimental results seem to indicate an extremely efficient transfer of mechanical force onto the chromophore, i.e. a force per molecule that is about two orders of magnitude higher than average. Therefore a more realistic view of the process may also have to add lateral interactions of the polymer chains with the side chains of the chromophore to promote its unwinding. Unwinding of the ground state as observed in the simulated experiments for uniaxial forces can also be achieved by applying torsional forces to the side-chains. For both mechanisms we expect qualitatively similar spectroscopic effects. The presence of an additional mechanism is supported by experiments using modified OPV5 carrying polymer chains attached to the hydroxyl endgroups as possible handles to enhance coupling of external forces from the matrix to the fluorophores (not

shown). No difference of the force dependant effects was observed between OPV5 and the modified OPV5.

3. Conclusion

In summary, we have explored possible applications of fluorophores as optical sensors for local mechanical forces. To that end a custom tailored chromophore consisting of an aromatic backbone strained by sterically demanding alkyloxy side-chains has been synthesized. A flexible PVC matrix served to align the fluorophores by stretching. Transfer of mechanical strain from the matrix induced a geometrical change in the chromophore. Consistent with the results of semiempirical calculations on the same system, this caused a decrease in the fluorescence lifetime by 2.5% (25 ps) and an increase of the emission energy by 0.2% which corresponds to a blue-shift of 1.2 nm at tensile stresses of 12 N mm^{-2}. From a different point of view the force of 0.2-0.55 nN acting on a single molecule can be interpreted as an equivalent energy difference of 0.15 – 0.8 kcal mol^{-1} (supporting information, Table 8).

Our study proves the feasibility of fluorescence-based local force probes for polymers under tension. Necessary improvements can be achieved by developing more sensitive fluorophores and possibly by increasing the efficiency of force transmission from the matrix to the probe, i.e. by using modified end-groups to attach additional polymer chains as handles. Improved optical sensors of this type should in principle be able to monitor local mechanical stress in transparent samples down to the single molecule level, which can be used for reliability studies of the materials and also harbor promising further applications in polymer and nano science and technology.

4. Experimental Section

OPV5: The yellow crystalline solid was purified by column chromatography using a 95 to 5 mixture of chloroform and acetone as an eluent. Yield 45% (synthesis see supporting information section 1)

^{1}H NMR (500 MHz, [D_8]THF, 25°C, TMS): δ = 0.81 (m, 12H, CH_3), 1.27-1.34 (m, 16H, CH_2), 1.48 (m, 8H, CH_2), 1.78 (m, 8H, CH_2), 3.99 (m, 8H, CH_2), 4.06 (m, 2H, OH), 4.46 (d, 4H, CH_2), 7.11-7.22 (m, 12H, CH), 7.38-7.46 (m, 12H, CH); MALDI-TOF MS: *m/z*: 1003[M^+]

PVC foil: PVC (0.3 g, Aldrich, CAS# 9002-86-2, Mn: 47000) was dissolved in THF (5 mL, Prolabo, CAS# 109-99-9, AnalaR NORMAPUR) together with hexamoll® (0.045 g, BASF Ludwigshafen, CAS# 166412-78-8) , a plasticizer which is necessary to make the foil flexible enough to be stretched. This solution was then cleaned with activated charcoal which was afterwards removed by centrifugation. To the polymer solution (5 mL) OPV5 (21.5 ng, 21.4 pmol, the concentration is far below excimer formation(Crenshaw and Weder 2005)) was added and filled into a petri dish. THF was evaporated at room temperature until the foil gained its solid state. Finally the foil was dried for 5 hours under highvacuum conditions, yielding substrates with a glass-temperature of 46°C. The resulting foil showed a thickness of around 50 µm, the exact value being determined by a z-scan of the laser focus through the sample prior and after each experiment. The effective cross section of each foil was calculated from its thickness and the width as measured by a caliper-gauge.

Fluorescence spectroscopy: The fluorescence and absorption spectra were measured with FluoroLog-3 (Jobin Yvon Horiba) and Cary-300 Bio (Varian), respectively. Time-correlated single photon counting (TCSPC) measurements were performed using a 5000 U (IBH) with a pulsed diode laser source at 471 nm (Picoquant). The combined force and fluorescence measurements were performed on a home-built setup(Widengren, Kudryavtsev et al. 2006). Linear polarized and pulsed light from a diode laser (Picoquant) at 468 nm and a repetition rate of 50 MHz is coupled into an inverted epifluorescent confocal microscope (Olympus, IX71) at a mean intensity of $I_0/2 \approx 2.5$ kW cm^{-2} in a near diffraction limited focus. The fluorescence was then separated with respect to polarization parallel and perpendicular to the laser light. These two components were further split by a dicroic beamsplitter (AHF, BS560) in a “green” fraction 487-548 nm (AHF, HQ 520/66) and a “red” fraction 548-644 nm (AHF, HQ 580/130) and finally focused on single photon avalanche diodes (Micro-Photon-Devices PDM 50CT (green), Perkin-Elmer SPCM-AQR-14 (red)). The signals of the detectors were recorded by two synchronized time-correlated single photon counting pc-boards (Becker & Hickl, SPC-150). In order to minimize photobleaching, for each data point a xy-scan of 98x98 μm^2 was performed with a piezo-scanner (PI, P-527). Taking into account an average number of ca. 360 dye molecules in the confocal detection volume element, pixel intensity distributions within each scan were shot-noise limited and gave no indication of additional heterogeneity (see supporting information section 2.7). The self-made PVC foils were stretched by a tensile stage (Deben, MTEST 200) which was mounted upside down on the inverted microscope.

Calculations: In view of the size of the OPV5 chromophore, its fluorescence lifetime was computed using semiempirical methods(Koslowski, Beck et al. 2003) Geometry optimizations were performed on two conformers of OPV5 in the ground state at the AM1/SCF level(Dewar, Zoebisch et al. 1985), one in C_2 symmetry (with the C_2 axis perpendicular to the central aromatic ring) and the other one in C_i symmetry. Spectral properties were computed at the AM1/MRCI level at the optimized (nearly planar) excited-state geometries, in particular the radiative lifetime τ_r of the first excited singlet state.

Acknowledgements

This work was financially supported by the Deutsche Forschungsgemeinschaft (SFB 663, Projects B4 and C4). The authors thank Dr. S. Kalinin and Dr. S. Felekyan.

Keywords: Analytical Chemistry · Optical Properties · Fluorescence Spectroscopy · Organic Chemistry · Theoretical Chemistry

[1] C. Löwe, C. Weder *Adv. Mater.* **2002**, 14, 1625-1629.
[2] J. W. Hofstraat, J. Veurink, B. Gebben, H. J. Verheij, J. W. Verhoeven *J. Fluoresc.* **1998**, 8, 335-342.
[3] T. Ikawa, T. Shiga, A. Okada *J. Appl. Polym. Sci.* **2002**, 83, 2600-2603.
[4] H. Springer, R. Neuert, F. D. Müller, G. Hinrichsen *Colloid Polym. Sci.* **1983**, 261, 800-804.
[5] T. Hugel, N. B. Holland, A. Cattani, L. Moroder, M. Seitz, H. E. Gaub *Science*. **2002**, 296, 1103-1106.

[6] U. F. Röhrig, U. Troppmann, I. Frank *Chem. Phys.* **2003**, 289, 381-388.

[7] S. Tretiak, A. Saxena, R. L. Martin, A. R. Bishop *Phys. Rev. Lett.* **2002**, 89, 097402.

[8] H. Meier, U. Stalmach, H. Kolshorn *Acta Polym.* **1997**, 48, 379-384.

[9] F. Schindler, J. M. Lupton, J. Feldmann, U. Scherf *Proc. Natl. Acad. Sci. USA*. **2004**, 101, 14695-14700.

[10] D. A. Vanden Bout, W. T. Yip, D. Hu, D. K. Fu, T. M. Swager, P. F. Barbara *Science*. **1997**, 277, 1074-1077.

[11] K. Becker, E. Da Como, J. Feldmann, F. Scheliga, E. Thorn Csányi, S. Tretiak, J. M. Lupton *J. Phys. Chem. B*. **2008**, 112, 4859-4864.

[12] H.-J. Egelhaaf, J. Gierschner, D. Oelkrug *Synth. Met.* **1996**, 83, 221-226.

[13] J. Gierschner, M. Ehni, H.-J. Egelhaaf, B. M. Medina, D. Beljonne, H. Benmansour, G. C. Bazan *J. Chem. Phys.* **2005**, 123, 9.

[14] M. Bothe, G. Schmidt-Naake *Macromol. Rapid Commun.* **2003**, 24, 609-613.

[15] R. A. W. Johnstone, M. E. Rose *Tetrahedron*. **1979**, 35, 2169-2173.

[16] Z. Bao, Y. Chen, R. Cai, L. Yu *Macromolecules*. **1993**, 26, 5281-5286.

[17] D. A. M. Egbe, C. P. Roll, E. Birckner, U. W. Grummt, R. Stockmann, E. Klemm *Macromolecules*. **2002**, 35, 3825-3837.

[18] T. Maddux, W. J. Li, L. P. Yu *J. Am. Chem. Soc.* **1997**, 119, 844-845.

[19] J. R. Fries, L. Brand, C. Eggeling, M. Köllner, C. A. M. Seidel *J. Phys. Chem. A*. **1998**, 102, 6601-6613.

[20] R. E. Di Paolo, J. S. de Melo, J. Pina, H. D. Burrows, J. Morgado, A. L. Macanita *ChemPhysChem*. **2007**, 8, 2657-2664.

[21] J. A. Odell, A. Keller *J. Polym. Sci. Pt. B-Polym. Phys.* **1986**, 24, 1889-1916.

[22] M. Klessinger, J. Michl, Lichtabsorption und Photochemie organischer Moleküle, VCH, Weinheim, **1989**.

[23] F. C. Spano *Chem. Phys.* **2002**, 116, 5877-5891.

[24] T. Damerau, M. Hennecke *J. Chem. Phys.* **1995**, 103, 6232-6240.

[25] J. G. Rider, E. Hargreaves *J. Phys. D: Appl. Phys.* **1970**, 3, 993-1008.

[26] S. A. Jabarin *Polym. Eng. Sci.* **1991**, 31, 638-643.

[27] L. Horner *J. Makromol. Chem.* **1943**, 1, 234-246.

[28] A. Ajji, M. C. Renaud *J. Appl. Polym. Sci.* **1991**, 42, 335-345.

[29] Y. Shindo, B. E. Read, R. S. Stein *Macromol. Chem. Phys.* **1968**, 118, 272-&.

[30] B. Yalcin, M. Cakmak *J. Polym. Sci. Pt. B-Polym. Phys.* **2005**, 43, 724-742.

[31] M. E. R. Robinson, D. I. Bower, W. F. Maddams *J. Polym. Sci. Pt. B-Polym. Phys.* **1978**, 16, 2115-2138.

[32] H. S. Ozkan, T. Oskay, H. Y. Guney, H. Dirim *J. Polym. Sci. Pt. B-Polym. Phys.* **1994**, 32, 631-640.

[33] D. Toptygin *J. Fluoresc.* **2003**, 13, 201-219.

[34] M. Grandbois, M. Beyer, M. Rief, H. Clausen-Schaumann, H. E. Gaub *Science*. **1999**, 283, 1727-1730.

[35] L. Onsager *J. Am. Chem. Soc.* **1936**, 58, 1486-1493.

[36] C. N. R. Rao, S. Singh, V. P. Senthilnathan *Chem. Soc. Rev.* **1976**, 5, 297-316.

[37] J. Gierschner, H. G. Mack, L. Lüer, D. Oelkrug *J. Chem. Phys.* **2002**, 116, 8596-8609.

[38] B. R. Crenshaw, C. Weder *Adv. Mater.* **2005**, 17, 1471-1476.

[39] J. Widengren, V. Kudryavtsev, M. Antonik, S. Berger, M. Gerken, C. A. M. Seidel *Anal. Chem.* **2006**, 78, 2039-2050.

[40] A. Koslowski, M. E. Beck, W. Thiel *J. Comput. Chem.* **2003**, 24, 714-726.

[41] M. J. S. Dewar, E. G. Zoebisch, E. F. Healy, J. J. P. Stewart *J. Am. Chem. Soc.* **1985**, 107, 3902-3909.

7.1.1 Supporting Information

Supporting Information

Fluorophores as optical sensors for local forces

Stefan Marawske, Denis Dörr, Daniel Schmitz, Axel Koslowski, You Lu, Helmut Ritter*, Walter Thiel *, Claus A.M. Seidel* and Ralf Kühnemuth*

1) Synthesis

The oligo(paraphenylenevinylene)-type fluorophor **5** was synthesized in a stepwise procedure shown in *Scheme 1*. In a first step the double Horner-Wadsworth-Emmons reaction of the phosphonate ester **1** and the aldehyde **2** gave the bis(iodo)-compound **4**, which was subsequently reacted with 4-vinylbenzyl alcohol **3** in terms of a Heck reaction to form the wanted OPV5 diol **5**.[1]

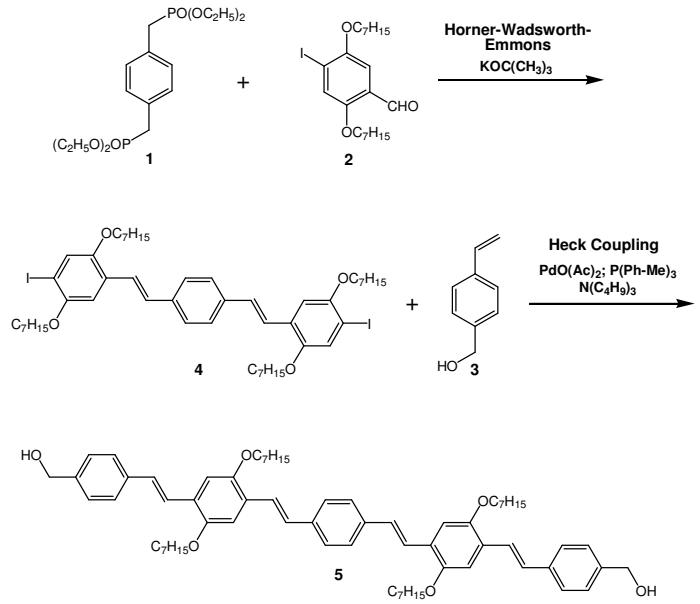

Scheme 1: Stepwise synthesis of the oligo(paraphenylenevinylene)-type fluorophor 5

The building blocks **1** to **3** were obtained as shown in *Scheme 2*. The phosphonate ester **1** was obtained in an Arbuzov-type reaction using 1,4-bis-(chloromethyl)benzene and triethyl phosphite as educts. Furthermore, hydroquinone, as a starting material, was etherified with 1-bromoheptane to generate 1,4-bis(heptyloxy)-benzene. The iodation of the ether gave 1,4-bis(iodo)-2,5-bis(heptyloxy)-benzene. On treatment with buthyllithium and subsequent addition of dimethylformamide building block **2** was formed. 4-Vinylbenzyl chloride was treated with sodium acetate to form 4-vinylbenzyl acetate. The following saponification gave 4-vinylbenzyl alcohol **3**. (Johnstone and Rose 1979; Bao, Chen et al. 1993; Egbe, Roll et al. 2002; Bothe and Schmidt-Naake 2003)

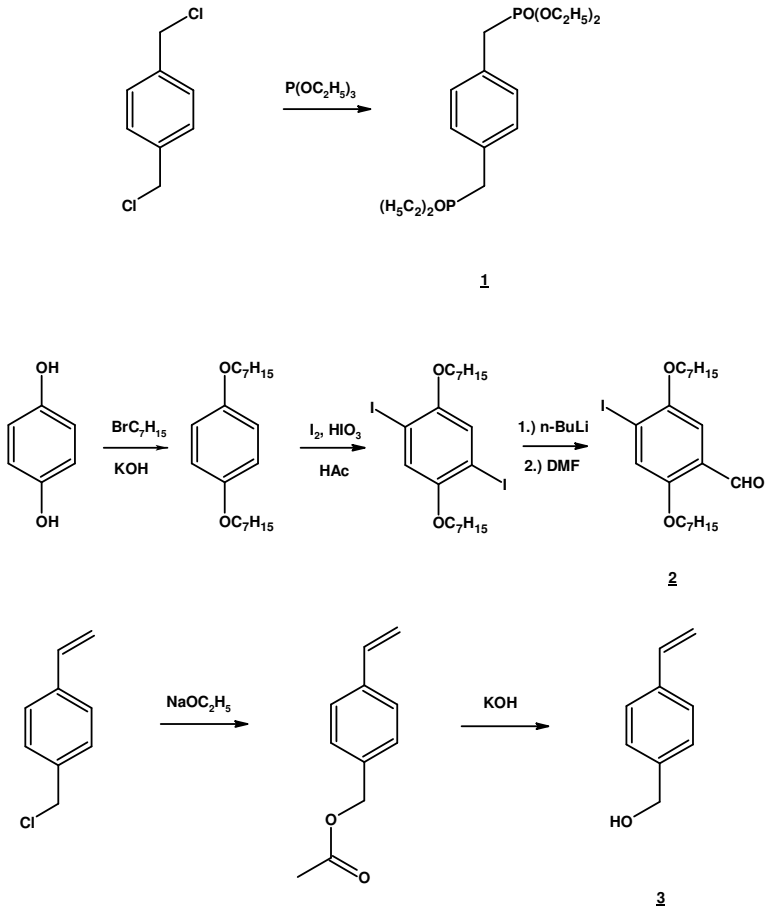

Scheme 2: **Synthesis of the monomeric buildingblocks 1 to 3**

Materials and Instruments

The chemical reagents were purchased from Acros or Aldrich Corp. and were used as received unless otherwise stated. All solvents were purified according to standard procedures. Column chromatography was performed on silica gel. NMR spectra were obtained on a Brucker Avance DRX 500 spectrometer at 500.13 MHz. MALDI-TOF MS measurements were performed on a Bruker Ultraflex TOF mass spectrometer.

Compounds

4-Formyl-1-iodo-2,5-bis(heptyloxy)benzene **2** and 4-vinylbenzyl alcohol **3** were synthesized according to literature proceedings.[2-4]

p-Xylylen-bis(diethyl)phosponate 1

A mixture of 1,4-bis(chloro-methyl)benzene (17.51 g, 0.1 mol) and triethyl phosphite (49.85 g, 0.3 mol) was slowly heated to 150-160°C. Simultaneously the emerging ethyl chloride was distilled off. After 4 hours of reaction time the mixture was heated to 180 °C and vacuum was applied for 1 hour to remove excessive triethyl phospite. After cooling to room temperature p-xylylen-bis(diethyl)-phosponate **1** was obtained in form of a colourless crystalline solid in quantitative yield.

^{1}H NMR (500 MHz, [D_1]$CHCl_3$, 25°C, TMS) δ= 1.17 (m, 12H, CH_3), 3.06 (d, 4H, CH_2), 3.94 (m, 8H, CH_2), 7.18 (s, 4H, CH)

Diiodo compound 4

A solution of 4-formyl-1-iodo-2,5-bis(heptyloxy)benzene **2** (4.60 g, 10 mmol) and p-xylylen-bis(diethyl)phosphonate **1** (1.89 g, 5 mmol) in dry toluene (20 mL) was heated to reflux under nitrogen atmosphere. In the course a suspension of potassium *tert*-butoxide (2.24 g, 20 mmol) in dry toluene was added bit by bit to the boiling solution. The mixture was refluxed for 3 hours under vigorous stirring. Subsequently hydrochloric acid (5%, 40 mL) was added. The organic phase was washed with water to neutrality and dried over magnesium sulfate. The solvent was removed under reduced pressure. The resulting pale yellow crystalline solid was purified by column chromatography using a 9 to 1 mixture of toluene and ethanol as an eluent. Yield 65%.

^{1}H NMR (500 MHz, [D_1]$CHCl_3$, 25°C, TMS) δ= 0.83 (m, 12H, CH_3), 1.26-1.32 (m, 16H, CH_2), 1.45 (m, 8H, CH_2), 1.78 (m, 8H, CH_2), 3.89-3.95 (m, 8H, CH_2), 6.96 (s, 2H, CH), 7.06 (d, 2H, CH), 7.21 (s, 2H, CH), 7.35 (d, 2H, CH), 7,43 (s, 2H, CH); MALDI-TOF MS: *m/z*: 991[M^+]

OPV diol 5

Under nitrogen atmosphere diiodo compound **4** (445 mg, 0.5 mmol), 4-vinylbenzyl alcohol **3** (135 mg, 1 mmol), tri(o-tolyl)phosphine (31 mg, 0.1 mmol) and palladium acetate (4.5 mg, 0.02 mmol) were solved under vigorous stirring in DMF (5 mL). Subsequently tributylamine (530 µL, 1.1 mmol) was added. The reaction mixture was heated to 80°C for 2 hours. The reaction mixture was cooled to room temperature and the product was precipitated in cold water, filtered off and dried. The resulting yellow crystalline solid was purified by column chromatography using a 95 to 5 mixture of chloroform and acetone as an eluent. Yield 45%.

^{1}H NMR (500 MHz, [D_8]THF, 25°C, TMS): δ = 0.81 (m, 12H, CH_3), 1.27-1.34 (m, 16H, CH_2), 1.48 (m, 8H, CH_2), 1.78 (m, 8H, CH_2), 3.99 (m, 8H, CH_2), 4.06 (m, 2H, OH), 4.46 (d, 4H, CH_2), 7.11- 7.22 (m, 12H, CH), 7.38-7.46 (m, 12H, CH); MALDI-TOF MS: *m/z*: 1003[M^+]

[1] M. Bothe, G. Schmidt-Naake, *Macromol. Rapid Commun.* **2003**, *24*, 609.
[2] R. A. W. Johnstone, M. E. Rose, *Tetrahedron* **1979**, *35*, 2169.
[3] Z. Bao, Y. Chen, R. Cai, L. Yu, *Macromolecules* **1993**, *26*, 5281.
[4] D. A. M. Egbe, C. P. Roll, E. Birckner, U. W. Grummt, R. Stockmann, E. Klemm, *Macromolecules* **2002**, *35*, 3825.

2) FORCE AND FLUORESCENCE EXPERIMENTS

The fluorescence and absorption spectra were measured with FluoroLog-3 (Jobin Yvon Horiba) and Cary-300 Bio (Varian), respectively. Time-correlated single photon counting (TCSPC) measurements were performed using a 5000 U (IBH) with a pulsed diode laser source at 471 nm (Picoquant).

2.1 The fluorescence quantum yield of OPV5 in THF

The fluorescence quantum yield of OPV5 (Φ_F(OPV5)) is determined with the help of Eq. 1(Lakowicz 1999),

$$\Phi_F(OPV5) = \Phi_F(Rh110)\frac{F_{opv5}\cdot E_{Rh110}\cdot n_{THF}^2}{F_{Rh110}\cdot E_{opv5}\cdot n_{water}^2} \quad (1)$$

where F is the integrated fluorescence intensity, E is the optical density, n_{THF}=1.407 and n_{water}=1.339. As a reference, Rhodamine 110 was used with a quantum yield of Φ_F(Rh110, EtOH) = 0.92 measured in EtOH.(Kubin and Fletcher 1982) From this the corresponding quantum yield in water was derived to Φ_F(Rh110, H_2O) = 0.95 (OPV5 was solved in THF whereas Rh110 was solved in water).
Given all this, the fluorescence quantum yield of OPV5 was calculated to Φ_F(OPV5) = 0.53±0.05.

2.2 Estimation of maximum force per polyvinylchloride molecule

With the molecular mass of PVC of M_n = 47000 g/mol and the density of ρ = 1.3927 g/cm³ the mean molecular volume can be calculated with Eq. 2,

$$V_{molec} = \frac{M_n}{\rho\cdot N_A} = 56.04 \text{ nm}^3 \quad (2)$$

where N_A is Avogadro's constant. As the molecular mass of a PVC monomer is M_n(mono) = 62.5 g/mol the average PVC molecule consists of around N_{mono} = 752 monomers.
The length of an average molecule can be estimated from Eq. 3,

$$L_{molec} = N_{mono}\cdot 2\cdot L_{C-C} * \sin(54.74°) = 189 \text{ nm} \quad (3)$$

where $L_{C\text{-}C}$ = 0.1541 nm is the typical length of a C-C bond.(1984) The corresponding mean cross section of the polymer chain is obtained by Eq. 4.

$$A_{molec} = \frac{V_{molec}}{L_{molec}} = 0.296 \text{ nm}^2 \quad (4)$$

Assuming a maximum mean tensile stress in our experiments of ca. 12 N/cm², we arrive at a maximum mean force on a single PVC molecule of F_{molec} = 3.55 pN.

This is only a mean value assuming a homogeneous force distribution in the substrate.

2.3 Estimation of the change of radiative lifetimes due to refractive index variations

Radiative lifetimes of excited states and energetic positions of ground and excited state are known to depend on the refractive index of the environment due to local electric fields acting on the molecular dipole moments. We first discuss the refractive index of PVC as a function of external strain (a), then estimate its influence on the optical properties of OPV5 in the limit of simple approximations (b, c) and finally summarize our results in tabular form (d):

(a) The index of refraction of the PVC matrix under tensile stress could not be measured in the thin foils directly. A rough estimation was performed using properties of stretched PVC from literature.
Using reported density changes from ρ = 1.3927 g/cm^3 at zero extension to ρ = 1.3937 g/cm^3 at 100% extension(Jabarin 1991) and applying the Lorentz-Lorenz equation:

$$n = \sqrt{\frac{M_w + 2\rho\, RD}{M_w - \rho\, RD}}; \qquad RD = \frac{M_w}{\rho}\frac{\left(n^2-1\right)}{\left(n^2+2\right)} \tag{5}$$

With the molecular weight M_w = 80000 g/mol we obtain a molar refraction of the polymer of RD = 17800 cm^3/mol. An initial index of refraction of n = 1.532(Horner 1943) would increase by $\Delta n = 4.6\text{x}10^{-4}$ upon stretching.
Birefringence of stressed PVC can exhibit much higher variations in n. For similar samples $\Delta n \approx 3.1\text{x}10^{-3}$ at 100% extension has been reported.(Rider and Hargreaves 1970; Jabarin 1991) Depending on the orientation of the chromophore inside the matrix this would be the upper limit for stress-induced refractive index variations that could affect the radiative lifetime.

(b) Changes in radiative lifetimes can be calculated according to Toptygin by a modified Strickler-Berg approach.(Toptygin 2003)
The empty spherical cavity model (ESC, Toptygin, eq. 59) was found to successfully describe radiative lifetimes of small fluorophores in solution:

$$k_r = \left(\tau_r\right)^{-1} = \left(\frac{3n^2}{2n^2+1}\right)^2 n\, k_{r,0} \tag{6a}$$

$$\frac{\tau_{r,2}}{\tau_{r,1}} = \left(\frac{n_1}{n_2}\right)^5 \left(\frac{2n_2^2+1}{2n_1^2+1}\right)^2$$

$$\Rightarrow \Delta\tau_r = \tau_{r,2} - \tau_{r,1} = \tau_{r,1}\left(\left(\frac{n_1}{n_2}\right)^5 \left(\frac{2n_2^2+1}{2n_1^2+1}\right)^2 - 1\right) \tag{6b}$$

$\tau_{r,1}$ and n_1 are radiative lifetime and index of refraction in the relaxed foil; $n_2 = n_1 + \Delta n$.
The empty ellipsoidal cavity model (EEC) yields a more appropriate description for chromophores deviating significantly from a spherical shape. In the limit of transition dipoles aligned along the long axis of the cavity radiative decay rates are directly proportional to n (Toptygin, eq. 63 with $L_\mu = 0$):

$$k_r = (\tau_r)^{-1} = n\,k_{r,0} \tag{7a}$$

$$\frac{\tau_{r,2}}{\tau_{r,1}} = \frac{n_1}{n_2}$$

$$\Rightarrow \Delta\tau_r = \tau_{r,2} - \tau_{r,1} = \tau_{r,1}\left(\frac{n_1}{n_2} - 1\right) \tag{7b}$$

(c) Solvatochromic shifts of the emission can be estimated using Onsager theory as extended by Mataga et al.:(Onsager 1936; Mataga, Kaifu et al. 1955; Mataga, Kaifu et al. 1956)

$$\nu = \nu_0 + const.\left(\frac{n^2 - 1}{2n^2 + 1}\right) \tag{8}$$

where ν is the emission frequency.
From the emission maximum of OPV5 in THF of 485.2 nm and in PVC of 491.6 nm and the respective indices of refraction of n_{THF} = 1.407 and n_{PVC} = 1.532 the equation yields ν_0 = 21968 cm^{-1} and const. = -6875 cm^{-1}. The value of the slope is within the range of other reported OPV derivatives (Gierschner, Mack et al. 2002).

(d) The fluorescence quantum yield of OPV5 in the relaxed PVC matrix, Φ_F(OPV5, PVC), was estimated from the measured yield in THF, Φ_F(OPV5, THF) = 0.53 (see also 2.1), by scaling the radiative decay rate using the empty spherical cavity model:

$$\Phi_F(OPV5, PVC) = \frac{\tau_{F,PVC}}{\tau_{r,PVC}}$$

$$\approx \frac{\tau_{F,PVC}}{\tau_{r,THF}\left(\frac{n_{THF}}{n_{PVC}}\right)^5\left(\frac{2n_{PVC}^2 + 1}{2n_{THF}^2 + 1}\right)^2} = \Phi_F(OPV5, THF)\frac{\tau_{F,PVC}}{\tau_{F,THF}}\left(\frac{n_{PVC}}{n_{THF}}\right)^5\left(\frac{2n_{THF}^2 + 1}{2n_{PVC}^2 + 1}\right)^2 \tag{9}$$

With n_{THF} = 1.407, n_{PVC} = 1.532, $\tau_{F,\,THF}$ = 0.781 ns and $\tau_{F,\,PVC}$ = 1.03 ns results Φ_F(OPV5, PVC) = 0.81. The corresponding radiative lifetimes are $\tau_{r,THF}$ = 1.47 ns and $\tau_{r,PVC}$ = 1.27 ns, respectively.

For n_{PVC} (0 N) = 1.532, $\tau_{r,OPV,PVC}$ (0 N) = 1.27 ns and Φ_F(OPV5, PVC) = 0.81 (0 N) the predicted changes in τ_r, τ_F and λ due to variations in n after stretching are:

Δn	$\Delta\tau_r$(ESC) [ps]	$\Delta\tau_r$(EEC) [ps]	$\Delta\tau_F$(ESC) [ps]	$\Delta\tau_F$(EEC) [ps]	$\Delta\lambda$ [nm]
4.6×10^{-4}	-0.64 (0.05%)	-0.38 (0.03%)	-0.42 (0.04%)	-0.25 (0.02%)	0.022
3.1×10^{-3}	-4.36 (0.34%)	-2.56 (0.20%)	-2.87 (0.28%)	-1.69 (0.16%)	0.146

Table 1: Influence of the refractive index on the radiative and fluorescence lifetime assuming different cavity models for OPV5

Since the OPV5 chromophore is neither spherically shaped nor infinitely extended, the best approximation probably lies between the solutions of the ESC and the EEC models.

Δn = 3.1x10^{-3} from birefringence measurements is an upper limit and probably overestimates the true condition in the polymer.

Corresponding results for Rhodamine123 with $\tau_{F,Rh123,H2O}$ = 3.95 ns, Φ_F(Rh123, H_2O) = 0.95 and $\tau_{F,Rh123,PVC}$ (0 N) = 3.12, giving $\tau_{r,Rh123,PVC}$ (0 N) = 3.24 ns and Φ_F(Rh123, PVC) = 0.96 (0 N):

Δn	$\Delta\tau_r$(ESC) [ps]	$\Delta\tau_F$(ESC) [ps]	$\Delta\lambda$ [nm]
4.6x10^{-4}	-1.59 (0.05%)	-1.47 (0.05%)	0.063
3.1x10^{-3}	-10.71 (0.33%)	-9.92 (0.32%)	0.42

Table 2: Influence of the refractive index on the radiative and fluorescence lifetime assuming different cavity models for Rh 123

2.4 Negative control with Rh123 stained PVC foil

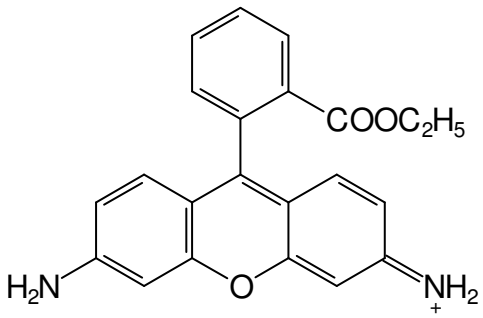

Scheme 3: Chemical structure of Rhodamine 123 (Rh 123)

The chromophore of Rhodamine 123 has a stiff molecular backbone and no significant external force-induced unwinding or deformation is expected under our experimental conditions. Therefore it can serve as a reference where possible lifetime effects or spectral shifts most likely are only induced by static interaction with the matrix, in particular by the local index of refraction. Experimental conditions and preparation of the foil are the same as mentioned before. Concentration of Rh 123 in PVC was also 100 nM.
As shown in Figure 1, the fluorescence anisotropy also correlates with the extension of the foil but much less pronounced than in the case of OPV5.
The fluorescence lifetime and the green to red signal ratio do not show any significant change dependant on the mean tensile stress within the statistical limits.

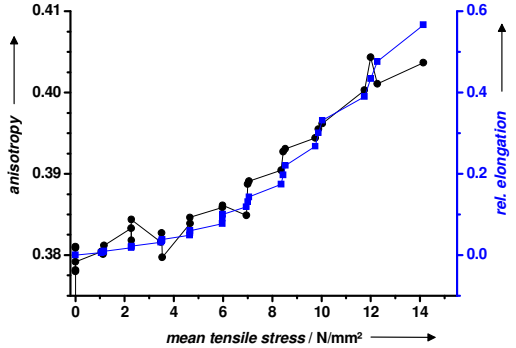

Figure 1: Relative elongation (blue) of the PVC foil and fluorescence anisotropy (black) of Rh 123 versus the mean tensile stress

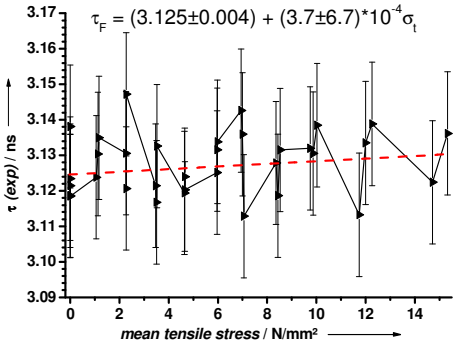

Figure 2. Fluorescence lifetime τ of Rh 123 vs. mean tensile stress with linear regression ($\Delta\tau_F$ = 4±8 ps at 12 N/mm^2).

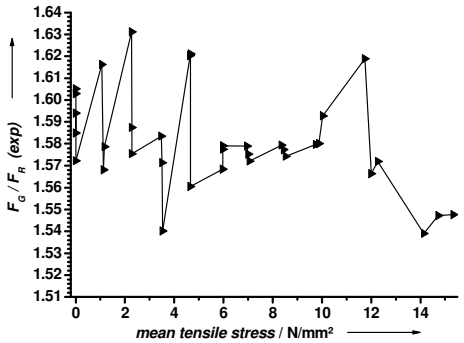

Figure 3a: Green to red ratio from experiment versus mean tensile stress for Rh 123

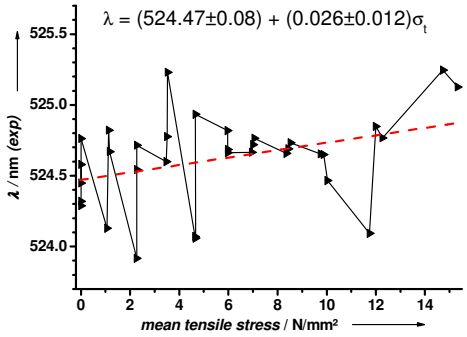

Figure 3b: Spectral position vs. mean tensile stress for Rh 123 with linear regression. ($\Delta\lambda$ = 0.31±0.14 nm at 12 N/mm^2)

2.5 Variations of the PVC matrix

In our experiments we observe different elasticities depending on the preparation condition of the foil.
(a) As a first example we present the extended results of the experiment already shown in the paper. As the tensile stage has a limited range of travel of 10mm, the foil was stretched in two steps. After the first pull the stage was returned to its starting position and the foil was readjusted for the second pull. After the first cycle the fluorescence lifetime (Figure 4) as well as the green to red intensity ratio (Figure 5) does not completely return to the initial values. After the second cycle both values almost return to the initial values. Here, the polymer molecules were already much more ordered in comparison to the unstretched foil, which results in a higher elasticity of the matrix.

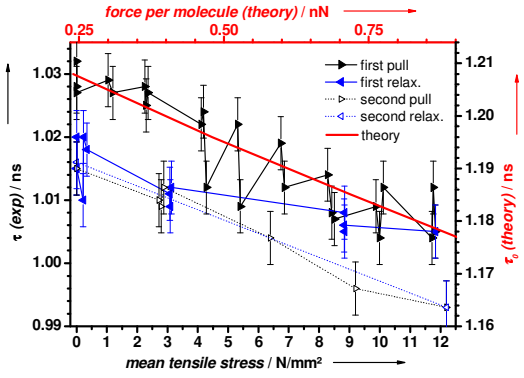

Figure 4: Comparison between fluorescence lifetime measurement and theory; the PVC foil was stretched in two steps (black) each with a relaxation (blue) afterwards; the fluorescence lifetime τ decreases with higher mean tensile stress, the statistical error of the lifetime fits was about 4 ps each; the maximum reduction is about 25 ps

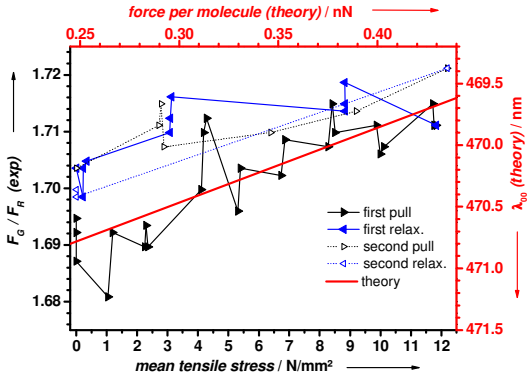

Figure 5: Green to red ratio from experiment versus mean tensile stress; the PVC foil was stretched in two steps (black) each with a relaxation (blue) afterwards

(b) As a second example we present a different type of measurement with less flexibility of the matrix although prepared under the same procedure as before. Here, a higher mean tensile stress was applied to the polymer matrix.
The anisotropy (Figure 6), the fluorescence lifetime (Figure 7) and the green to red intensity signal ratio (Figure 8) all show more pronounced effects as discussed before, but for all these parameters there is a plateau up to 14 N/mm² where there is nearly no change. This indicates that the polymer matrix is much stiffer and all the energy is needed at first to stretch the matrix before it is transferred to the fluorophores.

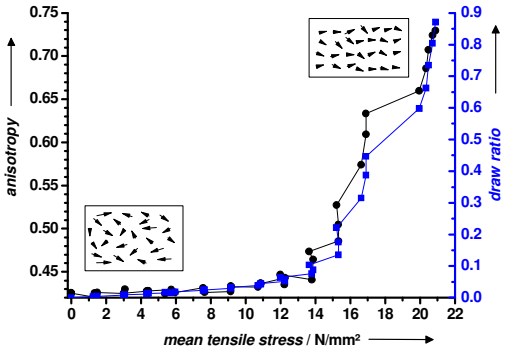

Figure 6: Relative elongation (blue) of the PVC foil and fluorescence anisotropy (black) of OPV5 versus the mean tensile stress

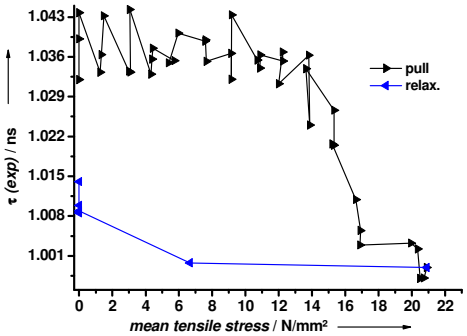

Figure 7: Fluorescence lifetime of OPV5 dependant on the mean tensile stress; a total lifetime change of 40 ps can be found.

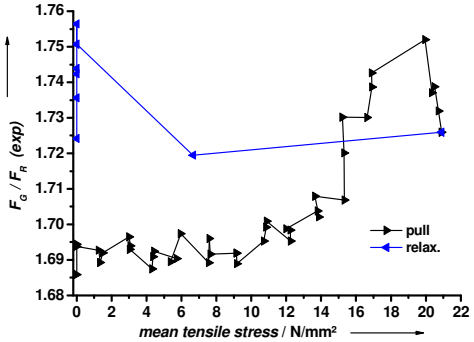

Figure 8: Green to red ratio from experiment versus mean tensile stress

2.6 Statistics

slope $\left[\frac{ns \cdot mm^2}{N}\right]$	error
-1.9×10^{-3}	1.4×10^{-4}
-2.1×10^{-3}	2.1×10^{-4}
-1.7×10^{-3}	2.4×10^{-4}
-2.8×10^{-3}	2.7×10^{-4}
-2.2×10^{-3}	2.6×10^{-4}
average	std
-2.14×10^{-3}	4.0×10^{-4}

Table 3: From different measurements the slope of the linear decreasing lifetime (e.g. see Figure 7) dependant on the mean tensile stress was fitted by linear regression.

2.7 Sample heterogeneity

To characterize spatial heterogeneity the intensity distribution for pixels in a single scan of an OPV5-doped foil was analyzed. From comparison of the width of the fitted gaussian of 25.5±0.5 with the shot-noise according to a mean number of 285 of $(285)^{0.5}$ = 16.9 we find a mean number of fluorophores per detection volume element of N ≈ (25.5^2 - 16.9^2) = 365 as being responsible for the additional broadening of the distribution.

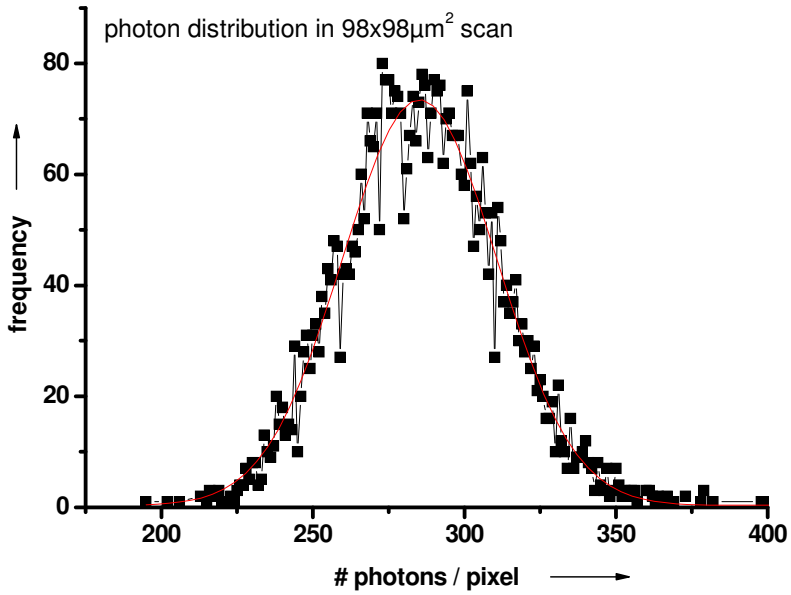

Figure 9: Photon distribution for single scan of OPV5-doped PVC foil with fitted gaussian (center $x_c = 285$, $\sigma = 25.5$

[5] J. R. Lakowicz, *Principles of Fluorescence Spectroscopy*, Kluwer Academic/ Plenum Publishers, New York, **1999**.

[6] R. F. Kubin, A. N. Fletcher, *J. Lumines.* **1982**, *27*, 455.

[7] Handbook of Chemistry and Physics, 65th ed. (Ed.: R. C. Weast), CRC Press, Inc., Boca Raton, Fl, **1984**.

[8] S. A. Jabarin, *Polym. Eng. Sci.* **1991**, *31*, 638.

[9] L. Horner, *J. Makromol. Chem.* **1943**, *1*, 234.

[10] J. G. Rider, E. Hargreaves, *J. Phys. D: Appl. Phys.* **1970**, *3*, 993.

[11] D. Toptygin, *J. Fluoresc.* **2003**, *13*, 201.

[12] L. Onsager, *J. Am. Chem. Soc.* **1936**, *58*, 1486.

[13] N. Mataga, Y. Kaifu, M. Koizumi, *Bull. Chem. Soc. Jpn.* **1955**, *28*, 690.

[14] N. Mataga, Y. Kaifu, M. Koizumi, *Bull. Chem. Soc. Jpn.* **1956**, *29*, 465.

[15] J. Gierschner, H. G. Mack, L. Lüer, D. Oelkrug, *J. Chem. Phys.* **2002**, *116*, 8596.

3) THEORETICAL CALCULATIONS

In view of its size, the OPV5 chromophore was described by semiempirical methods. The theoretical study involved the selection of the most suitable semiempirical model, computation of ground-state potential curves for elongation of the chromophore, reoptimization of the resulting geometries in the first excited singlet state using multi-reference configuration interaction (MR-CI) methods(Koslowski, Beck et al. 2003), and calculation of spectral properties at this level.

Evaluation of the semiempirical methods

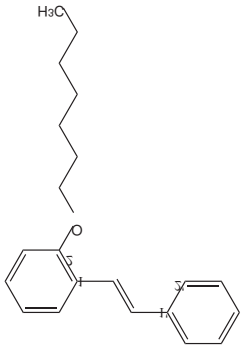

Scheme 4: Numbering of atoms in Heptoxystilbene.

To evaluate the performance of semiempirical methods, geometry optimizations and frequency analyses were carried out for three small model compounds at standard semiempirical, density functional, and ab initio levels.
The results for *E*-stilbene are listed in Table 4. All applied methods agree that the potential energy surface of this molecule is very flat (very low frequencies) with respect to the torsion of the phenyl rings against the plane of the central double bond. B3LYP, PM3 and SCC-DFTB predict a C_{2h} symmetric planar minimum, in contrast to the other methods listed in the table, for which the C_{2h} structure represents a second-order transition state and the minima have C_2 and C_i symmetry. The relative energies of these conformers are all very close (less than 1 kcal/mol in all cases).
Table 5 shows the results for phenetole (ethoxybenzene). In this case two C_2 conformations were considered, one with the side chain heavy atoms lying within the plane of the aromatic ring, and the other one with these atoms forming a plane orthogonal to the ring plane. All applied methods agree that the in-plane side chain conformation corresponds to a local minimum which has a lower energy than the out-of-plane side chain conformation. According to HF/6-31G**, the latter conformation is also a local minimum, in contrast to the other methods, which give a first-order saddle point.
In Table 6, stable conformations of heptoxystilbene (see Scheme 4) computed with various methods are listed. All applied methods except PM3 result in two conformers with an all-staggered side chain, one with the side chain heavy atoms being approximately coplanar to the adjacent aromatic ring, and the other one with these atoms forming a plane essentially perpendicular to the ring plane. For these methods except OM3, the conformer with the in-plane side chain is more stable. The planes of the aromatic rings and of the central double bond do not coincide. With PM3, we have found two conformers with the side chain pointing out of the plane of the adjacent aromatic ring, being tilted towards the second ring.

Method	Symmetry	Structure	Relative Energy kcal/mol	Dihedral Angle Deg	Lowest Vibrations cm^{-1}	
HF/6-31G**	C_2	minimum	0.00	24.0	A	30
	C_i	minimum	0.24	19.2	A_u	16
	C_{2h}	second-order saddle point	0.36	0.0	B_g A_u	-63 -25
MP2/6-31G**	C_2	minimum	0.00	26.7	A	36
	C_i	minimum	0.18	25.7	A_u	28
	C_{2h}	second-order saddle point	0.74	0.0	B_g A_u	-116 -32
B3LYP/6-31G**	C_{2h}	minimum		0.0	A_u A_u B_g B_u	7 60 68 82
B3LYP/cc-pVTZ	C_{2h}	minimum		0.0	A_u A_u B_g B_u	3 58 65 80
AM1	C_2	minimum	0.00	22.9	A	24
	C_i	minimum	0.09	20.7	A_u	17
	C_{2h}	second-order saddle point	0.21	0.0	B_g A_u	-61 -20
PM3	C_{2h}	minimum		0.0	A_u A_u B_u B_g	31 56 99 101
OM2	C_2	minimum	0.00	31.6	A	24
	C_i	minimum	0.21	28.4	A_u	16
	C_{2h}	second-order saddle point	0.42	0.0	B_g A_u	-56 -20
OM3	C_2	minimum	0.00	30.2	A	20
	C_i	minimum	0.15	25.9	A_u	12
	C_{2h}	second-order saddle point	0.25	0.0	B_g A_u	-41 -16
SCC-DFTB	C_{2h}	minimum		0.0	A_u A_u B_u B_g	27 54 85 95

Table 4: Structures and lowest vibrations of E-stilbene calculated with various methods.

Method	In-plane side chain			Out-of-plane side chain		
	Rel. Energy kcal/mol	Lowest Vibration cm^{-1}		Rel. Energy kcal/mol	Lowest Vibration cm^{-1}	
HF/6-31G**	0.00	A"	60	1.19	A"	43
MP2/6-31G**	0.00	A"	59	2.05	A"	-14
B3LYP/6-31G**	0.00	A"	63	2.87	A"	-35
AM1	0.00	A"	38	1.49	A"	-55
PM3	0.00	A"	34	0.86	A"	-55
OM3	0.00	A"	33	0.39	A"	-48

Table 5: Relative energies and lowest vibrations of C_ss of phenetole (ethoxybenzene) calculated with various methods.

Method	Rel. Energy kcal/mol	Dihedral Angles (deg) 1- -2-O-C	2-O-C-C	2--1-C=C	C=C-1'- -2'
HF/6-31G**	0.00	-179.7	180.0	149.7	-22.3
	0.47	-92.6	179.8	150.8	-22.3
B3LYP/6-31G**	0.00	-178.7	-179.0	163.4	-8.0
	2.27	-95.1	-178.4	162.6	-9.7
AM1	0.00	-179.7	179.8	159.5	-21.0
	1.13	-83.7	178.5	158.1	-22.2
PM3	0.00	-74.9	129.5	168.5	10.8
	0.00	-78.9	122.0	157.2	33.0
OM3	0.00	-97.0	-178.8	152.9	-26.2
	0.21	-173.5	176.6	157.2	-25.7

Table 6: Relative energies and geometric parameters of stable heptoxystilbene structures calculated with various methods. In the notation for the dihedral angles, –, =, and - - denote single, double, and aromatic bonds, respectively.

Ground-state optimizations and vertical excitations of OPV5

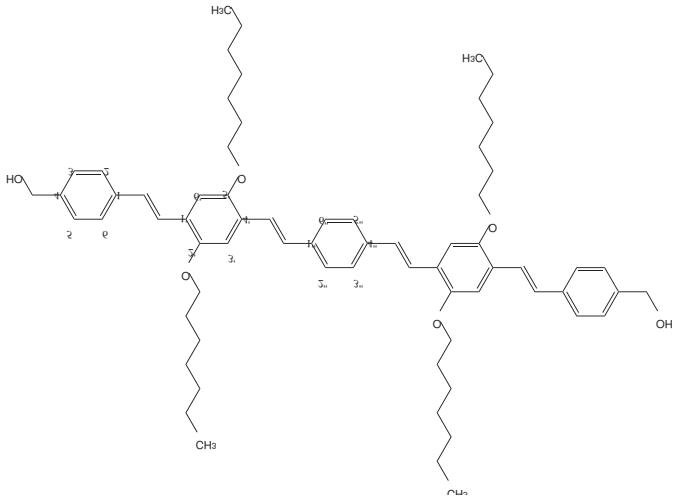

Scheme 5: Numbering of atoms in OPV5.

Geometry optimizations were performed on two conformers of OPV5 in the ground state at the AM1/SCF level, one in C_2 symmetry (with the C_2 axis perpendicular to the central aromatic ring) and the other one in C_i symmetry. Both conformers carry hydroxymethyl end groups and are local minima according to frequency analysis. After the initial full optimizations the distance r_{AB} of the outermost ring carbons was increased in steps of 0.1 Å or 0.2 Å and fixed during subsequent partial geometry optimizations. In Figure 10, the resulting relative energies of the elongated conformers and the corresponding forces are plotted against the distance of the outermost ring carbons. Forces were computed by analytical differentiation of a cubic-spline fit of the computed potential curves. It is obvious from Figure 10 that both conformers show essentially the same harmonic behavior upon elongation.

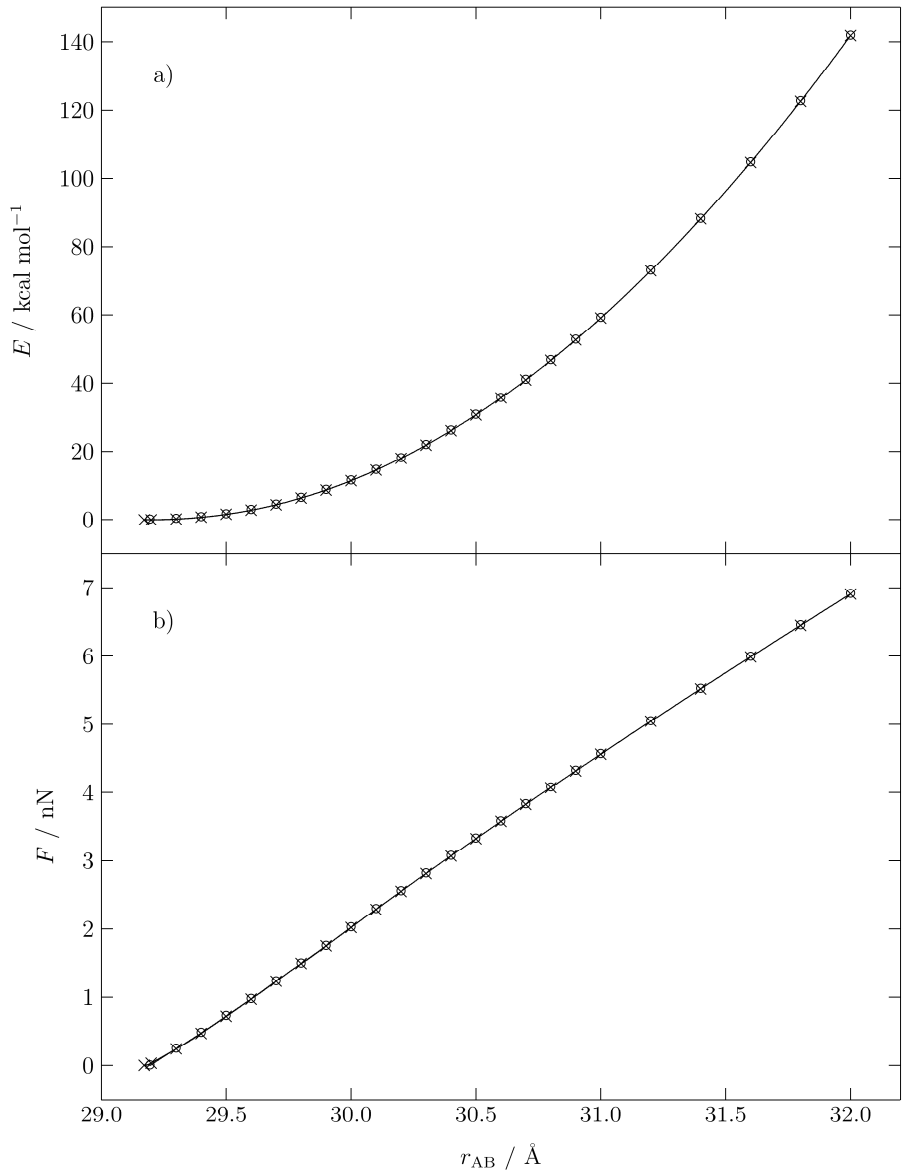

Figure 10: a) Ground-state potential curves and b) corresponding forces for stretching the OPV5 chromophore. × C_2 conformer, ◦ C_i conformer.

The geometries resulting from the ground state optimizations were used to compute the properties of the vertical excitation into the first excited state. A comparison of the performance of different CI expansions using the same geometry is shown in Table 7. Table 8 gives an overview over the computed data. The force F has been converted to nN using the following formula, where $N_A = 6.022142 \cdot 10^{23}$ mol^{-1} is Avogadro's constant.

$$\frac{1kcal\,mol^{-1} \cdot 4184\ J\,kcal^{-1}}{1\mathring{A} \cdot N_A} = \frac{1kcal\,mol^{-1} \cdot 4184\ J\,kcal^{-1}}{10^{-10}m \cdot 6.022142 \cdot 10^{23}mol^{-1}} = 6.947694 \cdot 10^{-11}N$$

Table 9 shows the changes of selected geometric parameters upon elongation of the C_i conformer. The non-planarity of the main chain near the minimum is essentially lost during stretching.

		CISDT	MR-CISD 10 Refs[1]	MR-CISD 4 Refs[2]	CIS
Ground state	SCF configuration	84.0%	84.1%	84.2%	100%
First excited state	HOMO→LUMO	49.2%	53.6%	53.4%	53.7%
	HOMO-1→LUMO+1	19.8%	20.1%	21.9%	23.4%
	HOMO-2→LUMO+2	5.3%	5.5%	5.5%	8.5%
Exitation energy	eV	3.00	3.11	3.14	2.87
Oscillator strength	f_{rp}	2.39	2.54	2.58	2.43
Number of CSFs		386169	139305	70185	145
CPU time (SP En. + Grad)	s (3.0 GHz Opteron)	651	165	94	41

Table 7: Comparison of calculated excited-state properties (vertical excitation) for the ground state minimum of the Ci conformer using different CI expansions with the 12 energetically highest doubly occupied and the 12 energetically lowest unoccupied molecular orbitals in the active space. [1] 1References are the ground configuration and nine singly excited configurations involving the orbitals HOMO–2 through LUMO+2; [2] References are the ground configuration and the three singly excited configurations mentioned in the table.

Distance r_{AB} Å	Relative Energies kcal/mol	Force nN	First transition eV	First transition cm^{-1}	Oscillator strength f_{rp}
29.195	0.000	0	3.11	25084	2.541
29.300	0.190	0.24	3.098	24987	2.565
29.400	0.700	0.48	3.081	24851	2.596
29.500	1.570	0.72	3.068	24743	2.622
29.600	2.790	0.97	3.056	24651	2.646
29.700	4.370	1.23	3.048	24588	2.67
29.800	6.340	1.49	3.049	24590	2.681
29.900	8.670	1.75	3.043	24542	2.713
30.000	11.390	2.02	3.052	24620	2.72
30.100	14.490	2.29	3.062	24699	2.726
30.200	17.980	2.55	3.072	24782	2.732
30.300	21.840	2.81	3.082	24860	2.737
30.400	26.080	3.07	3.092	24942	2.741
30.500	30.680	3.33	3.102	25024	2.745
30.600	35.650	3.58	3.113	25108	2.749
30.700	40.980	3.83	3.123	25193	2.752
30.800	46.670	4.07	3.134	25278	2.754
30.900	52.710	4.32	3.145	25364	2.756
31.000	59.100	4.56	3.156	25455	2.757
31.200	72.930	5.04	3.178	25635	2.756
31.400	88.140	5.52	3.202	25827	2.754
31.600	104.710	5.99	3.226	26024	2.746
31.800	122.610	6.45	3.252	26234	2.736
32.000	141.840	6.91	3.28	26452	2.72

Table 8: Relative energies, forces (AM1/SCF) and vertical transition properties (AM1/MR-CISD with 10 reference occupations and 12 doubly occupied and 12 unoccupied molecular orbitals in the active space) for stretching the C_i conformer of OPV5.

r_{AB}	1-C	3--4--5	1-C=C	6=1-C=C	C=C-1'--6'	3'--4'-C=C	C=C-1"--6"
Å	Å	deg	deg	deg	deg	deg	deg
29.195	1.453	119.4	124.6	19.9	22.2	-22.7	-19.7
29.300	1.454	119.0	125.2	18.0	21.9	-20.9	-17.1
29.400	1.456	118.6	125.8	14.3	20.3	-19.1	-14.4
29.500	1.457	118.2	126.4	11.4	18.6	-17.4	-10.6
29.600	1.459	117.8	126.9	7.8	16.8	-15.0	-7.5
29.700	1.461	117.4	127.4	5.1	13.6	-12.7	-2.1
29.800	1.463	117.0	127.9	5.4	11.7	-10.4	-1.3
29.900	1.465	116.6	128.3	2.7	1.0	2.5	-1.7
30.000	1.468	116.2	128.8	2.4	0.6	1.8	-1.6
30.100	1.470	115.8	129.3	2.3	0.3	1.4	-1.5
30.200	1.472	115.4	129.8	2.0	-0.2	1.1	-1.5
30.300	1.475	115.0	130.2	1.8	-0.4	1.2	-1.4
30.400	1.477	114.6	130.7	1.6	-0.7	1.1	-1.4
30.500	1.480	114.2	131.2	1.5	-1.0	1.1	-1.3
30.600	1.483	113.8	131.6	1.3	-1.3	1.2	-1.3
30.700	1.486	113.4	132.1	1.1	-1.5	1.2	-1.3
30.800	1.488	113.0	132.5	1.0	-1.8	1.2	-1.4
30.900	1.491	112.6	133.0	0.9	-2.1	1.3	-1.4
31.000	1.494	112.3	133.4	0.7	-2.3	1.4	-1.4
31.200	1.501	111.5	134.3	0.5	-2.8	1.5	-1.5
31.400	1.507	110.8	135.1	0.4	-3.3	1.7	-1.6
31.600	1.514	110.1	136.0	0.3	-3.8	2.0	-1.7
31.800	1.521	109.4	136.8	0.3	-4.4	2.3	-1.8
32.000	1.529	108.7	137.5	0.3	-4.9	2.7	-1.9

Table 9: Change of selected structural parameters (bond lengths, bond angles and dihedral angles) on stretching the C_i conformer of OPV5. In the notation for the dihedral angles, –, =, and --denote single, double, and aromatic bonds, respectively.

Excited-state optimizations and fluorescence lifetimes

The geometries of both OPV5 conformers were reoptimized in the first excited singlet state using the same constraints as before for the distance of the outermost ring carbons. The excited state was described by an MR-CI expansion with single and double substitutions relative to ten reference configurations (closed-shell ground-state and nine singly excited configurations involving the orbitals HOMO − 2 through LUMO + 2); the active space included 12 doubly occupied and 12 unoccupied molecular orbitals. Spectral properties were computed at the optimized (nearly planar) excited-state geometries, in particular the radiative lifetime τ (in s) of the first excited state:(Klessinger and Michl 1989)

$$\tau = \frac{3}{2 f \tilde{\nu}^2}$$

where f is the oscillator strength and $\tilde{\nu}$ is the wavenumber (in cm^{-1}) for emission (fluorescence). Table 10 lists the calculated emission energies, oscillator strengths, and fluorescence lifetimes of the C_i conformer as a function of the distance, and Figure 11 shows the corresponding graphs for both conformers. The results for the two conformers are again essentially the same, as expected. The computed fluorescence lifetimes show a marked

decrease upon elongation which is mostly caused by the increase in the calculated emission energies (see formula above).

Distance r_{AB} Å	Relative Energies kcal/mol	Force nN	Emission Energy eV	Emission Energy cm^{-1}	Oscillator Strength f_{rp}	Lifetime ns
29.2	0.00	0.00	2.633	21236	2.731	1.218
29.3	0.06	0.15	2.633	21239	2.753	1.208
29.4	0.50	0.45	2.641	21305	2.763	1.196
29.5	1.35	0.74	2.649	21369	2.772	1.185
29.6	2.62	1.02	2.657	21432	2.781	1.174
29.7	4.30	1.31	2.665	21494	2.789	1.164
29.8	6.38	1.58	2.672	21554	2.797	1.154
29.9	8.85	1.86	2.680	21614	2.804	1.145
30.0	11.72	2.12	2.687	21672	2.811	1.136
30.1	14.97	2.39	2.694	21730	2.818	1.127
30.2	18.60	2.65	2.701	21787	2.824	1.119
30.3	22.60	2.91	2.708	21843	2.829	1.111
30.4	26.98	3.17	2.715	21899	2.834	1.104
30.5	31.73	3.43	2.722	21955	2.838	1.097
30.6	36.85	3.68	2.729	22010	2.841	1.09
30.7	42.32	3.93	2.736	22065	2.844	1.083
30.8	48.16	4.18	2.742	22121	2.846	1.077
30.9	54.35	4.43	2.749	22176	2.848	1.071
31.0	60.90	4.67	2.756	22232	2.848	1.066
31.2	75.05	5.16	2.770	22345	2.847	1.055
31.4	90.60	5.64	2.785	22462	2.842	1.046
31.6	107.53	6.12	2.800	22582	2.833	1.038
31.8	125.83	6.59	2.815	22709	2.821	1.031
32.0	145.49	7.06	2.832	22843	2.803	1.025

Table 10: Potential curve, forces, optical properties, and fluorescence lifetimes of the Ci symmetric conformere of OPV5 after geometry optimization in the first excited state (AM1/MR-CISD with 10 reference occupations and 12 doubly occupied and 12 unoccupied molecular orbitals in the active space).

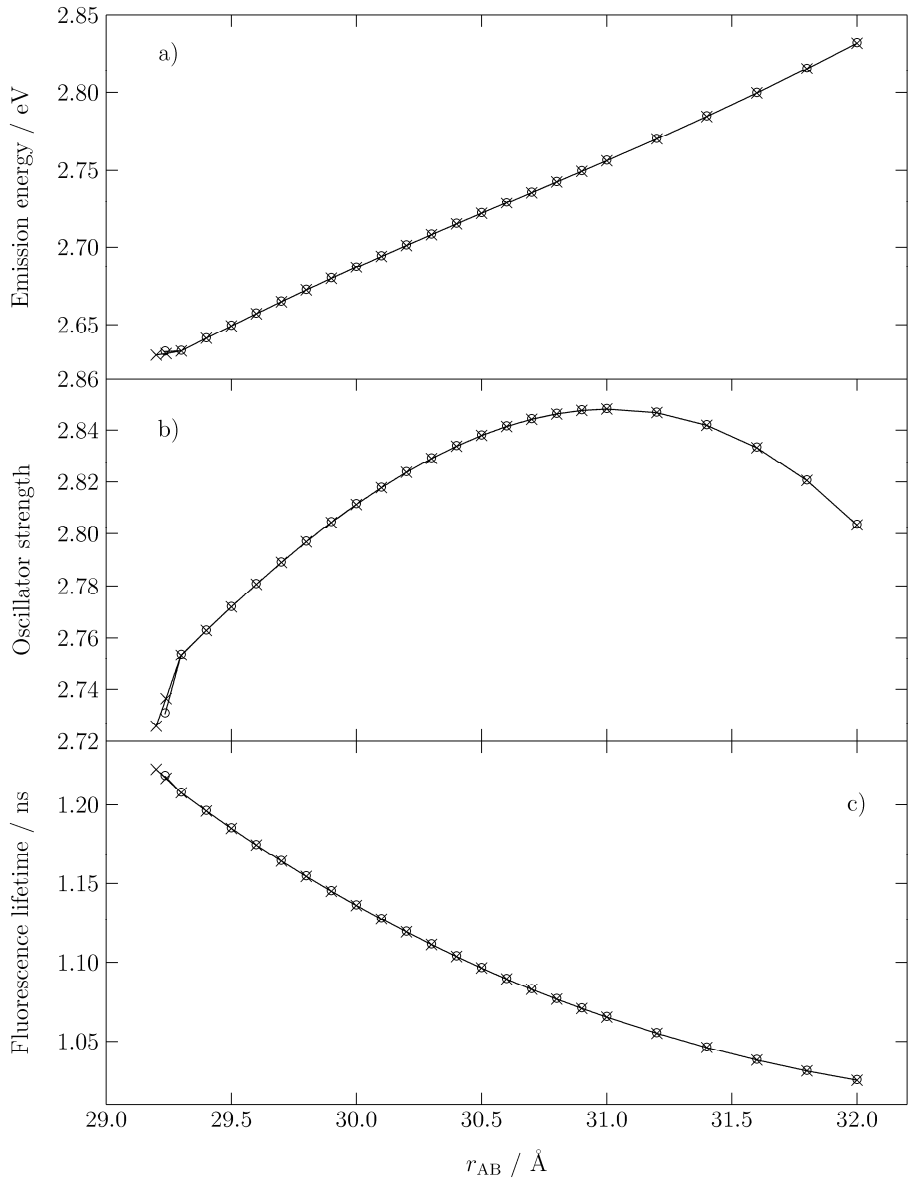

Figure 11: a) Emission energies, b) oscillator strengths, and c) fluorescence lifetimes after geometry optimization in the first excited state of OPV5 for C_2 and C_i symmetry.

8 Appendix

8.1 Unspecific immobilisation of biomolecules

The preparation steps 1 to 3 are the same as described in section 6.2.

4. PEGilation of surfaces
   - incubation of coverglasses with 2mM Epoxy-PEG-COOH in chloroform with triethylamine; coverglasses should be sandwiched
   - cleaning of the coverglasses with dichlormethane
   - thoroughly washing of coverglasses in ddH_2O
   - drying of coverglasses under nitrogen gas

5. Derivatisation with NHS
   - incubation of coverglasses with 100mM DSC and 100mM DMAP in DMF for 6h
   - thoroughly washing of coverglasses in dichlormethane
   - drying of coverglasses under nitrogen gas

6. Addition of untagged biomolecules

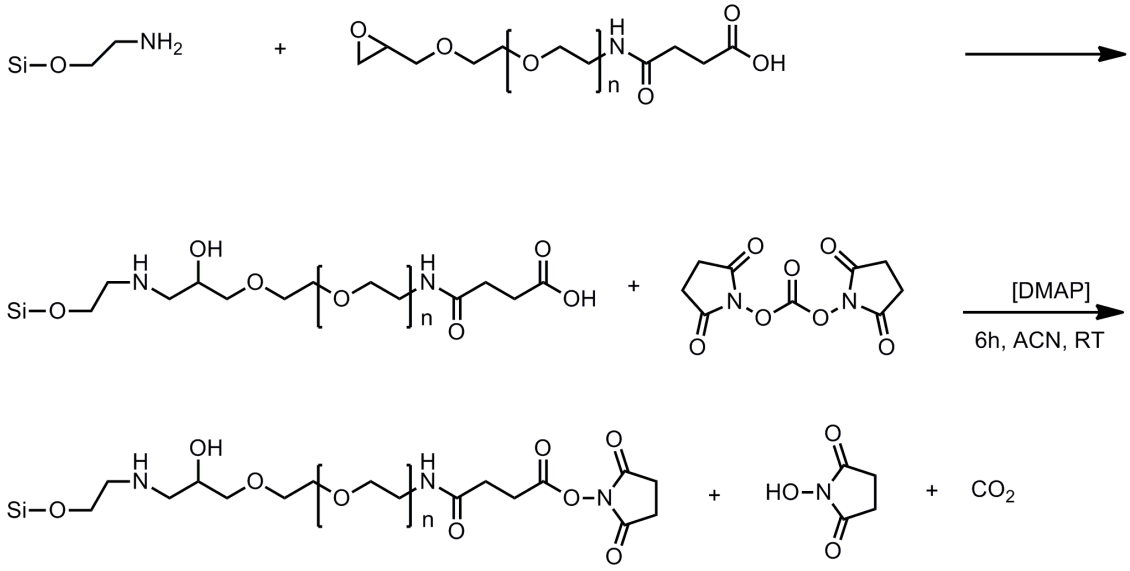

Figure 81 Reaction scheme of surface preparation for unspecific immobilisation of biomolecules

8.2 Immobilisation of His-tagged biomolecules

The preparation steps 1. to 5. are the same as described in section **Error! Reference source not found.**.

The synthesis protocol was adapted from (Cha, Guo et al. 2004).

6. Derivatisation with diethyliminodiacetat (DEIDA)
   - incubation of coverglasses with 200mM DEIDA and 100mM DMAP in acetonenitrile over night at RT
   - thoroughly washing of coverglasses in dichlormethane
   - drying of coverglasses under nitrogen gas

7. Deprotection of DEIDA
   - incubation of coverglasses with 100mM Bis(tributylzinn)oxide (BBTO) in diethylether for 6h at RT
   - thoroughly washing of coverglasses in diethylether, diluted HCL (pH 4) and acetone
   - drying of coverglasses under nitrogen gas

8. Activation with Cu^{2+}
   - incubation of coverglasses with 2mM CuSO4 in ethanole for 20min
   - thoroughly washing of coverglasses in ddH_2O
   - drying of coverglasses under nitrogen gas

9. Addition of His-tagged biomolecules

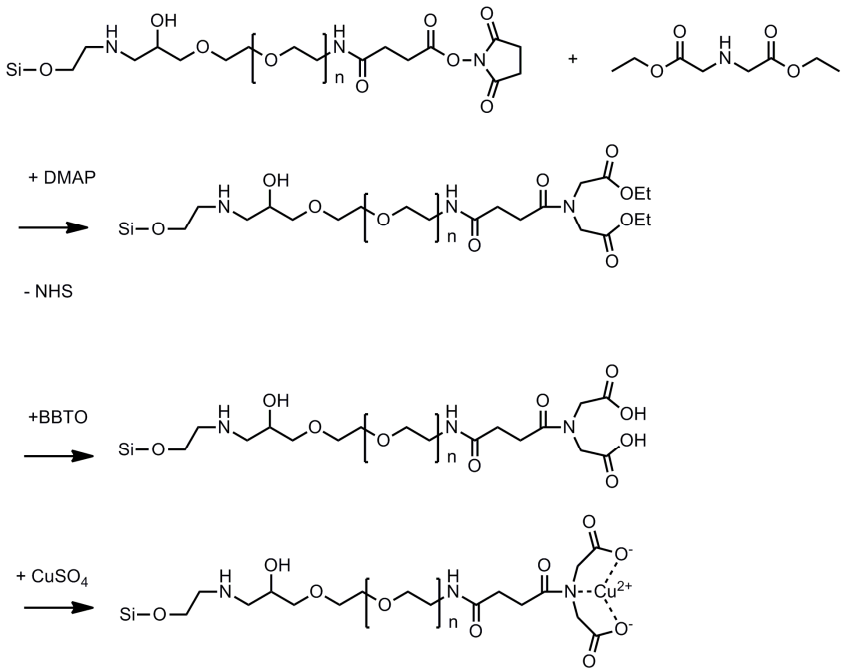

Figure 82 Reaction scheme of surface preparation to immobilise His-tagged biomolecules

9 Bibliography

(1984). CRC Handbook of Chemistry and Physics. R. C. Weast. Boca Raton, Fl, CRC Press, Inc.

Ajji, A. and M. C. Renaud (1991). "Mechanical properties of oriented poly(vinyl chloride) poly(caprolactone) blends." Journal of Applied Polymer Science **42**(2): 335-345.

Armitage, B. A. (2005). Cyanine dye-DNA interactions: Intercalation, groove binding, and aggregation. DNA Binders and Related Subjects. M. J. Waring and J. B. Chaires. Berlin, Springer-Verlag Berlin. **253:** 55-76.

Atkins, P. W. and J. de Paula (2001). Atkins' Physical Chemistry. Oxford, U.K., Oxford University Press.

Atto-Tec. (2011). "Fluorescence properties of Atto 647N." from https://www.atto-tec.com/attotecshop/product_info.php?info=p114_ATTO-647N.html&XTCsid=ucvoaehx.

Axelrod, D., T. P. Burghardt, et al. (1984). "Total internal-reflection fluorescence." Annual Review of Biophysics and Bioengineering **13**: 247-268.

Bao, Z., Y. Chen, et al. (1993). "Conjugated liquid-crystalline polymers - soluble and fusible poly(phenylenevinylene) by the Heck coupling reaction." Macromolecules **26**(20): 5281-5286.

Barbieri, B. (2010). "A short history of fluorescence." 2011, from http://www.fluorescence-foundation.org/lectures/madrid2010/lecture1.pdf.

Becker, K., E. Da Como, et al. (2008). "How chromophore shape determines the spectroscopy of phenylene-vinylenes: Origin of spectral broadening in the absence of aggregation." Journal of Physical Chemistry B **112**(16): 4859-4864.

Benesch, R. E. and R. Benesch (1953). "Enzymatic removal of oxygen for polarography and related methods." Science **118**(3068): 447-448.

Betzig, E., G. H. Patterson, et al. (2006). "Imaging intracellular fluorescent proteins at nanometer resolution." Science **313**(5793): 1642-1645.

Blom, H. (2010). Private discussions.

Bobroff, N. (1986). "Position measurement with a resolution and noise-limited instrument." Review of Scientific Instruments **57**(6): 1152-1157.

Born, M. and E. Wolf (1980). Principles of Optics, Cambridge University Press.

Bothe, M. and G. Schmidt-Naake (2003). "An improved catalytic method for alkoxyamine synthesis - Functionalized and biradical initiators for nitroxide-mediated radical polymerization." Macromolecular Rapid Communications **24**(10): 609-613.

Cha, T., A. Guo, et al. (2004). "Immobilization of oriented protein molecules on poly(ethylene glycol)-coated Si(111)." Proteomics **4**(7): 1965-1976.

Cheezum, M. K., W. F. Walker, et al. (2001). "Quantitative comparison of algorithms for tracking single fluorescent particles." Biophysical Journal **81**(4): 2378-2388.

Clegg, R. M. (1992). "Fluorescence resonance energy transfer and nucleic acids." Methods in Enzymology **211**: 353-388.

Condon, E. (1926). "A Theory of Intensity Distribution in Band Systems." Physical Review **28**(6): 1182.

Crenshaw, B. R. and C. Weder (2005). "Phase separation of excimer-forming fluorescent dyes and amorphous polymers: A versatile mechanism for sensor applications." Advanced Materials **17**(12): 1471-1476.

Damerau, T. and M. Hennecke (1995). "Determination of orientational order parameters of uniaxial films with a commercial 90-degrees angle fluorescence spectrometer." Journal of Chemical Physics **103**(14): 6232-6240.

Dewar, M. J. S., E. G. Zoebisch, et al. (1985). "Development and use of quantum mechanical molecular models. 76. AM1: a new general purpose quantum mechanical molecular model." Journal of the American Chemical Society **107**(13): 3902-3909.

Di Paolo, R. E., J. S. de Melo, et al. (2007). "Conformational relaxation of p-phenylenevinylene trimers in solution studied by picosecond time-resolved fluorescence." Chemphyschem **8**(18): 2657-2664.

Diez, M., B. Zimmermann, et al. (2004). "Proton-powered subunit rotation in single membrane-bound F0F1-ATP synthase." Nature Structural & Molecular Biology **11**(2): 135-141.

Dörr, D. (2011). Private discussions.

Egbe, D. A. M., C. P. Roll, et al. (2002). "Side Chain Effects in Hybrid PPV/PPE Polymers." Macromolecules **35**(10): 3825-3837.

Egelhaaf, H.-J., J. Gierschner, et al. (1996). "Characterization of oriented oligo(phenylenevinylene) films and nano-aggregates by UV/Vis-absorption and fluorescence spectroscopy." Synthetic Metals **83**(3): 221-226.

Eggeling, C., J. Widengren, et al. (2006). "Analysis of photobleaching in single-molecule multicolor excitation and forster resonance energy transfer measurement." Journal of Physical Chemistry A **110**(9): 2979-2995.

Enderlein, J., E. Toprak, et al. (2006). "Polarization effect on position accuracy of fluorophore localization." Optics Express **14**(18): 8111-8120.

Felekyan, S., R. Kuhnemuth, et al. (2005). "Full correlation from picoseconds to seconds by time-resolved and time-correlated single photon detection." Review of Scientific Instruments **76**(8).

Flors, C., C. N. J. Ravarani, et al. (2009). "Super-Resolution Imaging of DNA Labelled with Intercalating Dyes." Chemphyschem **10**(13): 2201-2204.

Förster, T. (1948). "Zwischenmolekulare Energiewanderung und Fluoreszenz." Annalen der Physik **437**(2): 55-75.

Franck, J. and E. G. Dymond (1926). "Elementary processes of photochemical reactions." Transactions of the Faraday Society **21**(February): 536-542.

Fries, J. R., L. Brand, et al. (1998). "Quantitative identification of different single-molecules by selective time-resolved confocal fluorescence spectroscopy." Journal of Physical Chemistry A **102**: 6601-6613.

Gansen, A., A. Valeri, et al. (2009). "Nucleosome disassembly intermediates characterized by single-molecule FRET." Proceedings of the National Academy of Sciences of the United States of America **106**(36): 15308-15313.

Gierschner, J., M. Ehni, et al. (2005). "Solid-state optical properties of linear polyconjugated molecules: pi-stack contra herringbone." Journal of Chemical Physics **123**(14).

Gierschner, J., H. G. Mack, et al. (2002). "Fluorescence and absorption spectra of oligophenylenevinylenes: Vibronic coupling, band shapes, and solvatochromism." Journal of Chemical Physics **116**(19): 8596-8609.

Grandbois, M., M. Beyer, et al. (1999). "How Strong Is a Covalent Bond?" Science **283**(5408): 1727-1730.

Ha, T., T. Enderle, et al. (1996). "Probing the interaction between two single molecules: Fluorescence resonance energy transfer between a single donor and a single acceptor." Proceedings of the National Academy of Sciences of the United States of America **93**(13): 6264-6268.

Heilemann, M., S. van de Linde, et al. (2008). "Subdiffraction-resolution fluorescence imaging with conventional fluorescent probes." Angewandte Chemie-International Edition **47**(33): 6172-6176.

Hell, S. W. and J. Wichmann (1994). "Breaking the diffraction resolution limit by stimulated-emission - stimulated-emission-depletion fluorescence microscopy." Optics Letters **19**(11): 780-782.

Hess, S. T., T. P. K. Girirajan, et al. (2006). "Ultra-high resolution imaging by fluorescence photoactivation localization microscopy." Biophysical Journal **91**(11): 4258-4272.

Hofstraat, J. W., J. Veurink, et al. (1998). "Charge-transfer fluorescent probes applied to the characterization of thermal and mechanical properties of polymers." Journal of Fluorescence **8**(4): 335-342.

Holden, S. J., S. Uphoff, et al. (2011). "DAOSTORM: an algorithm for high-density super-resolution microscopy." Nature Methods **8**(4): 279-280.

Horner, L. (1943). "Ein Beitrag zur Frage der Gültigkeit und Anwendung der Lorentz-Lorenz'schen Beziehung auf makromolekulare Stoffe." Journal für Makromolekulare Chemie **1**: 234-246.

Huang, B., M. Bates, et al. (2009). Super-Resolution Fluorescence Microscopy. Annual Review of Biochemistry. Palo Alto, Annual Reviews. **78:** 993-1016.

Hugel, T., N. B. Holland, et al. (2002). "Single-molecule optomechanical cycle." Science **296**(5570): 1103-1106.

Ikawa, T., T. Shiga, et al. (2002). "Measurement of residual stresses in injection-molded polymer parts by time-resolved fluorescence." Journal of Applied Polymer Science **83**(12): 2600-2603.

Invitrogen. (2011). "Fluorescence Properties of Alexa dyes." from http://www.invitrogen.com/site/us/en/home/References/Molecular-Probes-The-Handbook/Technical-Notes-and-Product-Highlights/The-Alexa-Fluor-Dye-Series.html.

ISS. (2011). "Lifetime data of selected fluorophores." from http://www.iss.com/resources/reference/data_tables/LifetimeDataFluorophores.html.

Jabarin, S. A. (1991). "Orientation studies of poly(vinyl chloride). Part I: Intrinsic birefringence." Polymer Engineering and Science **31**(9): 638-643.

Janissen, R. (2008). Biomolecular based nano-manipulation with a combined atomic force microscope and single molecule fluorescence setup. Institut für Physikalische Chemie Düsseldorf, Heinrich-Heine Universität.

Johnstone, R. A. W. and M. E. Rose (1979). "A rapid, simple, and mild procedure for alkylation of phenols, alcohols, amides and acids." Tetrahedron **35**(18): 2169-2173.

Jones, S. A., S. H. Shim, et al. (2011). "Fast, three-dimensional super-resolution imaging of live cells." Nature Methods **8**(6): 499-U496.

Joo, C., S. A. McKinney, et al. (2004). "Exploring rare conformational species and ionic effects in DNA Holliday junctions using single-molecule spectroscopy." Journal of Molecular Biology **341**(3): 739-751.

Jungmann, R., C. Steinhauer, et al. (2010). "Single-Molecule Kinetics and Super-Resolution Microscopy by Fluorescence Imaging of Transient Binding on DNA Origami." Nano Letters **10**(11): 4756-4761.

Kalinin, S., S. Felekyan, et al. (2007). "Probability distribution analysis of single-molecule fluorescence anisotropy and resonance energy transfer." Journal of Physical Chemistry B **111**(34): 10253-10262.

Kalinin, S., A. Valeri, et al. (2010). "Detection of Structural Dynamics by FRET: A Photon Distribution and Fluorescence Lifetime Analysis of Systems with Multiple States." Journal of Physical Chemistry B **114**(23): 7983-7995.

Kasha, M. (1950). "Characterization of electronic transitions in complex molecules." Discussion of the Faraday Society **9**: 14.

Kasper, R., B. Harke, et al. (2010). "Single-Molecule STED Microscopy with Photostable Organic Fluorophores." Small **6**(13): 1379-1384.

Keller, P. J., A. D. Schmidt, et al. (2010). "Fast, high-contrast imaging of animal development with scanned light sheet-based structured-illumination microscopy." Nature Methods **7**(8): 637-U655.

Keller, P. J., A. D. Schmidt, et al. (2008). "Reconstruction of Zebrafish Early Embryonic Development by Scanned Light Sheet Microscopy." Science **322**(5904): 1065-1069.

Kittel, R. J., C. Wichmann, et al. (2006). "Bruchpilot promotes active zone assembly, Ca2+ channel clustering, and vesicle release." Science **312**(5776): 1051-1054.

Klàn, P. and J. Wirz (2009). Photochemistry of Organic Compounds. West Sussex, Wiley-Blackwell.

Klessinger, M. and J. Michl (1989). Lichtabsorption und Photochemie organischer Moleküle. Weinheim, VCH.

Koslowski, A., M. E. Beck, et al. (2003). "Implementation of a general multireference configuration interaction procedure with analytic gradients in a semiempirical context using the graphical unitary group approach." Journal of Computational Chemistry **24**(6): 714-726.

Kubin, R. F. and A. N. Fletcher (1982). "Fluorescence quantum yields of some rhodamine dyes." Journal of Luminescence **27**(4): 455-462.

Kühnemuth, R. and C. A. M. Seidel (2001). "Principles of Single Molecule Multiparameter Fluorescence Spectroscopy." Single Molecules **2**(4): 251-254.

Kural, C., H. Balci, et al. (2005). "Molecular motors one at a time: FIONA to the rescue." Journal of Physics-Condensed Matter **17**(47): S3979-S3995.

Kusba, J. and J. R. Lakowicz (1999). "Definition and properties of the emission anisotropy in the absence of cylindrical symmetry of the emission field: Application to the light quenching experiments." Journal of Chemical Physics **111**(1): 89-99.

Lakowicz, J. R. (1999). Principles of Fluorescence Spectroscopy. New York, Kluwer Academic/ Plenum Publishers.

Lakowicz, J. R. (2006). Principles of Fluorescence Spectroscopy. New York, Springer.

Lee, J., S. Lee, et al. (2010). "Single-Molecule Four-Color FRET." Angewandte Chemie-International Edition **49**(51): 9922-9925.

Lee, S., J. Lee, et al. (2010). "Single-Molecule Three-Color FRET with Both Negligible Spectral Overlap and Long Observation Time." Plos One **5**(8).

Lepecq, J. B. and C. Paoletti (1967). "A fluorescent complex between ethidium bromide and nucleic acids - physical-chemical characterization." Journal of Molecular Biology **27**(1): 87-&.

Löwe, C. and C. Weder (2002). "Oligo(p-phenylene vinylene) excimers as molecular probes: Deformation-induced color changes in photoluminescent polymer blends." Advanced Materials **14**(22): 1625-1629.

Maddux, T., W. J. Li, et al. (1997). "Stepwise synthesis of substituted oligo(phenylenevinylene) via an orthogonal approach." Journal of the American Chemical Society **119**(4): 844-845.

Mataga, N., Y. Kaifu, et al. (1955). "The solvent effect on fluorescence spectrum - change of solute-solvent interaction during lifetime of excited solute molecule." Bulletin of the Chemical Society of Japan **28**(8): 690-691.

Mataga, N., Y. Kaifu, et al. (1956). "Solvent effects upon fluorescence spectra and the dipolemoments of excited molecules." Bulletin of the Chemical Society of Japan **29**(4): 465-470.

McCann, J. J., U. B. Choi, et al. (2010). "Optimizing Methods to Recover Absolute FRET Efficiency from Immobilized Single Molecules." Biophysical Journal **99**(3): 961-970.

McKinney, S. A., A. C. Declais, et al. (2003). "Structural dynamics of individual Holliday junctions." Nature Structural Biology **10**(2): 93-97.

Meier, H., U. Stalmach, et al. (1997). "Effective conjugation length and UV/vis spectra of oligomers." Acta Polymerica **48**: 379-384.

Micro-Photon-Devices. (2011). "PDM series Datasheet." 2011, from http://www.microphotondevices.com/media/pdf/PDM.pdf.

Microscopy-Resource-Center. (2011). "Alignment of objective-based TIRF systems." 2011, from http://www.olympusmicro.com/primer/techniques/fluorescence/tirf/objectivealign.html.

Nygren, J., N. Svanvik, et al. (1998). "The interactions between the fluorescent dye thiazole orange and DNA." Biopolymers **46**(1): 39-51.

Odell, J. A. and A. Keller (1986). "Flow-induced chain fracture of isolated linear macromolecules in solution." Journal of Polymer Science Part B-Polymer Physics **24**(9): 1889-1916.

Onsager, L. (1936). "Electric moments of molecules in liquids." Journal of the American Chemical Society **58**: 1486-1493.

Ozkan, H. S., T. Oskay, et al. (1994). "The mechanical anisotropy of stratified polyvinyl-chloride." Journal of Polymer Science Part B-Polymer Physics **32**(4): 631-640.

Perkin-Elmer. (2011). "Single Photon Counting Module - SPCM-AQR Series." 2011, from http://www.htds.fr/doc/optronique/scientifiqueBiomedical/SPCM-AQR.pdf.

Petty, J. T., J. A. Bordelon, et al. (2000). "Thermodynamic characterization of the association of cyanine dyes with DNA." Journal of Physical Chemistry B **104**(30): 7221-7227.

Pfiffi, D. (2010). Steigerung der Signalstärke und der Photostabilität von Fluorophoren in der Einzelmolekülspektroskopie. Institut für Physikalische Chemie Düsseldorf, Heinrich-Heine-Universität.

Rao, C. N. R., S. Singh, et al. (1976). "Spectroscopic studies of solute-solvent interactions." Chemical Society Reviews **5**(3): 297-316.

Rasnik, I., S. A. McKinney, et al. (2006). "Nonblinking and longlasting single-molecule fluorescence imaging." Nature Methods **3**(11): 891-893.

Richert, M. (2011). Private discussions.

Rider, J. G. and E. Hargreaves (1970). "Optical anisotropy in oriented polyvinyl chloride." Journal of Physics D-Applied Physics **3**(7): 993-1008.

Robinson, M. E. R., D. I. Bower, et al. (1978). "Molecular-orientation in polyvinyl-chloride studied by raman-spectroscopy and birefringence measurements." Journal of Polymer Science Part B-Polymer Physics **16**(12): 2115-2138.

Röhrig, U. F., U. Troppmann, et al. (2003). "Organic chromophores under tensile stress." Chemical Physics **289**(2-3): 381-388.

Roy, R., S. Hohng, et al. (2008). "A practical guide to single-molecule FRET." Nature Methods **5**(6): 507-516.

Rust, M. J., M. Bates, et al. (2006). "Sub-diffraction-limit imaging by stochastic optical reconstruction microscopy (STORM)." Nature Methods **3**(10): 793-795.

Schermelleh, L., R. Heintzmann, et al. (2010). "A guide to super-resolution fluorescence microscopy." Journal of Cell Biology **190**(2): 165-175.

Schindler, F., J. M. Lupton, et al. (2004). "A universal picture of chromophores in Ò-conjugated polymers derived from single-molecule spectroscopy." Proceedings of the National Academy of Sciences of the United States of America **101**(41): 14695-14700.

Schmitz, D. (2009). Polymergebundene Chromophore: Optische Kraftsensoren und photoprotektive Komponenten in gelben Intraokularlinsen. Institut für Organische Chemie und Makromolekulare Chemie. Düsseldorf, Heinrich-Heine Universität.

Schoen, I., J. Ries, et al. (2011). "Binding-activated localization microscopy of DNA structures." Nano Letters **11**(9): 4008-4011.

Schuler, B. and W. A. Eaton (2008). "Protein folding studied by single-molecule FRET." Current Opinion in Structural Biology **18**(1): 16-26.

Schuler, B., E. A. Lipman, et al. (2002). "Probing the free-energy surface for protein folding with single-molecule fluorescence spectroscopy " Nature **419**: 743-747.

Sharonov, A. and R. M. Hochstrasser (2006). "Wide-field subdiffraction imaging by accumulated binding of diffusing probes." Proceedings of the National Academy of Sciences of the United States of America **103**(50): 18911-18916.

Shindo, Y., B. E. Read, et al. (1968). "Study of orientation of polyvinyl chloride films by means of birefringence and infrared, visible and ultraviolet dichroism." Macromolecular Chemistry and Physics **118**(NOV): 272-312.

Sieber, J. J., K. I. Willig, et al. (2006). "The SNARE motif is essential for the formation of syntaxin clusters in the plasma membrane." Biophysical Journal **90**(8): 2843-2851.

Sin, K. K., C. P. Y. Chan, et al. (2006). "A highly sensitive fluorescent immunoassay based on avidin-labeled nanocrystals." Analytical and Bioanalytical Chemistry **384**(3): 638-644.

Sindbert, S., S. Kalinin, et al. (2011). "Accurate distance determination of nucleic acids via Förster resonance energy transfer: implications of dye linker length and rigidity." Journal of the American Chemical Society **133**(8): 2463-2480.

Sisamakis, E., A. Valeri, et al. (2010). "Accurate single-molecule FRET studies using multiparameter fluorescence detection." Methods in enzymology **475**: 455-514.

Spano, F. C. (2002). "Absorption and emission in oligo-phenylene vinylene nanoaggregates: The role of disorder and structural defects." Chemical Physics **116**(13): 5877-5891.

Springer, H., R. Neuert, et al. (1983). "Orientation of fluorescent-probes and polymer segments in uniaxially drawn polycarbonate and polyvinylchloride films as revealed by dichroism, fluorescence polarization and birefringence." Colloid and Polymer Science **261**(10): 800-804.

Stallinga, S. and B. Rieger (2010). "Accuracy of the Gaussian Point Spread Function model in 2D localization microscopy." Optics Express **18**(24): 24461-24476.

Stokes, G. G. (1852). "On the Change of Refrangibility of Light." Philosophical Transactions of the Royal Society of London **142**: 463-562.

Strickler, S. J. and R. A. Berg (1962). "Relationship between absorption intensity and fluorescence lifetime of molecules." Journal of Chemical Physics **37**: 814-822.

Stryer, L. (1978). "Fluorescence energy transfer as a spectroscopic ruler." Annual Review of Biochemistry **47**: 819-846.

TAP. (2011). "Teaching Advanced Physics, Episode 323: Diffraction." 2011, from http://tap.iop.org/vibration/superpostion/323/page_46776.html.

Thompson, R. E., D. R. Larson, et al. (2002). "Precise nanometer localization analysis for individual fluorescent probes." Biophysical Journal **82**(5): 2775-2783.

Toptygin, D. (2003). "Effects of the solvent refractive index and its dispersion on the radiative decay rate and extinction coefficient of a fluorescent solute." Journal of Fluorescence **13**(3): 201-219.

Tretiak, S., A. Saxena, et al. (2002). "Conformational dynamics of photoexcited conjugated molecules." Physical Review Letters **89**(9): 097402.

Turro, N. J. (1991). Modern Molecular Photochemistry. Mill Valley, CA, University Science Books.

Uphoff, S., K. Gryte, et al. (2011). "Improved Temporal Resolution and Linked Hidden Markov Modeling for Switchable Single-Molecule FRET." Chemphyschem **12**(3): 571-579.

Valeri, A. (2009). Fluorescence Resonance Energy Transfer between multiple chromophores studied by single-molecule spectroscopy. Institut für Physikalische Chemie Düsseldorf, Heinrich-Heine Universität.

Valeri, A., S. Felekyan, et al. (2011). "Single-molecule FRET measures intermediates and fast dynamics of a DNA Holliday junction." unpublished work.

van de Linde, S., M. Sauer, et al. (2008). "Subdiffraction-resolution fluorescence imaging of proteins in the mitochondrial inner membrane with photoswitchable fluorophores." Journal of Structural Biology **164**(3): 250-254.

Vanden Bout, D. A., W. T. Yip, et al. (1997). "Discrete intensity jumps and intramolecular electronic energy transfer in the spectroscopy of single conjugated polymer molecules." Science **277**(5329): 1074-1077.

Vogel, S. S., C. Thaler, et al. (2009). Time-resolved fluorescence anisotropy. FLIM Microscopy in Biology and Medicine. A. Periasamy and R. M. Clegg, Taylor & Francis Ltd**:** 472.

Westphal, V., S. O. Rizzoli, et al. (2008). "Video-rate far-field optical nanoscopy dissects synaptic vesicle movement." Science **320**(5873): 246-249.

Widengren, J., V. Kudryavtsev, et al. (2006). "Single-molecule detection and identification of multiple species by multiparameter fluorescence detection." Analytical Chemistry **78**(6): 2039-2050.

Widengren, J., E. Schweinberger, et al. (2001). "Two new concepts to measure fluorescence resonance energy transfer via fluorescence correlation spectroscopy: Theory and experimental realizations." Journal of Physical Chemistry A **105**(28): 6851-6866.

Wozniak, A. K., G. F. Schroder, et al. (2008). "Single-molecule FRET measures bends and kinks in DNA." Proceedings of the National Academy of Sciences of the United States of America **105**(47): 18337-18342.

Yalcin, B. and M. Cakmak (2005). "Molecular orientation behavior of poly(vinyl chloride) as influenced by the nanoparticles and plasticizer during uniaxial film stretching in the rubbery stage." Journal of Polymer Science Part B-Polymer Physics **43**(6): 724-742.

Yildiz, A. and P. R. Selvin (2005). "Fluorescence imaging with one manometer accuracy: Application to molecular motors." Accounts of Chemical Research **38**(7): 574-582.

ZEISS. (2011). "Practical Aspects of PALM Imaging." 2011, from http://zeiss-campus.magnet.fsu.edu/articles/superresolution/palm/practicalaspects.html.

10 Danksagung

An dieser Stelle möchte ich all den Menschen ein Dankeschön aussprechen, die mich im Laufe der letzten Jahre begleitet haben und zum Gelingen dieser Arbeit beigetragen haben.

Zuerst möchte ich mich bei meinem Betreuer Prof. Claus Seidel bedanken, der mir die Möglichkeit gegeben hat, dass ich die verschiedenen Projekten um das Thema Fluoreszenz bearbeiten durfte. Dazu wurden mir die neuesten technischen Geräte und alle benötigten Chemikalien unabhängig von den Kosten zur Verfügung gestellt. Seine Anmerkungen und Ideen haben mich immer wieder in die richtige Richtung gelenkt.

Dem Koreferenten Prof. Dr. P. Gilch möchte ich herzlich für die umkomplizierte Kooperation zur fristgerechten Abgabe und bei der Terminwahl für die Verteidigung dieser Arbeit danken.

Ein ganz besonderer Dank gilt Dr. Ralf Kühnemuth, der mich über die gesamte Zeit intensiv betreut hat. Die vielen „Hier, geht doch"-Situationen, nachdem man stundenlang nach Lösungen gesucht hat, waren sehr lehrreich.

Meinem Mitstreiter Denis Dörr danke ich für die vielen gemeinsamen Stunden im dunklen Labor auf der Suche nach der Nadel im Heuhaufen. Die Zusammenarbeit mit ihm ging weit über das Maß hinaus, was man von einem Kollegen erwarten kann.

Dr. Stanislav Kalinin und Dr. Suren Felekyan danke ich für ihre tatkräftige Hilfe bei der Lösung von Programmieraufgaben. Ohne ihre Hilfe wäre diese Arbeit in der Form sicher nicht realisierbar gewesen.

Für die Entwicklung und Ausarbeitungen der in dieser Arbeit verwendeten Oberflächenprotokolle bedanke ich mich bei Dr. Richard Janissen. Die vielen gemeinsamen Treffen auch abseits der Forschung werden mir in guter Erinnerung bleiben.

Markus Richert danke ich insbesondere für seine Fachkenntnisse bei der Mitarbeit und Verbesserung der verwendeten Oberflächenprotokolle und Pufferzusammensetzungen. Ausserdem hatten wir hier eine sehr lustige gemeinsame Zeit, aus der eine intensive Freundschaft entstanden ist.

Dem Bachelorstudenten Igor Svetec möchte ich für die gute Zusammenarbeit bei der Durchführung und Auswertung der iPAINT- und FRET-Experimente danken.

Meiner Bürokollegin Stephanie Grabowski danke ich für die gemeinsame Arbeit an unseren Projekten und für Ihre Geduld, mich ständig in Ihrer Nähe zu haben.

Unserem Netzwerkadministrator Marcel Merkwitz danke ich ganz besonders für die schnelle Hilfe bei Computerproblemen jeglicher Art. Aber noch einmal trage ich seine Rigips-Platten nicht bis unter das Dach.

Bei Martin Schramm bedanke ich mich für die Entwicklung des Simpots und weiteren zuverlässig abeitenden elektronischen Bauteilen.

Unseren Sekretärinnen Veronika Mendorf, Bärbel Hofmann und Bettina Kerbl danke ich dafür, dass Sie für uns viele Aufgaben erledigen, damit wir unsere Forschung betreiben können.

Bei allen aktuellen und ehemaligen Mitarbeitern unseres Institutes möchte ich mich allgemein für das freundliche Arbeitsklima und die gemeinsame Zusammenarbeit herzlichst bedanken.

Bei meinen Eltern möchte ich mich für die liebevolle Erziehung und das von Ihnen geschaffene solide Fundament bedanken, auf dem ich alle meine bisherigen Lebensabschnitte aufbauen konnte.

Meiner restlichen Familie und der Familie meiner Verlobten Tanja danke ich für Ihre Liebe und Unterstützung in allen Lebenslagen.

Meiner großen Liebe Tanja gilt das Schlusswort. Ohne sie wäre das ganze Leben nur halb so schön.

11 Erklärung

Hiermit erkläre ich, dass ich die Promotion mit dem Thema

"Fluorescence Spectroscopy and Imaging of polymer bound fluorophores and immobilised biomolecules"

am Institut für Physikalische Chemie und Elektrochemie II der Heinrich-Heine- Universität Düsseldorf unter der Leitung von Prof. Dr. Claus A.M. Seidel eigenständig und ohne unerlaubte Hilfe angefertigt und in der vorgelegten oder in ähnlicher Form noch bei keiner anderen Institution eingereicht habe.

Es existieren keine vorherigen Promotionsversuche.

Düsseldorf, den 23.11.2011